FREE AND FORCED VIBRATION ANALYSIS OF FUNCTIONALLY GRADED PIEZOELECTRIC ENERGY HARVESTERS USING WEAK FORM QUADRATURE ELEMENT METHOD

A THESIS SUBMITTED TO
THE GRADUATE SCHOOL OF NATURAL AND APPLIED SCIENCES
OF
MIDDLE EAST TECHNICAL UNIVERSITY

BY

RAGIP SARPER YILDIZ

IN PARTIAL FULFILLMENT OF THE REQUIREMENTS
FOR
THE DEGREE OF MASTER OF SCIENCE
IN
MECHANICAL ENGINEERING

AUGUST 2023

Approval of the thesis:

FREE AND FORCED VIBRATION ANALYSIS OF FUNCTIONALLY GRADED PIEZOELECTRIC ENERGY HARVESTERS USING WEAK FORM QUADRATURE ELEMENT METHOD

submitted by **RAGIP SARPER YILDIZ** in partial fulfillment of the requirements for the degree of **Master of Science in Mechanical Engineering, Middle East Technical University** by,

Prof. Dr. Halil Kalıpçılar
Dean, Graduate School of **Natural and Applied Sciences** _____

Prof. Dr. M.A. Sahir Arıkan
Head of the Department, **Mechanical Engineering** _____

Prof. Dr. Serkan Dağ
Supervisor, **Mechanical Engineering, METU** _____

Examining Committee Members:

Prof. Dr. F. Suat Kadıoğlu
Mechanical Eng, METU _____

Prof. Dr. Serkan Dağ
Mechanical Eng, METU _____

Assoc. Prof. Dr. Ulaş Yaman
Mechanical Eng, METU _____

Assist. Prof. Dr. Hakan Çalışkan
Mechanical Eng, METU _____

Assoc. Prof. Dr. Mehmet Nurullah Balcı
Mechanical Eng, Hacettepe Uni. _____

Date: 23.08.2023

I hereby declare that all information in this document has been obtained and presented in accordance with academic rules and ethical conduct. I also declare that, as required by these rules and conduct, I have fully cited and referenced all material and results that are not original to this work.

Name Last name : Ragıp Sarper Yıldız

Signature :

ABSTRACT

FREE AND FORCED VIBRATION ANALYSIS OF FUNCTIONALLY GRADED PIEZOELECTRIC ENERGY HARVESTERS USING WEAK FORM QUADRATURE ELEMENT METHOD

Yıldız, Ragıp Sarper
Master of Science, Mechanical Engineering
Supervisor: Prof. Dr. Serkan Dağ

August 2023, 197 pages

The weak form quadrature element method is used in this study to examine the free and forced vibration behavior of functionally graded piezoelectric energy harvester Timoshenko beams. Six piezoelectric energy harvester structures with and without tip mass are formulated, including unimorph and series- or parallel-connected bimorph types. Piezoelectric constitutive equations that couple mechanical strain with electrical displacement are derived to specify piezoelectric materials' electrical and mechanical characteristics. The Timoshenko Beam Theory is used to determine the displacement fields. The beam's total kinetic, strain, and internal electrical energies and the non-conservative mechanical and electrical forces are computed to obtain the equation of motion by applying the extended Hamilton's principle. The quadrature beam element is constructed after a detailed description of the weak-form quadrature element method principles. The displacement functions are altered in accordance with the numerical technique. The free and forced vibration governing formulations are defined separately. Harmonic base displacement is applied to the equation of motion for a steady-state response. In contrast, the work equivalent method is implemented to incorporate externally applied forces into the numerical computation for forced vibration. The used external load types are uniformly distributed step, concentrated step, concentrated harmonic, and concentrated

impulsive loads. Dynamic outcomes are achieved by applying the Houbolt and Newmark methods. The steady-state behavior of the piezoelectric energy harvester under base excitation is formulated to validate the methodology by comparing the voltage output frequency response function and natural frequency values in open- and short-circuit states with experimental findings in the literature. Moreover, an analytical solution constructed for the beam displacement response under the four types of external loads is used to validate the numerical method's efficiency for forced vibration. In parametric analysis, while the Mori-Tanaka micromechanical model is used to demonstrate the influence of substructure material inhomogeneity, Voigt's rule serves for the piezoelectric characteristics. Frequency response curves and dynamic analysis results are analyzed for six piezoelectric energy harvester configurations regarding load resistance, power-law exponent, tip mass addition, boundary condition, and material structure changes. The weak form quadrature element method is an alternative numerical analysis approach that gives accurate and precise free and forced vibration results that can be easily applied in the design and analysis studies of non-homogeneous functionally graded materials.

Keywords: Functionally Graded Piezoelectric Material, WQEM, Timoshenko Beam Theory, Frequency Response Function, Dynamic Analysis

ÖZ

FONKSİYONEL OLARAK DERECELENDİRİLMİŞ PİEZOELEKTRİK ENERJİ TOPLAYICILARIN ZAYIF BİÇİMLİ KARELEME ELEMAN YÖNTEMİ İLE SERBEST VE ZORLANMIŞ TİTREŞİM ANALİZİ

Yıldız, Ragıp Sarper
Yüksek Lisans, Makina Mühendisliği
Tez Yöneticisi: Prof. Dr. Serkan Dağ

Ağustos 2023, 197 sayfa

Bu çalışmada, fonksiyonel olarak derecelendirilmiş piezoelektrik enerji toplayıcı Timoshenko kirişlerine serbest ve zorlanmış titreşim davranışını incelemek için zayıf biçimli kareleme eleman metodu uygulanmaktadır. Ucunda harici kütlesi olan ve olmayan altı piezoelektrik enerji toplayıcı, tek biçimli ve seri veya paralel bağlı çift biçimli yapılarda formülize edilmektedir. Piezo malzemelerin elektriksel ve mekanik özelliklerini belirtmek için mekanik gerinimi elektriksel yer değiştirmeyle ilişkilendiren piezoelektrik kurucu denklemler türetilmiştir. Timoshenko Kiriş Teorisi, yer değiştirme alanlarını belirlemek için kullanılır. Genişletilmiş Hamilton prensibi uygulayarak hareket denklemini elde etmek için kirişin toplam kinetik, gerinim, dahili elektrik enerjileri ile korunumlu olmayan mekanik ve elektrik kuvvetleri hesaplanır. Karelenmiş kiriş elemanı, zayıf biçimli kareleme eleman yöntemi ilkelerinin ayrıntılı bir açıklamasından sonra oluşturulmaktadır. Yer değiştirme fonksiyonları sayısal tekniğe uygun olarak değiştirilir. Serbest ve zorlanmış titreşimi yöneten formülasyonlar ayrı ayrı tanımlanmaktadır. Kararlı hal titreşim sonuçları için hareket denklemine harmonik baz yer değiştirmesi uygulanır. Buna karşılık, zorlanmış titreşim sonuçları için sayısal hesaplamaya harici olarak uygulanan kuvvetleri dahil etmek için iş eşdeğeri yöntemi uygulanmaktadır.

Uygulanan harici yük türleri, düzgün dağılmış adım tipi, konsantre adım tipi, konsantre harmonik ve konsantre itici yüklerdir. Houbolt ve Newmark yöntemleri kullanılarak dinamik sonuçlar elde edilir. Piezoelektrik enerji toplayıcının baz uyarımı altında kararlı durum davranışı, voltaj frekans cevap fonksiyonu çıktıları ve açık - kısa devre durumlarındaki doğal frekans değerlerini literatürdeki deneysel bulgular ile karşılaştırarak metodu doğrulaması nedeniyle formülize edilmiştir. Ek olarak, zorlanmış titreşim sonuçları için sayısal yöntemin etkinliğini doğrulamak üzere, dört farklı dış yük altında kiriş yer değiştirme tepkisi için oluşturulmuş bir analitik çözüm kullanılır. Parametrik analizde, temel yapı malzemesinin homojensizlik etkisini göstermek için Mori-Tanaka mikromekanik modeli kullanılırken, piezoelektrik özellikler için Voigt kuralı uygulanır. Altı piezoelektrik enerji toplayıcı konfigürasyonu için oluşturulan frekans cevap eğrileri ve dinamik analiz sonuçları kullanılarak yük direnci, kuvvet kanunu üssü, uç kütle ilavesi, sınır koşulu ve malzeme yapısı değişiklikleri ile ilgili sonuçlar analiz edilir. Zayıf biçimli kareleme eleman yöntemi, homojen olmayan fonksiyonel derecelendirilmiş malzemelerin tasarım ve analiz çalışmalarında kolaylıkla uygulanabilen doğru ve kesin serbest ve zorlanmış titreşim sonuçları veren alternatif bir sayısal analiz metodudur.

Anahtar Kelimeler: Fonksiyonel Derecelendirilmiş Piezoelektrik Malzeme, WQEM, Timoshenko Kiriş Teorisi, Frekans Cevap Fonksiyonu, Dinamik Analiz

To my wife Melahat and my family

ACKNOWLEDGMENTS

First of all, I would like to express my special thanks to my supervisor, Prof. Dr. Serkan Dağ, for his unending support, guidance, and perspective throughout my MSc. study. This long-term study could not have been accomplished without his guidance.

Secondly, I would like to thank the jury members for their informative comments and suggestions.

Additionally, I appreciate the support from Dr. Hüseyin Emrah Konokman and Mehmet Sarper Yavuz, who are my superiors at The Scientific and Technological Research Council of Turkey (TUBITAK) Defense Industries Research and Development Institute (SAGE).

Finally, I would be happy to express my thanks to my wife, Melahat Yapıcı Yıldız, who has kept me motivated throughout this research. It is wonderful to feel her support behind me every moment. The most considerable effort belongs to my family, especially my mother, Dilek Yıldız. I owe them my gratitude.

TABLE OF CONTENTS

LIST OF TABLES

TABLES

LIST OF FIGURES

FIGURES

LIST OF ABBREVIATIONS

ABBREVIATIONS

BC: Boundary Condition

CLG: Chebyshev-Lobatto-Gauss

DQ: Differential Quadrature

FEM: Finite Element Method

FG: Functionally Graded

FGM: Functionally Graded Material

FGPM: Functionally Graded Piezoelectric Material

FRF: Frequency Response Function

GLL: Gauss-Lobatto-Legendre

PEH: Piezoelectric Energy Harvester

PVDF: Polyvinylidene Fluoride

PZT: Lead Zirconate Titanate

SDOF: Single-Degree-of-Freedom

TBT: Timoshenko Beam Theory

WQEM: Weak-form Quadrature Element Method

LIST OF SYMBOLS

SYMBOLS

A_{11}^{pl}: Extensional shear rigidity of the lower piezoelectric material

A_{11}^{pu}: Extensional shear rigidity of the upper piezoelectric material

A_{11}^{s}: Extensional shear rigidity of the substructure

B_{11}^{pl}: Coupling shear rigidity of the lower piezoelectric material

B_{11}^{pu}: Coupling shear rigidity of the upper piezoelectric material

B_{11}^{s}: Coupling shear rigidity of the substructure

D_{11}^{pl}: Bending shear rigidity of the lower piezoelectric material

D_{11}^{pu}: Bending shear rigidity of the upper piezoelectric material

D_{11}^{s}: Bending shear rigidity of the substructure

F_{55}^{pl}: Transverse shear rigidity of the lower piezoelectric material

F_{55}^{pu}: Transverse shear rigidity of the upper piezoelectric material

F_{55}^{s}: Transverse shear rigidity of the substructure

B_{bp}^{pl}: Lower piezoelectric material coupling term for voltage and extension in parallel-connected bimorph configuration

B_{bs}^{pl}: Lower piezoelectric material coupling term for voltage and extension in series-connected bimorph configuration

B_{bp}^{pu}: Upper piezoelectric material coupling term for voltage and extension in parallel-connected bimorph configuration

B_{bs}^{pu}: Upper piezoelectric material coupling term for voltage and extension in series-connected bimorph configuration

B_u^{pu}: Upper piezoelectric material coupling term for voltage and extension in unimorph configuration

C_{bp}^{p}: Internal capacitance of the piezoelectric material in parallel-connected bimorph configuration

C_{bs}^{p}: Internal capacitance of the piezoelectric material in series-connected bimorph configuration

C_u^{p}: Internal capacitance of the piezoelectric material in unimorph configuration

I_1^{pl}: Kinetic energy constant 1 for the lower piezoelectric material

I_1^{pu}: Kinetic energy constant 1 for the upper piezoelectric material

I_1^{s}: Kinetic energy constant 1 for the substructure

I_2^{pl}: Kinetic energy constant 2 for the lower piezoelectric material

I_2^{pu}: Kinetic energy constant 2 for the upper piezoelectric material

I_2^{s}: Kinetic energy constant 2 for the substructure

I_3^{pl}: Kinetic energy constant 3 for the lower piezoelectric material

I_3^{pu}: Kinetic energy constant 3 for the upper piezoelectric material

I_3^{s}: Kinetic energy constant 3 for the substructure

J_{bp}^{pl}: Lower piezoelectric material coupling term for voltage and curvature in parallel-connected bimorph configuration

J_{bs}^{pl}: Lower piezoelectric material coupling term for voltage and curvature in series-connected bimorph configuration

J_{bp}^{pu}: Upper piezoelectric material coupling term for voltage and curvature in parallel-connected bimorph configuration

J_{bs}^{pu}: Upper piezoelectric material coupling term for voltage and curvature in series-connected bimorph configuration

J_{u}^{pu}: Upper piezoelectric material coupling term for voltage and curvature in unimorph configuration

b: Width of the piezoelectric material and substructure

h^{p}: Height of the piezoelectric material

h^{s}: Height of the substructure

h^{t}: Height of the tip mass

I_{t}: Tip mass moment of inertia

M_{t}: Tip mass

L: Length of the piezoelectric material and substructure

L^{t}: Length of the tip mass

k: Power-law exponent

B^{s}: Bulk modulus of the substructure

E^{s}: Elastic modulus of the substructure material

V^{s}: Volume fraction of the substructure

V_{l}^{s}: Volume fraction of the substructure lower portion

V_{u}^{s}: Volume fraction of the substructure upper portion

B_{e}^{s}: Effective bulk modulus of the substructure

E_{l}^{s}: Elastic modulus of the substructure material lower portion

μ^{s}: Shear modulus of the substructure material

μ_{e}^{s}: Effective shear modulus of the substructure

λ^s: Lame's constant

$\bar{c}_{11}^E$: Elastic modulus of the piezoelectric material at constant electric field

$\bar{c}_{55}^E$: Shear modulus of the piezoelectric material at constant electric field

ν^p: Poisson's ratio of the piezoelectric material

ν^s: Poisson's ratio of the substructure

ρ^{pl}: Density of the lower piezoelectric material

ρ^{pu}: Density of the upper piezoelectric material

ρ^s: Density of the substructure

ρ_l^s: Density of the substructure lower portion

ρ_u^s: Density of the substructure upper portion

A_{eq}: Equivalent area for the series-connected bimorph PEH without tip mass configuration

E_{eq}: Equivalent elastic modulus for the series-connected bimorph PEH without tip mass configuration

I_{eq}: Equivalent area moment of inertia for the series-connected bimorph PEH without tip mass configuration

ν_{eq}: Equivalent Poisson's ratio for the series-connected bimorph PEH without tip mass configuration

μ_{eq}: Equivalent shear modulus for the series-connected bimorph PEH without tip mass configuration

ρ_{eq}: Equivalent density for the series-connected bimorph PEH without tip mass configuration

W_m: Forced vibration analytical solution time-dependent variable

Q_m: Forced vibration analytical solution coefficient

m: Odd number used for forced vibration analytical solution

α_m: Forced vibration analytical solution natural frequency coefficient - 1

β_m: Forced vibration analytical solution natural frequency coefficient - 2

δ_m: Forced vibration analytical solution natural frequency coefficient - 3

θ_m: Forced vibration analytical solution natural frequency coefficient - 4

D: Electric displacement

$\overline{E}$: Electric field

$\overline{E}^{bpl}$: Electric field component of series-connected bimorph PEH for the lower piezoelectric material

$\overline{E}^{bpu}$: Electric field component of series-connected bimorph PEH for the top piezoelectric material

$\overline{E}^{bs}$: Electric field component of series-connected bimorph PEH

$\overline{E}^{u}$: Electric field component of unimorph PEH

d: Piezoelectric constant

$\bar{e}_{31}$: Effective piezoelectric stress constant

s^E: Elastic compliance constant at the constant electric field for the piezoelectric material

ϵ^{ε}: Permittivity (dielectric) constant at constant strain for piezoelectric material

ϵ^{σ}: Permittivity (dielectric) constant at constant stress for piezoelectric material

R_l: Resistive electrical load

v_b^p: Voltage for parallel-connected bimorph configuration

v_b^s: Voltage for series-connected bimorph configuration

v_u: Voltage for unimorph configuration

T: Kinetic energy

U: Strain energy

W_{ie}: Internal electrical energy

W_{nc}: Non-conservative mechanical and electrical energy

Q_e: Electrical charge output

A_{ij}: First-order derivative weighting coefficient with respect to x

H_j: Quadrature weight

l_j: Lagrange interpolation function

N: Node number

$\widetilde{N}$: Integration point

x_j: Quadrature abscissa on the Cartesian coordinate system

ξ: Quadrature abscissa on the natural coordinate system

x_0: Load applying point on the Cartesian coordinate system

ξ_0: Load applying point on the natural coordinate system

ν: Node deflection at the quadrature beam

ν_i: Node displacement vector

$\bar{\bar{\beta}}$: Newmark beta coefficient

$\bar{\bar{\gamma}}$: Newmark gama coefficient

ζ: Damping ratio

$\hat{\mu}$: Mass proportionality constant

$\hat{\gamma}$: Stiffness proportionality constant

q: Generalized coordinate

Q: Generalized non-conservative load

f: General time-dependent loading

f_0: Uniformly distributed load intensity

F: Concentrated load intensity

$\bar{F}$: Impulsive load intensity

F_i: Work equivalent load vector

H: Heaviside unit step function

δ: Dirac delta function

$[M]$: Mass matrix

$[K]$: Stiffness matrix

$[D]$: Damping matrix

$[Q]$: Force matrix

$[\theta]$: Electrical voltage matrix

$[q]$: Nodal displacement matrix

$[G]$: Steady-state response matrix

w_b: Base displacement

g: Base transverse displacement

h: Base rotational displacement

p_i: Base displacement constant

W_0: Base transverse displacement constant

θ_0: Base rotational displacement constant

e: Euler's number

σ: Stress

σ^l: Stress component for lower piezoelectric material

σ^u: Stress component for upper piezoelectric material

ε: Strain

ε^l: Strain component for lower piezoelectric material

ε^u: Strain component for upper piezoelectric material

γ: Shear strain

λ: Free vibration frequency parameter

ω: Excitation frequency

ω_0: Natural frequency

ω_p: Applied frequency

κ_s: Shear correction factor

t: Time

Δt: Time step

x: Axial direction

y: Longitudinal direction

z: Transverse direction

u_x: Axial displacement

u_y: Longitudinal displacement

u_z: Transverse displacement

u: Axial displacement of the Timoshenko beam

φ: Cross-sectional rotation on the central plane of the Timoshenko beam

w: Transverse displacement of the Timoshenko beam

U: Steady-state generalized axial coordinate

Φ: Steady-state generalized rotational coordinate

W: Steady-state generalized transverse coordinate

V: Steady-state generalized voltage coordinate

CHAPTER 1

INTRODUCTION

The quest for low-density and long-lasting materials has started concurrently with technological advancements since conventional materials can no longer satisfy engineers' and researchers' objectives. Especially in the highly competitive aviation industry, it is preferable for aircraft materials to be lighter without surrendering their strength and durability in order to save fuel. The researchers concentrated on composite materials to combine the most favorable properties of two or more materials to get the desired material quality. Composite materials provide various advantages over the properties of single materials such as metals, polymers, and ceramics. In addition, laminated composites constitute the majority for use as structural composite components. Materials with the desired strength, hardness, and impact resistance can be manufactured by arranging the laminates in different orientations. However, stress concentration at the junction of the laminates can cause fracture or adhesive bond separation. Since the 1980s, scientists have been developing functionally graded materials (FGMs) as a solution to this issue.

The environment contains various FGMs that might be either natural or manufactured. Teeth, bone, and bamboo are examples of natural FGMs. A typical bone structure's porosity and volume fraction varies from the inside to the exterior. The engineers applied gradation in composite materials as a result of being inspired by this situation observed in nature. First, different properties of metal and ceramic materials were integrated into FGMs. Metals that possess greater fracture toughness and ceramics with higher thermal resistance were merged to prevent stress concentration in the composite material. Furthermore, the mechanical characteristics of FGMs change continuously and smoothly from one surface to the next. The FGM may achieve both thermal conductivity and thermal barrier formation at the same time. FGMs are also used in armor plates and bulletproof vests due to one of their

most crucial qualities, crack propagation prevention. This property makes FGMs very important in the defense industry. Researchers have developed numerous techniques for characterizing the properties of FGMs. The two most commonly utilized systems are Voigt's rule of the mixture and Mori-Tanaka schemes [1]. The more well-known and uncomplicated Voigt mixing scheme is based on a simple mixing rule with power, exponential, and sigmoidal laws. However, the Mori-Tanaka scheme is used in this study for the core beam since it is more suited for the discontinuous particle phase of graded composites. The Mori-Tanaka approach enhances the accuracy of material characteristics of FGMs in numerical computations.

FGMs, unlike metals, do not possess isotropic characteristics. The mechanical characterization of FGMs that do not exhibit the same properties in all directions requires many more parameters. Their complexity makes the computation and experimentation of structural analysis more difficult. Furthermore, researchers prioritize numerical analysis methods because analytical formulations are complex as well. As a result, various numerical techniques for examining the dynamic analysis of FGMs have been developed. The finite element method (FEM) is the most extensively used of these numerical approaches, although research on numerical solution methods that produce simpler, faster, and more precise results is proceeding. The weak form quadrature element method (WQEM) is one of these techniques that is open to development and has the potential to become extensively used. The main advantage of this approach, which uses the rules of the differential quadrature (DQ) method, is that it converges quicker and yields precise results without requiring an explicit description of the shape function, as FEM does, allowing for the avoidance of unnecessary approaches caused by the shape function [2]. The WQEM has been used in the literature to analyze beams for static, buckling, and free vibration. Although forced vibration studies of beam materials are critical for researchers, studies employing the WQEM are minimal compared to other types of research. There have yet to be any studies specifically on piezoelectric energy harvesters (PEHs) using the WQEM, including dynamic forced vibration analysis.

This study aims to draw attention to the advantages of the WQEM and eliminate the shortcomings observed in the literature. In particular, the benefits of FGMs are coupled in PEHs, and the WQEM is used to generate solutions for free and forced vibration analysis.

Traditional battery systems can be challenging to maintain and replace in case of failure due to the inaccessibility of the parts where the battery is located. At the same time, batteries, which cause an increase in chemical waste, have encouraged researchers to develop alternative energy storage devices. PEHs were discovered to be significant since they can transform ambient residual energy into electrical energy to power small electronic devices. For instance, the continuous energy supply of base-excited PEHs on the wings of unmanned aerial vehicles can be given. In this way, the energy requirements of various electronic gadgets can be easily satisfied while the airplane is in flight. The Euler-Bernoulli, Rayleigh, and Timoshenko beam models are used in the literature to analyze PEHs. The Timoshenko Beam Theory (TBT), which considers shear deformation and axial and rotational inertia effects, deserves special consideration in these beam formulations. The present study accurately analyzes the free and forced vibrations of inhomogeneous functionally graded (FG) PEHs by applying the TBT. In summary, this study should be regarded as research that uses the WQEM, which can be easily applied to the design and analysis studies of PEHs to provide accurate and exact results.

1.1 Review of Functionally Graded Materials

FGM is an advanced inhomogeneous composite material in which two or more mechanical properties, such as Young's modulus of elasticity, shear modulus of elasticity, Poisson's ratio, and material density, change continuously and smoothly according to power-law form from one surface to the next. Japanese material scientists invented FGM in 1984 as a solution to the cracking or delamination of laminated composite space shuttle panels [3]. They first developed an FGM with the properties displayed in Figure 1.1 to prevent the separation of the ceramic material

that had been adhered to the metal due to stress concentration. High stresses appear at the interface due to the difference in thermal expansion coefficients of the metal and ceramic components, resulting in composite deterioration.

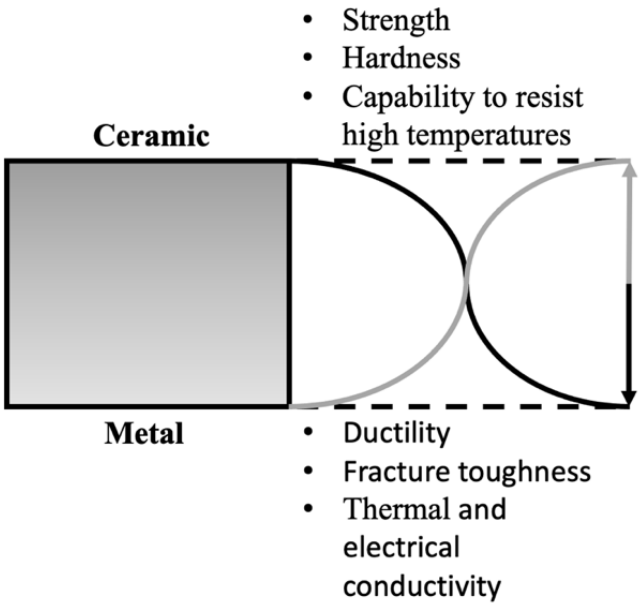

Figure 1.1. Varying properties of FG metal and ceramic materials.

It is possible to produce FGMs with varying properties that alter progressively or gradually. The composition and microstructure of the material change in the axial or transverse direction in a progressively changed FGM exhibit continuous property change. In contrast, a step-by-step transition is evident in the gradual change, similar to the laminated composite material structure. The FGMs may be graded based on the properties of volume fraction, shape, orientation, and size, as illustrated in Figure 1.2.

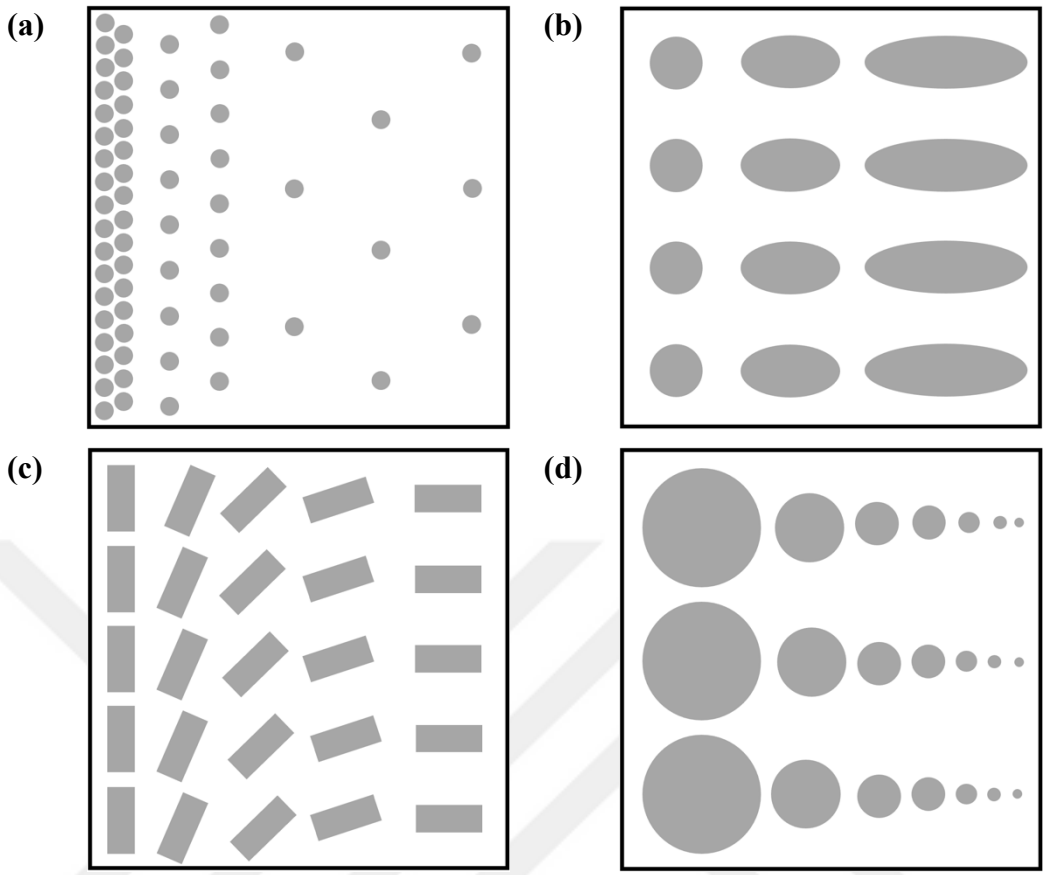

Figure 1.2. Gradation of FGMs based on (a) volume fraction, (b) shape, (c) orientation, and (d) size.

Researchers have developed many production methods for producing FGMs in the automotive, aerospace, defense, energy, and biomedical sectors. Manufacturing light, robust, and long-lasting parts in industries that employ FGMs is feasible. FGM production methods are divided into thin coating fabrication and bulk material fabrication. Thin coating procedures include chemical and physical vapor depositions and friction mixing, whereas powder metallurgy, casting, and additive manufacturing are used in bulk material production processes. The powder metallurgy process is the most significant and commonly utilized, in which two materials are mixed in the proper ratios in a ball- or V-shaped mill. The combined material is subsequently placed in molds that enable grading, as indicated in Figure 1.2, and sintering occurs. The FGM generated using this approach is an FG stepwise manner since it is hard to construct a continuously shifting section without applying

centrifugal force. The drawback of this centrifugal force used manufacturing technique is that the materials created are only cylindrical and simple in shape. The phases can be metal-metal, metal-ceramic, ceramic-ceramic, and metal-polymer.

FGM is also employed in PEHs due to its favorable structure. Including functionally graded piezoelectric material (FGPM) improves the reliability and operating performance of PEHs in both empirical and theoretical studies. The qualities of the materials used influence the efficiency of PEHs. Researchers have developed materials with high strength and electrical constants in order to generate energy without fracture propagation. PZT (lead zirconate titanate) for piezoceramics and PVDF (polyvinylidene fluoride) for piezopolymers are two examples of these materials. In this work, several metal and piezoceramic material combinations are employed to illustrate the effectiveness of PEHs.

1.2 Review of Piezoelectric Energy Harvesters

The production of a charge due to the inherent dipole moment in the material on certain crystals' surfaces when a load is applied is known as piezoelectricity, which Jacques and Pierre Curie discovered in 1880. Piezoelectric materials include quartz, Rochelle salt, and topaz. In the presence of an electric field, insulators align their electrical charges in the same direction as the electric field. The material can return to neutrality when the electric field is removed, but this is not the case with piezoelectric materials. "Poling" refers to polarizing piezoelectric materials that retain their polarized state even after removing the electric field influence.

Renewable energy sources such as wind, water, and the sun have traditionally been used to generate electricity since they do not have depletion limitations as fossil fuels. The two options for energy harvesting are small-scale and large-scale. mW or μW energy is collected on a small scale, whereas kW or MW energy is harvested on a large scale. Small-scale energy harvesting collects tiny amounts of energy from various ambient sources, mainly mechanical vibration, and stores it for later use,

allowing devices to create their power sources in an eco-friendly way. Energy harvesting eliminates the need for a battery system with a short lifespan, high maintenance expenses, and a heavy design. Electromagnetic, piezoelectric, and electrostatic mechanisms can transform vibrational energy into electrical energy. Typical sources of vibrational energy are fluid flow in pipelines, people walking, aircraft wings exposed to airflow, rotating machinery, conveyor belts, and vehicle movement. Piezoelectric energy conversion is distinguished by its high-power density and portable, simple construction. PEHs can supply power to tiny, low-power electronic components used in mechanical, aerospace, civil, and medical fields. PEHs necessitate the collaboration of mechanical, materials, and electrical engineers.

Piezoceramics and piezopolymers are piezoelectric materials that transform mechanical energy into electrical energy (direct effect) or generate mechanical strain in an electric field (inverse effect). Piezoceramics are more brittle than piezopolymers, although they produce more power because of their high electromechanical constants and a broad range of vibrational accessibility. PZT was invented as a piezoelectric transducer at the Tokyo Institute of Technology in the 1950s, and its several variants (especially PZT-5A and PZT-5H) are the most widely used engineering piezoceramics today. The most commonly used piezopolymer, PVDF, is a flexible semi-crystalline polymer that can be easily elongated, and it is suitable for shoes and backpacks because it bends easily and has a lower density than piezoceramics.

As shown in Figure 1.3, a typical PEH consists of one (unimorph) or series and parallel connections of two (bimorph) active piezoelectric materials connected to a cantilever-type inactive substructure layer with and without tip mass. A PEH is constructed from upper and lower piezoelectric materials and the core substructure. In this study, all layers exhibit FG properties in the z-direction. The Cartesian coordinate system passes through the midplane of the beam. In other words, $-h^s/2 - h^p \leq z \leq h^s/2 + h^p$ represents the change in a transverse direction. Cantilever-type PEH is preferred because of its straightforward construction, large

vibration displacements at the free end, maximum power production at resonance, and ease of fabrication. In addition, the clamped end undergoes base motion, and the voltage difference between the electrodes is caused by strain in the piezoelectric materials.

(a)

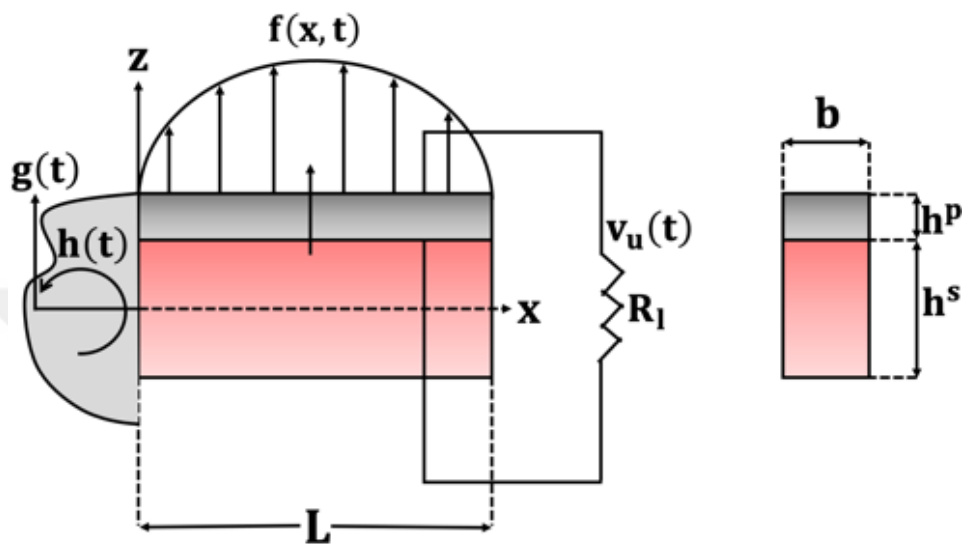

(b)

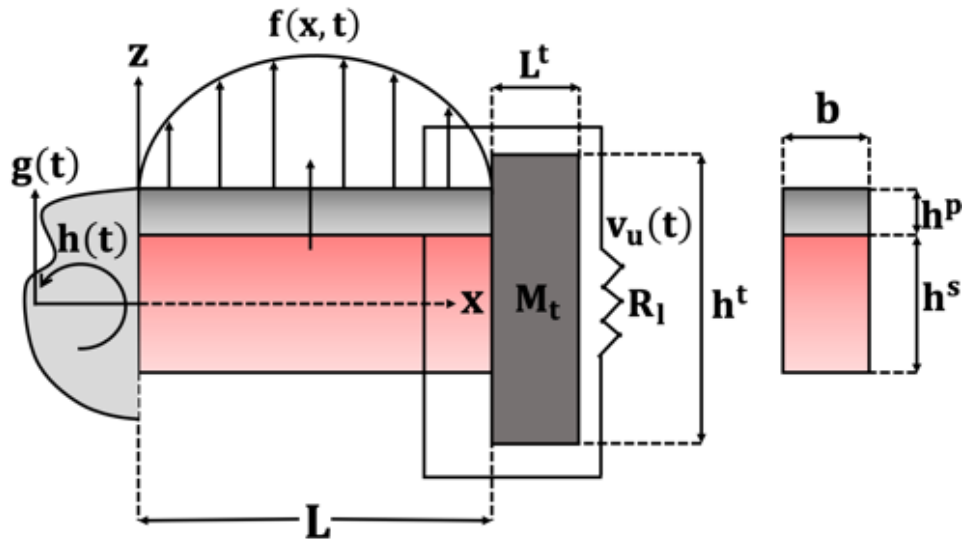

(c)

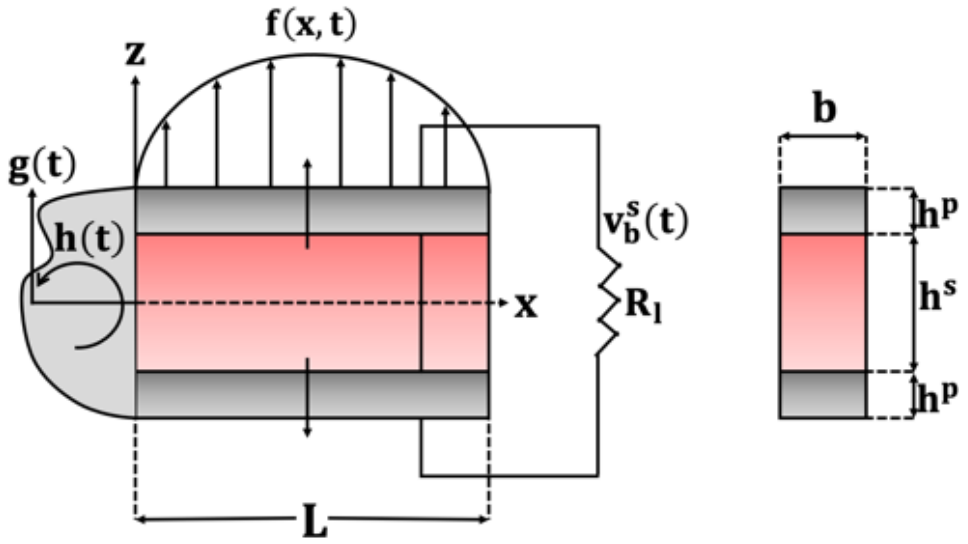
f(x, t)
z
g(t)
h(t)
x
$v_b^s(t)$
R_l
L
b
h^p
h^s
h^p

(d)

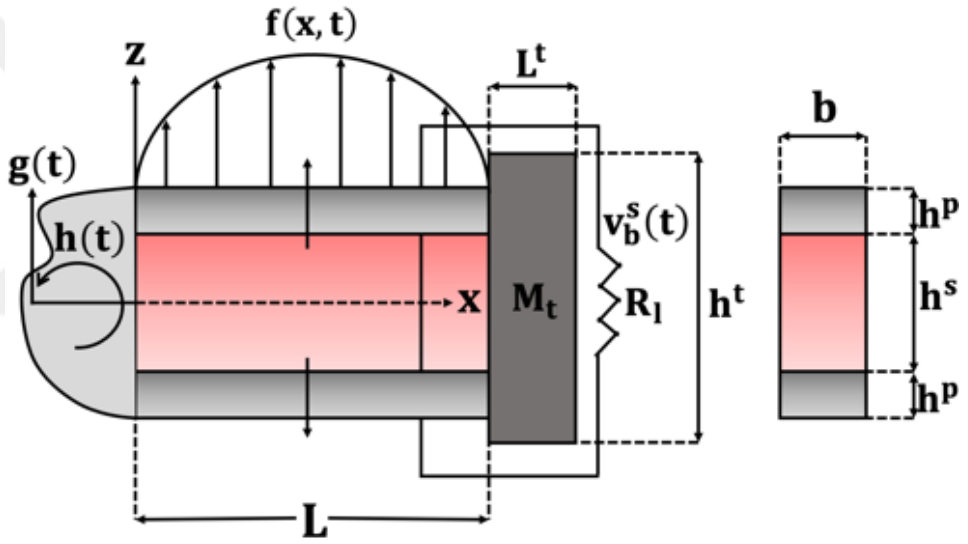
f(x, t)
z
L^t
g(t)
h(t)
x
M_t
$v_b^s(t)$
R_l
h^t
L
b
h^p
h^s
h^p

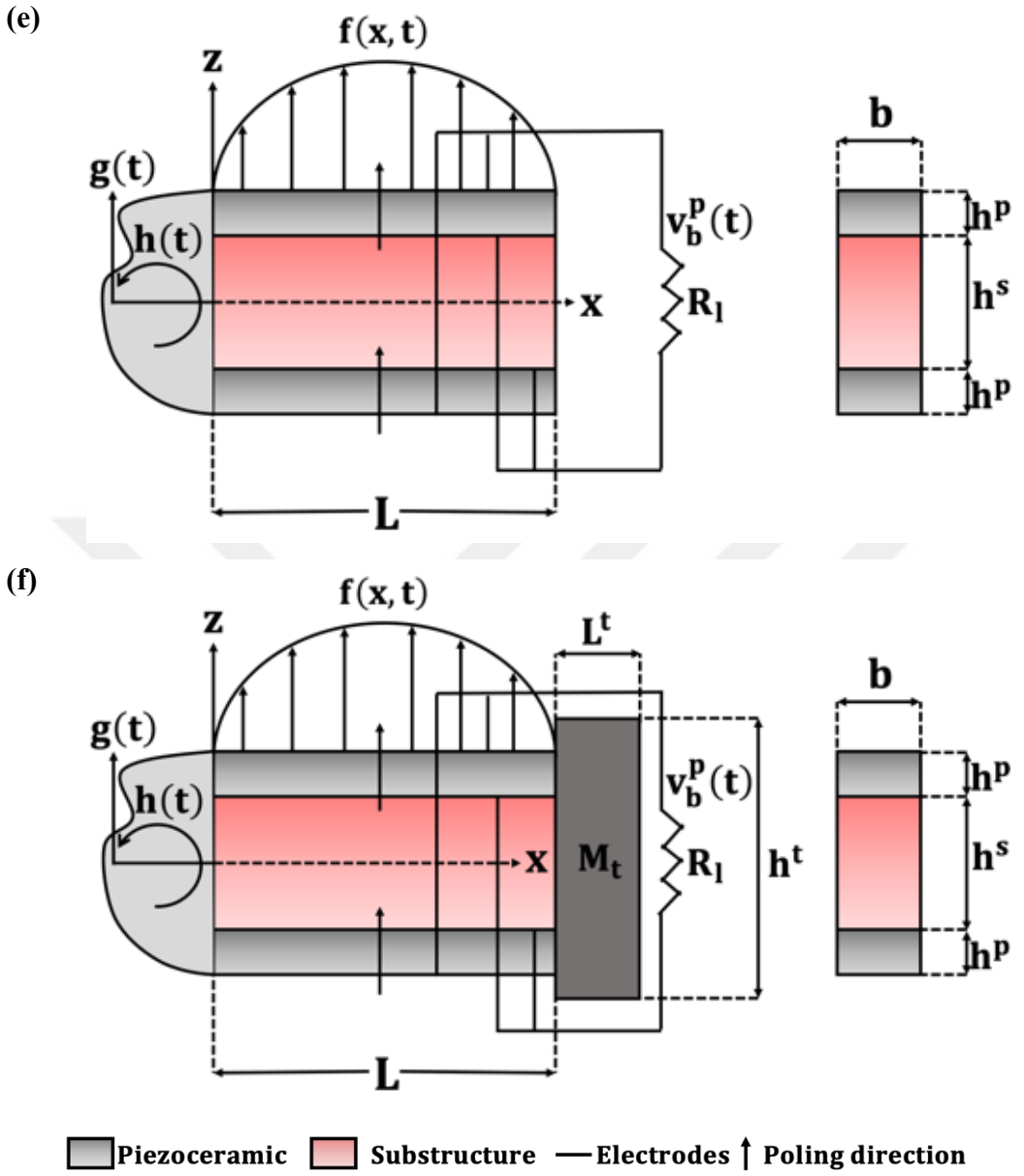

Figure 1.3 The geometric configuration of PEH, consisting of FG piezoelectric material and substructure under the influence of a uniformly distributed load: (a) unimorph without tip mass, (b) unimorph with tip mass at x = L, (c) series-connected bimorph without tip mass, (d) series-connected bimorph with tip mass at x = L, (e) parallel-connected bimorph without tip mass, (f) parallel-connected bimorph with tip mass at x = L.

The ideal form and configuration of the PEH must be determined since the produced voltage mainly depends on the size and geometry of the piezoelectric materials and the load type. The lumped parameter approach and the distributed parameter technique are two distinct configurations used to characterize the behavior of the PEH under excited vibration. The single-degree-of-freedom (SDOF) lumped parameter model is the simplest mathematical modeling method to formulate PEH. The output power performance is evaluated by solving the second-order differential equation for which equivalent mass, damping, and stiffness matrices are created for the equation of motion. The SDOF lumped parameter model is only suitable for simple calculations since it gives a single-mode vibration solution and does not provide accurate strain values. The distributed parameter system methodology, on the other hand, is better suited to PEH formulation because this solution method offers more accurate results. The equation of motion in this system is formed by applying displacement functions appropriate for the beam model employed before using Hamilton's principle. The Euler-Bernoulli model, commonly used in beam numerical calculations, is compared to the SDOF lumped-parameter model. It is demonstrated that the Euler-Bernoulli model simplifies less and produces more accurate results [4]. In contrast to the Timoshenko beam model, the Euler-Bernoulli model does not give exact results for microdomain beams. In addition, the natural frequencies are higher in the Euler-Bernoulli model due to the absence of rotating inertia and shear deformation effects. Apart from this, analytical solutions confined to a single vibration mode have been proposed for the PEHs vibration solution.

1.3 Review of Weak Form Quadrature Element Method

The WQEM is formulated using the principle of minimum potential energy or the weak form of the integral or the variational statement. The phrase "weak form" highlights the method's variational principles. The DQ rule yields highly accurate outcomes with the least computational effort and round-off errors. The problem space is divided into the fewest integrable regions using the WQEM. Quadrature

elements refer to each integrable region as a sub-domain. In theory, the WQEM combines the generality of the FEM with the accuracy of spectral methods like the time-domain spectral element method. WQEM differs from FEM in that the distribution of element nodes is not regular. The formulation of the stiffness, damping, and mass matrix is also different from the spectral element method in that it is more flexible and less complicated.

The energy expression is first formulated in WQEM instead of the governing differential equation of motion. The procedure is finished by defining the weak-form integrals, using the natural-to-Cartesian geometric mapping technique, and explicitly using the DQ criteria to get the weighting coefficients at the integration points. The WQEM does not have the challenges associated with applying the multiple boundary conditions (BCs), loading, and geometric discontinuities on complicated geometry. This approach makes it easier to analyze irregular geometries without explicitly indicating shape functions. The Lagrange or Hermite interpolation functions are frequently used as shape functions in WQEM. Moreover, the quadrature element can be created using numerous node types like uniformly distributed nodes, Chebyshev-Lobatto-Gauss (CLG) nodes, and Gauss-Lobatto-Legendre (GLL) nodes. Although uniformly distributed nodes are simple to use, they become more challenging to implement as the number of nodes rises. GLL points are commonly adopted to obtain the symmetric stiffness, damping, and mass matrices to simplify the solution. Thus, while finding artificial eigenvalues is avoided, the number of element nodes that can be used is unlimited. The DQ rule allows the strain fields at the GLL points to be expressed as the weighted sum of the related generalized displacements at each node throughout the whole element. As a result, the WQEM performs numerical integration before estimating derivatives.

1.4 Literature Survey

Researchers' interest in FGMs has recently grown. Many investigations are conducted in order to express complicated material behavior accurately. There are

several numerical analysis techniques utilized for dynamic analysis. First, Wu et al. [5] employed the FEM to analyze static, free, and forced vibrations in an FG porous beam. The beam formulation is based on both TBT and Euler-Bernoulli beam theory. The time-domain analysis system uses Rayleigh's damping factor to incorporate a damping effect. Young's modulus and density on FGM are graded in the thickness direction, and the porosity coefficient is utilized to explain porosity distribution. The beam is exposed to concentrated moving harmonic load, and dynamic analysis is achieved using Newmark's approach. Similarly, Songsuwan et al. [6] used Ritz and Newmark techniques to perform free and forced vibration analysis for FG sandwich Timoshenko beams with moving harmonic loads and shape functions appropriate for various BCs. Ansari et al. [7] used the unique numerical technique known as generalized DQ to describe the forced vibration of FG carbon nanotube-reinforced composite Timoshenko beams. The generalized DQ approach makes use of CLG grid points. The study depicts time domain forced vibration analysis and frequency response curves for various factors such as volume fraction, slenderness ratio, damping parameter, etc. The complementary functions method is another numerical approach utilized in Calim's [8] analysis of the free and forced vibration axially FG Timeshenko beam on a two-parameter viscoelastic basis. The beam is subjected to triangular impulsive loads in the Laplace domain, and the effects of the gradient index, foundation parameters, and BCs are investigated. The Runge-Kutta technique resolves the initial value problem by applying multiple BCs. Durbin's technique transforms the Laplace domain into a time domain. In a different study, Wattanasakulpong and Mao [9] applied the Chebyshev collocation method to resolve Timoshenko FG beams free vibrational analysis. The Chebyshev collocation method uses CLG to build the grid points for the Chebyshev interpolation. The power-law, exponential, and Mori-Tanaka models are used to assess the material characteristics of FGM beams. The investigation includes several parametric analyses, including the material volume fraction index, beam thickness, length-to-height ratios, spring constant factors, etc. Using the domain-boundary element method, Eshraghi and Dag [10] examined the forced vibration behavior under various loading types for the FG

Timoshenko beam. They confirmed the accuracy of the procedure by comparing their findings to the analytical solutions. The Houbolt method was employed as the time-domain analysis time incrementation technique.

In addition to the techniques already described, researchers are still looking for methods that produce findings more quickly and accurately. WQEM is a relatively new methodology used to solve various problems to show the method's effectiveness and reliability. It has found widespread use in a variety of element forms. Zhong and Yu [11] performed the static analysis of the plane elasticity problems under a uniformly distributed load and unidirectional tensional stress by employing the WQEM. The elastic isotropic environment was split into quadrature components and converted from the physical domain to the square domain. The shape function that they implemented was the Lagrange interpolation function. The Cook panel, Kirsch, and Hertz problems were solved to validate the effectiveness of the method by presenting the displacement and stress data of the Lobatto nodes. Similarly, Zhong and Yue [12] expanded the plate element flexural and vibrational analysis for isotropic and homogeneous thin plates with the same type of shape function, node points, and load types. The interpolation shape functions of the Hermitian type were employed for edge points. Apart from this, limit analysis is essential for geological engineers when measuring soil-bearing capacity. Using WQEM, Yuan and Du [13] investigated the stability of a vertical slope, the impact of discharge rate, the effect of the location of the subsurface water table, and the carrying capacity of a footing on an unsaturated slope when doing the unsaturated soil limit analysis. Unconfined seepage problems, which are crucial for civil engineering, are being researched by Yuan and Zhong [14] in order to expand two-dimensional seepage problems with free surfaces into three-dimensional ones by the WQEM's efficiency and reliability by using adaptive mesh. In another research conducted by Jin et al. [15], expanded Chebyshev nodes were used to beam and bar elements. They compared expanded Chebyshev nodes with uniformly distributed and GLL nodes to demonstrate the availability of analyses supporting longer time steps. It allows a longer time step as there is no accumulation at the nodes near the BCs. According to the study conducted

by Wang and Wang [16], a three-layer sandwich beam with a core and top and bottom layer is introduced in order to free vibration WQEM analysis using the extended high-order sandwich panel theory. The top and bottom layers are isotropic, whereas the core is orthotropic. They formulated the beam elements using the Euler-Bernoulli beam theory, and Chebyshev grids were implemented. The proposed method's efficiency is demonstrated by comparing the results to the FEM solution. In order to undertake a large deformation analysis using WQEM, Xiao and Zhong [17] used geometrically exact beam theory to model isotropic planar beam frames. The element formulation is based on the linear elastic constitutive law. The beam is subjected to distributed and concentrated external loads to present bending and buckling analyses. The Newton-Raphson method is used to calculate the displacement vector incrementally. The geometrically exact beam theory is also employed by Zhang and Zhong [18] for the dynamic analysis of spatial beams undergoing large displacements and rotations. Triangular impulsive loading and torques are applied to the endpoint to investigate tip displacement. In related research, He and Zhong [19] used the Euler-Bernoulli beam theory to investigate large deflection elastoplastic analysis of frames. The applied load is uniformly distributed and concentrated, and Newton-Raphson iteration is employed in the computing process. Research performed by Zhou et al. [20] provides that the proposed method is used in order to examine TBT-based 5-MW curved and twisted rotating and non-rotating composite wind blades. Centrifugal force is implemented into the equation of motion for rotating dynamic analysis. Nonlinear static and dynamic analyses are verified by comparing tip displacements to analytical, experimental, and ABAQUS solutions. Static problems are solved using the Newton-Raphson iteration method. GLL nodes are employed, and each boundary node has three degrees of freedom, while the interior nodes have two. Twist and shear deformation are interpolated using the Lagrange interpolation function, whereas tension and bending displacements are interpolated using the Hermite interpolation function. Hou and He [21] did another Timoshenko quadrature beam study. They used straight, two-layer composite beams with different cross-sections and materials

subjected to distributed load. The virtual work principle is utilized instead of Hamilton's principle. Each layer comprises a homogeneous, isotropic, and linearly elastic material, which makes Hooke's law applicable. When the mid-span deflection, the system's natural frequency, and free vibration mode analysis are compared with FEM, the convergence rate is higher in the WQEM solution. The numerical smoothness tests are performed, and the results demonstrate that employing WQEM can reduce the smoothness issue of FEM. Kim et al. [22] investigated the linear and nonlinear forced vibration analysis, frequency response characteristics, and stability analysis of the four-layer laminated composite beam element using the reduced-order and the incremental harmonic balance method after constructing a mass, damping, and stiffness matrix based on WQEM. The computation time is decreased when utilizing the reduced-order model. TBT defines the displacement field, and each node has three degrees of freedom. Also, the equivalent moduli of each ply are characterized using simplified homogenized beam theory. Another forced vibration solution was developed by Trabellsi et al. [23] for Timoshenko nanobeams. Eringen's nonlocal theory is established to estimate nonlocal stresses. The nanobeam is designated as nonhomogenous with an isotropic stress-strain law. In the study of forced vibration, they obtained a steady-state solution for various excitation frequencies to compute the system's frequency response curves by transforming the Lagrange interpolation shape functions to mode shape-based functions and applying the Galerkin techniques. Force is defined as a linear, nonlinear, periodic, and shear coefficient of a nonlinear medium.

Several researchers have applied WQEM to study FGM in the literature. Jin and Wang [24] utilized WQEM to illustrate the technique's efficiency in the free vibration analysis on FG Euler-Bernoulli beams. To achieve that, stiffness and mass matrices are obtained using the GLL quadrature. Results are validated against solutions found in the literature, and a convergence study is carried out. It is demonstrated that the thin beam element that has been presented may provide exact frequencies with a limited number of nodal points. Accurate results are reported for FG beams with nine BCs and eight power-law exponents. Ri et al. [25] employed

the WQEM to gather stiffness and mass matrices to investigate the internal resonance phenomena of the composite shaft disk system. The disk is treated as a rigid element, whereas the composite shaft is handled as a beam element. The disk's imbalanced mass generates a force that is referred to as an external excitation force. The TBT expresses the shaft element's strain-displacement relationship. There are five degrees of freedom for each node. The incremental harmonic balance method is used to solve the motion equation, and the reduced-order model is used to solve the nonlinear equations of motion more quickly. The Jeffcott rotor's frequency-response characteristic curves are obtained. In another study, Wang et al. [26] extend the WQEM application to examine the multi-directional FGM parallelepipeds' three-dimensional free vibration analysis under general BCs. For comparison with WQEM, the FEM results are obtained using commercial software ABAQUS. Natural frequency values and mode shapes for the uni-, bi-, and tri-directional FGM square plates have been found, and the influence of the power-law exponent and BCs has been investigated. The study results of the forced vibration caused by a moving point load were also examined by Wang et al. [27] by employing the proposed method for the FG Euler-Bernoulli beam. Dynamic response results were obtained using a central finite difference method algorithm. In a different research, Shen et al. [28] looked into the geometrically nonlinear dynamic analysis of FG carbon nanotube-reinforced composite rectangular plates exposed to blast loads and step uniform distributed load. The nonlinear incremental dynamic equilibrium problem was solved using the Newmark time integration method and the Newton-Raphson iteration approach. Reddy's higher-order shear deformation theory was applied to the plate element. Studies of comparison and convergence were carried out to validate the accuracy, effectiveness, and numerical stability of the proposed WQEM formulation. Furthermore, Jin and Wang [29] used the WQEM formulation for two different TBT formulations in order to look into the outcomes of the FG beams' free vibration.

The PEHs have been the subject of extensive investigation. Sodano et al. [30] created a bimorph cantilever non-homogeneous beam model for energy harvesting using the

Rayleigh-Ritz technique and the Euler-Bernoulli beam theory. The necessary size and transverse vibration levels were calculated to generate sufficient energy for the electronic devices. Additionally, the model is empirically checked to ensure its accuracy. They incorporated the material damping coefficient into their formulation. In a finite element plate model research, the unimorph and bimorph with tip mass and wing spar with integrated piezoceramics PEH plates based on the Kirchhoff plate theory are examined by Junior et al. [31]. They confirmed their formulation by comparing frequency response function (FRF) solutions to the published research results from the literature. Zhou et al. [32] extended the PEH concept with a TBT-based composite curved-beam structure. The beam is under the effect of base excitation to explore the consequences of forced vibration. They developed and compared the analytical formulation to FEM-based COMSOL commercial software and experimental data. It was achievable to correctly compute the mechanical and electrical responses and the system resonant frequencies and eigenmodes by resolving the electromechanical equations. Erturk [33] introduces a more comprehensive structure for the electromechanical modeling of base-excited PEHs. The assumed-modes method was used for the electromechanical formulation with the Euler-Bernoulli, Rayleigh, and Timoshenko beam methods. Model validations were demonstrated by comparing the electromechanical frequency response functions to those obtained experimentally in the absence and presence of a tip mass. Wang [34] employed the Erturk study's [33] TBT and Euler-Bernoulli beam theory formulation. The spectral finite element approach was used to develop bimorph PEH. The comparison of the two beam models was used to conduct parametric research. Amini et al. [35] used FEM to examine turbulent flow-induced flexible PEH. The produced voltage and tip displacement results correlate well with the experimental results.

A study topic has emerged in the literature for FGPMs, which utilize the characteristics of FGM. Yang and Xiang [36] used the TBT to examine the static bending, free vibration, and dynamic response of unimorph, bimorph, and multi-morph actuators fabricated of non-homogeneous FGPMs under a thermal-electro-

mechanical load. The governing differential equations were solved using the DQM to determine the deflection, response force, natural frequencies, and dynamic responsiveness of numerous FGPMs. A parametric investigation over a range of BCs demonstrated the effect of shear deformation, temperature rise, material composition, slenderness ratio, end support, and the overall number of layers on the thermo-electro-mechanical characteristics. It was assumed that material characteristics in the beam formulation were independent of temperature. Like the previous study, Doroushi et al. [37] conducted free and forced vibration studies of unimorph FGPM beams under thermo-electro-mechanical load. In contrast, the beam was modeled using high-order shear deformation beam theory, and the equation of motion was established using FEM. The Newmark method is used to explore the FGPM beam's transient response to a rapidly imposed lateral load. In another study, Amini et al. [38] formulated the FEM for modeling the FG PEHs in unimorph or bimorph (series or parallel connections) layouts. The analytical solutions validated the findings of the FEM. Rayleigh damping was incorporated into the formulation. The frequency response function due to the harmonic base excitation was obtained. Additionally, Parashar and Sharma [39] have performed a modal analysis on the Timoshenko FGPM unimorph beam. The governing equation was solved using the generalized DQ method to determine the system's natural frequency and mode shapes. The impacts of slenderness ratios and volume fraction indices on natural frequencies were investigated. In a different study, nonlinear free and forced vibration of the bimorph FG PEH with a tip mass was investigated analytically using the multiple time scales perturbation approach by Derayatifar et al. [40]. The beam model was based on the Rayleigh beam theory. The influence of various design and excitation factors on the system's nonlinear frequency response was investigated.

1.5 Motivation and Scope of Study

This study aims to employ WQEM to perform free and forced vibration analysis on FG PEH Timoshenko beams satisfying various BCs. The piezoelectric constitutive

equations are established, and the displacement field and stress equations are calculated using the TBT. The governing differential equations of motion are constructed using the extended Hamilton's principle, like Ertürk's study [33], and the electromechanical Lagrange's equations are produced to establish the equation of motion. The modulus of elasticity, Poisson's ratio, and material density are developed to change along the thickness according to the Mori-Tanaka micromechanics model [41] in order to formulate the FG substructure layer of PEH. Voigt's rule of the mixture is utilized to ascertain the material characteristics of piezoelectric materials. The displacement field is assumed to be consistent with the DQ specifications to construct an FG quadrature PEH Timoshenko beam element. The relevant displacement fields are applied to the kinetic, strain, and internal work energy equations to create a mass, stiffness, and electrical voltage matrix, respectively. The Rayleigh damping factor is implemented to calculate the damping coefficient. The equation of motion incorporates the damping effect by applying it to the stiffness and mass matrices. The force is represented using the work equivalent approach in the equation of motion. The study employs four distinct types of forces, which are uniformly distributed step, concentrated step, concentrated harmonic, and concentrated impulsive loads. The model includes the base excitation effect for steady-state response analyses. The Houbolt and Newmark methods are used to calculate the forced transient response. The consequences of adding tip mass, connecting the circuit in series or parallel, and constructing the circuit in different configurations, as expressed in Figure 1.3, together with the change of boundary condition, load resistance, power-law exponent, and load types, are shown in the parametric analysis. Furthermore, free vibration findings for the PEH's natural frequencies and electromechanical FRFs for the steady-state response are obtained. The WQEM in this study is applied to PEHs for the first time and differs from existing numerical solution methods with its ease of use and accuracy.

1.6 General Outline

Chapter 2 provides the constitutive equations for piezoelectric and Timoshenko beam formulations. The fundamental BCs for the Timoshenko beam are also mentioned.

Chapter 3 contains the constitutive DQ rules utilized in the WQEM formulation as well as the extended Hamilton's principle that constitutes the electromechanical Lagrange equations. As a result, PEH's equation of motion is established. Also, the WQEM applied stress computation, and free and forced vibration formulations are provided.

Chapter 4 validates the numerical method results using analytical and experimental solutions. This chapter also includes parametric analysis that looks at the characteristics of beams with varied features.

Chapter 5 provides a summary and recommendations for future studies.

CHAPTER 2

FORMULATION

The FG PEH geometric models under general time-dependent loading $f(x,t)$ are shown in Figure 1.3. All six of the geometric configurations are formulated. Piezoelectric materials are transversely isotropic materials, while substructure is isotropic material. The length of the piezoelectric material and substructure, the length of the tip mass, the height of the substructure, the height of the piezoelectric material, the height of the tip mass, and the width of the piezoelectric material and substructure are represented as L, L^t, h^s, h^p, h^t, b, respectively. The FG substructure and piezoelectric materials are expected to exhibit linear material behavior with small deformations since the excitation frequency is low. The substructure and piezoelectric materials are considered entirely bonded to one another. As a result, no two materials are moving relative to each other. The prestress from the piezoelectric material, electrode, and substructure contacting each other are neglected since it is considered that the materials are almost touching. The electrodes cover each surface of the piezoelectric materials, which are considered all the same, are conductive, and their thickness is negligible. Therefore, a single electric potential difference is stated between them. It is anticipated that the instantaneous electric fields generated in the piezoelectric materials are homogeneous over the length of the beam. The built-in capacitance of the piezoelectric materials is taken into account in the circuit as a resistive electrical load designated by R_l. The piezoelectric material's leakage resistance is neglected. The top and bottom layers' instantaneous average bending strains at any point along the beam's length have the opposite signs, indicating that one layer is in tension and the other is in compression. Parallel-connected bimorph piezoelectric materials are poled the same in the thickness direction as opposed to series-connected ones, which are poled oppositely. Figure 1.3 illustrates the variation in poling direction between series and parallel systems with arrows.

2.1 Piezoelectric Constitutive Equations

Piezoelectric constitutive equations define the upper and lower piezoelectric materials of the PEH. The x-z plane is used to generate the coordinate system in Figure 1.3. The 12-plane is used in this piezoelectric constitutive equation description for piezoelectric material components. The 3-axis, or the z-axis, is the piezoelectric material's poling axis, and the beam configuration does not show symmetry across it. The piezoelectric field variables are the stress σ_{ij}, strain ε_{ij}, electric field $\overline{E}_k$, and electric displacement D_k components. The mechanical behavior of piezoelectric materials is determined by solving two coupled constitutive linear equations. The strain-electric displacement constitutive equations are expressed by stress and electric field components:

$$\varepsilon_{ij} = s^{E}_{ijkl} \cdot \sigma_{kl} + d_{kij} \cdot \overline{E}_k \tag{2-1}$$

$$D_i = d_{ikl} \cdot \sigma_{kl} + \epsilon^{\sigma}_{ik} \cdot \overline{E}_k \tag{2-2}$$

where s^{E}_{ijkl}, d_{ikl}, ϵ^{σ}_{ik} are the elastic compliance constant at constant electric field, the piezoelectric constant, and the permittivity (dielectric) constant at constant stress, respectively. In matrix form, equations (2-1) and (2-2) are as follows:

$$\begin{bmatrix} \varepsilon \\ D \end{bmatrix} = \begin{bmatrix} s^{E} & d' \\ d & \epsilon^{\sigma} \end{bmatrix} \cdot \begin{bmatrix} \sigma \\ \overline{E} \end{bmatrix} \tag{2-3}$$

where the superscripts E and σ indicate that the constants are evaluated at constant electric field and stress, respectively, and the superscript $(')$ represents the transpose. The expanded matrix representation of equation (2-3) is described as follows:

$$\begin{bmatrix} \varepsilon_{11} \\ \varepsilon_{22} \\ \varepsilon_{33} \\ 2\cdot\varepsilon_{23} \\ 2\cdot\varepsilon_{13} \\ 2\cdot\varepsilon_{12} \\ D_{11} \\ D_{22} \\ D_{33} \end{bmatrix} = \begin{bmatrix} s_{11}^{E} & s_{12}^{E} & s_{13}^{E} & 0 & 0 & 0 & 0 & 0 & d_{31} \\ s_{12}^{E} & s_{11}^{E} & s_{13}^{E} & 0 & 0 & 0 & 0 & 0 & d_{31} \\ s_{13}^{E} & s_{13}^{E} & s_{33}^{E} & 0 & 0 & 0 & 0 & 0 & d_{33} \\ 0 & 0 & 0 & s_{55}^{E} & 0 & 0 & 0 & d_{15} & 0 \\ 0 & 0 & 0 & 0 & s_{55}^{E} & 0 & d_{15} & 0 & 0 \\ 0 & 0 & 0 & 0 & 0 & s_{66}^{E} & 0 & 0 & 0 \\ 0 & 0 & 0 & 0 & d_{15} & 0 & \epsilon_{11}^{\sigma} & 0 & 0 \\ 0 & 0 & 0 & d_{15} & 0 & 0 & 0 & \epsilon_{11}^{\sigma} & 0 \\ d_{31} & d_{31} & d_{33} & 0 & 0 & 0 & 0 & 0 & \epsilon_{33}^{\sigma} \end{bmatrix} \cdot \begin{bmatrix} \sigma_{11} \\ \sigma_{22} \\ \sigma_{33} \\ \sigma_{23} \\ \sigma_{13} \\ \sigma_{12} \\ \overline{E}_{11} \\ \overline{E}_{22} \\ \overline{E}_{33} \end{bmatrix} \tag{2-4}$$

The stresses other than σ_{11} (the stress component in the axial direction) and σ_{13} (the transverse shear stress) are insignificant ($\sigma_{22} = \sigma_{33} = \sigma_{23} = \sigma_{12} = 0$) since the structure's piezoelectricity is to be represented as a Timoshenko beam. The following constitutive equations for the Timoshenko beam after employing negligible stresses are produced as follows:

$$\begin{bmatrix} \varepsilon_{11} \\ 2\cdot\varepsilon_{13} \\ D_{33} \end{bmatrix} = \begin{bmatrix} s_{11}^{E} & 0 & d_{31} \\ 0 & s_{55}^{E} & 0 \\ d_{31} & 0 & \epsilon_{33}^{\sigma} \end{bmatrix} \cdot \begin{bmatrix} \sigma_{11} \\ \sigma_{13} \\ \overline{E}_{33} \end{bmatrix} \tag{2-5}$$

The piezoelectric materials' stress and electrical displacement values are obtained by calculating the inverse of equation (2-5):

$$\begin{bmatrix} \sigma_{11} \\ \sigma_{13} \\ D_{33} \end{bmatrix} = \begin{bmatrix} \overline{c}_{11}^{E} & 0 & -\overline{e}_{31} \\ 0 & \kappa_s \cdot \overline{c}_{55}^{E} & 0 \\ \overline{e}_{31} & 0 & \epsilon_{33}^{\varepsilon} \end{bmatrix} \cdot \begin{bmatrix} \varepsilon_{11} \\ 2\cdot\varepsilon_{13} \\ \overline{E}_{33} \end{bmatrix} \tag{2-6}$$

where the superscript ε denotes that the respective constant is evaluated at constant strain. $\overline{c}_{11}^{E}$ is the elastic modulus of the piezoelectric material at constant electric field, $\overline{c}_{55}^{E}$ is the shear modulus of the piezoelectric material at constant electric field, $\overline{e}_{31}$ is the effective piezoelectric stress constant, and $\epsilon_{33}^{\varepsilon}$ is the permittivity component at constant strain with the plane-stress assumption for a beam. Accordingly, they defined as:

$$\overline{c}_{11}^{E} = \frac{1}{s_{11}^{E}} \tag{2-7}$$

$$\bar{c}_{55}^{E} = \frac{1}{s_{55}^{E}} \tag{2-8}$$

$$\bar{e}_{31} = \frac{d_{31}}{s_{11}^{E}} \tag{2-9}$$

$$\epsilon_{33}^{\varepsilon} = \epsilon_{33}^{\sigma} - \frac{{d_{31}}^{2}}{s_{11}^{E}} \tag{2-10}$$

The transverse shear stress in equation (2-6) is adjusted due to the shear correction factor being applied by TBT. κ_s is the shear correction factor equal to $5/6$ for a rectangular cross-section. The shear correction factor explains the asymmetric distribution of the shear stress in the beam cross-section. Several formulas for the shear correction factor have been developed in the literature. Timoshenko [42] theoretically deduced $\kappa_s = (5 + 5 \cdot \nu^p)/(6 + 5 \cdot \nu^p)$ for rectangular cross-sections. Cowper [43] uses $\kappa_s = (10 + 10 \cdot \nu^p)/(12 + 11 \cdot \nu^p)$ as a shear correction factor, which is also extensively adopted. ν^p is Poisson's ratio of the piezoelectric material. Determination of the shear correction factor is also valid for the substructure using the appropriate Poisson's ratio.

2.2 Displacement Field

The displacement field is introduced using the TBT, and the following three-dimensional displacement functions are displayed:

$$u_x(x, z, t) = u(x, t) - z \cdot \varphi(x, t) \tag{2-11}$$

$$u_y(x, z, t) = 0 \tag{2-12}$$

$$u_z(x, z, t) = w(x, t) \tag{2-13}$$

where $u_x(x, z, t)$, $u_y(x, z, t)$, and $u_z(x, z, t)$ are the axial, longitudinal, and transverse displacement components, respectively. The axial and transverse displacements, and the cross-sectional rotation on the central plane of the beam, are represented by $u(x, t)$, $w(x, t)$, and $\varphi(x, t)$, respectively. t is the time.

2.3 Strain Displacement Relations

The transverse shear strain γ_{xz} depicted in Figure 2.1 is regarded as constant, and all material characteristics are in continuous function in the z-direction.

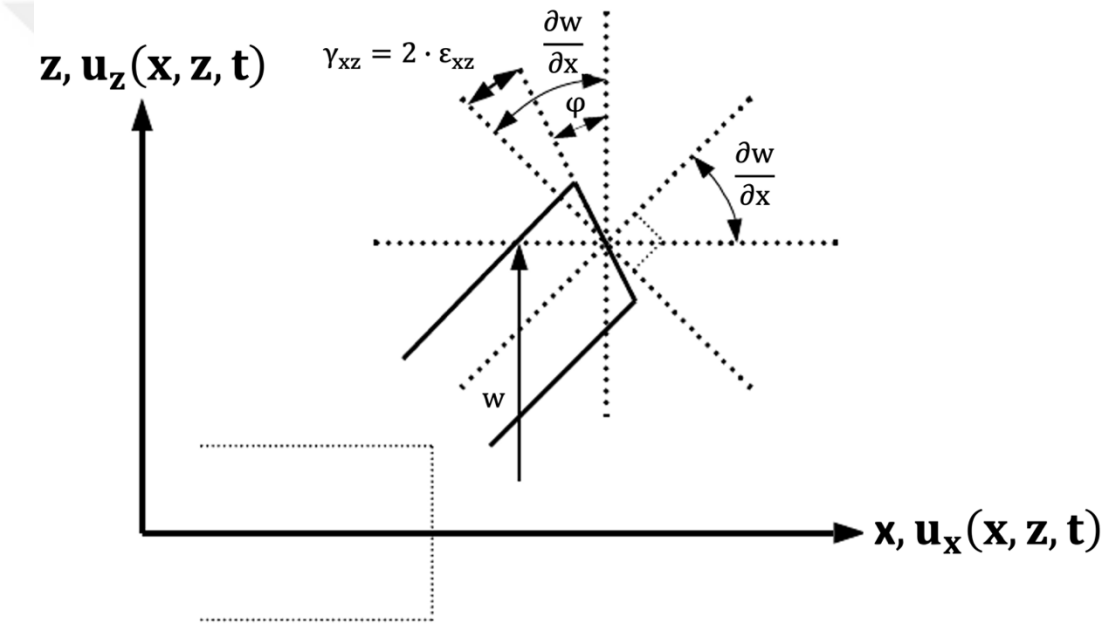

Figure 2.1 FG piezoelectric Timoshenko beam element deformed shape.

Strains ε of the substructure and piezoelectric material are defined using the infinitesimal strain theory as follows:

$$\begin{bmatrix} \varepsilon_{xx} & \varepsilon_{xy} & \varepsilon_{xz} \\ \varepsilon_{yx} & \varepsilon_{yy} & \varepsilon_{yz} \\ \varepsilon_{zx} & \varepsilon_{zy} & \varepsilon_{zz} \end{bmatrix} = \begin{bmatrix} \dfrac{\partial u(x,t)}{\partial x} - z \cdot \dfrac{\partial \varphi(x,t)}{\partial x} & 0 & \dfrac{1}{2} \cdot \left(-\varphi(x,t) + \dfrac{\partial w(x,t)}{\partial x} \right) \\ 0 & 0 & 0 \\ \dfrac{1}{2} \cdot \left(\dfrac{\partial w(x,t)}{\partial x} - \varphi(x,t) \right) & 0 & 0 \end{bmatrix} \quad (2\text{-}14)$$

Stresses σ of the substructure layer are defined using the generalized Hooke's law and the strains specified in equation (2-14). They described as follows:

$$\begin{bmatrix}\sigma_{xx}\\ \sigma_{yy}\\ \sigma_{zz}\\ \sigma_{yz}\\ \sigma_{xz}\\ \sigma_{xy}\end{bmatrix}=\begin{bmatrix}2\cdot\mu^s+\lambda^s & \lambda^s & \lambda^s & 0 & 0 & 0\\ \lambda^s & 2\cdot\mu^s+\lambda^s & \lambda^s & 0 & 0 & 0\\ \lambda^s & \lambda^s & 2\cdot\mu^s+\lambda^s & 0 & 0 & 0\\ 0 & 0 & 0 & \kappa_s\cdot\mu^s & 0 & 0\\ 0 & 0 & 0 & 0 & \kappa_s\cdot\mu^s & 0\\ 0 & 0 & 0 & 0 & 0 & \kappa_s\cdot\mu^s\end{bmatrix}\cdot\begin{bmatrix}\varepsilon_{xx}\\ \varepsilon_{yy}\\ \varepsilon_{zz}\\ 2\cdot\varepsilon_{yz}\\ 2\cdot\varepsilon_{xz}\\ 2\cdot\varepsilon_{xy}\end{bmatrix} \quad (2\text{-}15)$$

where μ^s and λ^s are Lame's constants. μ^s is also the shear modulus of the PEH's substructure layer. They are defined as follows:

$$\mu^s=\frac{E^s(z)}{2\cdot\left(1+\nu^s(z)\right)} \quad (2\text{-}16)$$

$$\lambda^s=\frac{\nu^s(z)\cdot E^s(z)}{\left(1+\nu^s(z)\right)\cdot\left(1-2\cdot\nu^s(z)\right)} \quad (2\text{-}17)$$

where E^s is the modulus of elasticity of the substructure, and ν^s is Poisson's ratio of the substructure. σ_{xy} and σ_{yz} result in zero. Furthermore, the shear modulus of the piezoelectric material can be calculated as an alternative way of equation (2-8): $\bar{c}_{55}^E=\bar{c}_{11}^E/\left(2\cdot\left(1+\nu^p(z)\right)\right)$.

2.4 FGM Formulation

The elasticity modulus, mass density, and Poisson's ratio of the FG Timoshenko substructure beam are supposed to change in the transverse direction according to the power-law form. The Mori-Tanaka micromechanical model [41] is used to compute the FG PEH beam's substructure modulus of elasticity and Poisson's ratio. The model is detailed below:

$$E^s(z)=\frac{9\cdot B_e^s(z)\cdot\mu_e^s(z)}{3\cdot B_e^s(z)+\mu_e^s(z)} \quad (2\text{-}18)$$

$$\nu^s(z) = \frac{9 \cdot B_e^s(z) - 2 \cdot \mu_e^s(z)}{6 \cdot B_e^s(z) + \mu_e^s(z)} \tag{2-19}$$

where $B_e^s(z)$ and $\mu_e^s(z)$ are the effective bulk and shear modulus of the substructure, respectively, and represented as follows:

$$B_e^s(z) = \frac{V_u^s(z) \cdot (B_u^s - B_l^s)}{1 + \frac{(B_u^s - B_l^s) \cdot V_l^s(z)}{\frac{4 \cdot \mu_l^s}{3} + B_l^s}} + B_l^s \tag{2-20}$$

$$\mu_e^s(z) = \frac{V_u^s(z) \cdot (\mu_u^s - \mu_l^s)}{1 + \frac{(\mu_u^s - \mu_l^s) \cdot V_l^s(z)}{\mu_l^s + \frac{(9 \cdot B_l^s + 8 \cdot \mu_l^s) \cdot \mu_l^s}{6 \cdot (B_l^s + 2 \cdot \mu_l^s)}}} + \mu_l^s \tag{2-21}$$

The upper and lower phases are represented by the subscripts u and l, respectively. V^s represents the volume fraction of the substructure. B^s is the bulk modulus of the substructure and is expressed as follows:

$$B^s = \frac{E^s(z)}{3 \cdot (1 - 2 \cdot \nu^s(z))} \tag{2-22}$$

The density function of the substructure ρ^s is evaluated using the mixtures rule and expressed in the form:

$$\rho^s(z) = \rho_l^s(z) \cdot V_l^s(z) + \rho_u^s(z) \cdot V_u^s(z) \tag{2-23}$$

A power function represents spatial variation in the upper volume fraction and is depicted using the power-law exponent k. Power-law exponent is a non-negative variable. $k = 0$ implies that the top division of the substructure layer is dominant, whereas $k = \infty$ shows that the bottom division of the substructure dominates. Volume fraction distribution should be considered when changing the value of k in the numerical results chapter.

$$V_u^s(z) = \left(\frac{z}{h^s} + \frac{1}{2}\right)^k \tag{2-24}$$

Volume fractions should sum up to one:

$$V_u^s(z) + V_l^s(z) = 1 \tag{2-25}$$

Using Voigt's rule of the mixture, the upper and lower piezoelectric materials' respective material and electrical properties are stated in equations (2-26) and (2-27), respectively:

$$X_u(z) = (X_u - X_l) \cdot \left[\frac{2 \cdot z - h^s}{2 \cdot h^p}\right]^k + X_l \qquad \text{for} \frac{h^s}{2} \le z \le \frac{h^s}{2} + h^p \tag{2-26}$$

$$X_l(z) = (X_u - X_l) \cdot \left[1 + \frac{2 \cdot z + h^s}{2 \cdot h^p}\right]^k + X_l \quad \text{for} -\frac{h^s}{2} - h^p \le z \le -\frac{h^s}{2} \tag{2-27}$$

Here, X will be replaced by elasticity modulus, mass density, Poisson's ratio, effective piezoelectric stress constant, and permittivity component at constant strain.

2.5 Extended Hamilton's Principle

The following is a summary of the extended Hamilton's principle for an electromechanical system without taking into account mechanical dissipative effects:

$$\int_{t_i}^{t_f} (\delta \cdot T - \delta \cdot U + \delta \cdot W_{ie} + \delta \cdot W_{nc}) \cdot dt = 0 \tag{2-28}$$

where $\delta \cdot T$, $\delta \cdot U$, $\delta \cdot W_{ie}$, $\delta \cdot W_{nc}$ represent the initial variations of the total kinetic energy, strain energy, internal electrical energy, and non-conservative mechanical and electrical components' virtual work, respectively. The specified initial and final times are t_i and t_f. Total kinetic energy $T(q_1, q_2, \dots, q_n, \dot{q}_1, \dot{q}_2, \dots, \dot{q}_n)$ is determined by the generalized coordinates and their time derivatives. In contrast, total strain $U(q_1, q_2, \dots, q_n)$ and internal electrical energy $W_{ie}(q_1, q_2, \dots, q_n)$ are defined only by the generalized coordinates. The electromechanical Lagrange equation is obtained using equation (2-28) and is shown as follows:

$$\frac{d}{dt}\left(\frac{\partial \cdot T}{\partial \cdot \dot{q}_k}\right) - \frac{\partial \cdot T}{\partial \cdot q_k} + \frac{\partial \cdot U}{\partial \cdot q_k} - \frac{\partial \cdot W_{ie}}{\partial \cdot q_k} = Q_k \tag{2-29}$$

where Q_k is the generalized non-conservative forces. The electromechanical Lagrange equations are developed in detail in Chapter 3. The following sections are formulations of the components that constitute equation (2-28).

2.5.1 Total Strain Energy of the PEH

The generalized strain energy equation defined for six different configurations is shown in equation (2-30):

$$\begin{aligned} U = \frac{1}{2}\cdot \int_{-\frac{h^s}{2}}^{\frac{h^s}{2}} \int_0^L \left(\mathbf{A}^{(2\text{-}30)}\right)\cdot b\cdot dz\cdot dx + \frac{1}{2}\cdot \int_{\frac{h^s}{2}}^{\frac{h^s}{2}+h^p} \int_0^L \left(\mathbf{B}^{(2\text{-}30)}\right)\cdot b\cdot dz\cdot dx \\ + \frac{1}{2}\cdot \int_{-\frac{h^s}{2}-h^p}^{-\frac{h^s}{2}} \int_0^L \left(\mathbf{C}^{(2\text{-}30)}\right)\cdot b\cdot dz\cdot dx \end{aligned} \tag{2-30}$$

$\mathbf{A}^{(2\text{-}30)}$, $\mathbf{B}^{(2\text{-}30)}$, and $\mathbf{C}^{(2\text{-}30)}$ take values based on six configurations illustrated in Figure 1.3, as shown in Table 2-1.

Table 2-1 The generalized strain energy equation constants for equation (2-30) based on six different configurations depicted in Figure 1.3.

PEH Configuration	$\mathbf{A}^{(2\text{-}30)}$	$\mathbf{B}^{(2\text{-}30)}$	$\mathbf{C}^{(2\text{-}30)}$
The unimorph PEH without tip mass. (Figure 1.3a)	$\sigma_{xx}\cdot\varepsilon_{xx} + 2\cdot\sigma_{xz}\cdot\varepsilon_{xz}$	$\sigma_{11}^u\cdot\varepsilon_{11}^u + 2\cdot\sigma_{13}^u\cdot\varepsilon_{13}^u$	0

Table 2-1 (continued)

The unimorph PEH with tip mass at x = L. (Figure 1.3b)	$\sigma_{xx} \cdot \varepsilon_{xx} + 2 \cdot \sigma_{xz} \cdot \varepsilon_{xz}$	$\sigma_{11}^{u} \cdot \varepsilon_{11}^{u} + 2 \cdot \sigma_{13}^{u} \cdot \varepsilon_{13}^{u}$	0
The series-connected bimorph PEH without tip mass. (Figure 1.3c)	$\sigma_{xx} \cdot \varepsilon_{xx} + 2 \cdot \sigma_{xz} \cdot \varepsilon_{xz}$	$\sigma_{11}^{u} \cdot \varepsilon_{11}^{u} + 2 \cdot \sigma_{13}^{u} \cdot \varepsilon_{13}^{u}$	$\sigma_{11}^{l} \cdot \varepsilon_{11}^{l} + 2 \cdot \sigma_{13}^{l} \cdot \varepsilon_{13}^{l}$
The series-connected bimorph PEH with tip mass at x = L. (Figure 1.3d)	$\sigma_{xx} \cdot \varepsilon_{xx} + 2 \cdot \sigma_{xz} \cdot \varepsilon_{xz}$	$\sigma_{11}^{u} \cdot \varepsilon_{11}^{u} + 2 \cdot \sigma_{13}^{u} \cdot \varepsilon_{13}^{u}$	$\sigma_{11}^{l} \cdot \varepsilon_{11}^{l} + 2 \cdot \sigma_{13}^{l} \cdot \varepsilon_{13}^{l}$
The parallel-connected bimorph PEH without tip mass. (Figure 1.3e)	$\sigma_{xx} \cdot \varepsilon_{xx} + 2 \cdot \sigma_{xz} \cdot \varepsilon_{xz}$	$\sigma_{11}^{u} \cdot \varepsilon_{11}^{u} + 2 \cdot \sigma_{13}^{u} \cdot \varepsilon_{13}^{u}$	$\sigma_{11}^{l} \cdot \varepsilon_{11}^{l} + 2 \cdot \sigma_{13}^{l} \cdot \varepsilon_{13}^{l}$
The parallel-connected bimorph PEH with tip mass at x = L. (Figure 1.3f)	$\sigma_{xx} \cdot \varepsilon_{xx} + 2 \cdot \sigma_{xz} \cdot \varepsilon_{xz}$	$\sigma_{11}^{u} \cdot \varepsilon_{11}^{u} + 2 \cdot \sigma_{13}^{u} \cdot \varepsilon_{13}^{u}$	$\sigma_{11}^{l} \cdot \varepsilon_{11}^{l} + 2 \cdot \sigma_{13}^{l} \cdot \varepsilon_{13}^{l}$

The unimorph configuration has a single top piezoelectric material, whereas the bimorph structure formulizes a second piezoelectric material beneath. For this

reason, the coefficient of $\mathbf{C}^{(2\text{-}30)}$ in unimorph structures equals zero. Also, the stress and strain values are shown as superscripts u and l for the upper and lower piezoelectric materials, respectively. The resulting strain energy formulation for the unimorph and bimorph configurations that results from applying the stress and strain formulas described in preceding sections is as follows:

$$\begin{aligned} \mathrm{U} = \frac{1}{2} \cdot \int_0^{\mathrm{L}} \Bigg[& \left(\mathbf{A}^{(2\text{-}31)}\right) \cdot \left(\frac{\partial \mathrm{u}(\mathrm{x},\mathrm{t})}{\partial \mathrm{x}}\right)^2 \\ & - 2 \cdot \left(\mathbf{B}^{(2\text{-}31)}\right) \cdot \left(\frac{\partial \mathrm{u}(\mathrm{x},\mathrm{t})}{\partial \mathrm{x}} \cdot \frac{\partial \varphi(\mathrm{x},\mathrm{t})}{\partial \mathrm{x}}\right) \\ & + \left(\mathbf{C}^{(2\text{-}31)}\right) \cdot \left(\frac{\partial \varphi(\mathrm{x},\mathrm{t})}{\partial \mathrm{x}}\right)^2 \\ & + \left(\mathbf{D}^{(2\text{-}31)}\right) \cdot \left(-\varphi(\mathrm{x},\mathrm{t}) + \frac{\partial \mathrm{w}(\mathrm{x},\mathrm{t})}{\partial \mathrm{x}}\right)^2 \\ & + \left(\mathbf{E}^{(2\text{-}31)}\right) \cdot \left(\mathbf{F}^{(2\text{-}31)}\right) \cdot \left(\frac{\partial \mathrm{u}(\mathrm{x},\mathrm{t})}{\partial \mathrm{x}}\right) \\ & - \left(\mathbf{E}^{(2\text{-}31)}\right) \cdot \left(\mathbf{G}^{(2\text{-}31)}\right) \cdot \left(\frac{\partial \varphi(\mathrm{x},\mathrm{t})}{\partial \mathrm{x}}\right) \Bigg] \cdot \mathrm{dx} \end{aligned} \tag{2-31}$$

$\mathbf{A}^{(2\text{-}31)}$, $\mathbf{B}^{(2\text{-}31)}$, $\mathbf{C}^{(2\text{-}31)}$, $\mathbf{D}^{(2\text{-}31)}$, $\mathbf{E}^{(2\text{-}31)}$, $\mathbf{F}^{(2\text{-}31)}$, and $\mathbf{G}^{(2\text{-}31)}$ take various values for six distinct configurations, as indicated in Table 2-2.

Table 2-2 The resulting strain energy equation constants for equation (2-31) based on six different configurations depicted in Figure 1.3.

PEH Configuration	$\mathbf{A}^{(2\text{-}31)}$	$\mathbf{B}^{(2\text{-}31)}$	$\mathbf{C}^{(2\text{-}31)}$	$\mathbf{D}^{(2\text{-}31)}$	$\mathbf{E}^{(2\text{-}31)}$	$\mathbf{F}^{(2\text{-}31)}$	$\mathbf{G}^{(2\text{-}31)}$
The unimorph PEH without tip mass. (Figure 1.3a)	$A_{11}^{s} + A_{11}^{pu}$	$B_{11}^{s} + B_{11}^{pu}$	$D_{11}^{s} + D_{11}^{pu}$	$F_{55}^{s} + F_{55}^{pu}$	$v_u(t)$	B_u^{pu}	J_u^{pu}
The unimorph PEH with tip mass at $x = L$. (Figure 1.3b)	$A_{11}^{s} + A_{11}^{pu}$	$B_{11}^{s} + B_{11}^{pu}$	$D_{11}^{s} + D_{11}^{pu}$	$F_{55}^{s} + F_{55}^{pu}$	$v_u(t)$	B_u^{pu}	J_u^{pu}
The series-connected bimorph PEH without tip mass. (Figure 1.3c)	$A_{11}^{s} + A_{11}^{pu} + A_{11}^{pl}$	$B_{11}^{s} + B_{11}^{pu} + B_{11}^{pl}$	$D_{11}^{s} + D_{11}^{pu} + D_{11}^{pl}$	$F_{55}^{s} + F_{55}^{pu} + F_{55}^{pl}$	$v_b^s(t)$	$B_{bs}^{pu} + B_{bs}^{pl}$	$J_{bs}^{pu} + J_{bs}^{pl}$
The series-connected bimorph PEH with tip mass at $x = L$. (Figure 1.3d)	$A_{11}^{s} + A_{11}^{pu} + A_{11}^{pl}$	$B_{11}^{s} + B_{11}^{pu} + B_{11}^{pl}$	$D_{11}^{s} + D_{11}^{pu} + D_{11}^{pl}$	$F_{55}^{s} + F_{55}^{pu} + F_{55}^{pl}$	$v_b^s(t)$	$B_{bs}^{pu} + B_{bs}^{pl}$	$J_{bs}^{pu} + J_{bs}^{pl}$

Table 2-2 (continued)

The parallel-connected bimorph PEH without tip mass (Figure 1.3e)	$A_{11}^{s} + A_{11}^{pu} + A_{11}^{pl}$	$B_{11}^{s} + B_{11}^{pu} + B_{11}^{pl}$	$D_{11}^{s} + D_{11}^{pu} + D_{11}^{pl}$	$F_{55}^{s} + F_{55}^{pu} + F_{55}^{pl}$	$v_b^p(t)$	$B_{bp}^{pu} + B_{bp}^{pl}$	$J_{bp}^{pu} + J_{bp}^{pl}$
The parallel-connected bimorph PEH with tip mass at $x = L$. (Figure 1.3f)	$A_{11}^{s} + A_{11}^{pu} + A_{11}^{pl}$	$B_{11}^{s} + B_{11}^{pu} + B_{11}^{pl}$	$D_{11}^{s} + D_{11}^{pu} + D_{11}^{pl}$	$F_{55}^{s} + F_{55}^{pu} + F_{55}^{pl}$	$v_b^p(t)$	$B_{bp}^{pu} + B_{bp}^{pl}$	$J_{bp}^{pu} + J_{bp}^{pl}$

A_{11}^{s}, B_{11}^{s}, D_{11}^{s}, and F_{55}^{s} are extensional, coupling, bending, and transverse shear rigidities, respectively, and A_{11}^{pu}, B_{11}^{pu}, D_{11}^{pu}, and F_{55}^{pu} are the conjugate of the coefficients for the upper piezoelectric material. At the same time, A_{11}^{pl}, B_{11}^{pl}, D_{11}^{pl}, and F_{55}^{pl} are the conjugates of the coefficients for the lower piezoelectric material. In addition, the piezoelectric coupling terms for upper piezoelectric material in the unimorph configuration are B_{u}^{pu} and J_{u}^{pu}. B_{u}^{pu} couples the voltage and the extension component, whereas J_{u}^{pu} couples the voltage and the curvature component. In addition, B_{bs}^{pu} and J_{bs}^{pu} are the piezoelectric coupling terms for upper piezoelectric material in the bimorph series-connected configuration, and B_{bs}^{pl} and J_{bs}^{pl} are the terms for lower piezoelectric material in the bimorph series-connected configuration. B_{bp}^{pu}, B_{bp}^{pl}, J_{bp}^{pu}, and J_{bp}^{pl} are the related terms for the parallel-connected bimorph configuration. The voltage across the electrodes is defined as $v_u(t)$, $v_b^s(t)$, and $v_b^p(t)$ in unimorph, series-connected bimorph, and parallel-connected bimorph configurations, respectively. All of the coefficients are depicted as follows:

$$(A_{11}^{s}, B_{11}^{s}, D_{11}^{s}) = b \cdot \int_{-\frac{h^s}{2}}^{\frac{h^s}{2}} \left(\frac{E^s(z) \cdot \left(1 - \nu^s(z)\right)}{\left(1 + \nu^s(z)\right) \cdot \left(1 - 2 \cdot \nu^s(z)\right)} \right) \cdot (1, z, z^2) \cdot dz \tag{2-32}$$

$$(F_{55}^{s}) = b \cdot \int_{-\frac{h^s}{2}}^{\frac{h^s}{2}} \left(\frac{E^s(z)}{2 \cdot \left(1 + \nu^s(z)\right)} \right) \cdot \kappa_s \cdot dz \tag{2-33}$$

$$\left(A_{11}^{pu}, B_{11}^{pu}, D_{11}^{pu}\right) = b \cdot \int_{\frac{h^s}{2}}^{\frac{h^s}{2}+h^p} \left(\frac{\bar{c}_{11}^{E}(z) \cdot \left(1 - \nu^p(z)\right)}{\left(1 + \nu^p(z)\right) \cdot \left(1 - 2 \cdot \nu^p(z)\right)} \right) \cdot (1, z, z^2) \cdot dz \tag{2-34}$$

$$\left(F_{55}^{pu}\right) = b \cdot \int_{\frac{h^s}{2}}^{\frac{h^s}{2}+h^p} \left(\frac{\bar{c}_{55}^{E}(z)}{2 \cdot \left(1 + \nu^p(z)\right)} \right) \cdot \kappa_s \cdot dz \tag{2-35}$$

$$\left(A_{11}^{pl}, B_{11}^{pl}, D_{11}^{pl}\right) = b \cdot \int_{-\frac{h^s}{2}-h^p}^{-\frac{h^s}{2}} \left(\frac{\bar{c}_{11}^{E}(z) \cdot \left(1 - \nu^p(z)\right)}{\left(1 + \nu^p(z)\right) \cdot \left(1 - 2 \cdot \nu^p(z)\right)} \right) \cdot (1, z, z^2) \cdot dz \tag{2-36}$$

$$\left(F_{55}^{pl}\right) = b \cdot \int_{-\frac{h^s}{2}-h^p}^{-\frac{h^s}{2}} \left(\frac{\bar{c}_{55}^{E}(z)}{2 \cdot \left(1 + \nu^p(z)\right)} \right) \cdot \kappa_s \cdot dz \tag{2-37}$$

$$\left(B_u^{pu}, J_u^{pu}\right) = b \cdot \int_{\frac{h^s}{2}}^{\frac{h^s}{2}+h^p} \bar{e}_{31}(z) \cdot \left(\frac{1}{h^p}\right) \cdot (1, z) \cdot dz \tag{2-38}$$

$$\left(B_{bs}^{pu}, J_{bs}^{pu}\right) = b \cdot \int_{\frac{h^s}{2}}^{\frac{h^s}{2}+h^p} \bar{e}_{31}(z) \cdot \left(\frac{1}{2 \cdot h^p}\right) \cdot (1, z) \cdot dz \tag{2-39}$$

$$\left(B_{bs}^{pl}, J_{bs}^{pl}\right) = -b \cdot \int_{-\frac{h^s}{2}-h^p}^{-\frac{h^s}{2}} \bar{e}_{31}(z) \cdot \left(\frac{1}{2 \cdot h^p}\right) \cdot (1, z) \cdot dz \tag{2-40}$$

$$\left(B_{bp}^{pu}, J_{bp}^{pu}\right) = b \cdot \int_{\frac{h^s}{2}}^{\frac{h^s}{2}+h^p} \bar{e}_{31}(z) \cdot \left(\frac{1}{h^p}\right) \cdot (1, z) \cdot dz \tag{2-41}$$

$$\left(B_{bp}^{pl}, J_{bp}^{pl}\right) = -b \cdot \int_{-\frac{h^s}{2}-h^p}^{-\frac{h^s}{2}} \bar{e}_{31}(z) \cdot \left(\frac{1}{h^p}\right) \cdot (1, z) \cdot dz \tag{2-42}$$

The strain energy equation is unaffected by the tip mass addition in unimorph and bimorph types' PEH. However, connecting in series or parallel for bimorph-type PEHs changes the piezoelectric coupling functions. The piezoelectric coupling terms differ in uniform, series-, and parallel-connected bimorph structures because the effective piezoelectric stress constant's $\bar{e}_{31}$ sign varies, and the electric field component $\overline{E}_{33}$ has distinct values. The electric field component should be expressed in terms of the respective voltage term for unimorph and bimorph configurations. It is worth adding that $\bar{e}_{31}$ has the opposite sign for the top and bottom piezoelectric

materials for the bimorph series connection case due to opposite poling so that the instantaneous electric fields are in the same direction. The electric field component of series-connected bimorph PEH's piezoelectric materials is described as $\overline{E}_{33}^{bs}(t) = -v_b^s(t)/(2 \cdot h^p)$. The effective piezoelectric stress constant has the same sign for top and bottom piezoelectric materials in a parallel configuration, so the electric fields are in the opposite direction. While the resulting electric field component for the top piezoelectric material is described as $\overline{E}_{33}^{bpu}(t) = -v_b^p(t)/h^p$, the bottom piezoelectric material is defined as $\overline{E}_{33}^{bpl}(t) = v_b^p(t)/h^p$. In addition, $\overline{E}_{33}^{u}(t) = -v_u(t)/h^p$ is used for the unimorph configuration.

2.5.2 Total Kinetic Energy of the PEH

In equation (2-43), the generalized kinetic energy equation for six configurations is depicted as follows:

$$
\begin{aligned}
T = \frac{1}{2} \cdot \int_{-\frac{h^s}{2}}^{\frac{h^s}{2}} \int_{0}^{L} \left(\mathbf{A}^{(2\text{-}43)}\right) \cdot \left[\left(\frac{\partial u_x(x,z,t)}{\partial t}\right)^2 + \left(\frac{\partial u_z(x,z,t)}{\partial t}\right)^2\right] \cdot b \cdot dz \cdot dx \\
+ \frac{1}{2} \\
\cdot \int_{\frac{h^s}{2}}^{\frac{h^s}{2}+h^p} \int_{0}^{L} \left(\mathbf{B}^{(2\text{-}43)}\right) \cdot \left[\left(\frac{\partial u_x(x,z,t)}{\partial t}\right)^2 + \left(\frac{\partial u_z(x,z,t)}{\partial t}\right)^2\right] \\
\cdot b \cdot dz \cdot dx + \frac{1}{2} \\
\cdot \int_{-\frac{h^s}{2}-h^p}^{-\frac{h^s}{2}} \int_{0}^{L} \left(\mathbf{C}^{(2\text{-}43)}\right) \cdot \left[\left(\frac{\partial u_x(x,z,t)}{\partial t}\right)^2 + \left(\frac{\partial u_z(x,z,t)}{\partial t}\right)^2\right] \\
\cdot b \cdot dz \cdot dx + \frac{1}{2} \cdot \left(\mathbf{D}^{(2\text{-}43)}\right) \cdot \left(\left.\frac{\partial u_z(x,z,t)}{\partial t}\right|_{x=L}\right)^2 \\
+ \frac{1}{2} \cdot \left(\mathbf{E}^{(2\text{-}43)}\right) \cdot \left(\left.\frac{\partial \varphi(x,t)}{\partial t}\right|_{x=L}\right)^2
\end{aligned}
\tag{2-43}
$$

Table 2-3 displays values for $\mathbf{A}^{(2\text{-}43)}$, $\mathbf{B}^{(2\text{-}43)}$, $\mathbf{C}^{(2\text{-}43)}$, $\mathbf{D}^{(2\text{-}43)}$, and $\mathbf{E}^{(2\text{-}43)}$ are based on six configurations.

Table 2-3 The generalized kinetic energy equation constants for equation (2-43) based on six different configurations depicted in Figure 1.3.

PEH Configuration	$\mathbf{A}^{(2\text{-}43)}$	$\mathbf{B}^{(2\text{-}43)}$	$\mathbf{C}^{(2\text{-}43)}$	$\mathbf{D}^{(2\text{-}43)}$	$\mathbf{E}^{(2\text{-}43)}$
The unimorph PEH without tip mass. (Figure 1.3a)	$\rho^{s}(z)$	$\rho^{pu}(z)$	0	0	0
The unimorph PEH with tip mass at $x = L$. (Figure 1.3b)	$\rho^{s}(z)$	$\rho^{pu}(z)$	0	M_t	I_t
The series-connected bimorph PEH without tip mass. (Figure 1.3c)	$\rho^{s}(z)$	$\rho^{pu}(z)$	$\rho^{pl}(z)$	0	0
The series-connected bimorph PEH with tip mass at $x = L$. (Figure 1.3d)	$\rho^{s}(z)$	$\rho^{pu}(z)$	$\rho^{pl}(z)$	M_t	I_t

Table 2-3 (continued)

The parallel-connected bimorph PEH without tip mass. (Figure 1.3e)	$\rho^{s}(z)$	$\rho^{pu}(z)$	$\rho^{pl}(z)$	0	0
The parallel-connected bimorph PEH with tip mass at $x = L$. (Figure 1.3f)	$\rho^{s}(z)$	$\rho^{pu}(z)$	$\rho^{pl}(z)$	M_t	I_t

ρ^{pu} and ρ^{pl} are the mass density of the upper and lower piezoelectric material, respectively. Also, M_t and I_t are the tip mass and mass moment of inertia, respectively. The following is a definition of the cube's ($L^t = h^t$) moment of inertia for tip mass:

$$I_t = \frac{M_t}{12} \cdot ((h^t)^2 + (L^t)^2) \tag{2-44}$$

For kinetic energy expression, transverse displacement component $u_z(x, z, t)$ is modified by including the base displacement $w_b(x, t)$ because PEHs are often placed in structures so that they are continually exposed to vibration:

$$u_z(x, z, t) = w(x, t) + w_b(x, t) \tag{2-45}$$

$w_b(x, t)$ is defined as follows:

$$w_b(x, t) = g(t) + x \cdot h(t) \tag{2-46}$$

where Figure 1.3 shows that g(t) and h(t) represent the base transverse and rotational displacement, respectively. The resultant kinetic energy formulation for the unimorph and bimorph configurations is as follows:

$$\begin{aligned} T = \frac{1}{2}\cdot\int_0^L \Bigg[& \left(\mathbf{A}^{(2\text{-}47)}\right)\cdot\left(\left(\frac{\partial u(x,t)}{\partial t}\right)^2+\left(\frac{\partial w(x,t)}{\partial t}+\frac{\partial w_b(x,t)}{\partial t}\right)^2\right) \\ & -2\cdot\left(\mathbf{B}^{(2\text{-}47)}\right)\cdot\left(\frac{\partial u(x,t)}{\partial t}\cdot\frac{\partial \varphi(x,t)}{\partial t}\right) \\ & +\left(\mathbf{C}^{(2\text{-}47)}\right)\cdot\left(\frac{\partial \varphi(x,t)}{\partial t}\right)^2\Bigg]\cdot dx \\ & +\frac{1}{2}\cdot\left(\mathbf{D}^{(2\text{-}47)}\right)\cdot\left(\left.\frac{\partial w(x,t)}{\partial t}\right|_{x=L}+\left.\frac{\partial w_b(x,t)}{\partial t}\right|_{x=L}\right)^2 \\ & +\frac{1}{2}\cdot\left(\mathbf{E}^{(2\text{-}47)}\right)\cdot\left(\left.\frac{\partial \varphi(x,t)}{\partial t}\right|_{x=L}\right)^2 \end{aligned} \qquad (2\text{-}47)$$

$\mathbf{A}^{(2\text{-}47)}$, $\mathbf{B}^{(2\text{-}47)}$, $\mathbf{C}^{(2\text{-}47)}$, $\mathbf{D}^{(2\text{-}47)}$, and $\mathbf{E}^{(2\text{-}47)}$ values are shown in Table 2-4 based on six configurations.

Table 2-4 The resulting kinetic energy equation constants for equation (2-47) based on six different configurations depicted in Figure 1.3.

PEH Configuration	$\mathbf{A}^{(2\text{-}47)}$	$\mathbf{B}^{(2\text{-}47)}$	$\mathbf{C}^{(2\text{-}47)}$	$\mathbf{D}^{(2\text{-}47)}$	$\mathbf{E}^{(2\text{-}47)}$
The unimorph PEH without tip mass. (Figure 1.3a)	$I_1^s + I_1^{pu}$	$I_2^s + I_2^{pu}$	$I_3^s + I_3^{pu}$	0	0

Table 2-4 (continued)

The unimorph PEH with tip mass at $x = L$. (Figure 1.3b)	$I_1^s + I_1^{pu}$	$I_2^s + I_2^{pu}$	$I_3^s + I_3^{pu}$	M_t	I_t
The series-connected bimorph PEH without tip mass. (Figure 1.3c)	$I_1^s + I_1^{pu} + I_1^{pl}$	$I_2^s + I_2^{pu} + I_2^{pl}$	$I_3^s + I_3^{pu} + I_3^{pl}$	0	0
The series-connected bimorph PEH with tip mass at $x = L$. (Figure 1.3d)	$I_1^s + I_1^{pu} + I_1^{pl}$	$I_2^s + I_2^{pu} + I_2^{pl}$	$I_3^s + I_3^{pu} + I_3^{pl}$	M_t	I_t
The parallel-connected bimorph PEH without tip mass. (Figure 1.3e)	$I_1^s + I_1^{pu} + I_1^{pl}$	$I_2^s + I_2^{pu} + I_2^{pl}$	$I_3^s + I_3^{pu} + I_3^{pl}$	0	0

Table 2-4 (continued)

The parallel-connected bimorph PEH with tip mass at $x = L$. (Figure 1.3f)	$I_1^s + I_1^{pu} + I_1^{pl}$	$I_2^s + I_2^{pu} + I_2^{pl}$	$I_3^s + I_3^{pu} + I_3^{pl}$	M_t	I_t

I_1^s, I_2^s, I_3^s, I_1^{pu}, I_2^{pu}, I_3^{pu}, I_1^{pl}, I_2^{pl}, and I_3^{pl} are expressed as follows:

$$(I_1^s, I_2^s, I_3^s) = b \cdot \int_{-\frac{h^s}{2}}^{\frac{h^s}{2}} \rho^s(z) \cdot (1, z, z^2) \cdot dz \tag{2-48}$$

$$\left(I_1^{pu}, I_2^{pu}, I_3^{pu}\right) = b \cdot \int_{\frac{h^s}{2}}^{\frac{h^s}{2}+h^p} \rho^{pu}(z) \cdot (1, z, z^2) \cdot dz \tag{2-49}$$

$$\left(I_1^{pl}, I_2^{pl}, I_3^{pl}\right) = b \cdot \int_{-\frac{h^s}{2}-h^p}^{-\frac{h^s}{2}} \rho^{pl}(z) \cdot (1, z, z^2) \cdot dz \tag{2-50}$$

Including the tip mass in the unimorph and bimorph designs adds two more factors: tip mass and moment of inertia. Additionally, the difference between unimorph and bimorph structures is due to the addition of the bottom piezoelectric material.

2.5.3 Total Internal Electrical Energy of the PEH

The internal energy of the unimorph and bimorph PEH of Timoshenko piezoelectric material beam elements are determined in equations (2-51).

$$W_{ie} = \frac{1}{2} \cdot \int_{\frac{h^s}{2}}^{\frac{h^s}{2}+h^p} \int_0^L \left(\mathbf{A}^{(2\text{-}51)}\right) \cdot b \cdot dz \cdot dx + \frac{1}{2} \cdot \int_{-\frac{h^s}{2}-h^p}^{-\frac{h^s}{2}} \int_0^L \left(\mathbf{B}^{(2\text{-}51)}\right) \cdot b \cdot dz \cdot dx \tag{2-51}$$

As indicated in Table 2-5, the values of $\mathbf{A}^{(2\text{-}51)}$ and $\mathbf{B}^{(2\text{-}51)}$ are based on six configurations.

Table 2-5 The internal electrical energy equation constants for equation (2-51) based on six different configurations depicted in Figure 1.3.

PEH Configuration	$\mathbf{A}^{(2\text{-}51)}$	$\mathbf{B}^{(2\text{-}51)}$
The unimorph PEH without tip mass. (Figure 1.3a)	$\overline{E}_{33}^{u}(t) \cdot D_{33}$	0
The unimorph PEH with tip mass at $x = L$. (Figure 1.3a)	$\overline{E}_{33}^{u}(t) \cdot D_{33}$	0

Table 2-5 (continued)

The series-connected bimorph PEH without tip mass. (Figure 1.3c)	$\overline{E}_{33}^{bs}(t) \cdot D_{33}$	$\overline{E}_{33}^{bs}(t) \cdot D_{33}$
The series-connected bimorph PEH with tip mass at $x = L$. (Figure 1.3d)	$\overline{E}_{33}^{bs}(t) \cdot D_{33}$	$\overline{E}_{33}^{bs}(t) \cdot D_{33}$
The parallel-connected bimorph PEH without tip mass. (Figure 1.3e)	$\overline{E}_{33}^{bpu}(t) \cdot D_{33}$	$\overline{E}_{33}^{bpl}(t) \cdot D_{33}$
The parallel-connected bimorph PEH with tip mass at $x = L$. (Figure 1.3f)	$\overline{E}_{33}^{bpu}(t) \cdot D_{33}$	$\overline{E}_{33}^{bpl}(t) \cdot D_{33}$

The final state of internal electrical energy equations for all six configurations is derived as follows:

$$W_{ie} = -\frac{1}{2} \cdot \int_0^L \left[\left(\mathbf{A}^{(2\text{-}52)}\right) \cdot \left(\mathbf{B}^{(2\text{-}52)}\right) \cdot \frac{\partial u(x,t)}{\partial x} - \left(\mathbf{A}^{(2\text{-}52)}\right) \cdot \left(\mathbf{C}^{(2\text{-}52)}\right) \cdot \frac{\partial \varphi(x,t)}{\partial x} \right] \cdot dx + \frac{1}{2} \cdot \left(\mathbf{A}^{(2\text{-}52)}\right)^2 \cdot \left(\mathbf{D}^{(2\text{-}52)}\right) \quad (2\text{-}52)$$

$\mathbf{A}^{(2\text{-}52)}$, $\mathbf{B}^{(2\text{-}52)}$, $\mathbf{C}^{(2\text{-}52)}$, and $\mathbf{D}^{(2\text{-}52)}$ values are shown in based on six configurations.

Table 2-6 The resulting internal electrical energy equation constants for equation (2-52) based on six different configurations depicted in Figure 1.3.

PEH Configuration	$\mathbf{A}^{(2\text{-}52)}$	$\mathbf{B}^{(2\text{-}52)}$	$\mathbf{C}^{(2\text{-}52)}$	$\mathbf{D}^{(2\text{-}52)}$
The unimorph PEH without tip mass. (Figure 1.3a)	$v_u(t)$	B_u^{pu}	J_u^{pu}	C_u^p
The unimorph PEH with tip mass at $x = L$. (Figure 1.3b)	$v_u(t)$	B_u^{pu}	J_u^{pu}	C_u^p
The series-connected bimorph PEH without tip mass. (Figure 1.3c)	$v_b^s(t)$	$B_{bs}^{pu} + B_{bs}^{pl}$	$J_{bs}^{pu} + J_{bs}^{pl}$	C_{bs}^p
The series-connected bimorph PEH with tip mass at $x = L$. (Figure 1.3d)	$v_b^s(t)$	$B_{bs}^{pu} + B_{bs}^{pl}$	$J_{bs}^{pu} + J_{bs}^{pl}$	C_{bs}^p

Table 2-6 (continued)

The parallel-connected bimorph PEH without tip mass. (Figure 1.3e)	$v_b^p(t)$	$B_{bp}^{pu} + B_{bp}^{pl}$	$J_{bp}^{pu} + J_{bp}^{pl}$	C_{bp}^p
The parallel-connected bimorph PEH with tip mass at $x = L$. (Figure 1.3f)	$v_b^p(t)$	$B_{bp}^{pu} + B_{bp}^{pl}$	$J_{bp}^{pu} + J_{bp}^{pl}$	C_{bp}^p

C_u^p, C_{bs}^p, and C_{bp}^p are the internal capacitance of the piezoelectric material in unimorph, series-connected bimorph, and parallel-connected bimorph configurations, respectively, and showed as follows:

$$C_u^p = b \cdot \int_0^L \left[\int_{\frac{h^s}{2}}^{\frac{h^s}{2}+h^p} \epsilon_{33}^{\varepsilon} \cdot \left(\frac{1}{h^p}\right)^2 \cdot dz \right] \cdot dx \tag{2-53}$$

$$C_{bs}^p = b \cdot \int_0^L \left[\int_{\frac{h^s}{2}}^{\frac{h^s}{2}+h^p} \epsilon_{33}^{\varepsilon} \cdot \left(\frac{1}{2 \cdot h^p}\right)^2 \cdot dz + \int_{-\frac{h^s}{2}-h^p}^{-\frac{h^s}{2}} \epsilon_{33}^{\varepsilon} \cdot \left(\frac{1}{2 \cdot h^p}\right)^2 \cdot dz \right] \cdot dx \tag{2-54}$$

$$C_{bp}^{p} = b \cdot \int_{0}^{L} \left[\int_{\frac{h^s}{2}}^{\frac{h^s}{2}+h^p} \epsilon_{33}^{\varepsilon} \cdot \left(\frac{1}{h^p}\right)^2 \cdot dz + \int_{-\frac{h^s}{2}-h^p}^{-\frac{h^s}{2}} \epsilon_{33}^{\varepsilon} \cdot \left(\frac{1}{h^p}\right)^2 \cdot dz \right] \cdot dx \quad (2\text{-}55)$$

2.5.4 Total Non-conservative Mechanical and Electrical Energy of the PEH

Work done by external time-dependent forces can be expressed as:

$$W_{nc} = \int_{0}^{L} f(x,t) \cdot w(x,t) \cdot dx \quad (2\text{-}56)$$

Four types of loading are considered: uniformly distributed step, concentrated step, concentrated harmonic, and concentrated impulsive loads. The following is the list of forcing functions:

$$f(x,t) = f_0 \cdot H(t), \quad \text{for uniformly distributed step load} \quad (2\text{-}57)$$

$$f(x,t) = F \cdot \delta(x - x_0) \cdot H(t), \quad \text{for concentrated step load} \quad (2\text{-}58)$$

$$f(x,t) = F \cdot \delta(x - x_0) \cdot \sin(\omega_p \cdot t), \quad \text{for concentrated harmonic load} \quad (2\text{-}59)$$

$$f(x,t) = \bar{F} \cdot \delta(x - x_0) \cdot \delta(t), \quad \text{for concentrated impulsive load} \quad (2\text{-}60)$$

Here f_0, H, F, δ, x_0, ω_p, $\bar{F}$ are the uniformly distributed load intensity, the Heaviside unit step function, the concentrated load intensity, the Dirac delta function, the load applying point on the Cartesian coordinate system, the applied frequency, and the impulsive load intensity, respectively.

2.6 Boundary Conditions

The clamped, simply supported, pinned, and free BCs are represented by the symbols C, S, P, and F, respectively. The free BC means the beam is in its natural state in space due to the lack of constraints. It signifies that the solution of the equations of motion does not need any modification. The following are the other essential BCs:

- Clamped End (C):

$$u(x,t) = w(x,t) = \varphi(x,t) = 0 \qquad (x = 0 \text{ or } x = L) \qquad (2\text{-}61)$$

- Simply Supported End (S):

$$u(x,t) = w(x,t) = 0 \qquad (x = 0 \text{ or } x = L) \qquad (2\text{-}62)$$

- Pinned End (P):

$$w(x,t) = 0 \qquad (x = 0 \text{ or } x = L) \qquad (2\text{-}63)$$

CHAPTER 3

WQEM FORMULATION AND GOVERNING EQUATIONS OF MOTION

The WQEM requires constructing a mass, stiffness, damping, electrical voltage, force matrix, and related coefficients to express the equations of motion since the numerical technique allows for varying the number of nodes N to achieve the required accuracy. First, fundamental concepts of the WQEM are presented, including integral and DQ rules. The extended Hamilton's principle from section 2.5 is then used to produce the electromechanical Lagrange equations. Free and forced vibration solutions are built following the formation of the equations of motion using the electromechanical Lagrange equations. Finally, it is possible to proceed to validation and parametric analysis studies in the numerical results chapter.

3.1 General Rules of Weak Form Quadrature Element Method

The definition of DQ rules is essential as it enables the displacement fields described in section 2.2 to be revised in accordance with WQEM. These formulations establish the N-node quadrature Timoshenko beam element.

3.1.1 Integral Quadrature

The following is used to express the numerical integration of f(x) in the range $[-1,1]$:

$$\int_{-1}^{1} f(x) \cdot dx = \sum_{j=1}^{N} H_j \cdot f(x_j) \tag{3-1}$$

where N is the total number of integral points, and H_j and x_j are the quadrature weights and abscissas of the physical coordinate system, respectively. Quadrature weight is indicated as follows:

$$H_j = \int_{-1}^{1} l_j(x) \cdot dx \qquad (j = 1,2, \dots, N) \qquad (3\text{-}2)$$

where shape function $l_j(x)$ denotes the Lagrange interpolation function and is described as follows:

$$\begin{aligned} l_j(x) &= \frac{(x - x_1) \cdot (x - x_2) \cdots (x - x_{j-1}) \cdot (x - x_{j+1}) \cdots (x - x_N)}{(x_j - x_1) \cdot (x_j - x_2) \cdots (x_j - x_{j-1}) \cdot (x_j - x_{j+1}) \cdots (x_j - x_N)} \\ &= \prod_{\substack{k=1 \\ k \neq j}}^{N} \frac{(x - x_k)}{(x_j - x_k)} \end{aligned} \qquad (3\text{-}3)$$

3.1.2 Differential Quadrature Method

The derivative of the one-dimensional $f(x)$ function in the $[-1,1]$ range is continuous and differentiable with respect to x.

$$\left(\frac{df(x)}{dx}\right)_{x=x_i} = \sum_{j=1}^{N} A_{ij} \cdot f(x_j) \qquad (i = 1,2, \dots, N) \qquad (3\text{-}4)$$

where A_{ij} is the first-order derivative weighting coefficient with respect to x. The first-order derivative explanation is enough because second, third, and higher-order derivatives are not required in the Timoshenko beam element formulation. The one-dimensional function $f(x)$ in the domain $[a, b]$ is continuous and differentiable with respect to x. Once x_j and $f(x_j)$ are provided, $f(x)$ can be represented using Lagrange interpolation functions as follows:

$$f(x) = \sum_{j=1}^{N} l_j(x) \cdot f(x_j) = \sum_{j=1}^{N} l_j(x) \cdot f_j \qquad (3\text{-}5)$$

where $a = x_1 < x_2 < \cdots < x_N = b$. As a result of the differentiation of f(x) with respect to x in equation (3-5), its solution at point x_i yields

$$\left(\frac{df(x)}{dx}\right)_{x=x_i} = \sum_{j=1}^{N}\left(\frac{dl_j(x)}{dx}\right)_{x=x_i} \cdot f(x_j) \qquad (i = 1,2,\dots,N) \qquad (3\text{-}6)$$

The first-order derivative weighting coefficient is thus determined by comparing equations (3-4) and (3-6) and is written as:

$$A_{ij} = \left(\frac{dl_j(x)}{dx}\right)_{x=x_i} \qquad (i,j = 1,2,\dots,N) \qquad (3\text{-}7)$$

where,

$$A_{ij} = \left(\frac{dl_j(x)}{dx}\right)_{x=x_i} = l_j'(x_i) = \begin{cases} \dfrac{\prod_{\substack{k=1 \\ k\neq i,j}}^{N}(x_i - x_k)}{\prod_{\substack{k=1 \\ k\neq j}}^{N}(x_j - x_k)} & (i \neq j) \\ \displaystyle\sum_{\substack{k=1 \\ k\neq i}}^{N}\frac{1}{(x_i - x_k)} & (i = j) \end{cases} \qquad (3\text{-}8)$$

3.2 Quadrature Piezoelectric Timoshenko Beam Element

An N-node quadrature PEH Timoshenko beam element is schematically illustrated in Figure 3.1.

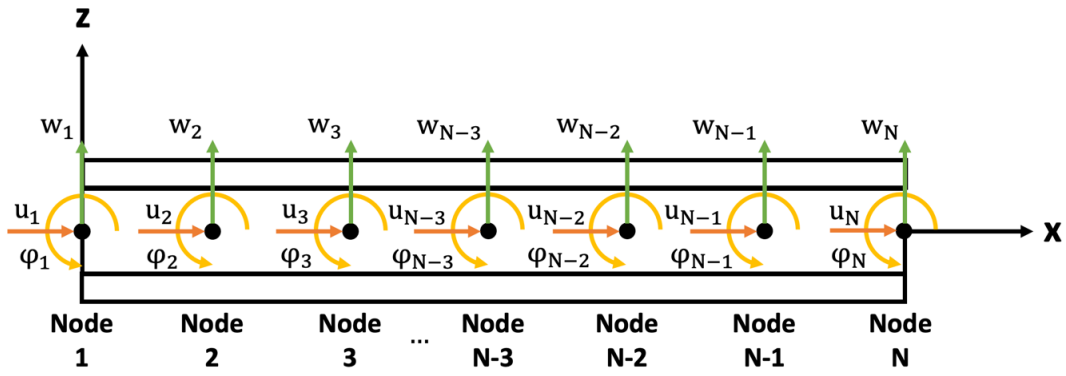

Figure 3.1 Sketch of a N-node quadrature piezoelectric Timoshenko beam element.

The generalized displacement functions for the N-node beam element are given by equations (3-9), (3-10), and (3-11). x_i coordinates N nodes, where $x_i \in [0, L]$. Each node has three degrees of freedom – u_j, φ_j, w_j $(j = 1,2, \dots, N)$ are nodal displacement vectors.

$$u(x,t) = \sum_{j=1}^{N} l_j(x) \cdot u(x_j,t) = \sum_{j=1}^{N} l_j(x) \cdot u_j(t) = \sum_{j=1}^{N} l_j(\xi) \cdot u_j(t) \qquad (3\text{-}9)$$

$$\varphi(x,t) = \sum_{j=1}^{N} l_j(x) \cdot \varphi(x_j,t) = \sum_{j=1}^{N} l_j(x) \cdot \varphi_j(t) = \sum_{j=1}^{N} l_j(\xi) \cdot \varphi_j(t) \qquad (3\text{-}10)$$

$$w(x,t) = \sum_{j=1}^{N} l_j(x) \cdot w(x_j,t) = \sum_{j=1}^{N} l_j(x) \cdot w_j(t) = \sum_{j=1}^{N} l_j(\xi) \cdot w_j(t) \qquad (3\text{-}11)$$

where ξ is the abscissa of the natural coordinate system. The abscissa and weight values created using GLL nodes change according to the number of nodes established on the Timoshenko beam element. The abscissa and weight values can be found with the help of the MATLAB code given in Appendix C. Incorporating displacement field functions for N-node beam elements into the strain, kinetic, work internal energy function, and total non-conservative mechanical and electrical energy is crucial. In the implementation process, drawing attention to the $l_i(x) = l_i(\xi)$ characteristic is essential. Figure 3.2 illustrates the natural-to-Cartesian geometric linear mapping using the formula $x = L \cdot (1 + \xi)/2$, so the differential of x can be expressed as $dx = L \cdot (d\xi/2)$. x can have a value between 0 and L, while ξ can be between -1 and 1.

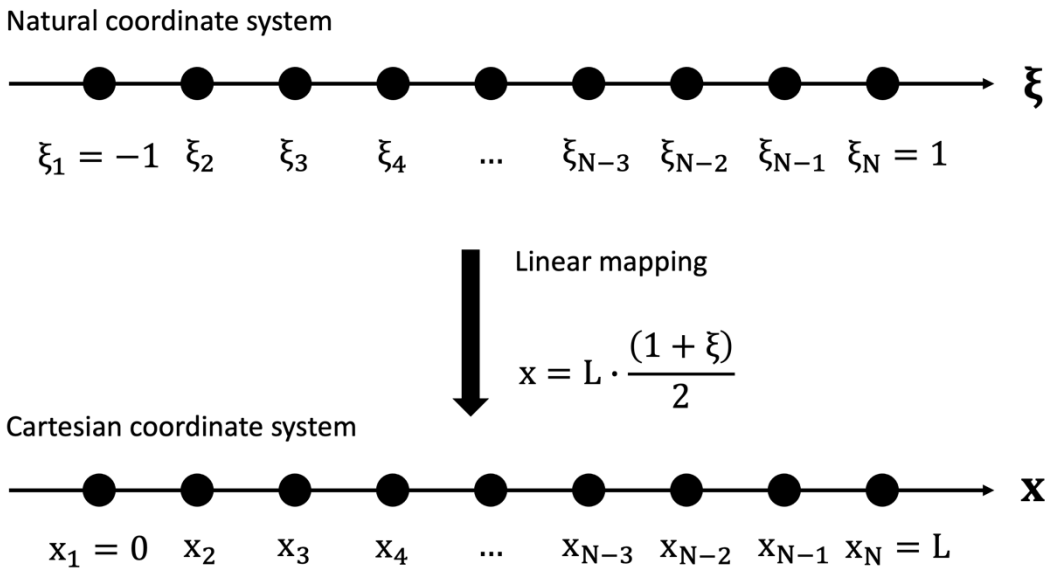

Figure 3.2 Linear mapping between natural and Cartesian coordinate systems for the grid points of the FG Timoshenko PEH beams.

The numerical integration is performed using the GLL quadrature. Displacement field functions expressed in equations (3-9), (3-10), and (3-11) are implemented into the strain energy function that is derived in equation (2-31), the kinetic energy function that is derived in equation (2-47), and the work internal energy function that is derived in equation (2-52) for six alternative PEH configurations. The coefficients of the stiffness and mass matrices for six PEH setups, which are utilized to define the strain energy function, the kinetic energy function, and the work internal energy function, are displayed in Appendix A and B both before and after the application of WQEM. Also, the remaining constants (θ_i^u, θ_i^φ, and θ_i^w) obtained to describe the strain energy equation are provided in Appendix A. Another constant p_i is identified to define the kinetic energy equation and is listed in Appendix B. The strain, kinetic, and work internal energy functions applied to the WQEM are shown in equations (3-12), (3-13), and (3-14).

$$
\begin{aligned}
U = \frac{1}{2} \cdot \Bigg[& K_{ij}^{uu} \cdot \left(\sum_{i=1}^{N} \left(u_i(t) \right) \cdot \sum_{j=1}^{N} \left(u_j(t) \right) \right) \\
& + K_{ij}^{u\varphi} \cdot \left(\sum_{i=1}^{N} \left(u_i(t) \right) \cdot \sum_{j=1}^{N} \left(\varphi_j(t) \right) \right) \\
& + K_{ij}^{\varphi u} \cdot \left(\sum_{i=1}^{N} \left(\varphi_i(t) \right) \cdot \sum_{j=1}^{N} \left(u_j(t) \right) \right) \\
& + K_{ij}^{\varphi\varphi} \cdot \left(\sum_{i=1}^{N} \left(\varphi_i(t) \right) \cdot \sum_{j=1}^{N} \left(\varphi_j(t) \right) \right) \\
& + K_{ij}^{\varphi w} \cdot \left(\sum_{i=1}^{N} \left(\varphi_i(t) \right) \cdot \sum_{j=1}^{N} \left(w_j(t) \right) \right) \\
& + K_{ij}^{w\varphi} \cdot \left(\sum_{i=1}^{N} \left(w_i(t) \right) \cdot \sum_{j=1}^{N} \left(\varphi_j(t) \right) \right) \\
& + K_{ij}^{ww} \cdot \left(\sum_{i=1}^{N} \left(w_i(t) \right) \cdot \sum_{j=1}^{N} \left(w_j(t) \right) \right) \\
& + \left(\mathbf{A}^{(3\text{-}12)} \right) \cdot \theta_i^{u} \cdot \left(\sum_{i=1}^{N} \left(u_i(t) \right) \right) \\
& - \left(\mathbf{A}^{(3\text{-}12)} \right) \cdot \theta_i^{\varphi} \cdot \left(\sum_{i=1}^{N} \left(\varphi_i(t) \right) \right) \Bigg]
\end{aligned}
\tag{3-12}
$$

$$
\begin{aligned}
T = \frac{1}{2}\cdot\Bigg[& M_{ij}^{uu}\cdot\left(\sum_{i=1}^{N}\left(\frac{du_i(t)}{dt}\right)\cdot\sum_{j=1}^{N}\left(\frac{du_j(t)}{dt}\right)\right) \\
& + M_{ij}^{ww}\cdot\left(\sum_{i=1}^{N}\left(\frac{dw_i(t)}{dt}\right)\cdot\sum_{j=1}^{N}\left(\frac{dw_j(t)}{dt}\right)\right) \\
& + 2\cdot p_i\cdot\left(\sum_{i=1}^{N}\left(\frac{dw_i(t)}{dt}\right)\right) \\
& + \int_0^L\left(\left(\mathbf{A}^{(3\text{-}13)}\right)\cdot\left(\frac{\partial w_b(x,t)}{\partial t}\right)^2\cdot dx\right) \\
& + M_{ij}^{u\varphi}\cdot\left(\sum_{i=1}^{N}\left(\frac{du_i(t)}{dt}\right)\cdot\sum_{j=1}^{N}\left(\frac{d\varphi_j(t)}{dt}\right)\right) \\
& + M_{ij}^{\varphi u}\cdot\left(\sum_{i=1}^{N}\left(\frac{d\varphi_i(t)}{dt}\right)\cdot\sum_{j=1}^{N}\left(\frac{du_j(t)}{dt}\right)\right) \\
& + M_{ij}^{\varphi\varphi}\cdot\left(\sum_{i=1}^{N}\left(\frac{d\varphi_i(t)}{dt}\right)\cdot\sum_{j=1}^{N}\left(\frac{d\varphi_j(t)}{dt}\right)\right) \\
& + M_t\cdot\left(\left.\frac{\partial w_b(x,t)}{\partial t}\right|_{x=L}\right)^2\Bigg]
\end{aligned}
\tag{3-13}
$$

$$
\begin{aligned}
W_{ie} = & -\frac{1}{2}\cdot\left(\mathbf{A}^{(3\text{-}12)}\right)\cdot\theta_i^u\cdot\sum_{i=1}^{N}\left(u_i(t)\right)+\frac{1}{2}\cdot\left(\mathbf{A}^{(3\text{-}12)}\right)\cdot\theta_i^{\varphi}\cdot\sum_{i=1}^{N}\left(\varphi_i(t)\right) \\
& + \frac{1}{2}\cdot\left(\mathbf{A}^{(3\text{-}12)}\right)^2\cdot\mathbf{A}^{(3\text{-}14)}
\end{aligned}
\tag{3-14}
$$

θ_i^u and θ_i^{φ} use six relevant configurations of $\mathbf{A}^{(A\ 10)}$ and $\mathbf{A}^{(A\ 11)}$ given in Appendix A. Table 3-1 lists the additional constants in equations (3-12), (3-13), and (3-14).

Table 3-1 The WQEM applied the strain, kinetic, and internal electrical energy equation constants for equations (3-12), (3-13), and (3-14) based on six different configurations depicted in Figure 1.3.

PEH Configuration	$\mathbf{A}^{(3\text{-}12)}$	$\mathbf{A}^{(3\text{-}13)}$	$\mathbf{A}^{(3\text{-}14)}$
The unimorph PEH without tip mass. (Figure 1.3a)	$v_u(t)$	$I_1^s + I_1^{pu}$	C_u^p
The unimorph PEH with tip mass at $x = L$. (Figure 1.3b)	$v_u(t)$	$I_1^s + I_1^{pu}$	C_u^p
The series-connected bimorph PEH without tip mass. (Figure 1.3c)	$v_b^s(t)$	$I_1^s + I_1^{pu} + I_1^{pl}$	C_{bs}^p
The series-connected bimorph PEH with tip mass at $x = L$. (Figure 1.3d)	$v_b^s(t)$	$I_1^s + I_1^{pu} + I_1^{pl}$	C_{bs}^p

Table 3-1 (continued)

The parallel-connected bimorph PEH without tip mass. (Figure 1.3e)	$v_b^p(t)$	$I_1^s + I_1^{pu} + I_1^{pl}$	C_{bp}^p
The parallel-connected bimorph PEH with tip mass at $x = L$. (Figure 1.3f)	$v_b^p(t)$	$I_1^s + I_1^{pu} + I_1^{pl}$	C_{bp}^p

3.2.1 Stress Computation for Quadrature Piezoelectric Timoshenko Beam Element

The generalized displacement functions are applied to the stresses indicated by equations (2-6) and (2-15) for stress computation of piezoelectric material and substructure, respectively. The WQEM stress values are shown as follows:

$$\sigma_{11}(x,z,t) = \bar{c}_{11}^{E}(z)\cdot\left(\frac{2}{L}\cdot\sum_{j=1}^{N}\left(A_{ij}\cdot u_i(t)\right) - z\cdot\frac{2}{L}\cdot\sum_{j=1}^{N}\left(A_{ij}\cdot\varphi_j(t)\right)\right) - \bar{e}_{31}(z)\cdot\bar{E}_{33} \tag{3-15}$$

$$\sigma_{13}(x,z,t) = \kappa_s\cdot\bar{c}_{55}^{E}(z)\cdot\left[-\left(\sum_{j=1}^{N} l_j(\xi_i)\cdot\varphi_j(t)\right) + \left(\sum_{j=1}^{N}\frac{2}{L}\cdot A_{ij}\cdot w_j(t)\right)\right] \tag{3-16}$$

$$\sigma_{xx}(x,z,t) = \frac{E^s(z)\cdot\left(1-\nu^s(z)\right)}{\left(1+\nu^s(z)\right)\cdot\left(1-2\cdot\nu^s(z)\right)} \cdot\left[\left(\sum_{j=1}^{N}\frac{2}{L}\cdot A_{ij}\cdot u_j(t)\right) - z\cdot\left(\sum_{j=1}^{N}\frac{2}{L}\cdot A_{ij}\cdot \varphi_j(t)\right)\right] \tag{3-17}$$

$$\sigma_{yy}(x,z,t) = \sigma_{zz}(x,z,t) = \frac{E^s(z)\cdot\nu^s(z)}{\left(1+\nu^s(z)\right)\cdot\left(1-2\cdot\nu^s(z)\right)} \cdot\left[\left(\sum_{j=1}^{N}\frac{2}{L}\cdot A_{ij}\cdot u_j(t)\right) - z\cdot\left(\sum_{j=1}^{N}\frac{2}{L}\cdot A_{ij}\cdot \varphi_j(t)\right)\right] \tag{3-18}$$

$$\sigma_{xz}(x,z,t) = \kappa_s\cdot\frac{E^s(z)}{2\cdot\left(1+\nu^s(z)\right)} \cdot\left[-\left(\sum_{j=1}^{N} l_j(\xi_i)\cdot\varphi_j(t)\right) + \left(\sum_{j=1}^{N}\frac{2}{L}\cdot A_{ij}\cdot w_j(t)\right)\right] \tag{3-19}$$

3.3 The Electromechanical Lagrange Equations of Quadrature Piezoelectric Timoshenko Beam Element

The electromechanical Lagrange equations, using the extended Hamilton's principle as a basis, as indicated in equation (2-29), are written as follows:

$$\frac{d}{dt}\left(\frac{\partial\cdot T}{\partial\cdot\left(\frac{du_r}{dt}\right)}\right) - \frac{\partial\cdot T}{\partial\cdot u_r} + \frac{\partial\cdot U}{\partial\cdot u_r} - \frac{\partial\cdot W_{ie}}{\partial\cdot u_r} = 0 \tag{3-20}$$

$$\frac{d}{dt}\left(\frac{\partial \cdot T}{\partial \cdot \left(\frac{d\varphi_r}{dt}\right)}\right) - \frac{\partial \cdot T}{\partial \cdot \varphi_r} + \frac{\partial \cdot U}{\partial \cdot \varphi_r} - \frac{\partial \cdot W_{ie}}{\partial \cdot \varphi_r} = 0 \tag{3-21}$$

$$\frac{d}{dt}\left(\frac{\partial \cdot T}{\partial \cdot \left(\frac{dw_r}{dt}\right)}\right) - \frac{\partial \cdot T}{\partial \cdot w_r} + \frac{\partial \cdot U}{\partial \cdot w_r} - \frac{\partial \cdot W_{ie}}{\partial \cdot w_r} = 0 \tag{3-22}$$

$$\frac{d}{dt}\left(\frac{\partial \cdot T}{\partial \cdot \left(\frac{dv}{dt}\right)}\right) - \frac{\partial \cdot T}{\partial \cdot v} + \frac{\partial \cdot U}{\partial \cdot v} - \frac{\partial \cdot W_{ie}}{\partial \cdot v} = Q_e \tag{3-23}$$

where the output electrical charge is denoted by Q_e and v is the collective representation of the six configurations of voltage terms represented by $v_u(t)$, $v_b^s(t)$, and $v_b^p(t)$. Equations (3-20), (3-21), (3-22), and (3-23) are used to get the solution to the electromechanical Lagrange equations to define the equations of motion.

3.3.1 The Solution of Electromechanical Lagrange Equation (3-20)

All components of equation (3-20) using WQEM implementation are described as follows:

$$\begin{aligned}\frac{d}{dt}\left(\frac{\partial \cdot T}{\partial \cdot \left(\frac{du_r}{dt}\right)}\right) &= \frac{1}{2} \\ &\cdot \left[M_{rj}^{uu} \cdot \sum_{j=1}^{N}\left(\frac{d^2u_j(t)}{dt^2}\right) + M_{jr}^{uu} \cdot \sum_{j=1}^{N}\left(\frac{d^2u_j(t)}{dt^2}\right)\right. \\ &\left. + M_{rj}^{u\varphi} \cdot \sum_{j=1}^{N}\left(\frac{d^2\varphi_j(t)}{dt^2}\right) + M_{jr}^{\varphi u} \cdot \sum_{j=1}^{N}\left(\frac{d^2\varphi_j(t)}{dt^2}\right)\right]\end{aligned} \tag{3-24}$$

$$\frac{\partial \cdot U}{\partial \cdot u_r} = \frac{1}{2} \cdot \left[K_{rj}^{uu} \cdot \sum_{j=1}^{N} \left(u_j(t) \right) + K_{jr}^{uu} \cdot \sum_{j=1}^{N} \left(u_j(t) \right) + K_{rj}^{u\varphi} \cdot \sum_{j=1}^{N} \left(\varphi_j(t) \right) + K_{jr}^{\varphi u} \cdot \sum_{j=1}^{N} \left(\varphi_j(t) \right) + v \cdot \theta_r^u \right] \tag{3-25}$$

$$-\frac{\partial \cdot W_{ie}}{\partial \cdot u_r} = \frac{1}{2} \cdot v \cdot \theta_r^u \tag{3-26}$$

The final state of equation (3-20) is written as follows:

$$\frac{1}{2} \cdot \left[M_{rj}^{uu} \cdot \sum_{j=1}^{N} \left(\frac{d^2 u_j(t)}{dt^2} \right) + M_{jr}^{uu} \cdot \sum_{j=1}^{N} \left(\frac{d^2 u_j(t)}{dt^2} \right) + M_{rj}^{u\varphi} \cdot \sum_{j=1}^{N} \left(\frac{d^2 \varphi_j(t)}{dt^2} \right) + M_{jr}^{\varphi u} \cdot \sum_{j=1}^{N} \left(\frac{d^2 \varphi_j(t)}{dt^2} \right) + K_{rj}^{uu} \cdot \sum_{j=1}^{N} \left(u_j(t) \right) + K_{jr}^{uu} \cdot \sum_{j=1}^{N} \left(u_j(t) \right) + K_{rj}^{u\varphi} \cdot \sum_{j=1}^{N} \left(\varphi_j(t) \right) + K_{jr}^{\varphi u} \cdot \sum_{j=1}^{N} \left(\varphi_j(t) \right) + v \cdot \theta_r^u + v \cdot \theta_r^u \right] = 0 \tag{3-27}$$

3.3.2 The Solution of Electromechanical Lagrange Equation (3-21)

All components of equation (3-21) using WQEM implementation are determined as follows:

$$\frac{\mathrm{d}}{\mathrm{dt}}\left(\frac{\partial\cdot \mathrm{T}}{\partial\cdot\left(\frac{\mathrm{d}\varphi_{\mathrm{r}}}{\mathrm{dt}}\right)}\right) = \frac{1}{2} \cdot \left[\mathrm{M}_{\mathrm{jr}}^{\mathrm{u}\varphi}\cdot\sum_{\mathrm{j}=1}^{\mathrm{N}}\left(\frac{\mathrm{d}^2\mathrm{u}_{\mathrm{j}}(\mathrm{t})}{\mathrm{dt}^2}\right) + \mathrm{M}_{\mathrm{rj}}^{\varphi\mathrm{u}}\cdot\sum_{\mathrm{j}=1}^{\mathrm{N}}\left(\frac{\mathrm{d}^2\mathrm{u}_{\mathrm{j}}(\mathrm{t})}{\mathrm{dt}^2}\right) + \mathrm{M}_{\mathrm{rj}}^{\varphi\varphi} \cdot\sum_{\mathrm{j}=1}^{\mathrm{N}}\left(\frac{\mathrm{d}^2\varphi_{\mathrm{j}}(\mathrm{t})}{\mathrm{dt}^2}\right) + \mathrm{M}_{\mathrm{jr}}^{\varphi\varphi}\cdot\sum_{\mathrm{j}=1}^{\mathrm{N}}\left(\frac{\mathrm{d}^2\varphi_{\mathrm{j}}(\mathrm{t})}{\mathrm{dt}^2}\right)\right] \tag{3-28}$$

$$\frac{\partial\cdot \mathrm{U}}{\partial\cdot\varphi_{\mathrm{r}}} = \frac{1}{2}\cdot\left[\mathrm{K}_{\mathrm{jr}}^{\mathrm{u}\varphi}\cdot\sum_{\mathrm{j}=1}^{\mathrm{N}}\left(\mathrm{u}_{\mathrm{j}}(\mathrm{t})\right) + \mathrm{K}_{\mathrm{rj}}^{\varphi\mathrm{u}}\cdot\sum_{\mathrm{j}=1}^{\mathrm{N}}\left(\mathrm{u}_{\mathrm{j}}(\mathrm{t})\right) + \mathrm{K}_{\mathrm{rj}}^{\varphi\varphi} \cdot\sum_{\mathrm{j}=1}^{\mathrm{N}}\left(\varphi_{\mathrm{j}}(\mathrm{t})\right) + \mathrm{K}_{\mathrm{jr}}^{\varphi\varphi}\cdot\sum_{\mathrm{j}=1}^{\mathrm{N}}\left(\varphi_{\mathrm{j}}(\mathrm{t})\right) + \mathrm{K}_{\mathrm{rj}}^{\varphi\mathrm{w}}\cdot\sum_{\mathrm{j}=1}^{\mathrm{N}}\left(\mathrm{w}_{\mathrm{j}}(\mathrm{t})\right) + \mathrm{K}_{\mathrm{jr}}^{\mathrm{w}\varphi}\cdot\sum_{\mathrm{j}=1}^{\mathrm{N}}\left(\mathrm{w}_{\mathrm{j}}(\mathrm{t})\right) - \mathrm{v}\cdot\theta_{\mathrm{r}}^{\varphi}\right] \tag{3-29}$$

$$-\frac{\partial\cdot \mathrm{W}_{\mathrm{ie}}}{\partial\cdot\varphi_{\mathrm{r}}} = -\frac{1}{2}\cdot\mathrm{v}\cdot\theta_{\mathrm{r}}^{\varphi} \tag{3-30}$$

The final state of equation (3-21) is described as follows:

$$\frac{1}{2}\cdot\left[M_{jr}^{u\varphi}\cdot\sum_{j=1}^{N}\left(\frac{d^2u_j(t)}{dt^2}\right)+M_{rj}^{\varphi u}\cdot\sum_{j=1}^{N}\left(\frac{d^2u_j(t)}{dt^2}\right)+M_{rj}^{\varphi\varphi}\right.$$
$$\cdot\sum_{j=1}^{N}\left(\frac{d^2\varphi_j(t)}{dt^2}\right)+M_{jr}^{\varphi\varphi}\cdot\sum_{j=1}^{N}\left(\frac{d^2\varphi_j(t)}{dt^2}\right)+K_{jr}^{u\varphi}$$
$$\cdot\sum_{j=1}^{N}\left(u_j(t)\right)+K_{rj}^{\varphi u}\cdot\sum_{j=1}^{N}\left(u_j(t)\right)+K_{rj}^{\varphi\varphi}\cdot\sum_{j=1}^{N}\left(\varphi_j(t)\right) \qquad (3\text{-}31)$$
$$+K_{jr}^{\varphi\varphi}\cdot\sum_{j=1}^{N}\left(\varphi_j(t)\right)+K_{rj}^{\varphi w}\cdot\sum_{j=1}^{N}\left(w_j(t)\right)+K_{jr}^{w\varphi}$$
$$\left.\cdot\sum_{j=1}^{N}\left(w_j(t)\right)-v\cdot\theta_r^{\varphi}-v\cdot\theta_r^{\varphi}\right]=0$$

3.3.3 The Solution of Electromechanical Lagrange Equation (3-22)

All components of equation (3-22) using WQEM implementation are indicated as follows:

$$\frac{d}{dt}\left(\frac{\partial\cdot T}{\partial\cdot\left(\frac{dw_r}{dt}\right)}\right)$$
$$=\frac{1}{2}$$
$$\cdot\left[M_{rj}^{ww}\cdot\sum_{j=1}^{N}\left(\frac{d^2w_j(t)}{dt^2}\right)+M_{jr}^{ww}\cdot\sum_{j=1}^{N}\left(\frac{d^2w_j(t)}{dt^2}\right)+2\right. \qquad (3\text{-}32)$$
$$\left.\cdot\frac{\partial\cdot p_r}{\partial\cdot t}\right]$$

$$\frac{\partial \cdot U}{\partial \cdot w_r} = \frac{1}{2} \cdot \left[K_{jr}^{\varphi w} \cdot \sum_{j=1}^{N} \left(\varphi_j(t) \right) + K_{rj}^{w\varphi} \cdot \sum_{j=1}^{N} \left(\varphi_j(t) \right) + K_{rj}^{ww} \cdot \sum_{j=1}^{N} \left(w_j(t) \right) + K_{jr}^{ww} \cdot \sum_{j=1}^{N} \left(w_j(t) \right) \right] \tag{3-33}$$

The final state of equation (3-22) is determined as follows:

$$\frac{1}{2} \cdot \left[M_{rj}^{ww} \cdot \sum_{j=1}^{N} \left(\frac{d^2 w_j(t)}{dt^2} \right) + M_{jr}^{ww} \cdot \sum_{j=1}^{N} \left(\frac{d^2 w_j(t)}{dt^2} \right) + 2 \cdot \frac{\partial \cdot p_r}{\partial \cdot t} + K_{jr}^{\varphi w} \cdot \sum_{j=1}^{N} \left(\varphi_j(t) \right) + K_{rj}^{w\varphi} \cdot \sum_{j=1}^{N} \left(\varphi_j(t) \right) + K_{rj}^{ww} \cdot \sum_{j=1}^{N} \left(w_j(t) \right) + K_{jr}^{ww} \cdot \sum_{j=1}^{N} \left(w_j(t) \right) \right] = 0 \tag{3-34}$$

3.3.4 The Solution of Electromechanical Lagrange Equation (3-23)

All components of equation (3-23) using WQEM implementation are defined as follows:

$$\frac{\partial \cdot U}{\partial \cdot v} = \frac{1}{2} \cdot \left[\theta_i^u \cdot \sum_{i=1}^{N} \left(u_i(t) \right) - \theta_i^{\varphi} \cdot \sum_{i=1}^{N} \left(\varphi_i(t) \right) \right] \tag{3-35}$$

$$-\frac{\partial \cdot W_{ie}}{\partial \cdot v} = \frac{1}{2} \cdot \left[\theta_i^u \cdot \sum_{i=1}^{N} \left(u_i(t) \right) - \theta_i^{\varphi} \cdot \sum_{i=1}^{N} \left(\varphi_i(t) \right) - 2 \cdot v \cdot \left(\mathbf{A}^{(3\text{-}14)} \right) \right] \tag{3-36}$$

The final state of equation (3-23) is indicated as follows:

$$\frac{1}{2}\cdot\left[\theta_i^u\cdot\sum_{i=1}^{N}\left(u_i(t)\right)-\theta_i^{\varphi}\cdot\sum_{i=1}^{N}\left(\varphi_i(t)\right)+\theta_i^u\cdot\sum_{i=1}^{N}\left(u_i(t)\right)-\theta_i^{\varphi}\cdot\sum_{i=1}^{N}\left(\varphi_i(t)\right)-2\cdot v\cdot\left(\mathbf{A}^{(3\text{-}14)}\right)\right]=Q_e \tag{3-37}$$

The electromechanical Lagrange equation (3-23) is solved by taking the time derivative of equation (3-37) and using $dQ_e/dt = v/R_l$ as follows:

$$-\theta_i^u\cdot\sum_{i=1}^{N}\left(\frac{du_i(t)}{dt}\right)+\theta_i^{\varphi}\cdot\sum_{i=1}^{N}\left(\frac{d\varphi_i(t)}{dt}\right)+\frac{dv}{dt}\cdot\left(\mathbf{A}^{(3\text{-}14)}\right)+\frac{v}{R_l}=0 \tag{3-38}$$

3.4 The Equations of Motion

First, the damping matrix $[D]$ is the last undefined element forming the equations of motion. Rayleigh's damping factor is used to construct the damping matrix to represent the mechanical dissipative effects. The following is a compact approach to expressing it:

$$[D]=\hat{\mu}\cdot[M]+\hat{\gamma}\cdot[K] \tag{3-39}$$

where the mass and stiffness proportionality constants are $\hat{\mu}$ and $\hat{\gamma}$, respectively. The mass and stiffness matrices are denoted by $[M]$ and $[K]$. The damping ratio ζ can be related to mass and stiffness proportionality constants as follows:

$$\zeta=\frac{1}{2}\cdot\left(\frac{\hat{\mu}}{\omega}+\hat{\gamma}\cdot\omega\right) \tag{3-40}$$

where ω is the excitation frequency. Either one or both constants can be considered in numerical modeling. This study computes the stiffness proportionality factor by eliminating $\hat{\mu}$ by $\hat{\gamma}=2\cdot\zeta/\omega$. The equations of motion are represented in the form of two coupled matrix representations using the electromechanical Lagrange equations (3-27), (3-31), (3-34), and (3-38). In addition, the damping matrix has been implemented into the equations of motion:

$$[M]\cdot\ddot{q}_j+[D]\cdot\dot{q}_j+[K]\cdot q_j+[\theta]\cdot v_j=[Q] \tag{3-41}$$

$$-[\theta]' \cdot q_j + \left(\mathbf{A}^{(3\text{-}14)}\right) \cdot \dot{v}_j + \frac{1}{R_l} \cdot v_j = 0 \tag{3-42}$$

where $[\theta]$ and $[Q]$ are electrical voltage and force matrices, respectively, and all matrices are defined as follows:

$$[M] = \begin{bmatrix} \frac{1}{2} \cdot \left(M_{ij}^{uu} + M_{ji}^{uu}\right) & \frac{1}{2} \cdot \left(M_{ij}^{u\varphi} + M_{ji}^{\varphi u}\right) & 0 \\ \frac{1}{2} \cdot \left(M_{ij}^{\varphi u} + M_{ji}^{u\varphi}\right) & \frac{1}{2} \cdot \left(M_{ij}^{\varphi\varphi} + M_{ji}^{\varphi\varphi}\right) & 0 \\ 0 & 0 & \frac{1}{2} \cdot \left(M_{ij}^{ww} + M_{ji}^{ww}\right) \end{bmatrix} \tag{3-43}$$

$$[D] = \begin{bmatrix} \hat{\mu} \cdot \frac{1}{2} \cdot \left(M_{ij}^{uu} + M_{ji}^{uu}\right) + \hat{\gamma} \cdot \frac{1}{2} \cdot \left(K_{ij}^{uu} + K_{ji}^{uu}\right) & \hat{\mu} \cdot \frac{1}{2} \cdot \left(M_{ij}^{u\varphi} + M_{ji}^{\varphi u}\right) + \hat{\gamma} \cdot \frac{1}{2} \cdot \left(K_{ij}^{u\varphi} + K_{ji}^{\varphi u}\right) & 0 \\ \hat{\mu} \cdot \frac{1}{2} \cdot \left(M_{ij}^{\varphi u} + M_{ji}^{u\varphi}\right) + \hat{\gamma} \cdot \frac{1}{2} \cdot \left(K_{ij}^{\varphi u} + K_{ji}^{u\varphi}\right) & \hat{\mu} \cdot \frac{1}{2} \cdot \left(M_{ij}^{\varphi\varphi} + M_{ji}^{\varphi\varphi}\right) + \hat{\gamma} \cdot \frac{1}{2} \cdot \left(K_{ij}^{\varphi\varphi} + K_{ji}^{\varphi\varphi}\right) & \hat{\gamma} \cdot \frac{1}{2} \cdot \left(K_{ij}^{\varphi w} + K_{ji}^{w\varphi}\right) \\ 0 & \hat{\gamma} \cdot \frac{1}{2} \cdot \left(K_{ij}^{w\varphi} + K_{ji}^{\varphi w}\right) & \hat{\mu} \cdot \frac{1}{2} \cdot \left(M_{ij}^{ww} + M_{ji}^{ww}\right) + \hat{\gamma} \cdot \frac{1}{2} \cdot \left(K_{ij}^{ww} + K_{ji}^{ww}\right) \end{bmatrix} \tag{3-44}$$

$$[K] = \begin{bmatrix} \frac{1}{2} \cdot \left(K_{ij}^{uu} + K_{ji}^{uu}\right) & \frac{1}{2} \cdot \left(K_{ij}^{u\varphi} + K_{ji}^{\varphi u}\right) & 0 \\ \frac{1}{2} \cdot \left(K_{ij}^{\varphi u} + K_{ji}^{u\varphi}\right) & \frac{1}{2} \cdot \left(K_{ij}^{\varphi\varphi} + K_{ji}^{\varphi\varphi}\right) & \frac{1}{2} \cdot \left(K_{ij}^{\varphi w} + K_{ji}^{w\varphi}\right) \\ 0 & \frac{1}{2} \cdot \left(K_{ij}^{w\varphi} + K_{ji}^{\varphi w}\right) & \frac{1}{2} \cdot \left(K_{ij}^{ww} + K_{ji}^{ww}\right) \end{bmatrix} \tag{3-45}$$

$$[\theta] = \begin{bmatrix} \theta_i^u \\ -\theta_i^\varphi \\ 0 \end{bmatrix} \tag{3-46}$$

$$[Q] = \begin{bmatrix} 0 \\ 0 \\ -\frac{\partial \cdot p_i}{\partial \cdot t} \end{bmatrix} \tag{3-47}$$

Also, the following is the structure of the nodal displacement vector:

$$\left[q_j\right]' = [u_1 \quad u_2 \quad \dots \quad u_N \quad \varphi_1 \quad \varphi_2 \quad \dots \quad \varphi_N \quad w_1 \quad w_2 \quad \dots \quad w_N] \tag{3-48}$$

3.5 The Free Vibration Solution and Steady-State Response of The PEH's System

First, the base displacement constant p_i specified in equation (B 10) in Appendix B is subjected to the harmonic base displacement of the form $g(t) = W_0 \cdot e^{i\cdot\omega\cdot t}$ and $h(t) = \theta_0 \cdot e^{i\cdot\omega\cdot t}$. The complex-valued variables are W_0 and θ_0.

$$-\frac{\partial \cdot p_i}{\partial \cdot t} = P \cdot e^{i\cdot\omega\cdot t} \tag{3-49}$$

where exponential i is a complex number which is defined as $i = \sqrt{-1}$, e is the Euler's number, and P is defined as follows:

$$P = \Sigma_i \cdot \omega^2 \cdot W_0 + \Delta_i \cdot \omega^2 \cdot \theta_0 \tag{3-50}$$

Σ_i and Δ_i are introduced as follows:

$$\Sigma_i = \left(\mathbf{A}^{(B\ 10)}\right) \cdot \frac{L}{2} \cdot \sum_{k=1}^{\tilde{N}} H_k \cdot l_i(\xi_k) + \left(\mathbf{B}^{(B\ 10)}\right) \cdot l_i(\xi_N) \tag{3-51}$$

$$\begin{aligned}\Delta_i = \left(\mathbf{A}^{(B\ 10)}\right) \cdot \frac{L}{2} \cdot \sum_{k=1}^{\tilde{N}} H_k \cdot l_i(\xi_k) \cdot \frac{L\cdot(1+\xi_k)}{2} \\ + \left(\mathbf{B}^{(B\ 10)}\right) \cdot l_i(\xi_N) \cdot \frac{L\cdot(1+\xi_N)}{2}\end{aligned} \tag{3-52}$$

The second step is to apply harmonic base displacement to equations of motion (3-41) and (3-42). The voltage output and the steady-state generalized coordinates are $v(t) = V \cdot e^{i\cdot\omega\cdot t}$, $u_j(t) = U \cdot e^{i\cdot\omega\cdot t}$, $\varphi_j(t) = \Phi \cdot e^{i\cdot\omega\cdot t}$, and $w_j(t) = W \cdot e^{i\cdot\omega\cdot t}$. V, U, Φ, and W are the complex values. Equations (3-41) and (3-42) are described in their steady-state form as follows:

$$
\begin{aligned}
U \cdot \Bigg(& -\omega^2 \cdot \frac{1}{2} \cdot \left(M_{ij}^{uu} + M_{ji}^{uu} \right) + i \cdot \omega \\
& \cdot \left(\hat{\mu} \cdot \frac{1}{2} \cdot \left(M_{ij}^{uu} + M_{ji}^{uu} \right) + \hat{\gamma} \cdot \frac{1}{2} \cdot \left(K_{ij}^{uu} + K_{ji}^{uu} \right) \right) + \frac{1}{2} \\
& \cdot \left(K_{ij}^{uu} + K_{ji}^{uu} \right) \Bigg) + \Phi \\
& \cdot \Bigg(-\omega^2 \cdot \frac{1}{2} \cdot \left(M_{ij}^{u\varphi} + M_{ji}^{\varphi u} \right) + i \cdot \omega \\
& \cdot \left(\hat{\mu} \cdot \frac{1}{2} \cdot \left(M_{ij}^{u\varphi} + M_{ji}^{\varphi u} \right) + \hat{\gamma} \cdot \frac{1}{2} \cdot \left(K_{ij}^{u\varphi} + K_{ji}^{\varphi u} \right) \right) + \frac{1}{2} \\
& \cdot \left(K_{ij}^{u\varphi} + K_{ji}^{\varphi u} \right) \Bigg) + V \cdot \left(\theta_i^u \right) = 0
\end{aligned}
\tag{3-53}
$$

$$
\begin{aligned}
U \cdot \Bigg(& -\omega^2 \cdot \frac{1}{2} \cdot \left(M_{ij}^{\varphi u} + M_{ji}^{u\varphi} \right) + i \cdot \omega \\
& \cdot \left(\hat{\mu} \cdot \frac{1}{2} \cdot \left(M_{ij}^{\varphi u} + M_{ji}^{u\varphi} \right) + \hat{\gamma} \cdot \frac{1}{2} \cdot \left(K_{ij}^{\varphi u} + K_{ji}^{u\varphi} \right) \right) + \frac{1}{2} \\
& \cdot \left(K_{ij}^{\varphi u} + K_{ji}^{u\varphi} \right) \Bigg) + \Phi \\
& \cdot \Bigg(-\omega^2 \cdot \frac{1}{2} \cdot \left(M_{ij}^{\varphi\varphi} + M_{ji}^{\varphi\varphi} \right) + i \\
& \cdot \omega \left(\hat{\mu} \cdot \frac{1}{2} \cdot \left(M_{ij}^{\varphi\varphi} + M_{ji}^{\varphi\varphi} \right) + \hat{\gamma} \cdot \frac{1}{2} \cdot \left(K_{ij}^{\varphi\varphi} + K_{ji}^{\varphi\varphi} \right) \right) + \frac{1}{2} \\
& \cdot \left(K_{ij}^{\varphi\varphi} + K_{ji}^{\varphi\varphi} \right) \Bigg) + W \\
& \cdot \left(i \cdot \omega \cdot \hat{\gamma} \cdot \frac{1}{2} \cdot \left(K_{ij}^{\varphi w} + K_{ji}^{w\varphi} \right) + \frac{1}{2} \cdot \left(K_{ij}^{\varphi w} + K_{ji}^{w\varphi} \right) \right) \\
& - V \cdot \left(\theta_i^{\varphi} \right) = 0
\end{aligned}
\tag{3-54}
$$

$$\Phi \cdot \left(i \cdot \omega \cdot \hat{\gamma} \cdot \frac{1}{2} \cdot \left(K_{ij}^{w\varphi} + K_{ji}^{\varphi w} \right) + \frac{1}{2} \cdot \left(K_{ij}^{w\varphi} + K_{ji}^{\varphi w} \right) \right) + W \cdot \left(-\omega^2 \cdot \frac{1}{2} \cdot \left(M_{ij}^{ww} + M_{ji}^{ww} \right) + i \cdot \omega \cdot \left(\hat{\mu} \cdot \frac{1}{2} \cdot \left(M_{ij}^{ww} + M_{ji}^{ww} \right) + \hat{\gamma} \cdot \frac{1}{2} \cdot \left(K_{ij}^{ww} + K_{ji}^{ww} \right) \right) + \frac{1}{2} \cdot \left(K_{ij}^{ww} + K_{ji}^{ww} \right) \right) = P \tag{3-55}$$

$$U \cdot \left(-i \cdot \omega \cdot \theta_i^u \right) + \Phi \cdot \left(i \cdot \omega \cdot \theta_i^{\varphi} \right) + V \cdot \left(i \cdot \omega \cdot \left(\mathbf{A}^{(3\text{-}14)} \right) + \frac{1}{R_l} \right) = 0 \tag{3-56}$$

The following V expression is derived from equation (3-56) and substituted in equations (3-53), (3-54), and (3-55).

$$V = i \cdot \omega \cdot \left(i \cdot \omega \cdot \left(\mathbf{A}^{(3\text{-}14)} \right) + \frac{1}{R_l} \right)^{-1} \cdot \left(U \cdot \theta_i^u - \Phi \cdot \theta_i^{\varphi} \right) \tag{3-57}$$

The resultant equations are defined in equations (3-58), (3-59), and (3-60).

$$U \cdot G_{uu} + \Phi \cdot G_{u\varphi} = 0 \tag{3-58}$$

$$U \cdot G_{\varphi u} + \Phi \cdot G_{\varphi\varphi} + W \cdot G_{\varphi w} = 0 \tag{3-59}$$

$$\Phi \cdot G_{w\varphi} + W \cdot G_{ww} = P \tag{3-60}$$

where,

$$
\begin{aligned}
G_{uu} = -\omega^2 \cdot \frac{1}{2} \cdot \left(M_{ij}^{uu} + M_{ji}^{uu}\right) + i \cdot \omega \\
\cdot \left(\hat{\mu} \cdot \frac{1}{2} \cdot \left(M_{ij}^{uu} + M_{ji}^{uu}\right) + \hat{\gamma} \cdot \frac{1}{2} \cdot \left(K_{ij}^{uu} + K_{ji}^{uu}\right)\right) + \frac{1}{2} \\
\cdot \left(K_{ij}^{uu} + K_{ji}^{uu}\right) + i \cdot \omega \cdot \left(i \cdot \omega \cdot \left(\mathbf{A}^{(3\text{-}14)}\right) + \frac{1}{R_l}\right)^{-1} \cdot \theta_i^u \\
\cdot \theta_j^u
\end{aligned}
\tag{3-61}
$$

$$
\begin{aligned}
G_{u\varphi} = -\omega^2 \cdot \frac{1}{2} \cdot \left(M_{ij}^{u\varphi} + M_{ji}^{\varphi u}\right) + i \cdot \omega \\
\cdot \left(\hat{\mu} \cdot \frac{1}{2} \cdot \left(M_{ij}^{u\varphi} + M_{ji}^{\varphi u}\right) + \hat{\gamma} \cdot \frac{1}{2} \cdot \left(K_{ij}^{u\varphi} + K_{ji}^{\varphi u}\right)\right) + \frac{1}{2} \\
\cdot \left(K_{ij}^{u\varphi} + K_{ji}^{\varphi u}\right) - i \cdot \omega \cdot \left(i \cdot \omega \cdot \left(\mathbf{A}^{(3\text{-}14)}\right) + \frac{1}{R_l}\right)^{-1} \cdot \theta_i^{\varphi} \\
\cdot \theta_j^u
\end{aligned}
\tag{3-62}
$$

$$
\begin{aligned}
G_{\varphi u} = -\omega^2 \cdot \frac{1}{2} \cdot \left(M_{ij}^{\varphi u} + M_{ji}^{u\varphi}\right) + i \cdot \omega \\
\cdot \left(\hat{\mu} \cdot \frac{1}{2} \cdot \left(M_{ij}^{\varphi u} + M_{ji}^{u\varphi}\right) + \hat{\gamma} \cdot \frac{1}{2} \cdot \left(K_{ij}^{\varphi u} + K_{ji}^{u\varphi}\right)\right) + \frac{1}{2} \\
\cdot \left(K_{ij}^{\varphi u} + K_{ji}^{u\varphi}\right) - i \cdot \omega \cdot \left(i \cdot \omega \cdot \left(\mathbf{A}^{(3\text{-}14)}\right) + \frac{1}{R_l}\right)^{-1} \cdot \theta_i^u \\
\cdot \theta_j^{\varphi}
\end{aligned}
\tag{3-63}
$$

$$G_{\varphi\varphi} = -\omega^2 \cdot \frac{1}{2} \cdot \left(M_{ij}^{\varphi\varphi} + M_{ji}^{\varphi\varphi}\right) + i \cdot \omega \left(\hat{\mu} \cdot \frac{1}{2} \cdot \left(M_{ij}^{\varphi\varphi} + M_{ji}^{\varphi\varphi}\right) + \hat{\gamma} \cdot \frac{1}{2} \cdot \left(K_{ij}^{\varphi\varphi} + K_{ji}^{\varphi\varphi}\right)\right) + \frac{1}{2} \cdot \left(K_{ij}^{\varphi\varphi} + K_{ji}^{\varphi\varphi}\right) + i \cdot \omega \cdot \left(i \cdot \omega \cdot \left(\mathbf{A}^{(3\text{-}14)}\right) + \frac{1}{R_l}\right)^{-1} \cdot \theta_i^{\varphi} \cdot \theta_j^{\varphi} \tag{3-64}$$

$$G_{\varphi w} = i \cdot \omega \cdot \hat{\gamma} \cdot \frac{1}{2} \cdot \left(K_{ij}^{\varphi w} + K_{ji}^{w\varphi}\right) + \frac{1}{2} \cdot \left(K_{ij}^{\varphi w} + K_{ji}^{w\varphi}\right) \tag{3-65}$$

$$G_{w\varphi} = i \cdot \omega \cdot \hat{\gamma} \cdot \frac{1}{2} \cdot \left(K_{ij}^{w\varphi} + K_{ji}^{\varphi w}\right) + \frac{1}{2} \cdot \left(K_{ij}^{w\varphi} + K_{ji}^{\varphi w}\right) \tag{3-66}$$

$$G_{ww} = -\omega^2 \cdot \frac{1}{2} \cdot \left(M_{ij}^{ww} + M_{ji}^{ww}\right) + i \cdot \omega \cdot \left(\hat{\mu} \cdot \frac{1}{2} \cdot \left(M_{ij}^{ww} + M_{ji}^{ww}\right) + \hat{\gamma} \cdot \frac{1}{2} \cdot \left(K_{ij}^{ww} + K_{ji}^{ww}\right)\right) + \frac{1}{2} \cdot \left(K_{ij}^{ww} + K_{ji}^{ww}\right) \tag{3-67}$$

The steady-state response matrix G is constructed as:

$$[G] = \begin{bmatrix} [G^{uu}] & [G^{u\varphi}] & 0 \\ [G^{\varphi u}] & [G^{\varphi\varphi}] & [G^{\varphi w}] \\ 0 & [G^{w\varphi}] & [G^{ww}] \end{bmatrix} \tag{3-68}$$

It is possible to determine the short and open-circuit natural frequencies of the system by setting the mechanical damping terms equal to zero ($[D] = 0$) and adjusting the $R_l = 0$ (for the short-circuit natural frequency) or $R_l = \infty$ (for the open-circuit natural frequency). The characteristic equation for the free vibration ($P = 0$) problem is obtained using the following equation:

$$\det(G) = \begin{vmatrix} [G^{uu}] & [G^{u\varphi}] & 0 \\ [G^{\varphi u}] & [G^{\varphi\varphi}] & [G^{\varphi w}] \\ 0 & [G^{w\varphi}] & [G^{ww}] \end{vmatrix} = 0 \quad (3\text{-}69)$$

The formulation is then created to determine the PEH system's steady-state response. From equation (3-58),

$$U = -{G_{uu}}^{-1} \cdot G_{u\varphi} \cdot \Phi \quad (3\text{-}70)$$

Substituting equation (3-70) into equation (3-59) gives:

$$W = {G_{\varphi w}}^{-1} \cdot \left(G_{\varphi u} \cdot {G_{uu}}^{-1} \cdot G_{u\varphi} - G_{\varphi\varphi}\right) \cdot \Phi \quad (3\text{-}71)$$

The Φ vector of complex generalized coordinates is obtained as follows by applying equation (3-71) to equation (3-60):

$$\Phi = \left(G_{w\varphi} + G_{ww} \cdot {G_{\varphi w}}^{-1} \cdot \left(G_{\varphi u} \cdot {G_{uu}}^{-1} \cdot G_{u\varphi} - G_{\varphi\varphi}\right)\right)^{-1} \cdot P \quad (3\text{-}72)$$

Afterward, equation (3-72) is included in equations (3-70) and (3-71) to get the complex generalized coordinates of the U and W vectors. The resultant generalized coordinates are thus derived:

$$\begin{aligned} U = -{G_{uu}}^{-1} \cdot G_{u\varphi} \\ \cdot \left(G_{w\varphi} + G_{ww} \cdot {G_{\varphi w}}^{-1}\right. \\ \left. \cdot \left(G_{\varphi u} \cdot {G_{uu}}^{-1} \cdot G_{u\varphi} - G_{\varphi\varphi}\right)\right)^{-1} \cdot P \end{aligned} \quad (3\text{-}73)$$

$$\begin{aligned} W = {G_{\varphi w}}^{-1} \cdot \left(G_{\varphi u} \cdot {G_{uu}}^{-1} \cdot G_{u\varphi} - G_{\varphi\varphi}\right) \\ \cdot \left(G_{w\varphi} + G_{ww} \cdot {G_{\varphi w}}^{-1}\right. \\ \left. \cdot \left(G_{\varphi u} \cdot {G_{uu}}^{-1} \cdot G_{u\varphi} - G_{\varphi\varphi}\right)\right)^{-1} \cdot P \end{aligned} \quad (3\text{-}74)$$

Finally, equations (3-72) and (3-73) are substituted in equation (3-57) to obtain the complex voltage term V:

$$V = i \cdot \omega \cdot \left(i \cdot \omega \cdot \left(\mathbf{A}^{(3\text{-}14)}\right) + \frac{1}{R_l}\right)^{-1} \cdot \left(-\theta_i^u \cdot \left(G_{uu}{}^{-1} \cdot G_{u\varphi}\right) - \theta_i^{\varphi}\right) \cdot \left(G_{w\varphi} + G_{ww} \cdot G_{\varphi w}{}^{-1} \cdot \left(G_{\varphi u} \cdot G_{uu}{}^{-1} \cdot G_{u\varphi} - G_{\varphi\varphi}\right)\right)^{-1} \cdot P \quad (3\text{-}75)$$

The axial displacement, cross-section rotation, transverse displacement, and voltage responses at steady-state are obtained by substituting the elements of U, Φ, W, and V into equations (3-9), (3-10), (3-11), and $v(t) = V \cdot e^{i\cdot\omega\cdot t}$, respectively:

$$u(x,t) = \sum_{j=1}^{N} l_j(\xi) \cdot U_j \cdot e^{i\cdot\omega\cdot t} \quad (3\text{-}76)$$

$$\varphi(x,t) = \sum_{j=1}^{N} l_j(\xi) \cdot \Phi_j \cdot e^{i\cdot\omega\cdot t} \quad (3\text{-}77)$$

$$w(x,t) = \sum_{j=1}^{N} l_j(\xi) \cdot W_j \cdot e^{i\cdot\omega\cdot t} \quad (3\text{-}78)$$

$$v(t) = i \cdot \omega \cdot \left(i \cdot \omega \cdot \left(\mathbf{A}^{(3\text{-}14)}\right) + \frac{1}{R_l}\right)^{-1} \cdot \left(-\theta_i^u \cdot \left(G_{uu}{}^{-1} \cdot G_{u\varphi}\right) - \theta_i^{\varphi}\right) \cdot \left(G_{w\varphi} + G_{ww} \cdot G_{\varphi w}{}^{-1} \cdot \left(G_{\varphi u} \cdot G_{uu}{}^{-1} \cdot G_{u\varphi} - G_{\varphi\varphi}\right)\right)^{-1} \cdot P \cdot e^{i\cdot\omega\cdot t} \quad (3\text{-}79)$$

3.6 The Forced Vibration Solution of the PEH's System

The response is transitory if a structure is activated by a non-periodic excitation applied abruptly because steady-state oscillations are not created. The condition where the forces are applied for a brief period is referred to as a "transient" situation.

The structure will next move through free vibration, which will decrease because of the dampening already in place. The forced vibration response of the element is created by the force change, which is typically continuous and results in the force matrix changing every time interval. The Houbolt and Newmark techniques solve the time-dependent ordinary differential equations of motion.

3.6.1 The Houbolt Method

The Houbolt method includes backward difference formulae to express the velocity, acceleration, and first and second-order derivate of voltage outputs at time t_{j+1} in terms of the displacement and voltage at times t_{j-2} to t_{j+1}. These are derived by fitting a cubic polynomial function inside the interval (t_{j-2}, t_{j+1}) to the response curve shown in Figure 3.3.

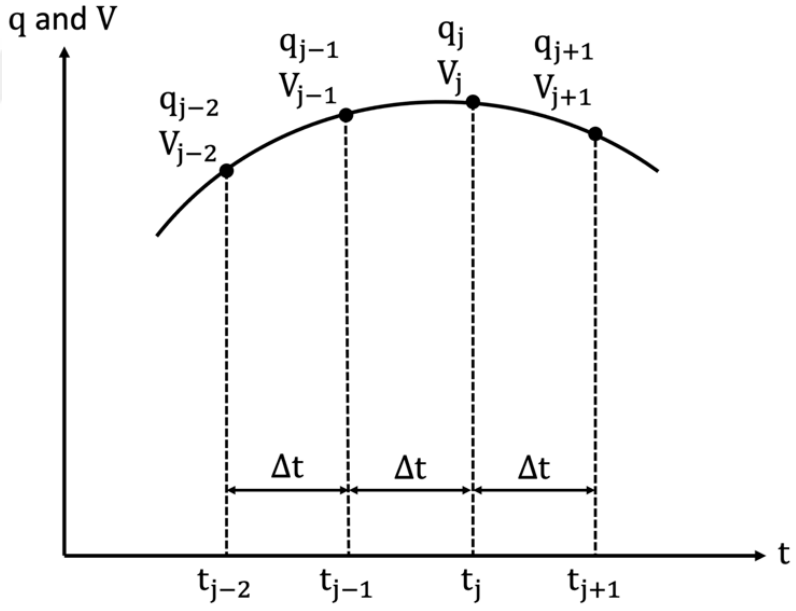

Figure 3.3 Backward difference approximation for displacement and voltage terms.

The Houbolt method yields results from the third time interval t_3 since $j = 2$ is the starting point. In other words, the displacement q_3 and voltage V_3 can be determined if the displacements q_0, q_1, and q_2, and the voltage terms V_0, V_1, and V_2 are known.

q_0, $\dot{q}_0$, V_0, $\dot{V}_0$, and $\ddot{V}_0$ are equal to zero while $\ddot{q}_0$ is calculated by using $\ddot{q}_0 = Q_0/[M]$ so no special starting procedure is required. In the Houbolt method, the displacement and voltage term, together with its first and second derivatives, are defined as follows:

$$
\begin{aligned}
q_{j+1} = &\left[\frac{2\cdot[M]}{(\Delta t)^2} + \frac{11\cdot[D]}{6\cdot\Delta t} + [K] + [\theta]\cdot\left(\left(\mathbf{A}^{(3\text{-}14)}\right)\cdot\frac{11}{6\cdot\Delta t} + \frac{1}{R_l}\right)^{-1}\right. \\
&\left.\cdot[\theta]'\cdot\frac{11}{6\cdot\Delta t}\right]^{-1} \\
&\cdot\left[Q_{j+1}\right. \\
&+\left[\frac{5\cdot[M]}{(\Delta t)^2} + \frac{3\cdot[D]}{\Delta t} + [\theta]\cdot\left(\left(\mathbf{A}^{(3\text{-}14)}\right)\cdot\frac{11}{6\cdot\Delta t} + \frac{1}{R_l}\right)^{-1}\right. \\
&\left.\cdot[\theta]'\cdot\frac{3}{\Delta t}\right]\cdot q_j \\
&-\left[\frac{4\cdot[M]}{(\Delta t)^2} + \frac{3\cdot[D]}{2\cdot(\Delta t)} - [\theta]\cdot\left(\left(\mathbf{A}^{(3\text{-}14)}\right)\cdot\frac{11}{6\cdot\Delta t} + \frac{1}{R_l}\right)^{-1}\right. \\
&\left.\cdot[\theta]'\cdot\frac{3}{2\cdot\Delta t}\right]\cdot q_{j-1} \\
&+\left[\frac{[M]}{(\Delta t)^2} + \frac{[D]}{3\cdot(\Delta t)} + [\theta]\cdot\left(\left(\mathbf{A}^{(3\text{-}14)}\right)\cdot\frac{11}{6\cdot\Delta t} + \frac{1}{R_l}\right)^{-1}\right. \\
&\left.\cdot[\theta]'\cdot\frac{1}{3\cdot\Delta t}\right]\cdot q_{j-2} + [\theta]\cdot\left(\left(\mathbf{A}^{(3\text{-}14)}\right)\cdot\frac{11}{6\cdot\Delta t} + \frac{1}{R_l}\right)^{-1} \\
&\cdot\left(\mathbf{A}^{(3\text{-}14)}\right)\cdot\frac{1}{6\cdot\Delta t}\cdot\left(-2\cdot V_{j-2} + 9\cdot V_{j-1} - 18\cdot V_j\right)\Bigg]
\end{aligned}
\tag{3-80}
$$

$$
\dot{q}_{j+1} = \frac{1}{6\cdot\Delta t}\cdot\left(-2\cdot q_{j-2} + 9\cdot q_{j-1} - 18\cdot q_j + 11\cdot q_{j+1}\right) \tag{3-81}
$$

$$\ddot{q}_{j+1} = \frac{1}{(\Delta t)^2} \cdot \left(-q_{j-2} + 4 \cdot q_{j-1} - 5 \cdot q_j + 2 \cdot q_{j+1}\right) \tag{3-82}$$

$$\begin{aligned} V_{j+1} = \left(\left(\mathbf{A}^{(3\text{-}14)}\right) \cdot \frac{1}{6 \cdot \Delta t} \cdot 11 + \frac{1}{R_l}\right)^{-1} \\ \cdot \left[[\theta]' \cdot \frac{1}{6 \cdot \Delta t}\right. \\ \cdot \left(-2 \cdot q_{j-2} + 9 \cdot q_{j-1} - 18 \cdot q_j + 11 \cdot q_{j+1}\right) \\ \left. + \left(\mathbf{A}^{(3\text{-}14)}\right) \cdot \frac{1}{6 \cdot \Delta t} \cdot \left(2 \cdot V_{j-2} - 9 \cdot V_{j-1} + 18 \cdot V_j\right)\right] \end{aligned} \tag{3-83}$$

$$\dot{V}_{j+1} = \frac{1}{6 \cdot \Delta t} \cdot \left(-2 \cdot V_{j-2} + 9 \cdot V_{j-1} - 18 \cdot V_j + 11 \cdot V_{j+1}\right) \tag{3-84}$$

$$\ddot{V}_{j+1} = \frac{1}{(\Delta t)^2} \cdot \left(-V_{j-2} + 4 \cdot V_{j-1} - 5 \cdot V_j + 2 \cdot V_{j+1}\right) \tag{3-85}$$

where Δt is the time step. The inaccuracy in the approximations $\dot{q}_{j+1}$, $\dot{V}_{j+1}$, $\ddot{q}_{j+1}$ and $\ddot{V}_{j+1}$ is considered to be of the order $(\Delta t)^3$.

3.6.2 The Newmark Method

The Newmark technique has been used to discover the t_1 and t_2 solutions using the initial conditions at t_0. The linear acceleration approach is generalized by the Newmark method. This latter approach assumes that the acceleration and second-order voltage terms vary linearly between (t_j, t_{j+1}), as seen in Figure 3.4. In other words, the second-order derivative of generalized coordinates and voltage are assumed to be constant and equal to the average value $(\ddot{q}_j + \ddot{q}_{j+1})/2$ and $(\ddot{v}_j + \ddot{v}_{j+1})/2$ during the interval (t_j, t_{j+1}). The time history of the response is obtained by taking $j = 0$ and 1. After $j = 2$, the Houbolt method is valid.

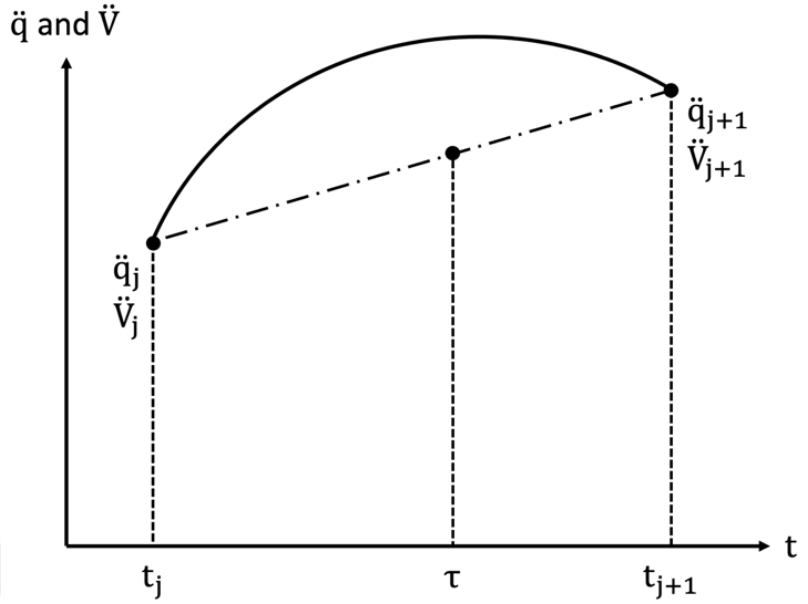

Figure 3.4 Linear acceleration approximation for displacement and voltage terms.

The displacement and voltage terms are stated similarly for the Newmark technique:

$$
\begin{aligned}
q_{j+1} = & \left[\frac{[M]}{\bar{\bar{\beta}} \cdot (\Delta t)^2} + \frac{\bar{\bar{\gamma}} \cdot [D]}{\bar{\bar{\beta}} \cdot \Delta t} + [K] + [\theta] \cdot \left(\left(\mathbf{A}^{(3\text{-}14)} \right) \cdot \frac{\bar{\bar{\gamma}}}{\bar{\bar{\beta}} \cdot \Delta t} + \frac{1}{R_l} \right)^{-1} \right. \\
& \left. \cdot [\theta]' \cdot \frac{\bar{\bar{\gamma}}}{\bar{\bar{\beta}} \cdot \Delta t} \right]^{-1} \\
& \cdot \left[Q_{j+1} - [\theta] \cdot \left(\left(\mathbf{A}^{(3\text{-}14)} \right) \cdot \frac{\bar{\bar{\gamma}}}{\bar{\bar{\beta}} \cdot \Delta t} + \frac{1}{R_l} \right)^{-1} \right. \\
& \cdot \left(-[\theta]' \cdot \frac{\bar{\bar{\gamma}}}{\bar{\bar{\beta}} \cdot \Delta t} \cdot q_j + [\theta]' \cdot \left(1 - \frac{\bar{\bar{\gamma}}}{\bar{\bar{\beta}}} \right) \cdot \dot{q}_j + [\theta]' \cdot \Delta t \right. \\
& \cdot \left(1 - \frac{\bar{\bar{\gamma}}}{2 \cdot \bar{\bar{\beta}}} \right) \cdot \ddot{q}_j + \left(\mathbf{A}^{(3\text{-}14)} \right) \cdot \frac{\bar{\bar{\gamma}}}{\bar{\bar{\beta}} \cdot \Delta t} \cdot V_j - \left(\mathbf{A}^{(3\text{-}14)} \right) \\
& \cdot \left(1 - \frac{\bar{\bar{\gamma}}}{\bar{\bar{\beta}}} \right) \cdot \dot{V}_j - \left(\mathbf{A}^{(3\text{-}14)} \right) \cdot \Delta t \cdot \left(1 - \frac{\bar{\bar{\gamma}}}{2 \cdot \bar{\bar{\beta}}} \right) \cdot \ddot{V}_j \Big) \\
& + \left[\frac{[M]}{\bar{\bar{\beta}} \cdot (\Delta t)^2} + \frac{\bar{\bar{\gamma}} \cdot [D]}{\bar{\bar{\beta}} \cdot \Delta t} \right] \cdot q_j + \left[\frac{[M]}{\bar{\bar{\beta}} \cdot \Delta t} - [D] \cdot \left(1 - \frac{\bar{\bar{\gamma}}}{\bar{\bar{\beta}}} \right) \right] \\
& \cdot \dot{q}_j + \left[[M] \cdot \left(\frac{1}{2 \cdot \bar{\bar{\beta}}} - 1 \right) - [D] \cdot \Delta t \cdot \left(1 - \frac{\bar{\bar{\gamma}}}{2 \cdot \bar{\bar{\beta}}} \right) \right] \cdot \ddot{q}_j \Big]
\end{aligned}
\tag{3-86}
$$

$$
\dot{q}_{j+1} = \frac{\bar{\bar{\gamma}}}{\bar{\bar{\beta}} \cdot \Delta t} \cdot \left(q_{j+1} - q_j \right) + \left(1 - \frac{\bar{\bar{\gamma}}}{\bar{\bar{\beta}}} \right) \cdot \dot{q}_j + \Delta t \cdot \left(1 - \frac{\bar{\bar{\gamma}}}{2 \cdot \bar{\bar{\beta}}} \right) \cdot \ddot{q}_j \tag{3-87}
$$

$$
\ddot{q}_{j+1} = \frac{1}{\bar{\bar{\beta}} \cdot (\Delta t)^2} \cdot \left(q_{j+1} - q_j \right) - \frac{1}{\bar{\bar{\beta}} \cdot \Delta t} \cdot \dot{q}_j - \left(\frac{1}{2 \cdot \bar{\bar{\beta}}} - 1 \right) \cdot \ddot{q}_j \tag{3-88}
$$

$$V_{j+1} = \left(\left(\mathbf{A}^{(3\text{-}14)} \right) \cdot \frac{\bar{\bar{\gamma}}}{\bar{\bar{\beta}} \cdot \Delta t} + \frac{1}{R_l} \right)^{-1} \cdot \left[[\theta]' \cdot \frac{\bar{\bar{\gamma}}}{\bar{\bar{\beta}} \cdot \Delta t} \cdot q_{j+1} - [\theta]' \cdot \frac{\bar{\bar{\gamma}}}{\bar{\bar{\beta}} \cdot \Delta t} \cdot q_j + [\theta]' \cdot \left(1 - \frac{\bar{\bar{\gamma}}}{\bar{\bar{\beta}}} \right) \cdot \dot{q}_j + [\theta]' \cdot \Delta t \cdot \left(1 - \frac{\bar{\bar{\gamma}}}{2 \cdot \bar{\bar{\beta}}} \right) \cdot \ddot{q}_j + \left(\mathbf{A}^{(3\text{-}14)} \right) \cdot \frac{\bar{\bar{\gamma}}}{\bar{\bar{\beta}} \cdot \Delta t} \cdot V_j - \left(\mathbf{A}^{(3\text{-}14)} \right) \cdot \left(1 - \frac{\bar{\bar{\gamma}}}{\bar{\bar{\beta}}} \right) \cdot \dot{V}_j - \left(\mathbf{A}^{(3\text{-}14)} \right) \cdot \Delta t \cdot \left(1 - \frac{\bar{\bar{\gamma}}}{2 \cdot \bar{\bar{\beta}}} \right) \cdot \ddot{V}_j \right] \tag{3-89}$$

$$\dot{V}_{j+1} = \frac{\bar{\bar{\gamma}}}{\bar{\bar{\beta}} \cdot \Delta t} \cdot \left(V_{j+1} - V_j \right) + \left(1 - \frac{\bar{\bar{\gamma}}}{\bar{\bar{\beta}}} \right) \cdot \dot{V}_j + \Delta t \cdot \left(1 - \frac{\bar{\bar{\gamma}}}{2 \cdot \bar{\bar{\beta}}} \right) \cdot \ddot{V}_j \tag{3-90}$$

$$\ddot{V}_{j+1} = \frac{1}{\bar{\bar{\beta}} \cdot (\Delta t)^2} \cdot \left(V_{j+1} - V_j \right) - \frac{1}{\bar{\bar{\beta}} \cdot \Delta t} \cdot \dot{V}_j - \left(\frac{1}{2 \cdot \bar{\bar{\beta}}} - 1 \right) \cdot \ddot{V}_j \tag{3-91}$$

where $\bar{\bar{\gamma}} = 1/2$ and $\bar{\bar{\beta}} = 1/4$, and it implies that the linear acceleration technique is valid. It is a variant of the Newmark method.

3.6.3 The Work Equivalent Method and Loads

In the forced vibration solution, the work equivalent approach is used to build the force matrix $[Q]$ in the equations of motion. The displacement of an N-node quadrature beam element under load $f(x,t)$ yields:

$$\nu(x,t) = \sum_{i=1}^{N} l_i(x) \cdot \nu(x_i,t) = \sum_{i=1}^{N} l_i(x) \cdot \nu_i = \sum_{i=1}^{N} l_i(\xi) \cdot \nu_i \tag{3-92}$$

where $\nu(x,t)$ is the node displacement at the beam. The following equation is obtained when the work equivalent method is applied.

$$W = \frac{1}{2} \cdot F_i \cdot \nu_i = \frac{1}{2} \cdot \int_0^L q(x,t) \cdot \nu(x,t) \cdot dx \tag{3-93}$$

where F_i is the work equivalent load vector, and ν_i is the nodal displacement vector. A work equivalent load vector is formed by adding equation (3-92) to the right side of equation (3-93):

$$F_i = \int_0^L q(x,t) \cdot l_i(x) \cdot dx \tag{3-94}$$

In other words, F_i is the nodal force component corresponding to the nodal displacement component ν_i. In parametric analysis, four types of loading are considered. In the numerical technique, inserting the force equations into the work equivalent load vector expresses the external force section of the equations of motion. The work equivalent load vectors for the loads mentioned earlier types are defined as follows:

$$F_i = \frac{1}{2} \cdot f_0 \cdot L \cdot H(t) \cdot H_i, \qquad \text{for uniformly distributed step load} \tag{3-95}$$

$$F_i = F \cdot H(t) \cdot l_i(\xi_0), \qquad \text{for concentrated step load} \tag{3-96}$$

$$F_i = F \cdot \sin(\omega_p \cdot t) \cdot l_i(\xi_0), \qquad \text{for concentrated harmonic load} \tag{3-97}$$

$$F_i = \bar{F} \cdot \delta(t) \cdot l_i(\xi_0), \qquad \text{for concentrated impulsive load} \tag{3-98}$$

where ξ_0 is the load-applying point on the natural coordinate system. Dirac delta function $\delta(t)$ in work equivalent load vector for the concentrated impulsive load can be represented as shown in equation (3-99). Impulsive load functions can be applied in a rectangular or triangular shape. In this study, the rectangular one is adopted, and the corresponding force function is shown in Figure 3.5.

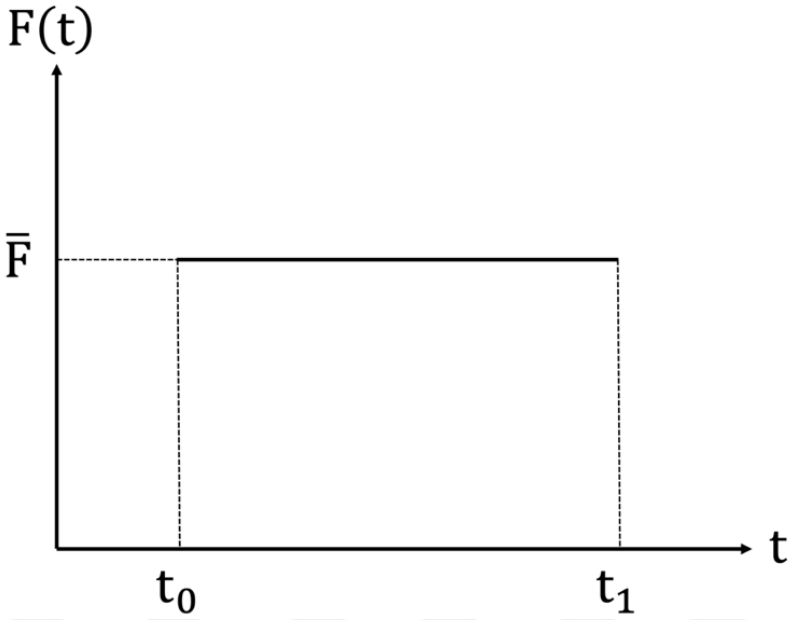

Figure 3.5 Rectangular impulsive load representation (t_0 and t_1 are very small).

$$\delta(t) = \frac{1}{t_1 - t_0} \cdot \big(H(t - t_0) - H(t - t_1)\big) \tag{3-99}$$

The resulting work equivalent load vector for the concentrated impulsive load can be represented as follows:

$$F_i = \bar{F} \cdot \frac{1}{t_1 - t_0} \cdot \big(H(t - t_0) - H(t - t_1)\big) \cdot l_i(\xi_0) \tag{3-100}$$

CHAPTER 4

NUMERICAL RESULTS AND DISCUSSION

The correctness of the WQEM is first demonstrated through validation studies. The performance of an FG PEH under free and forced vibration is then examined in convergence and parametric analysis solutions. Studies on forced vibration verification and natural frequency values do not consider the dampening effect. The damping is taken into consideration in all of the remaining findings. Table 4-1 displays the geometric characteristics of the PEH beam employed in the numerical results section.

Table 4-1 The geometric properties of the Timoshenko PEH beam for numerical tests of WQEM.

Property	Value	Units
b	6.400	millimeter
L	24.530	millimeter
h^s	0.140	millimeter
h^p	0.265	millimeter
L^t	3.175	millimeter
h^t	3.175	millimeter
M_t	0.239	gram

The material characteristics of PZT-5H, PZT-5A, brass, and aluminum are listed in Table 4-2, Table 4-3, Table 4-4, and Table 4-5, respectively.

Table 4-2 The material properties of the PZT-5H.

Property	Value	Units
ρ^{p}	7500	kilogram/meter^3
s_{11}^{E}	$16.5 \cdot 10^{-12}$	meter^2/Newton
s_{55}^{E}	$43.5 \cdot 10^{-12}$	meter^2/Newton
d_{31}	$-274 \cdot 10^{-12}$	meter/Volt
ϵ_{33}^{σ}	$3.010428 \cdot 10^{-8}$	Farad/meter

Table 4-3 The material properties of the PZT-5A.

Property	Value	Units
ρ^{p}	7750	kilogram/meter^3
s_{11}^{E}	$16.4 \cdot 10^{-12}$	meter^2/Newton
s_{55}^{E}	$47.5 \cdot 10^{-12}$	meter^2/Newton
d_{31}	$-171 \cdot 10^{-12}$	meter/Volt
ϵ_{33}^{σ}	$1.505214 \cdot 10^{-8}$	Farad/meter

Table 4-4 The material properties of the brass.

Property	Value	Units
E^{s}	105	gigapascal
μ^{s}	40	gigapascal
ρ^{s}	9000	kilogram/meter^3

Table 4-5 The material properties of aluminum.

Property	Value	Units
E^s	70	gigapascal
μ^s	26.9	gigapascal
ρ^s	2702	kilogram/meter^3

The configuration used in free and forced vibration validation studies is shown in Figure 4.1.

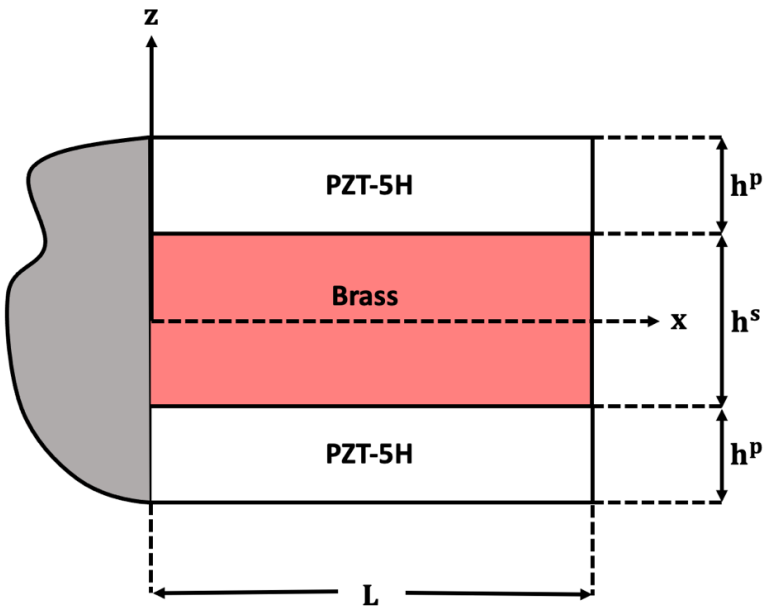

Figure 4.1 Configuration of the PEH used for validation analysis.

The materials used to produce the PEH beam for free and forced vibration convergence and parametric analysis are supposed to be PZT-5H, PZT-5A, aluminum, and brass. Their configuration is shown in Figure 4.2.

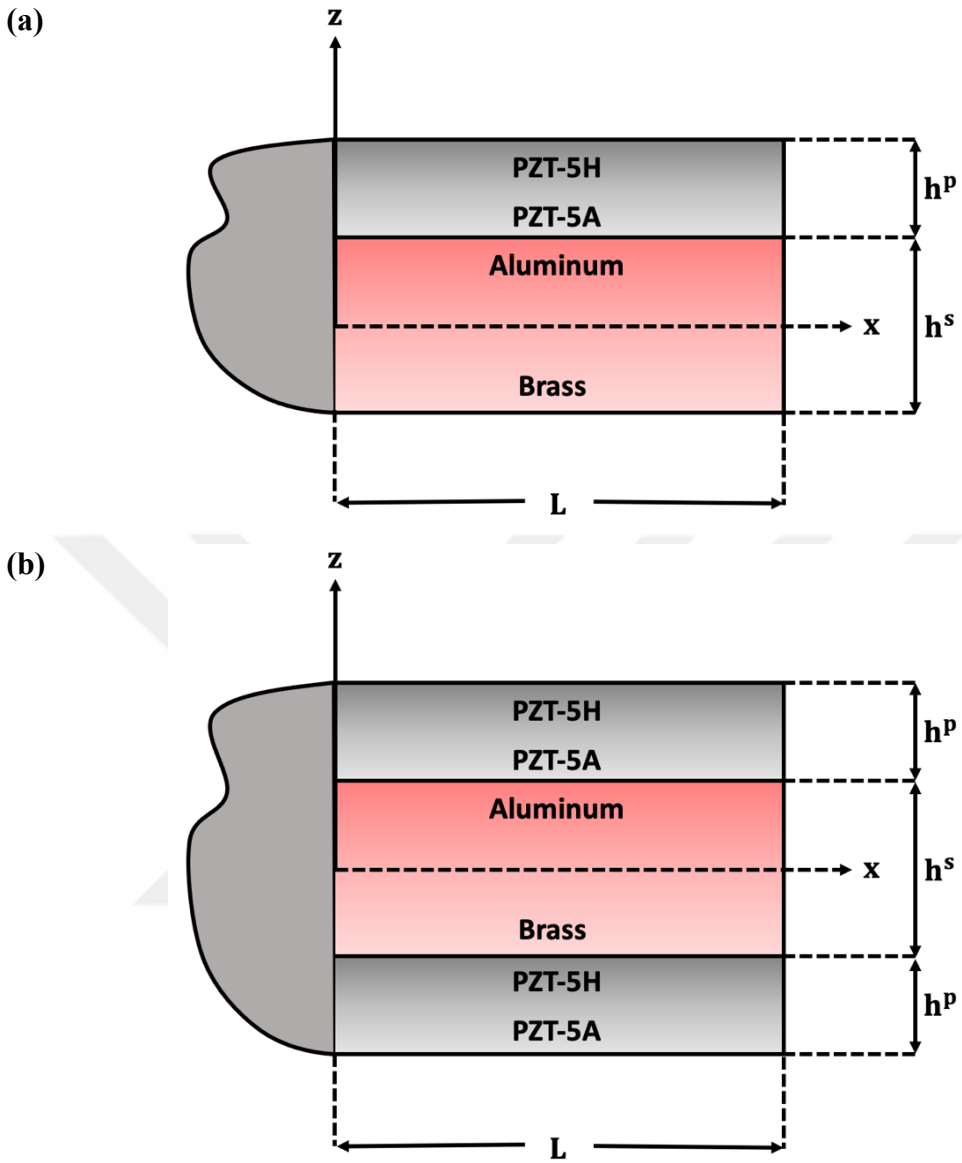

Figure 4.2 Configuration of the PEH used for convergence and parametric analysis in (a) unimorph structures and (b) bimorph structures.

While the top portion ($z = h^s/2 + h^p$) of piezoelectric material is all PZT-5H, the below part ($z = h^s/2$) is entirely PZT-5A. The upper and lower piezoelectric materials are identical. Also, the top section ($z = h^s/2$) of the substructure's material is aluminum, while the lower portion ($z = -h^s/2$) is brass. The variation of elastic modulus, density, and Poisson's ratio in the z-transverse direction depending on the power-law exponent of the PEH beam is shown in Figure 4.3 for Figure 4.2b configuration. While the Mori-Tanaka micromechanical [41] model is used to define

the substructure properties, Voigt's rule of mixture describes the piezoelectric material characteristics.

(a)

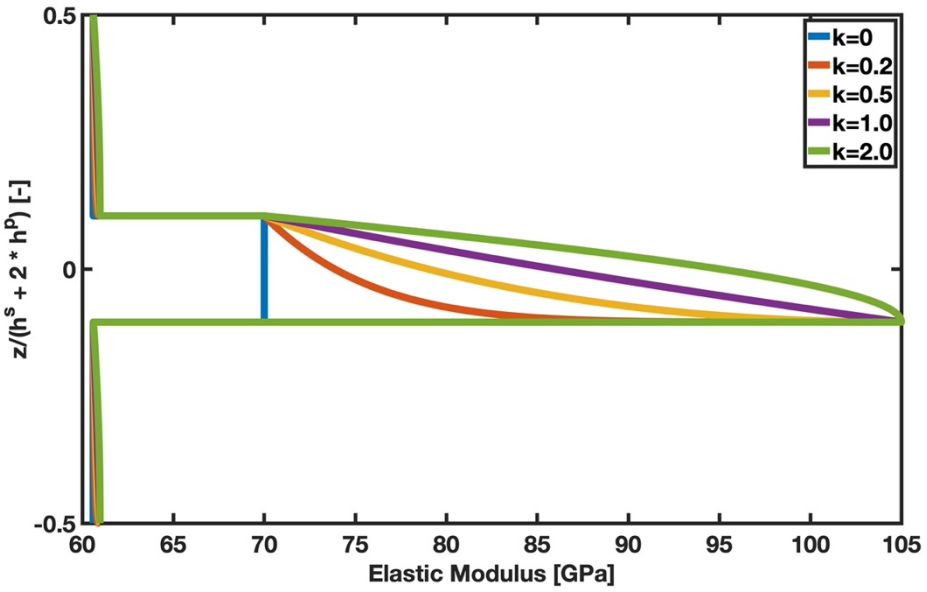

(b)

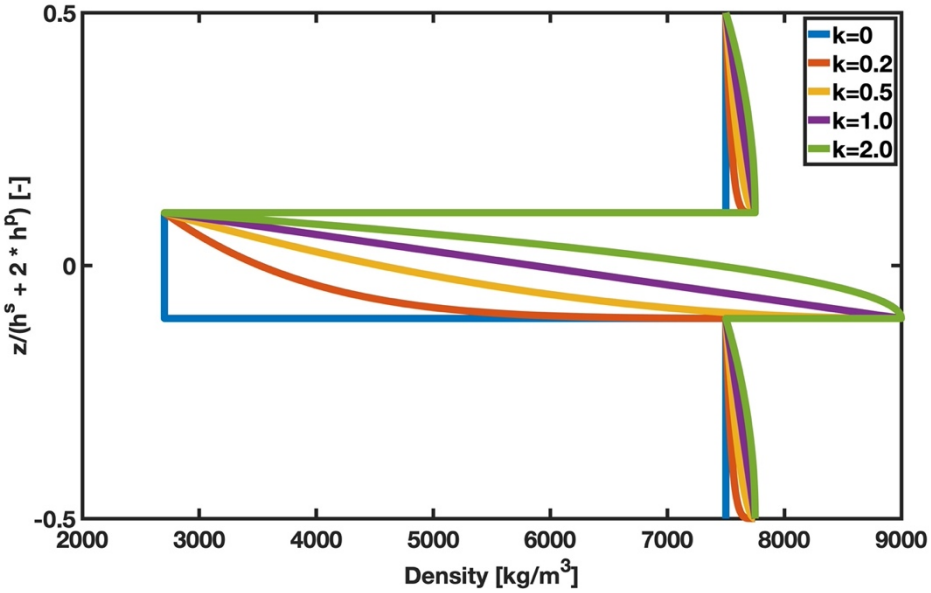

(c)

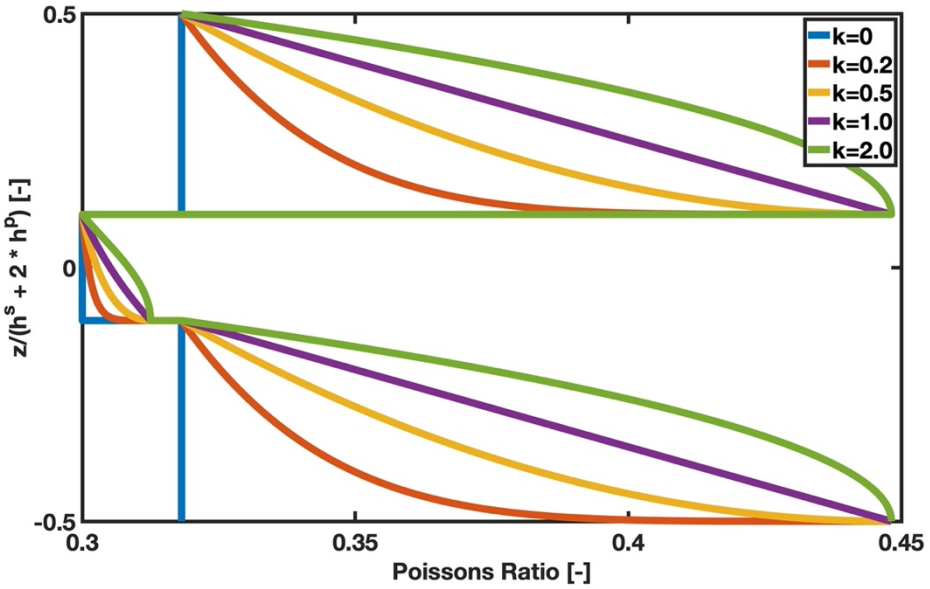

Figure 4.3 Variation of (a) modulus of elasticity, (b) density, and (c) Poisson's ratio throughout the thickness of the FG Timoshenko PEH beam using Mori-Tanaka micromechanical model [41] and Voigt's rule of mixture.

4.1 Validation of the WQEM

Verification studies are carried out separately for free and forced vibration studies.

4.1.1 Free Vibration and Steady-State Response Validation

The free vibration results and steady-state responses of the homogeneous isotropic PEH using the WQEM are compared with the experimental investigations conducted by Ertürk [33]. A cantilevered state PEH with upper- and lower-piezoelectric material PZT-5H is serially coupled in free vibration and steady-state response validation investigations. Brass is the substructure material, so the material configuration illustrated in Figure 4.1 is valid.

4.1.1.1 FRF Computation

The voltage output FRF calculation of PEH base excitation in the transverse direction is indicated by equation (4-1). In this scenario, the Δ_i value in the P stated in equation (3-50) is treated as zero. The P value obtained in this approach takes its place in equation (3-79).

$$FRF_v^{W_0} = \frac{v(t)}{\omega^2 \cdot W_0 \cdot e^{i\cdot\omega\cdot t}} \tag{4-1}$$

The other FRF functions of transverse velocity, current, and power output are also introduced as follows:

$$FRF_{\dot{w}}^{W_0} = \frac{\frac{dw(x,t)}{dt}}{\omega^2 \cdot W_0 \cdot e^{i\cdot\omega\cdot t}} \tag{4-2}$$

$$FRF_i^{W_0} = \frac{\frac{v(t)}{R_l}}{\omega^2 \cdot W_0 \cdot e^{i\cdot\omega\cdot t}} \tag{4-3}$$

$$FRF_W^{W_0} = FRF_v^{W_0} \cdot FRF_i^{W_0} = \frac{v(t)}{\omega^2 \cdot W_0 \cdot e^{i\cdot\omega\cdot t}} \cdot \frac{\frac{v(t)}{R_l}}{\omega^2 \cdot W_0 \cdot e^{i\cdot\omega\cdot t}} \tag{4-4}$$

4.1.1.2 Comparison of Free Vibration and Steady-State Response WQEM and Experimental Results

The experiments make use of a bimorph series-connected PEH with PZT-5H piezoceramics that are strengthened with brass substructure, and the BC is C-F. For BCs, the first letter denotes the left end, while the second indicates the right end. The experimental setup for series-connected bimorph PEH with and without tip mass is illustrated in Figure 4.4, and it is employed for the electromechanical voltage output FRF measurements.

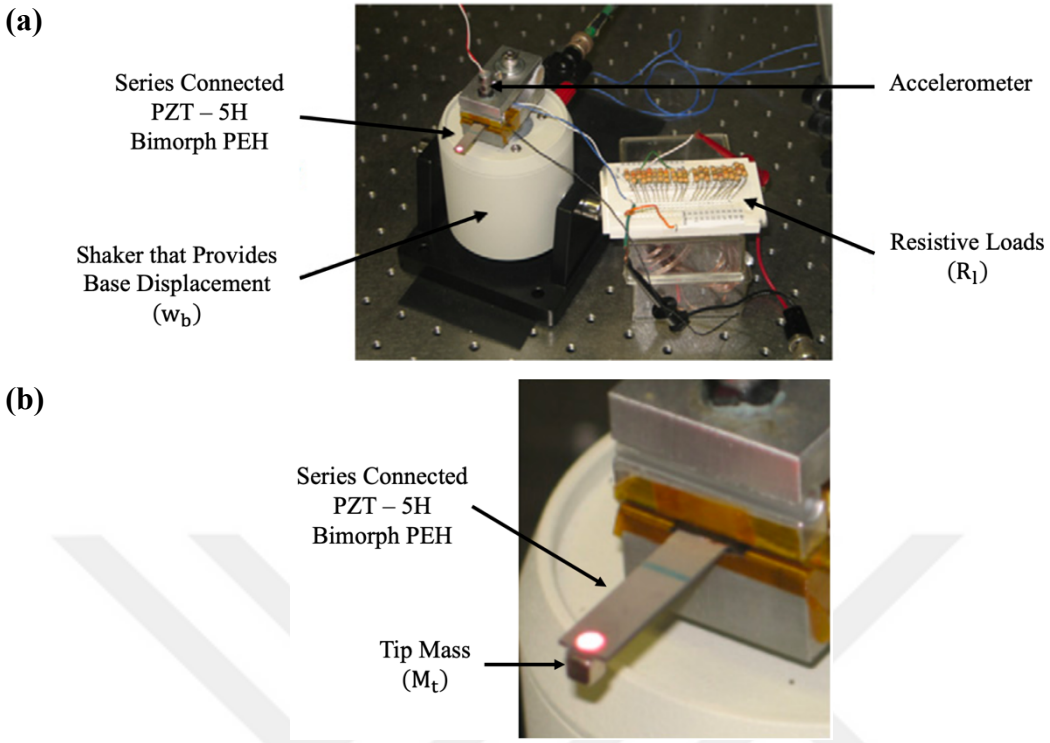

Figure 4.4 The experimental setup of Ertürk's study [33] utilized in validation studies shows the brass-reinforced PZT-5H bimorph PEH fastened to the shaker and included resistive loads (a) without and (b) with tip mass.

The electromagnetic shaker in the experimental setup provides the base displacement. An accelerometer is used to measure the base acceleration. Voltage FRF per base acceleration input of the PEH is used to provide the comparison in the natural frequency range. The approach is also explored and utilized to validate the natural frequencies in open- and short-circuit circumstances. The series-connected PEH without and with tip mass scenarios depicted in Figure 1.3c and Figure 1.3d are the subjects of all validation experiments. The phrase $\left(E^s(z)\cdot\left(1-\nu^s(z)\right)\right)/\left(\left(1+\nu^s(z)\right)\cdot\left(1-2\cdot\nu^s(z)\right)\right)$ in equation (2-32) and $\left(\bar{c}_{11}^E(z)\cdot\left(1-\nu^p(z)\right)\right)/\left(\left(1+\nu^p(z)\right)\cdot\left(1-2\cdot\nu^p(z)\right)\right)$ in equations (2-34) and (2-36) are changed to $E^s(z)$ and $\bar{c}_{11}^E(z)$, respectively, because the homogeneous isotropic Timoshenko beams are used for the comparison. It is crucial to specify the modal mechanical damping ratio ζ accurately. In this study, the modal damping ratio is defined as 0.00874 for the case where no tip mass is added to the end of the beam

and 0.00845 for the case when tip mass is included. Table 4-6 displays the short-circuit ($R_l = 470\ \Omega$) and open-circuit ($R_l = 995\ k\Omega$) fundamental frequency values of tip mass excluded configuration. The fundamental frequency is the lowest frequency, also known as the natural frequency. Although it holds when the short-circuit condition is $R_l = 0$ and the open-circuit state is $R_l = \infty$, the theoretical calculations can not be represented in this way in the experimental setup because the cables also have resistance. For this reason, the resistive load is chosen nearly in a short- and open-circuit situation.

Table 4-6 Comparison of fundamental short- and open-circuit resonance frequencies for the series-connected PZT-5H bimorph PEH without tip mass between the WQEM and the experimental results obtained in [33].

Configuration of Circuit	**Experimental Resonance Frequency** [33]	**WQEM Resonance Frequency**	**Error (%)**
Short-circuit	502.5 Hz	502.5 Hz	0
Open-circuit	524.7 Hz	524.3 Hz	0.08

Figure 4.5 compares the voltage output FRF for a load resistance R_l of 470 Ω, 1.2 kΩ, 44.9 kΩ, and 995 kΩ at 400-600 Hz vibration frequency range obtained experimentally [33] and via WQEM for the tip mass excluded configuration. Equation (4-1) is multiplied by gravity g since the voltage output is shown in Figure 4.5 and Figure 4.7 per gravity in Ertürk's study [33]. The WQEM resonance frequency and voltage output FRF graphs are computed by taking the number of nodes N as 5. The numerical results correlate well with the experimental data.

(a)

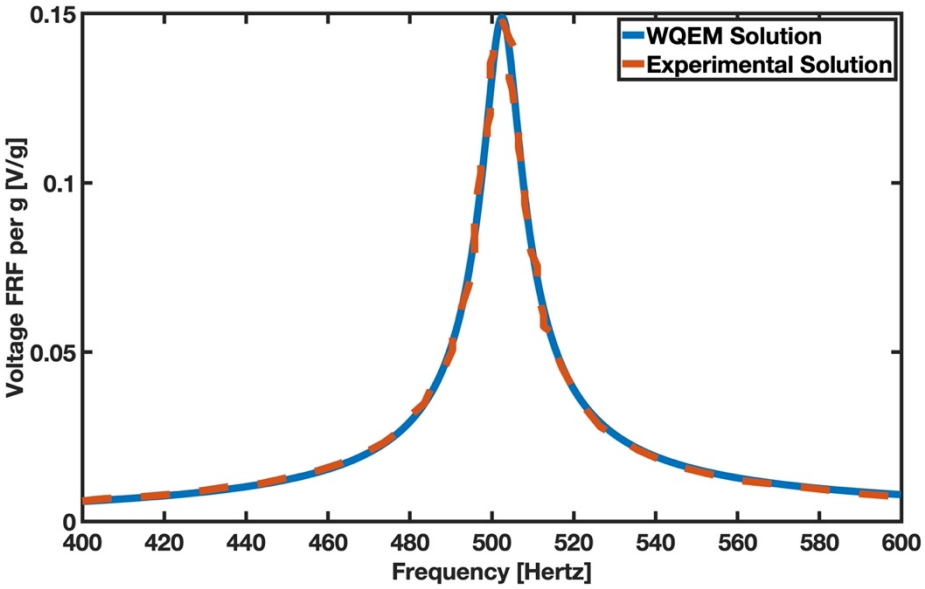
WQEM Solution
Experimental Solution
Voltage FRF per g [V/g]
Frequency [Hertz]
0.15
0.1
0.05
0
400
420
440
460
480
500
520
540
560
580
600

(b)

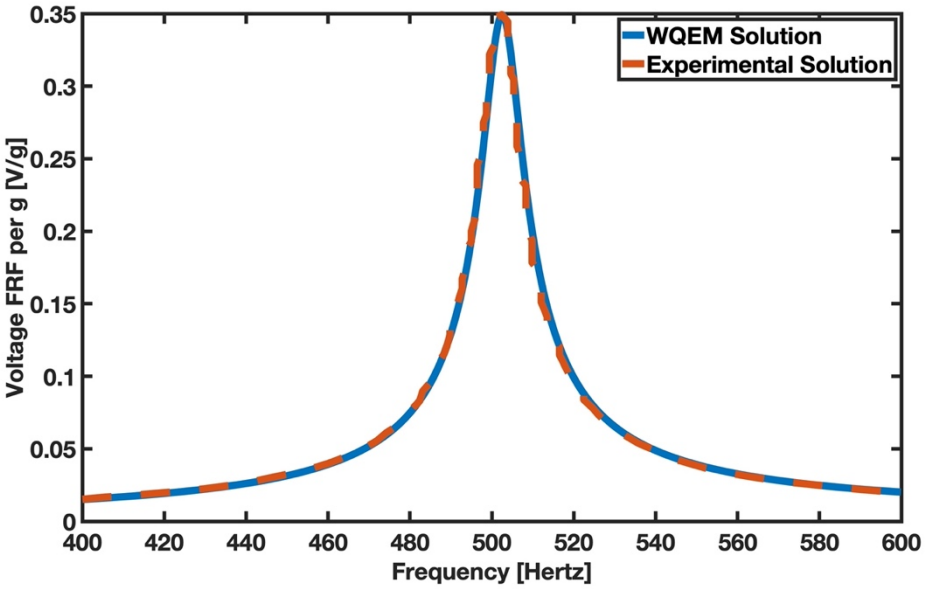
WQEM Solution
Experimental Solution
Voltage FRF per g [V/g]
Frequency [Hertz]
0.35
0.3
0.25
0.2
0.15
0.1
0.05
0
400
420
440
460
480
500
520
540
560
580
600

(c)

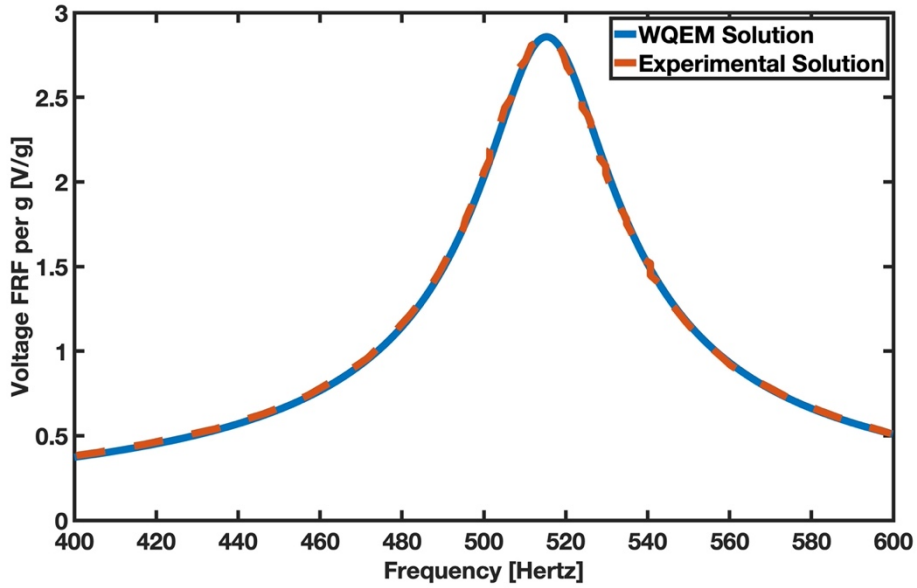

(d)

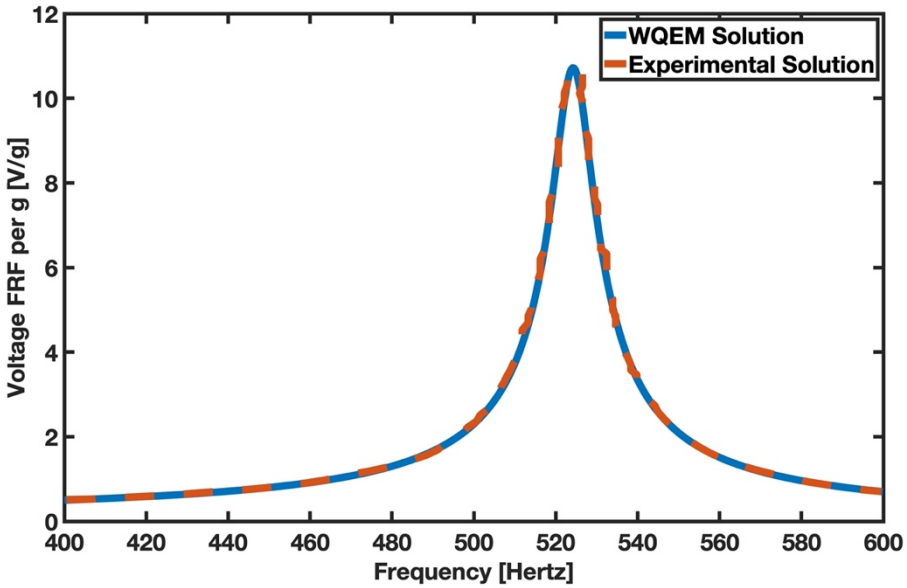

Figure 4.5 The voltage output FRF per gravity of the series-connected PZT-5H bimorph PEH without tip mass obtained via WQEM and experimentally [33] for a load resistance (a) R_l = 470 Ω, (b) R_l = 1.2 kΩ, (c) R_l = 44.9 kΩ, and (d) R_l = 995 kΩ.

The peak in Figure 4.5a and Figure 4.5d's FRF plot proves the validity of the natural frequency values in Table 4-6. The natural frequency value rises and shifts to the right with increased resistance.

The series-connected bimorph PEH illustrated in Figure 1.3d with the tip mass added configuration undergoes FRF voltage output validation. As a result of Ertürk placing the tip mass in the experiment [33], as shown in Figure 4.6, the inertia formulation is altered to $I_t = M_t \cdot [(h^t + L^t)^2/12 + (h^s/2 + h^p + h^t/2)^2]$ using parallel axis theorem.

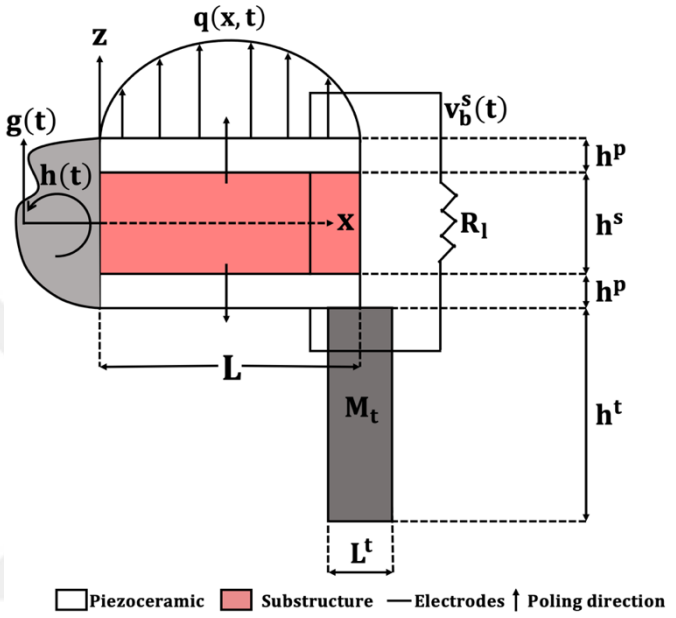

Figure 4.6 The schematic representation of series-connected PZT-5H bimorph PEH with tip mass used in Ertürk's experiment [33].

Table 4-7 displays the short-circuit ($R_l = 470\ \Omega$) and open-circuit ($R_l = 995\ k\Omega$) natural frequency values for tip mass added configuration.

Table 4-7 Comparison of fundamental short- and open-circuit resonance frequencies for the tip mass added series-connected bimorph PEH between the WQEM and the experimental results obtained in [33].

Configuration of Circuit	**Experimental Resonance Frequency** [33]	**WQEM Resonance Frequency**	**Error (%)**
Short-circuit	338.4	338.4	0
Open-circuit	356.3	355.2	0.31

Figure 4.7 compares the voltage FRF for a load resistance R_l of 470 Ω, 1.2 kΩ, 44.9 kΩ, and 995 kΩ at 200-500 Hz vibration frequency range obtained experimentally and via WQEM for tip mass added configuration. The peak in Figure 4.7a and Figure 4.7d's FRF plot also proves the validity of the natural frequency values in Table 4-7. The node number N is 5. The numerical results and the experimental data agree well.

(a)

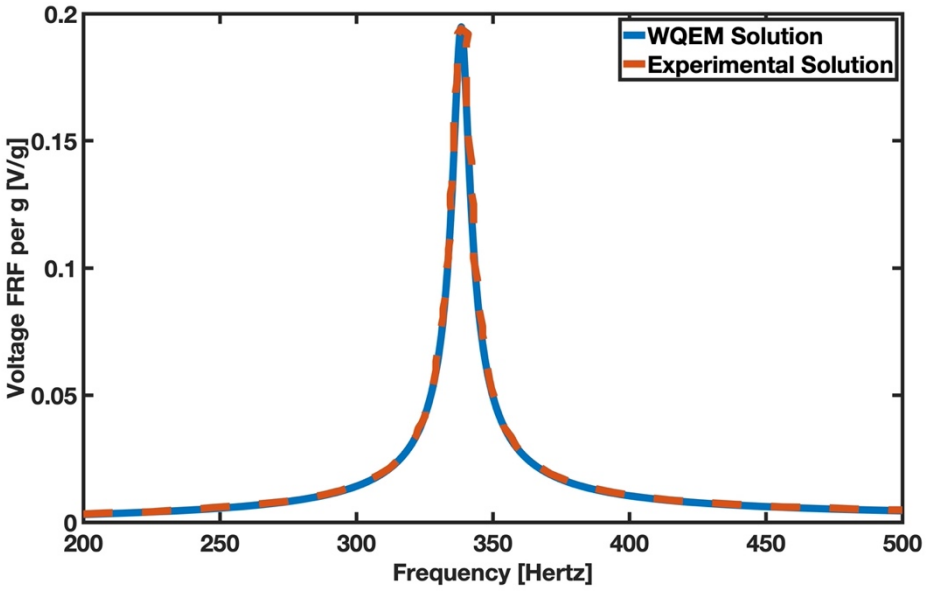

(b)

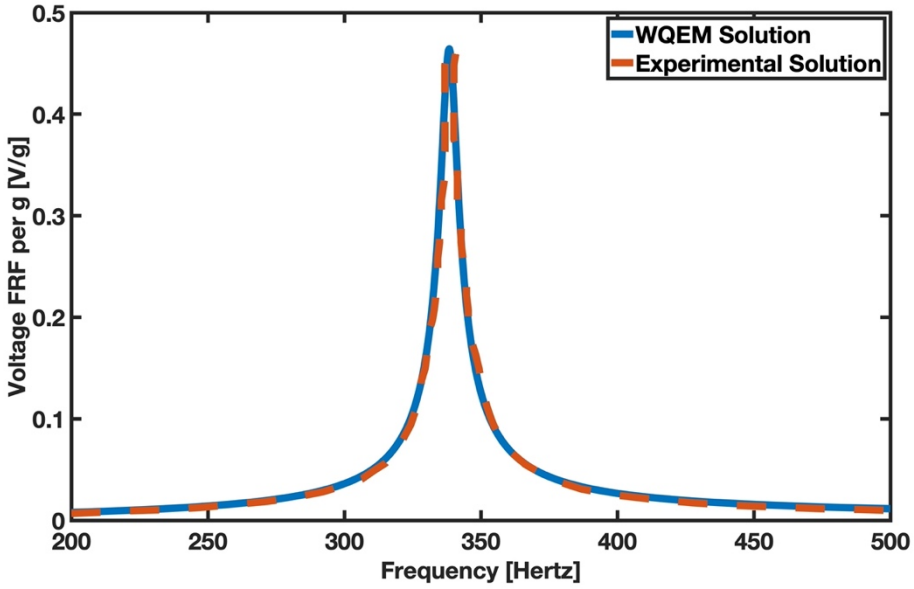

(c)

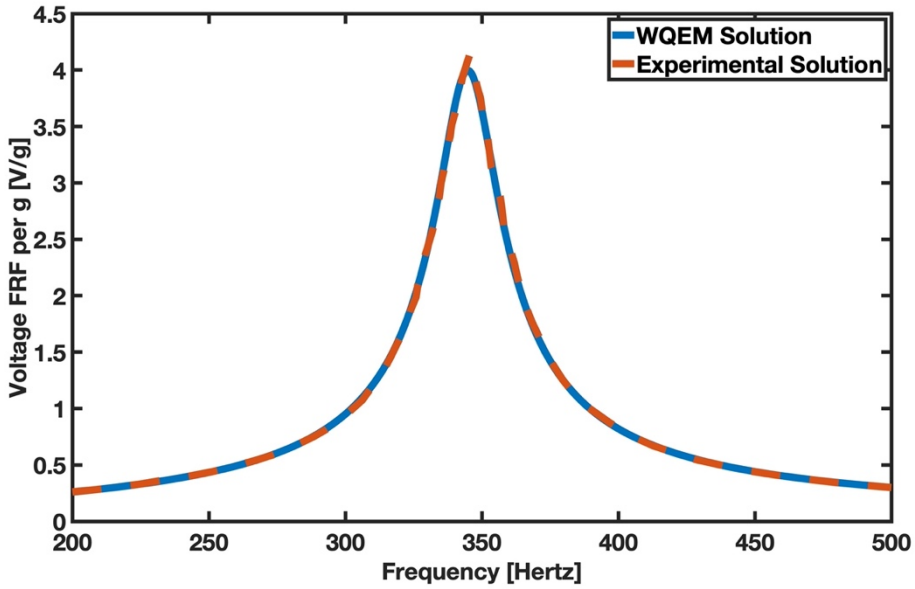

(d)

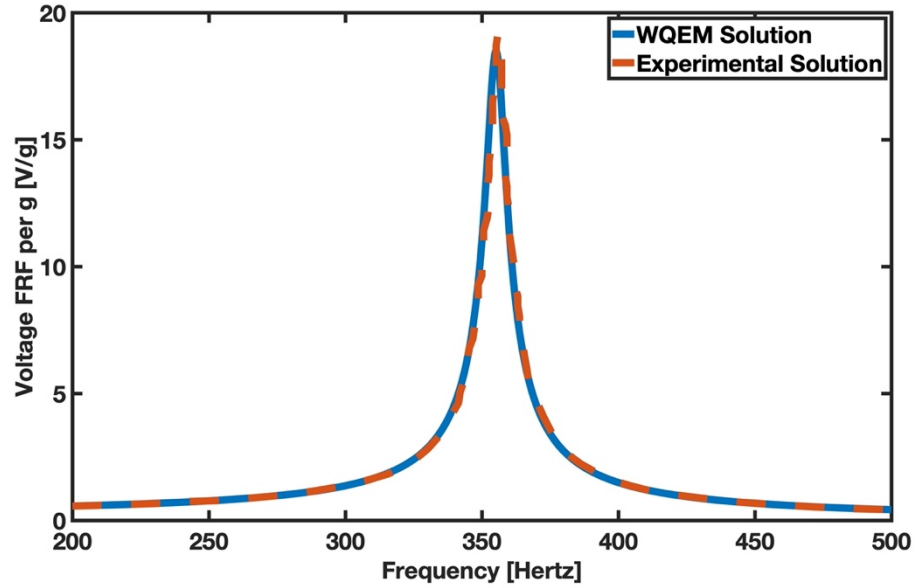

Figure 4.7 The voltage output FRF per gravity of the series-connected PZT-5H bimorph PEH with tip mass obtained via WQEM and experimentally [33] for a load resistance (a) $R_l = 470\ \Omega$, (b) $R_l = 1.2\ k\Omega$, (c) $R_l = 44.9\ k\Omega$, and (d) $R_l = 995\ k\Omega$.

4.1.2 Forced Vibration Validation

The tip mass excluded Timoshenko PEH beam is verified by comparing it to the analytical solution [44] for the P-P BC, to which forced vibration is applied. The PEH beam's material characteristics are balanced using equations (4-7), (4-8), (4-9), (4-10), (4-11), and (4-12) to ensure homogeneity. The damping effect and base displacement for forced vibration validation are neglected because the analytic formulation does not include them. In all of the forced vibration validation studies, the beam contains 21 nodes, and the time step is $1 \cdot (10)^{-6}$ s.

4.1.2.1 Forced Vibration Analytical Solutions

The analytical solutions [44] for the P-P beam are considered to be of the following form by applying the standard approach of the separation of variables:

$$w(x,t) = \sum_{m=1,3,5}^{\infty} W_m(t) \cdot \sin\left(\frac{m \cdot \pi \cdot x}{L}\right) \tag{4-5}$$

where W_m is the time-dependent variable, and m is an odd number that goes to infinity. The following is a general formula for the time-dependent variable W_m:

$$W_m(t) = \left[\rho_{eq} \cdot I_{eq} \cdot \ddot{Q}_m(t) + \left[E_{eq} \cdot I_{eq} \cdot \left(\frac{m \cdot \pi}{L}\right)^2 + \kappa_s \cdot \mu_{eq} \cdot A_{eq}\right] \cdot Q_m(t)\right] \cdot \frac{1}{\kappa_s \cdot \mu_{eq} \cdot A_{eq} \cdot \left(\frac{m \cdot \pi}{L}\right)} \tag{4-6}$$

where ρ_{eq}, I_{eq}, E_{eq}, μ_{eq}, A_{eq} are the equivalent density, area moment of inertia of the cross-section with respect to the z-axis, elastic modulus, shear modulus, and area of the beam cross-section for the series-connected bimorph PEH without tip mass configuration, and they defined as follows:

$$\rho_{eq} = \frac{2 \cdot \rho^p \cdot h^p + \rho^s \cdot h^s}{2 \cdot h^p + h^s} \tag{4-7}$$

$$I_{eq} = \frac{1}{12} \cdot b \cdot (2 \cdot h^p + h^s)^3 \tag{4-8}$$

$$E_{eq} = \frac{E^s \cdot (h^s)^3 + 8 \cdot \bar{c}_{11}^E \cdot \left[\left(h^p + \frac{h^s}{2}\right)^3 - \frac{(h^s)^3}{8}\right]}{(2 \cdot h^p + h^s)^3} \tag{4-9}$$

$$\mu_{eq} = \frac{E_{eq}}{2 \cdot (1 + \nu_{eq})} \tag{4-10}$$

$$A_{eq} = b \cdot (2 \cdot h^p + h^s) \tag{4-11}$$

where ν_{eq} is the equivalent Poisson's ratio for the series-connected bimorph PEH without tip mass configuration, and it is defined as follows:

$$\nu_{eq} = \frac{2 \cdot \nu^p \cdot h^p + \nu^s \cdot h^s}{2 \cdot h^p + h^s} \tag{4-12}$$

The expressions for Q_m and $\ddot{Q}_m$ change based on the type of load. $\ddot{Q}_m$ is simply calculated from the expression of Q_m. For the case of the uniformly distributed step load defined as $f(x,t) = f_0$:

$$\begin{aligned} Q_m(t) = \frac{4 \cdot f_0 \cdot L^3}{E_{eq} \cdot I_{eq} \cdot (m \cdot \pi)^4 \cdot \left({\delta_m}^2 - {\theta_m}^2\right)} \\ \cdot \left[{\theta_m}^2 \cdot \cos(\delta_m \cdot t) - {\delta_m}^2 \cdot \cos(\delta_m \cdot t) \right. \\ \left. + \left({\delta_m}^2 - {\theta_m}^2\right)\right] \end{aligned} \tag{4-13}$$

In the case of a concentrated step load of intensity F, applies in the position $x = x_0$, defined as $f(x,t) = F \cdot \delta(x - x_0)$:

$$\begin{aligned} Q_m(t) = \frac{2 \cdot F \cdot L^2}{E_{eq} \cdot I_{eq} \cdot (m \cdot \pi)^3 \cdot \left({\delta_m}^2 - {\theta_m}^2\right)} \\ \cdot \left[{\theta_m}^2 \cdot \cos(\delta_m \cdot t) - {\delta_m}^2 \cdot \cos(\delta_m \cdot t) \right. \\ \left. + \left({\delta_m}^2 - {\theta_m}^2\right)\right] \end{aligned} \tag{4-14}$$

For the case of the concentrated harmonic load of intensity F, frequency ω_p applied at $x = x_0$, defined as $f(x,t) = F \cdot \delta(x - x_0) \cdot \sin(\omega_p \cdot t)$:

$$Q_m(t) = \frac{2 \cdot F}{L^2} \cdot \frac{m \cdot \pi}{\left(\frac{{\rho_{eq}}^2 \cdot I_{eq}}{\kappa_s \cdot \mu_{eq}}\right)} \cdot \left[\frac{\omega_p}{\left({\delta_m}^2 - {\theta_m}^2\right)} \cdot \left[\frac{\sin(\theta_m \cdot t)}{\theta_m \cdot \left({\omega_p}^2 - {\theta_m}^2\right)} - \frac{\sin(\delta_m \cdot t)}{\delta_m \cdot \left({\omega_p}^2 - {\delta_m}^2\right)}\right] + \frac{\sin(\omega_p \cdot t)}{\left({\omega_p}^2 - {\theta_m}^2\right) \cdot \left({\omega_p}^2 - {\delta_m}^2\right)}\right] \cdot \sin\left(\frac{m \cdot \pi \cdot x_0}{L}\right) \tag{4-15}$$

Finally, for the case of the concentrated impulsive load of intensity $\bar{F}$ applied at $x = x_0$ and $t = 0$, defined as $f(x,t) = \bar{F} \cdot \delta(x - x_0) \cdot \delta(t - 0)$:

$$Q_m(t) = \frac{2 \cdot \bar{F}}{L^2} \cdot \frac{m \cdot \pi}{\left(\frac{{\rho_{eq}}^2 \cdot I_{eq}}{\kappa_s \cdot \mu_{eq}}\right)} \cdot \left(\frac{\sin(\theta_m \cdot t)}{\theta_m} - \frac{\sin(\delta_m \cdot t)}{\delta_m}\right) \cdot \frac{\sin\left(\frac{m \cdot \pi \cdot x_0}{L}\right)}{{\delta_m}^2 - {\theta_m}^2} \tag{4-16}$$

For all the Q_m expressions, the natural frequencies θ_m and δ_m are defined as follows:

$$\theta_m = \sqrt{\alpha_m - \beta_m} \tag{4-17}$$

$$\delta_m = \sqrt{\alpha_m + \beta_m} \tag{4-18}$$

where

$$\alpha_m = \frac{\rho_{eq} \cdot A_{eq} + \rho_{eq} \cdot I_{eq} \cdot \left(1 + \frac{E_{eq}}{\kappa_s \cdot \mu_{eq}}\right) \cdot \left(\frac{m \cdot \pi}{L}\right)^2}{2 \cdot \left(\frac{{\rho_{eq}}^2 \cdot I_{eq}}{\kappa_s \cdot \mu_{eq}}\right)} \tag{4-19}$$

$$\beta_m = \frac{\sqrt{(\rho_{eq} \cdot A_{eq})^2 + 2 \cdot (\rho_{eq} \cdot A_{eq}) \cdot (\rho_{eq} \cdot I_{eq}) \cdot \left(1 + \frac{E_{eq}}{\kappa_s \cdot \mu_{eq}}\right) \cdot \left(\frac{m \cdot \pi}{L}\right)^2 + (\rho_{eq} \cdot I_{eq})^2 \cdot \left(1 - \frac{E_{eq}}{\kappa_s \cdot \mu_{eq}}\right)^2 \cdot \left(\frac{m \cdot \pi}{L}\right)^4}}{2 \cdot \left(\frac{{\rho_{eq}}^2 \cdot I_{eq}}{\kappa_s \cdot \mu_{eq}}\right)} \quad (4\text{-}20)$$

4.1.2.2 Comparison of Forced Vibration WQEM and Analytical Results

The time-varying displacement of the midpoint of the series-connected bimorph PEH beam $w(L/2, t)$ by applying a uniformly distributed step load is demonstrated in Figure 4.8 by comparing the WQEM with the analytical solution [44]. The BC of the beam is P-P and $f_0 = 10\ N/m$. R_l is 470 Ω. A perfect match is observed between the results obtained by WQEM and the analytical results for the loading mentioned above.

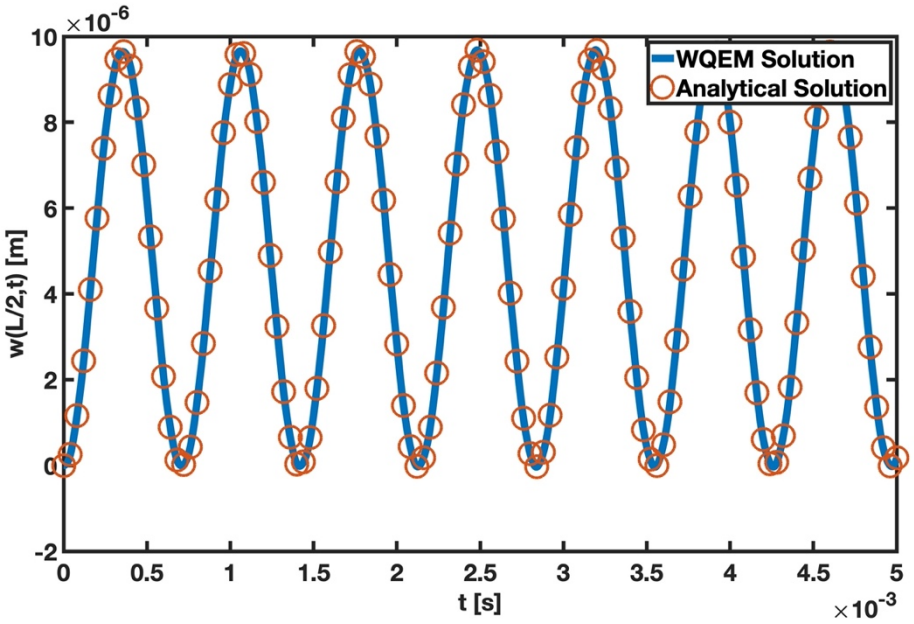

Figure 4.8 Dynamic responses of a P-P series-connected bimorph PEH beam under uniformly distributed step load using WQEM and the analytical formula, $f_0 = 10$ N/m.

The midpoint displacement comparison result for the other loading type, the concentrated step load, for the P–P series-connected bimorph PEH beam is shown in Figure 4.9. Concentrated load intensity F is 0.2 N and acts at $x_0 = L/2$. R_l is 470 Ω.

The analytical and WQEM results demonstrate that the numerical technique developed for forced vibration analysis works with excellent accuracy.

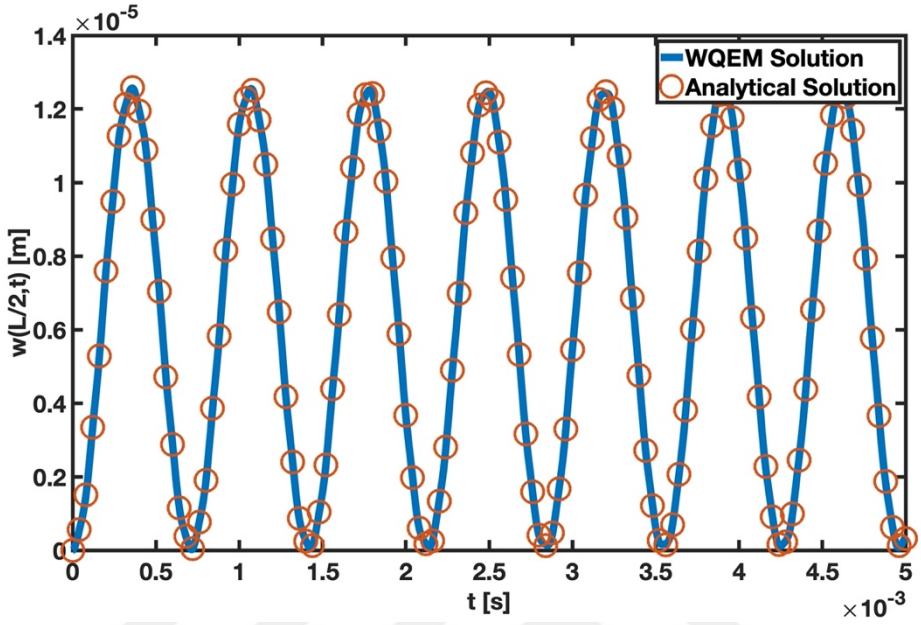

Figure 4.9 Dynamic responses of a P-P series-connected bimorph PEH beam under concentrated step load using WQEM and the analytical formula, F = 0.2 N, x_0 = L/2.

Figure 4.10 displays the analytical and the WQEM results for a P-P series-connected bimorph PEH beam exposed to a concentrated harmonic load. F is the loading intensity at $x_0 = L/2$, and it is 0.2 N. The applied frequency ω_p is 1409 Hz, and $R_l = 470\ \Omega$. The frequency applied to the system is set to be the same as its natural frequency. It can be shown that the time variation of the midpoint deviation produced by the WQEM agrees perfectly with the analytical result.

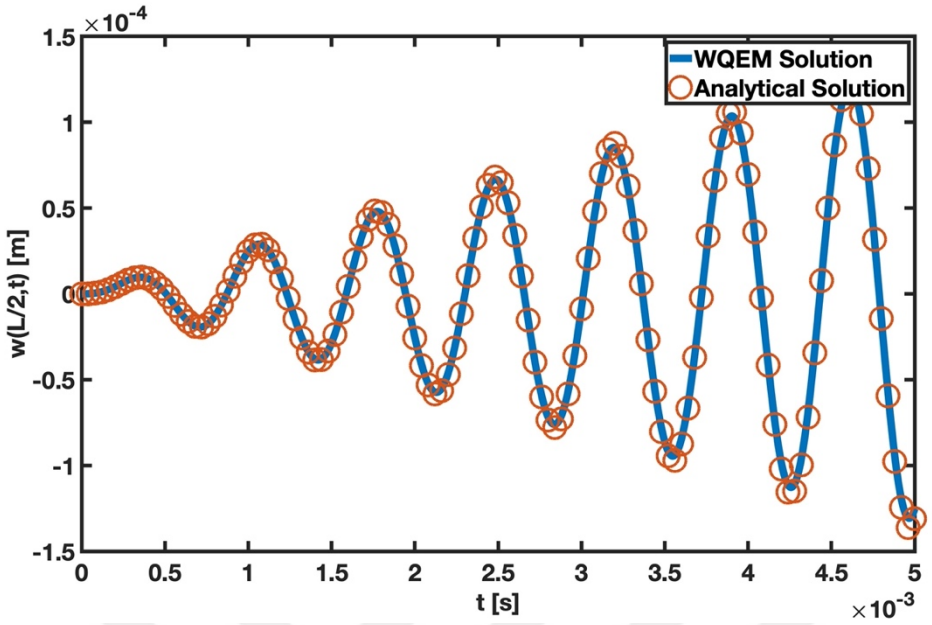

Figure 4.10 Dynamic responses of a P-P series-connected bimorph PEH beam under concentrated harmonic load using WQEM and the analytical formula, F = 0.2 N, ω_p = 1409 Hz, x_0 = L/2.

Finally, validation for concentrated impulsive load is conducted, as illustrated in Figure 4.11. For the P-P series-connected bimorph PEH beam exposed to the mentioned load, analytical and WQEM values are produced. The impulsive load amplitude of $\bar{F}$ is specified as 0.00003 N · s, applied at $x_0 = L/2$. R_l equals 470 Ω. Rectangular impulsive load, as described in Figure 3.5, has a start time t_0 of $1 \cdot (10)^{-5}$ s and an end time t_1 of $2 \cdot (10)^{-5}$ s. Excellent agreement has also been established for the concentrated impulsive force, and the WQEM has been proven to be quite accurate.

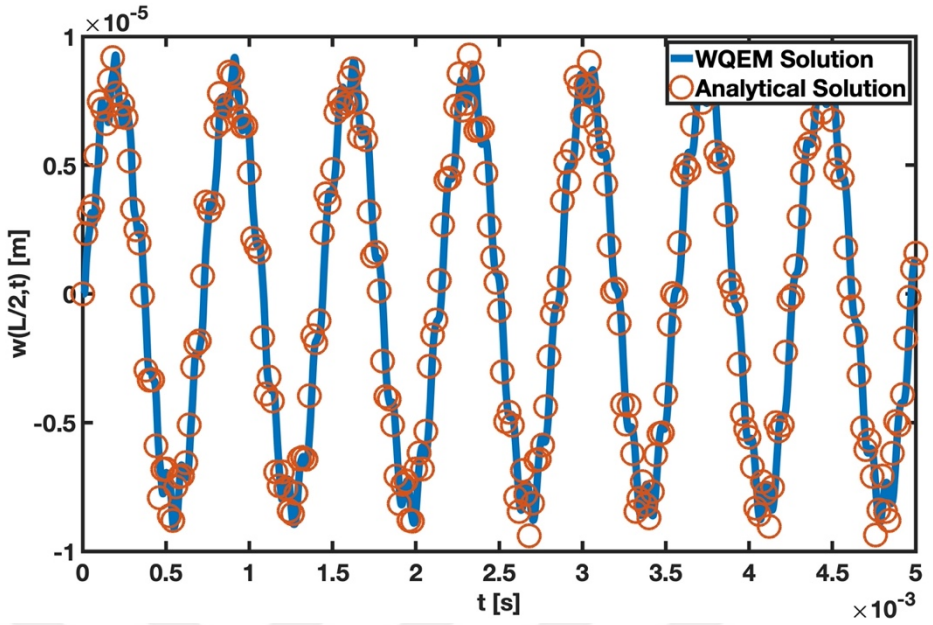

Figure 4.11 Dynamic responses of a P-P series-connected bimorph PEH beam under concentrated impulsive load using WQEM and the analytical formula, $\bar{F}$ = 0.00003 N·s, $t_0 = 1\cdot(10)^{-5}$ s, $t_1 = 2\cdot(10)^{-5}$ s, $x_0 = L/2$.

4.2 Convergence Study and Parametric Analysis

The geometric illustration of the FG Timoshenko PEH beam utilized in parametric analyses is displayed in Figure 1.3. The material configuration depicted in Figure 4.2 is valid. This section illustrates the dampening effect. Before conducting any study, the fundamental frequency is acquired to determine the stiffness proportionality factor. The dampening modal coefficients, as reported in the validation experiments, are considered to be the same as those from Ertürk's study [33]. Convergence and parametric analysis studies are divided into free and forced vibration analyses.

4.2.1 Free Vibration and Steady-State Response Convergence Study and Parametric Analysis

In free vibration and steady-state response studies, convergence and parametric analysis are examined separately in two categories.

4.2.1.1 Free Vibration and Steady-State Response Convergence Study

Firstly, the frequency parameter λ is defined in order to demonstrate the free vibration behavior.

$$\lambda = \frac{\omega_0 \cdot L^2}{h^s} \cdot \sqrt{\frac{\rho_l^s}{E_l^s}} \tag{4-21}$$

Natural frequency in rad/s, lower portion density, and lower portion elasticity of substructure material are represented by ω_0, ρ_l^s, and E_l^s, respectively. The convergence of the free vibration results is examined in a situation where the number of nodes N ranges from 5 to 13. Figure 4.12 illustrates the relationship between the first five frequency parameters and the number of nodes for the C-F FG series-connected bimorph Timoshenko PEH beam without tip mass. Load resistance is ignored. The power-law exponent k is equal to 0.5. Convergence is mainly achieved when the number of nodes equals 5 for the first vibrational frequency. Additionally, convergence is totally established at $N = 11$ for all five modes.

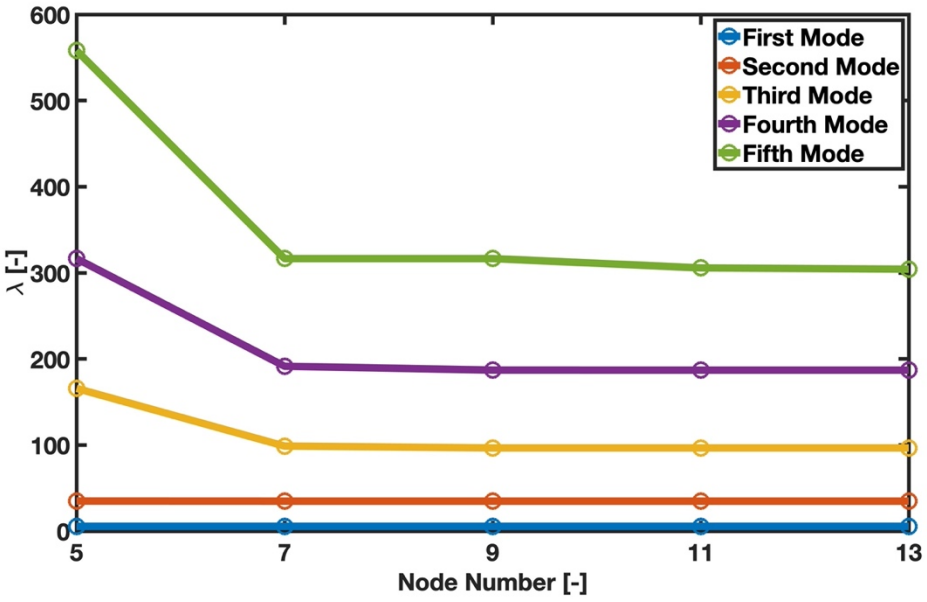

Figure 4.12 Convergence of the first five mode frequencies of the series-connected bimorph C-F FG Timoshenko PEH beam without tip mass for power-law exponent $k = 0.5$.

Table 4-8 displays CPU times of the convergence analysis depicted in Figure 4.12 using MATLAB R2023a for five node numbers from 5 to 13. Here are some details about the computer: macOS Ventura 13.4.1 (c), RAM 8 GB 2133 MHz LPDDR3, and CPU 3.1GHz Dual-Core Intel Core i5.

Table 4-8 Free vibration convergence study CPU time in seconds for series-connected bimorph C-F FG Timoshenko PEH beam without tip mass using power-law exponent $k = 0.5$.

N	CPU Time (s)
5	2.04
7	3.54
9	5.90
11	10.60
13	20.96

The fundamental frequency values defined in equation (4-21) varying with power-law exponent for six combinations of BCs are obtained using the C, S, P, and F ends, as shown in Table 4-9. The displacement of the left and right BC letters has no effect on the fundamental frequency values but alters the mode shapes. The node number is 5 for the natural frequency calculation. It is seen that the fundamental frequency value increases in all BCs as the k value goes up. Furthermore, when the boundary conditions' constraint grows, so does the fundamental frequency.

Table 4-9 The fundamental frequency values of the series-connected bimorph FG Timoshenko PEH beam without tip mass changing with the power-law exponent with various BCs.

BC's	k				
	0	**0.2**	**0.5**	**1.0**	**2.0**
C-C	32.56980	33.46459	35.07749	37.33802	40.03443
C-S	22.63636	23.26538	24.40147	25.99675	27.89827
C-P	22.63636	23.26425	24.39552	25.98271	27.87961
C-F	5.17964	5.32477	5.58615	5.95331	6.39303
S-S	14.52187	14.93221	15.68191	16.73970	17.98663
S-P	14.52187	14.92789	15.65913	16.68598	17.91523

4.2.1.2 Free Vibration and Steady-State Response Parametric Analysis

The effects of load resistance, the power-law exponent, the PEH layout, and the material structure are investigated in free vibration parametric analysis. The steady-state responses of base displacement applied PEHs are contrasted. Five nodes are used in these analyses.

4.2.1.2.1 Load Resistance Change

Examining the tip velocity, voltage, current, and power output FRFs while accounting for the scenarios where the load resistance is 470 Ω, 1.2 kΩ, 44.9 kΩ, and 995 kΩ allows us to analyze the influence of load resistance variation. The series-connected, mass-free form of the PEH shown in Figure 1.3c is the examined configuration. The power-law exponent is taken as 0.5. The BC is C-F. The output FRFs are shown in Figure 4.13.

(a)

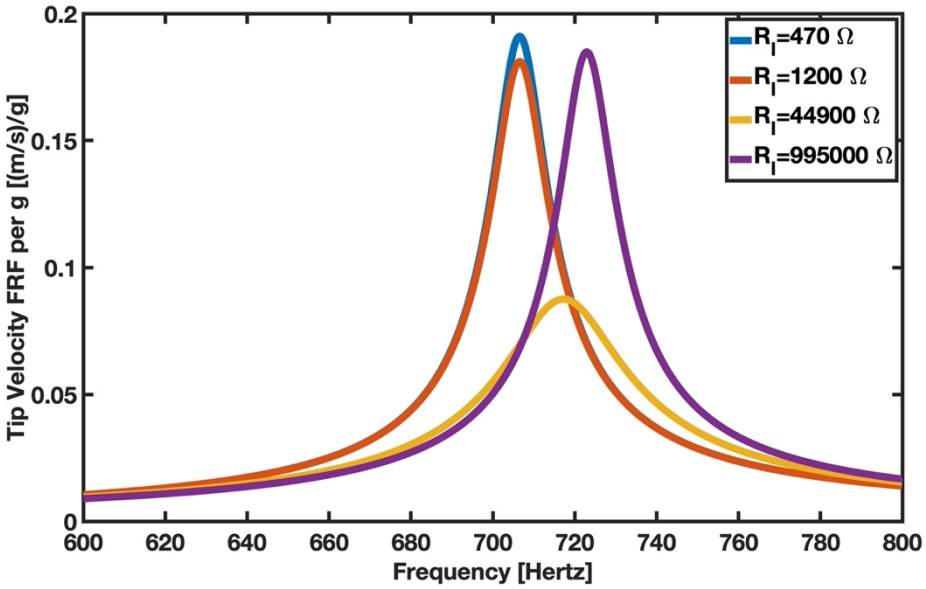
Tip Velocity FRF per g [(m/s)/g]
Frequency [Hertz]
R_l=470 Ω
R_l=1200 Ω
R_l=44900 Ω
R_l=995000 Ω

(b)

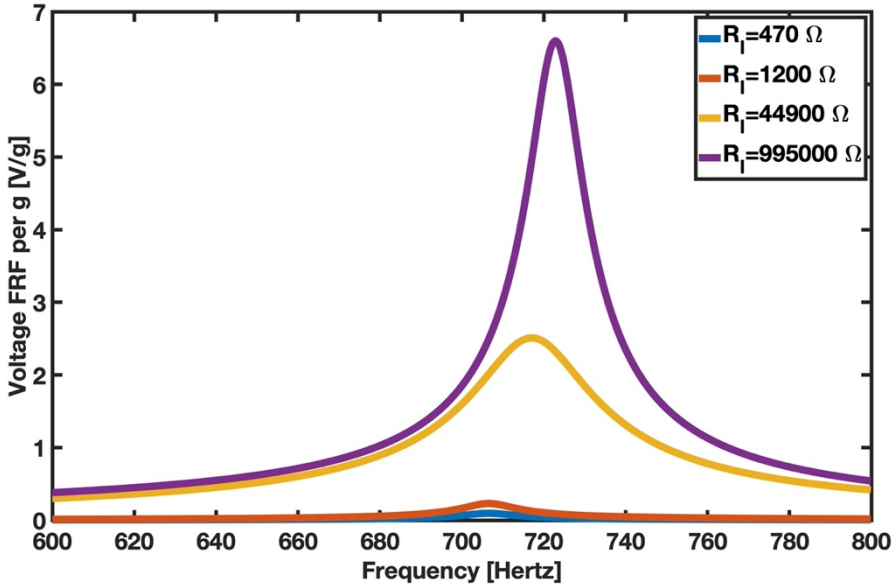
Voltage FRF per g [V/g]
Frequency [Hertz]
R_l=470 Ω
R_l=1200 Ω
R_l=44900 Ω
R_l=995000 Ω

(c)

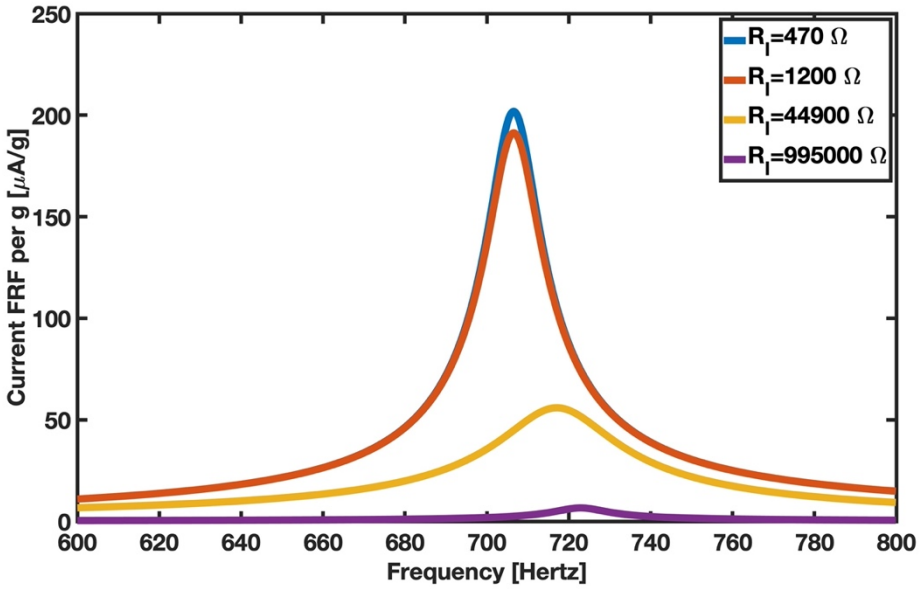

(d)

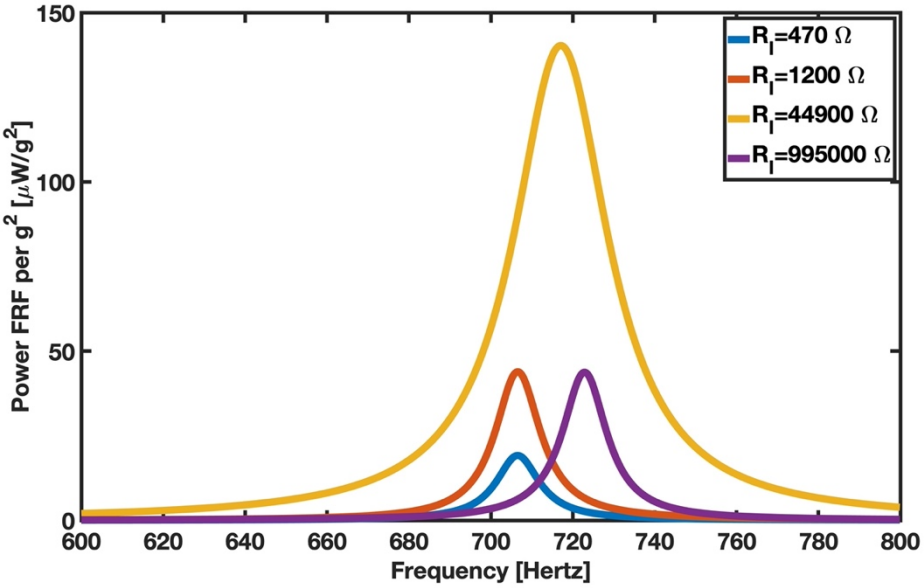

Figure 4.13 Output FRFs of the series-connected bimorph PEH cantilever without tip mass in terms of (a) tip displacement, (b) voltage, (c) current, and (d) power for 470 Ω, 1.2 kΩ, 44.9 kΩ, and 995 kΩ resistive loads.

The magnitude of the tip velocity FRF first declines as load resistance rises. The response amplitude grows again when the system approaches the open-circuit condition and saturation occurs. Researchers should examine the four FRF outputs to attain maximum voltage, current, and power output levels. The voltage output rises as the open-circuit situation approaches, whereas the current level increases as

the short-circuit condition does. $R_l = 44.9\ k\Omega$ yields the intermediate value of the tip velocity, voltage, and current output while providing the greatest power output. Properly adjusting load resistance can produce more power while oscillating less at resonance. Finally, the peak points of the FRF results move to the right as the load resistance increases, which means the natural frequencies rise.

4.2.1.2.2 Power-Law Exponent Change

The power-law exponent effect is studied using a series-connected tip mass excluded C-F bimorph PEH with a load resistance of 470 Ω. The power-law exponent is assumed to be 0, 0.2, 0.5, and 1. Increasing the k value means examining the PZT-5H and aluminum dominant FRF results. The tip velocity, voltage, current, and power FRF outputs are shown in Figure 4.14.

(a)

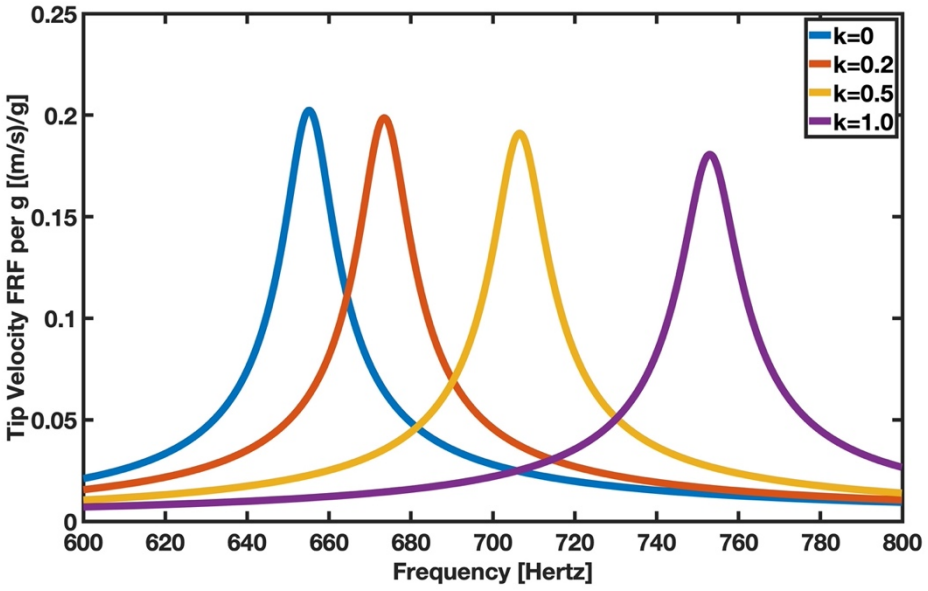

(b)

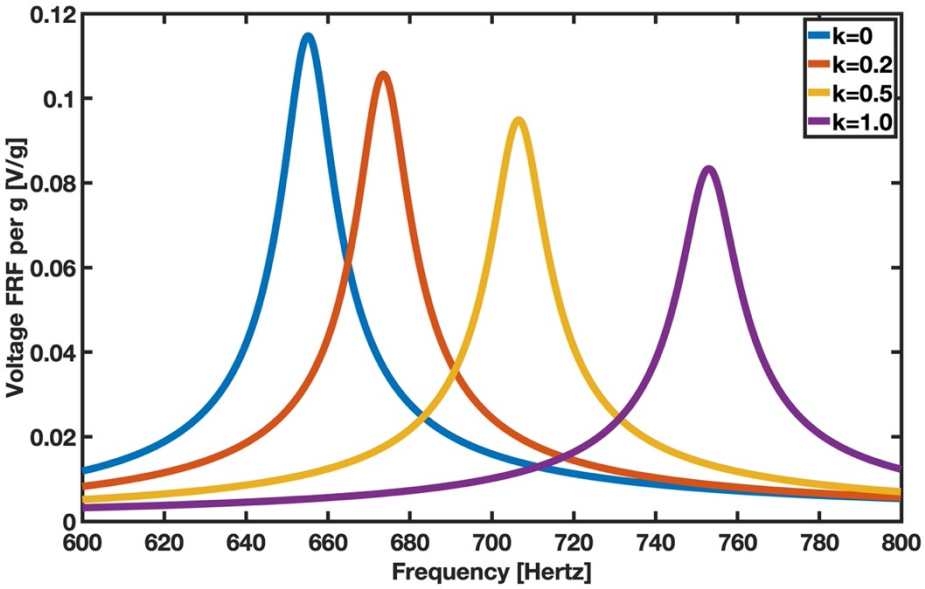
0.12
0.1
0.08
0.06
0.04
0.02
0
Voltage FRF per g [V/g]
600
620
640
660
680
700
720
740
760
780
800
Frequency [Hertz]
k=0
k=0.2
k=0.5
k=1.0

(c)

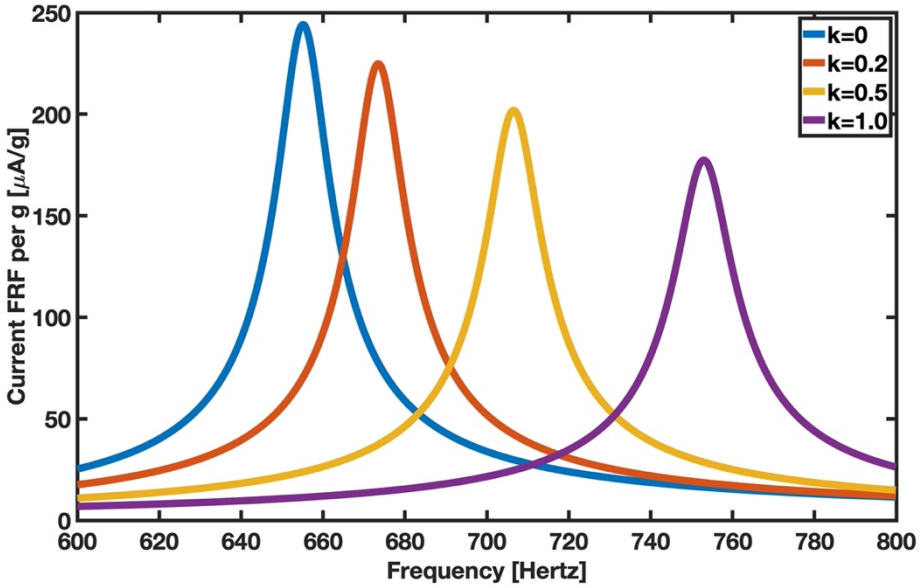
250
200
150
100
50
0
Current FRF per g [μA/g]
600
620
640
660
680
700
720
740
760
780
800
Frequency [Hertz]
k=0
k=0.2
k=0.5
k=1.0

(d)

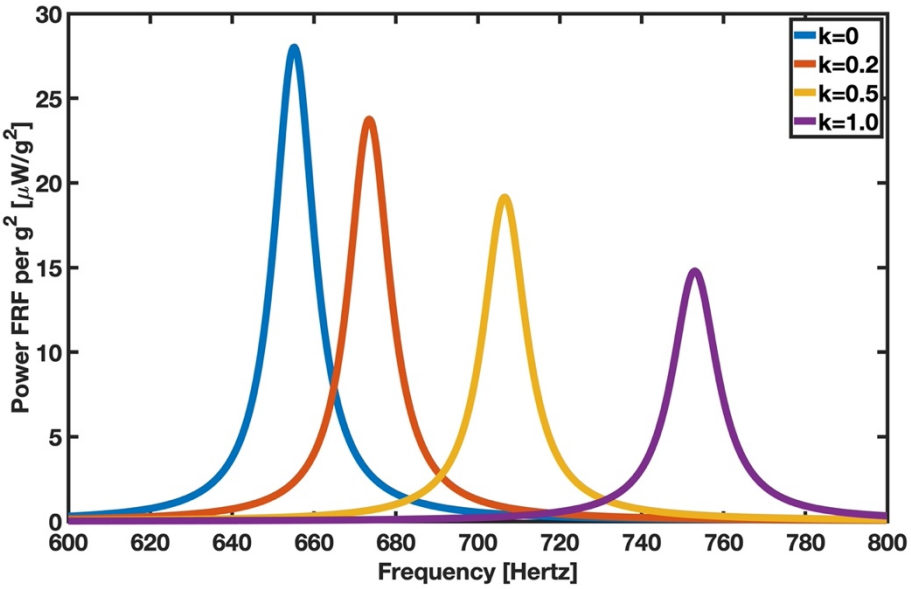

Figure 4.14 Output FRFs of the series-connected bimorph PEH cantilever without tip mass in terms of (a) tip displacement, (b) voltage, (c) current, and (d) power for 0, 0.2, 0.5, and 1 power-law exponents.

The PEH beam's natural frequency rises as the k value increases, but the tip velocity, voltage, current, and power outputs fall. As shown in Figure 4.3, the cause of this situation is the increase in the elastic modulus, density, and Poisson's ratio with an increase in the power-law exponent value.

4.2.1.2.3 PEH Configuration Change

The steady-state response FRFs are built to compare the C-F PEH structures shown in Figure 1.3. The load resistance in the analysis is 470 Ω, and the k value is 0.5. The graphs used to evaluate vibrational and electrical characteristics are shown in Figure 4.15.

(a)

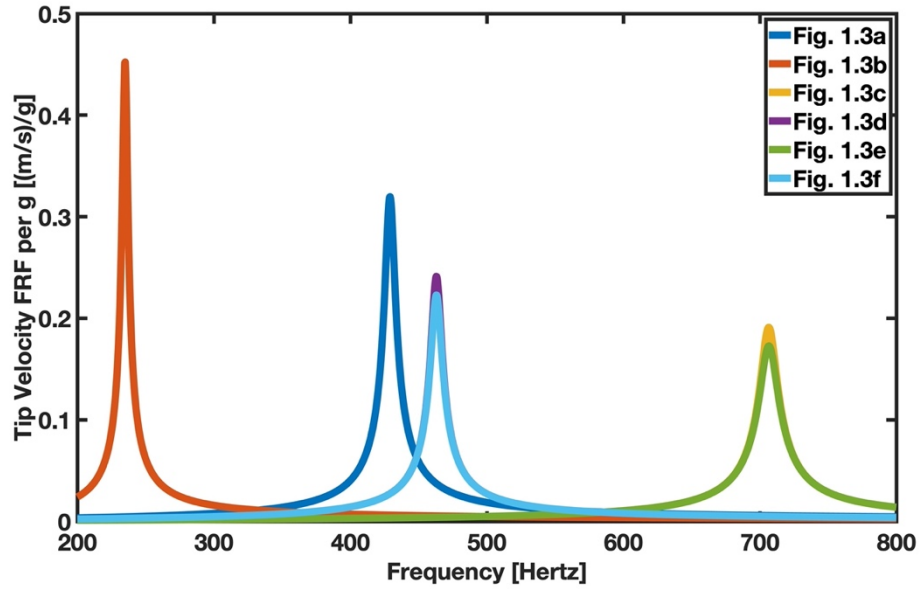
Tip Velocity FRF per g [(m/s)/g]
Frequency [Hertz]
Fig. 1.3a
Fig. 1.3b
Fig. 1.3c
Fig. 1.3d
Fig. 1.3e
Fig. 1.3f

(b)

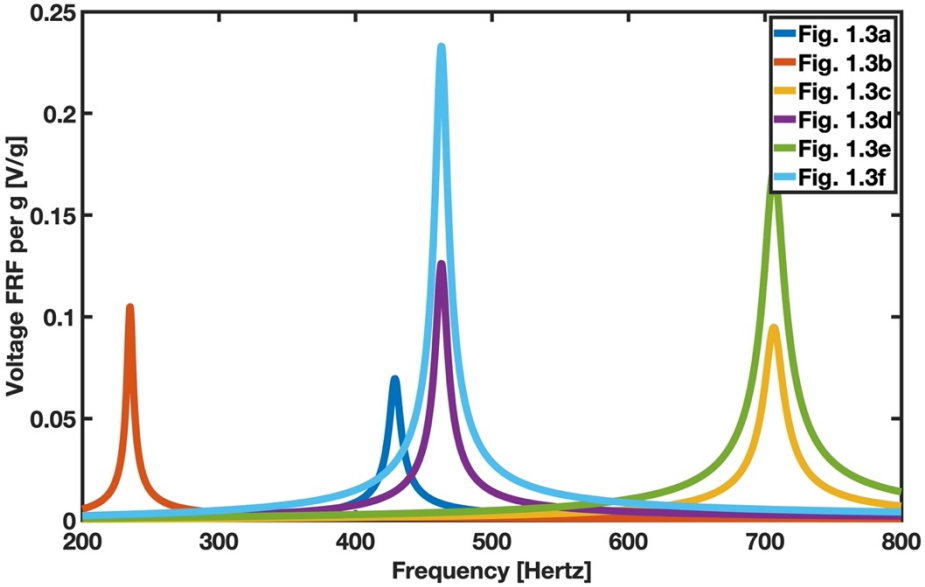
Voltage FRF per g [V/g]
Frequency [Hertz]
Fig. 1.3a
Fig. 1.3b
Fig. 1.3c
Fig. 1.3d
Fig. 1.3e
Fig. 1.3f

(c)

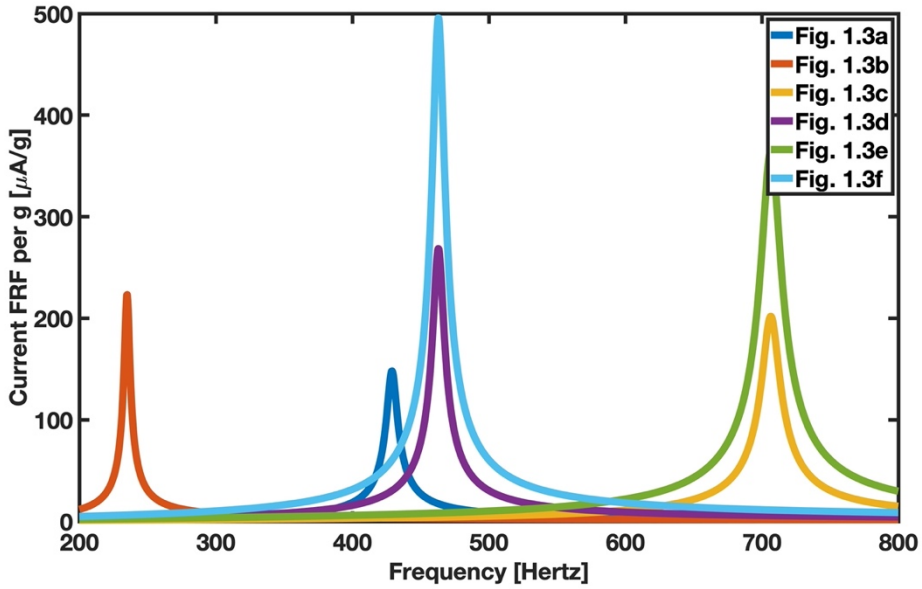

(d)

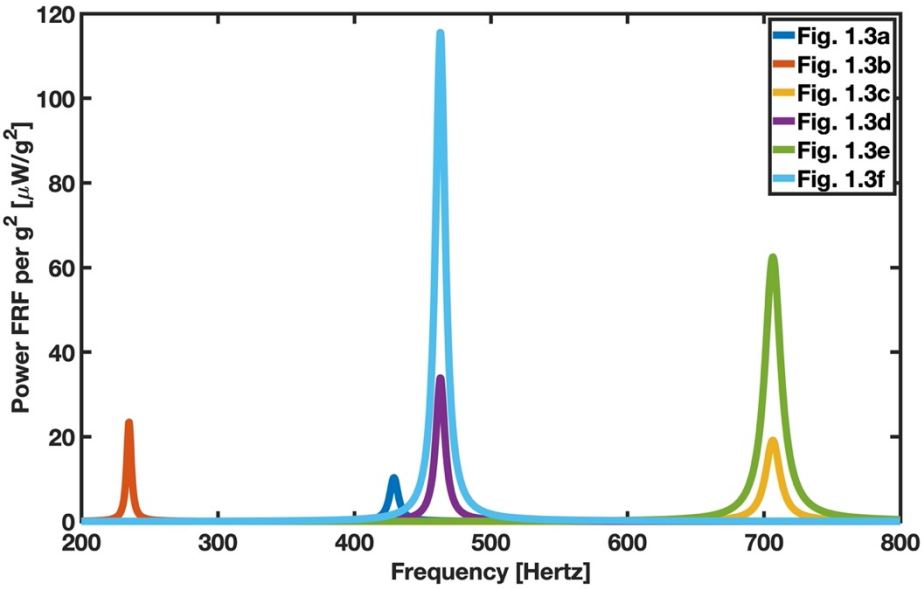

Figure 4.15 Output FRFs of the PEH cantilever in terms of (a) tip displacement, (b) voltage, (c) current, and (d) power for six configurations depicted in Figure 1.3.

The system may be connected in either series or parallel without changing the fundamental frequency. The natural frequency is reduced when the tip mass and the PEH are combined. In the unimorph structure, the lowest natural frequency value is seen. The voltage, current, and power output are at their maximum levels in the bimorph structure, even though the beams in the unimorph state exhibit enormous

vibration in the resonance state. The parallel-connected form without tip mass has the lowest vibration response, whereas the unimorph tip mass-added structure has the maximum values. In order to get the most significant electrical outputs, it makes the most sense to employ a parallel-connected PEH with tip mass. The FRF values grow when tip mass is added. The electrical responses are increased when a bimorph arrangement is used. Additionally, employing parallel connections yields higher outcomes. An alternative to the series-connected no-tip mass design can be a structure with an unimorph tip mass attached.

4.2.1.2.4 Material Structure Change

The FG and homogeneous series-connected C-F PEH without tip mass structures are compared using steady-state response FRFs. In other words, the structures of Figure 4.1 and Figure 4.2b are examined. The analysis's load resistance is 470 Ω, and the FG configuration's k value is 0.5. Figure 4.16 displays the plots utilized to assess the vibrational and electrical properties.

(a)

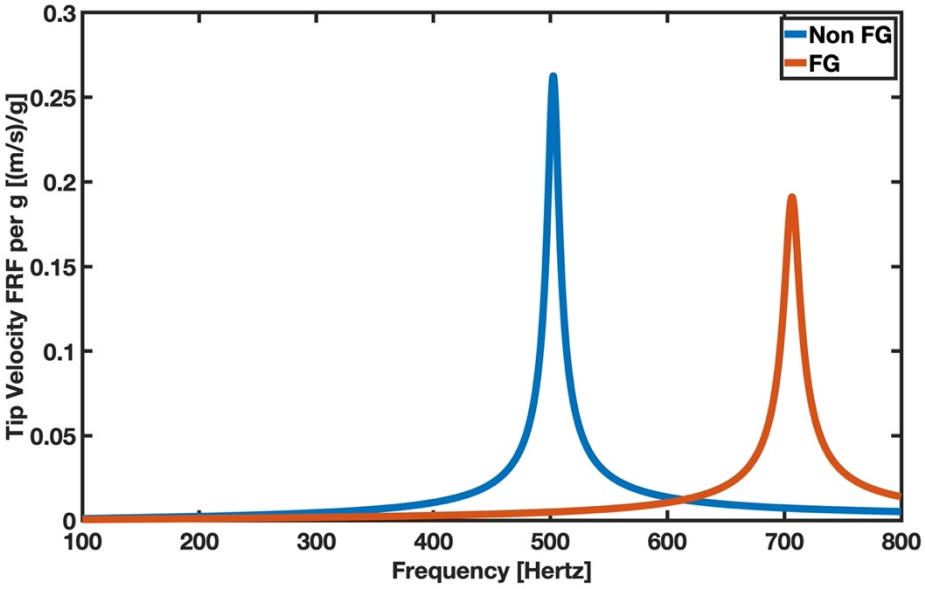

(b)

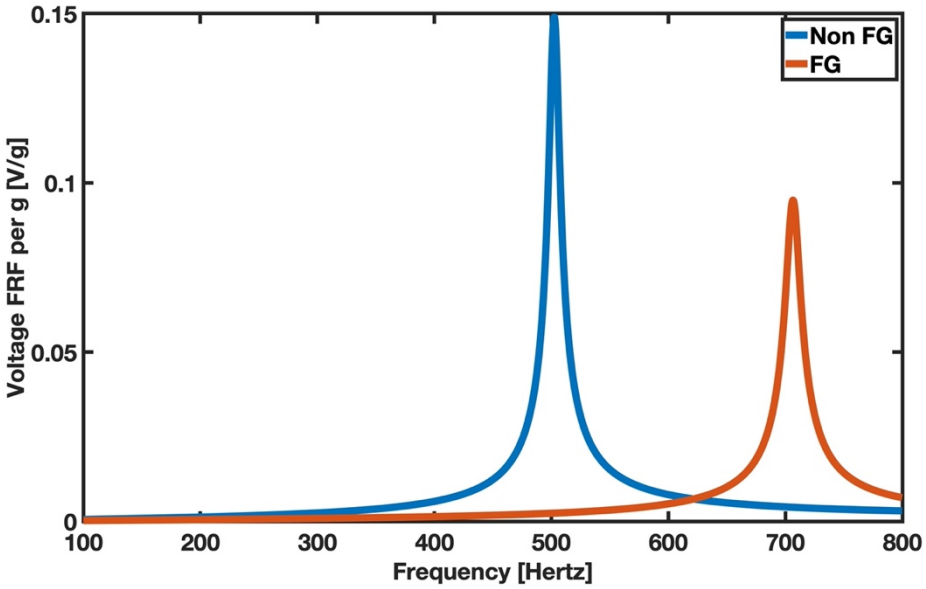
0.15
0.1
0.05
0
Voltage FRF per g [V/g]
100
200
300
400
500
600
700
800
Frequency [Hertz]
Non FG
FG

(c)

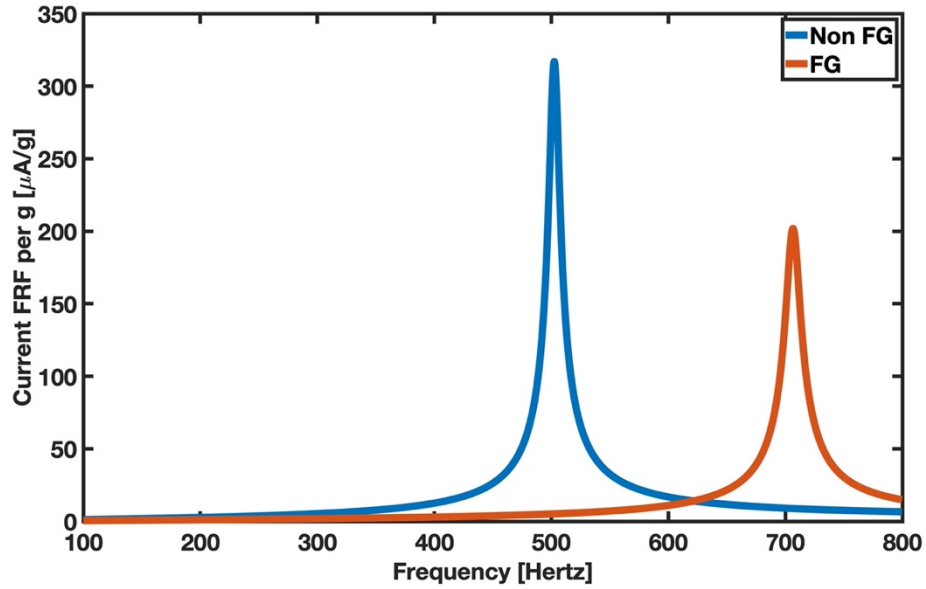
350
300
250
200
150
100
50
0
Current FRF per g [μA/g]
100
200
300
400
500
600
700
800
Frequency [Hertz]
Non FG
FG

(d)

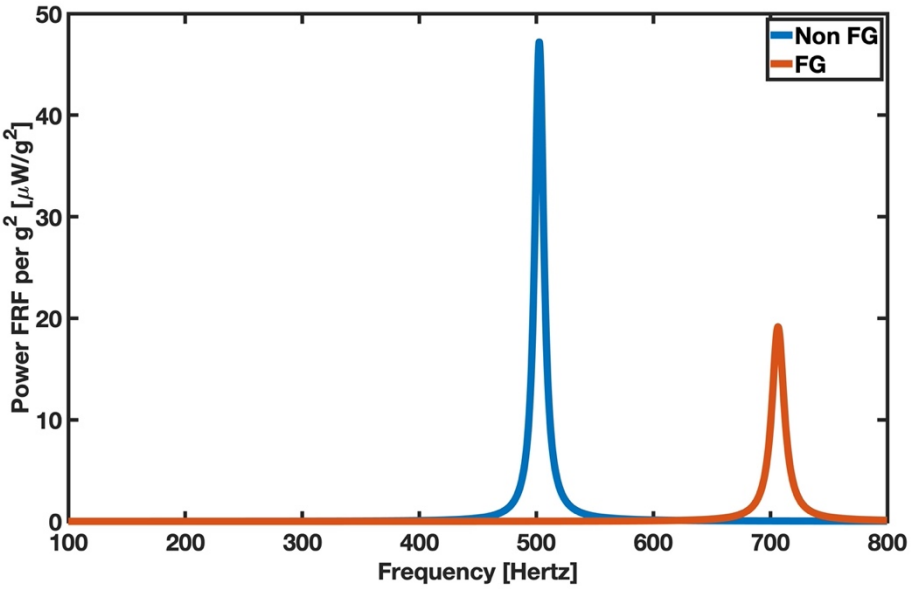

Figure 4.16 Output FRFs of the PEH cantilever in terms of (a) tip displacement, (b) voltage, (c) current, and (d) power for material structure change.

The material structure comparison findings demonstrate the significance of the materials used. As the tip displacement grows, so do the voltage, current, and power output. The major components in the power output include selecting the appropriate piezoelectric and substructure materials and precisely modifying the material structure in the transverse z direction. PZT-5A and aluminum lessen vibration response, and they have an adverse effect on electrical outcomes. However, the natural frequency is raised when PZT-5A and aluminum are used. Desired electrical results with the relevant properties can be obtained by selecting the suitable material.

4.2.2 Forced Vibration Convergence Study and Parametric Analysis

The forced vibration convergence study and parametric analysis are considered by applying the uniformly distributed step, concentrated step, concentrated harmonic, and concentrated impulsive loads. Base displacement is not applied because the applied forces' lean effect is investigated. The distributed, step and impulsive load intensities are stated as $f_0 = 10\,\mathrm{N/m}$, $F = 0.2\,\mathrm{N}$, and $\bar{F} = 0.00003\,\mathrm{N \cdot s}$, respectively. For concentrated harmonic load, the applied frequency ω_p is 600 Hz.

The step, harmonic and impulsive loads are applied at the beam's midpoint $x_0 = L/2$. The time step for all load computations is $1 \cdot (10)^{-6}$ s. For concentrated impulsive load, t_0, and t_1 are defined as $1 \cdot (10)^{-5}$ s, and $2 \cdot (10)^{-5}$ s, respectively. The load resistance R_l is taken as 470 Ω.

4.2.2.1 Forced Vibration Convergence Study

For the forced vibration response, a convergence study is also performed. The series-connected FG Timoshenko PEH beam without tip mass is subjected to specified loads, and their dynamic response is shown in Figure 4.17. The midpoint displacement $w(L/2, t)$ with respect to time is presented for four different values of the node number N. The boundary condition is determined as C-F, and the power-law exponent is specified as $k = 0.5$.

(a)

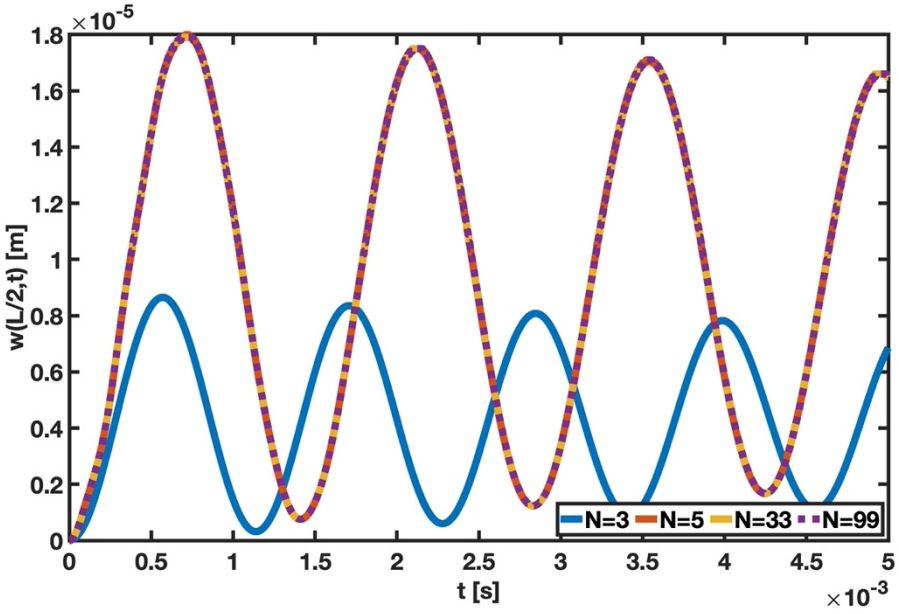

(b)

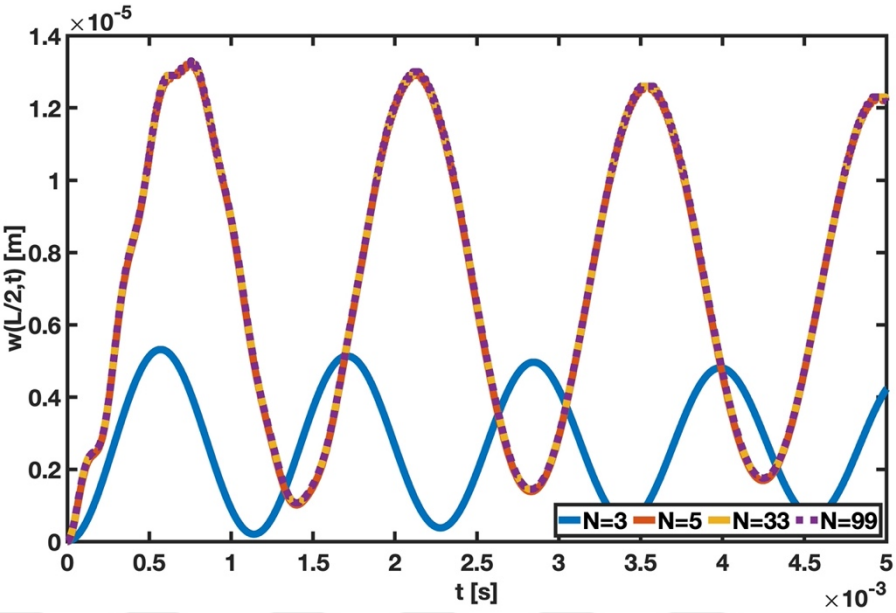
×10^-5
1.4
1.2
1
0.8
0.6
0.4
0.2
0
w(L/2,t) [m]
0
0.5
1
1.5
2
2.5
3
3.5
4
4.5
5
t [s]
×10^-3
N=3
N=5
N=33
N=99

(c)

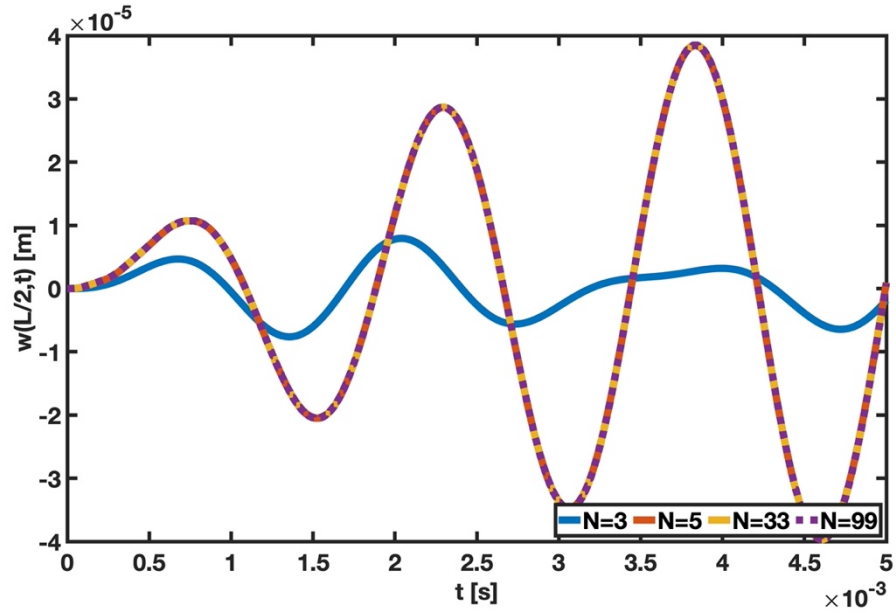
×10^-5
4
3
2
1
0
-1
-2
-3
-4
w(L/2,t) [m]
0
0.5
1
1.5
2
2.5
3
3.5
4
4.5
5
t [s]
×10^-3
N=3
N=5
N=33
N=99

(d)

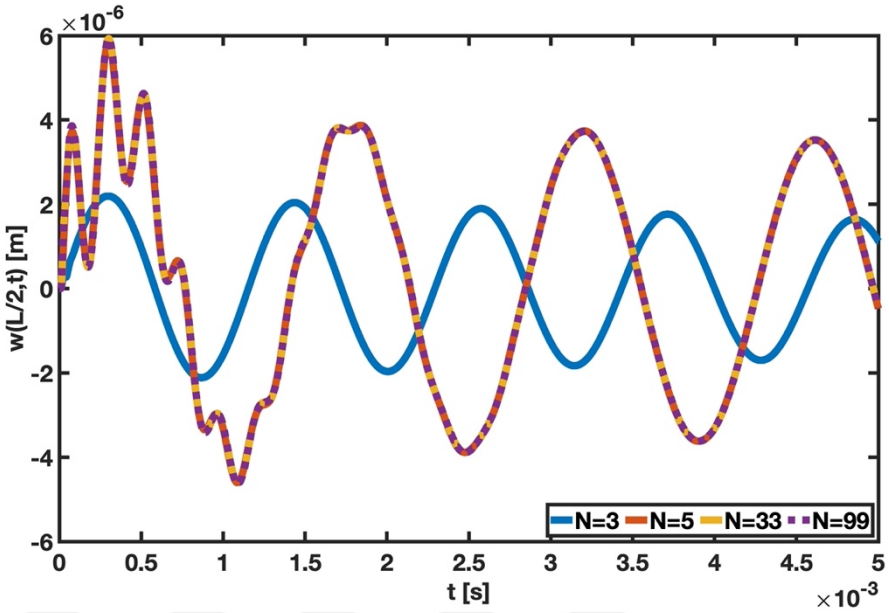

Figure 4.17 Convergence analysis of a C-F FG Timoshenko PEH beam under (a) uniformly distributed step loading, (b) concentrated step loading, (c) concentrated harmonic loading, and (d) concentrated impulsive loading for power-law exponent $k = 0.5$.

The midpoint deviations and percentage changes over time for four load types are shown in

Table 4-11, Table 4-12, Table 4-13, and Table 4-14 to determine the exact number of nodes at which convergence occurs. It proves that the convergence for all loading types is reached to a great extent at $N = 5$. All the solutions are acquired rapidly because fewer nodes are used, and a minimal mass, stiffness, damping, voltage, and force matrix is generated. Table 4-10 displays CPU times using MATLAB R2023a for all force types.

Table 4-10 Forced vibration convergence study CPU time in seconds for all load types affected C-F FG Timoshenko PEH beam without tip mass using power-law exponent $k = 0.5$.

Load Type	**N**			
	3	**5**	**33**	**99**
Uniformly Distributed Step Load	0.94 s	1.45 s	31.64 s	333.05 s
Concentrated Step Load	0.85 s	1.34 s	34.10 s	300.80 s
Concentrated Harmonic Load	0.76 s	1.13 s	25.28 s	224.55 s
Concentrated Impulsive Load	0.84 s	1.49 s	42.03 s	373.61 s

The percent difference PD is an absolute calculation of the displacement difference between two successive node values. For example, for $N = 5$, the percent difference is determined as follows:

$$PD = \frac{|w(\text{for } N = 5) - w(\text{for } N = 3)|}{|w(\text{for } N = 3)|} \cdot 100 \tag{4-22}$$

Table 4-11 Displacement w(L/2, t) in mm and percent differences calculated for a uniformly distributed step-loaded C-F FG Timoshenko PEH beam. f_0 = 10 N/m, k = 0.5, and R_l = 470 Ω.

t [ms]	**N**			
	3	**5**	**33**	**99**
0.5	w = 0.0083	w = 0.0145	w = 0.0145	w = 0.0145
		PD = 73.6	PD = 0.1	PD = 0
1.0	w = 0.0015	w = 0.0117	w = 0.0117	w = 0.0117
		PD = 698.9	PD = 0.1	PD = 0
1.5	w = 0.0060	w = 0.0014	w = 0.0014	w = 0.0014
		PD = 77.2	PD = 0.2	PD = 0
2.0	w = 0.0043	w = 0.0163	w = 0.0163	w = 0.0163
		PD = 279.1	PD = 0.1	PD = 0
2.5	w = 0.0031	w = 0.0085	w = 0.0085	w = 0.0085
		PD = 174.4	PD = 0.3	PD = 0
3.0	w = 0.0069	w = 0.0034	w = 0.0034	w = 0.0034
		PD = 50.8	PD = 0.5	PD = 0
3.5	w = 0.0012	w = 0.0170	w = 0.0169	w = 0.0169
		PD = 1271.4	PD = 0.1	PD = 0
4.0	w = 0.0078	w = 0.0058	w = 0.0058	w = 0.0058
		PD = 25.6	PD = 0.6	PD = 0
4.5	w = 0.0013	w = 0.0060	w = 0.0059	w = 0.0059
		PD = 371.7	PD = 0.6	PD = 0
5.0	w = 0.0069	w = 0.0165	w = 0.0165	w = 0.0165
		PD = 140.3	PD = 0	PD = 0

Table 4-12 Displacement w(L/2, t) in mm and percent differences calculated for a concentrated step-loaded C-F FG Timoshenko PEH beam. F = 0.2 N, k = 0.5, R_l = 470 Ω, and x_0 = L/2.

t [ms]	**N**			
	3	**5**	**33**	**99**
0.5	w = 0.0051	w = 0.0107	w = 0.0107	w = 0.0107
		PD = 108.3	PD = 0.3	PD = 0
1.0	w = 0.0009	w = 0.0089	w = 0.0090	w = 0.0090
		PD = 878.4	PD = 0.7	PD = 0
1.5	w = 0.0037	w = 0.0015	w = 0.0016	w = 0.0016
		PD = 59.0	PD = 4.5	PD = 0
2.0	w = 0.0026	w = 0.0120	w = 0.0121	w = 0.0121
		PD = 354.8	PD = 0.4	PD = 0
2.5	w = 0.0019	w = 0.0065	w = 0.0066	w = 0.0066
		PD = 241.1	PD = 1.1	PD = 0
3.0	w = 0.0042	w = 0.0029	w = 0.0029	w = 0.0029
		PD = 31.4	PD = 1.5	PD = 0
3.5	w = 0.0008	w = 0.0125	w = 0.0126	w = 0.0126
		PD = 1531.1	PD = 0.4	PD = 0
4.0	w = 0.0048	w = 0.0046	w = 0.0047	w = 0.0047
		PD = 3.8	PD = 1.8	PD = 0
4.5	w = 0.0008	w = 0.0047	w = 0.0048	w = 0.0048
		PD = 502.9	PD = 0.7	PD = 0
5.0	w = 0.0042	w = 0.0122	w = 0.0122	w = 0.0122
		PD = 188.6	PD = 0.5	PD = 0

Table 4-13 Displacement w(L/2, t) in mm and percent differences calculated for a concentrated harmonic-loaded C-F FG Timoshenko PEH beam. F = 0.2 N, k = 0.5, $R_l = 470\ \Omega$, $\omega_p = 600$ Hz and $x_0 = L/2$.

t [ms]	**N**			
	3	**5**	**33**	**99**
0.5	$w = 0.0035$	$w = 0.0068$	$w = 0.0069$	$w = 0.0069$
		$PD = 96.3$	$PD = 0.7$	$PD = 0$
1.0	$w = -0.0005$	$w = 0.0048$	$w = 0.0047$	$w = 0.0047$
		$PD = 1026.8$	$PD = 0.8$	$PD = 0$
1.5	$w = -0.0060$	$w = -0.0204$	$w = -0.0204$	$w = -0.0204$
		$PD = 239.0$	$PD = 0.1$	$PD = 0$
2.0	$w = 0.0078$	$w = 0.0117$	$w = 0.0117$	$w = 0.0117$
		$PD = 49.5$	$PD = 0.2$	$PD = 0$
2.5	$w = -0.0026$	$w = 0.0188$	$w = 0.0188$	$w = 0.0188$
		$PD = 826.9$	$PD = 0.1$	$PD = 0$
3.0	$w = -0.0028$	$w = -0.0336$	$w = -0.0336$	$w = -0.0336$
		$PD = 1095.4$	$PD = 0.1$	$PD = 0$
3.5	$w = 0.0017$	$w = 0.0088$	$w = 0.0088$	$w = 0.0088$
		$PD = 412.1$	$PD = 0.4$	$PD = 0$
4.0	$w = 0.0032$	$w = 0.0299$	$w = 0.0300$	$w = 0.0300$
		$PD = 834.6$	$PD = 0.3$	$PD = 0$
4.5	$w = -0.0039$	$w = -0.0361$	$w = -0.0361$	$w = -0.0361$
		$PD = 825.0$	$PD = 0.1$	$PD = 0$
5.0	$w = -0.0018$	$w = 0.0009$	$w = 0.0008$	$w = 0.0008$
		$PD = 152.0$	$PD = 10.9$	$PD = 0$

Table 4-14 Displacement w(L/2, t) in mm and percent differences calculated for a concentrated impulsively-loaded C-F FG Timoshenko PEH beam. $\bar{F}$ = 0.00003 N·s, k = 0.5, R_l = 470 Ω, $t_0 = 1\cdot(10)^{-5}$ s, $t_1 = 2\cdot(10)^{-5}$ s, and x_0 = L/2.

t [ms]	**N**			
	3	**5**	**33**	**99**
0.5	$w = 0.0010$	$w = 0.0045$	$w = 0.0045$	$w = 0.0045$
		$PD = 364.4$	$PD = 0.1$	$PD = 0$
1.0	$w = -0.0016$	$w = -0.0033$	$w = -0.0033$	$w = -0.0033$
		$PD = 111.0$	$PD = 2.1$	$PD = 0$
1.5	$w = 0.0019$	$w = 0.0011$	$w = 0.0012$	$w = 0.0012$
		$PD = 41.1$	$PD = 2.6$	$PD = 0$
2.0	$w = -0.0020$	$w = 0.0021$	$w = 0.0021$	$w = 0.0021$
		$PD = 207.6$	$PD = 0.1$	$PD = 0$
2.5	$w = 0.0017$	$w = -0.0039$	$w = -0.0039$	$w = -0.0039$
		$PD = 321.7$	$PD = 0.3$	$PD = 0$
3.0	$w = -0.0013$	$w = 0.0024$	$w = 0.0024$	$w = 0.0024$
		$PD = 288.2$	$PD = 0.7$	$PD = 0$
3.5	$w = 0.0007$	$w = 0.0009$	$w = 0.0009$	$w = 0.0009$
		$PD = 31.7$	$PD = 2.1$	$PD = 0$
4.0	$w = 0.0000$	$w = -0.0033$	$w = -0.0033$	$w = -0.0033$
		$PD = 151442.8$	$PD = 0$	$PD = 0$
4.5	$w = -0.0006$	$w = 0.0031$	$w = 0.0031$	$w = 0.0031$
		$PD = 591.0$	$PD = 0.4$	$PD = 0$
5.0	$w = 0.0011$	$w = -0.0005$	$w = -0.0005$	$w = -0.0005$
		$PD = 142.4$	$PD = 4.5$	$PD = 0$

4.2.2.2 Forced Vibration Parametric Analysis

Forced vibration parametric analysis is used to investigate the power-law exponent, tip mass addition, PEH layout, boundary condition, and material structure change effect. Investigations are conducted by examining the midpoint displacement, the midpoint axial stress on the top surface of the substructure, the midpoint axial stress on the lower surface of the upper piezoelectric material, and the voltage difference, current, and power generated between the electrodes. The node number N is taken as 21. Load resistance is equal to 470 Ω.

4.2.2.2.1 Power-Law Exponent Change

Dynamic analytical results are produced to study the impact of the power-law exponent modification. Series-connected bimorph FG Timoshenko PEH beam without tip mass configuration is investigated. There are five different values of k, ranging from zero to two. The response values under a uniformly distributed step load are shown in Figure 4.18.

(a)

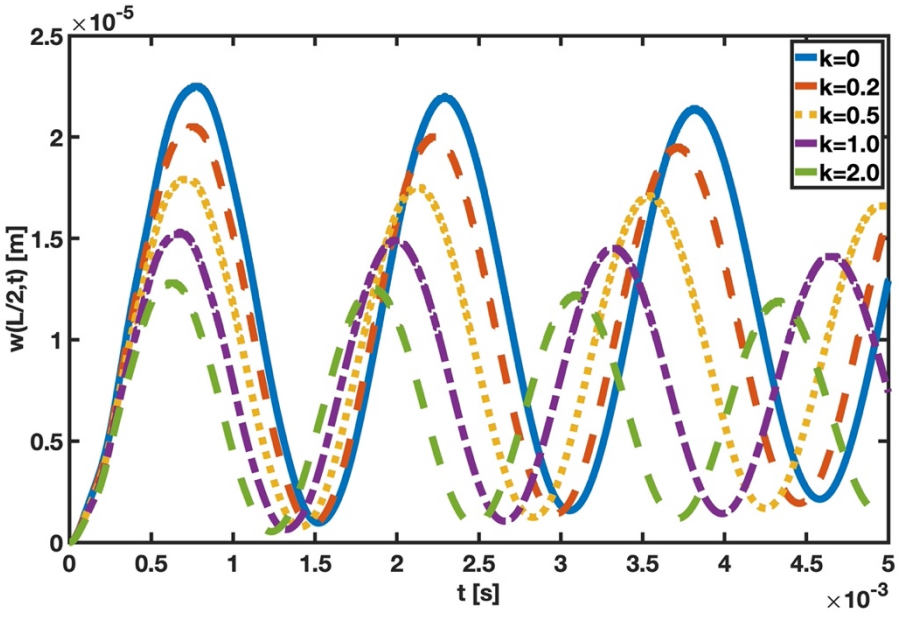

(b)

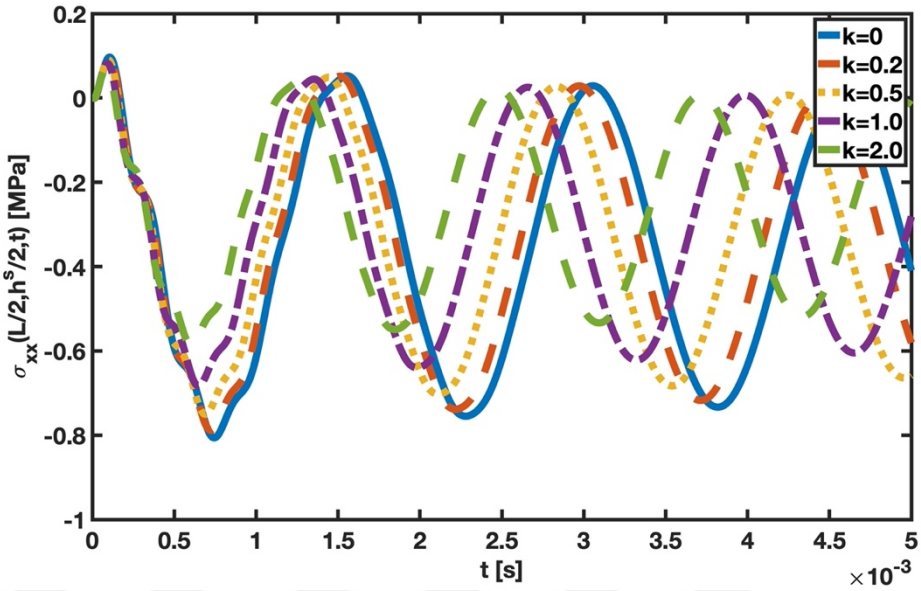
k=0
k=0.2
k=0.5
k=1.0
k=2.0
$\sigma_{xx}(L/2,h^s/2,t)$ [MPa]
t [s]
$\times 10^{-3}$

(c)

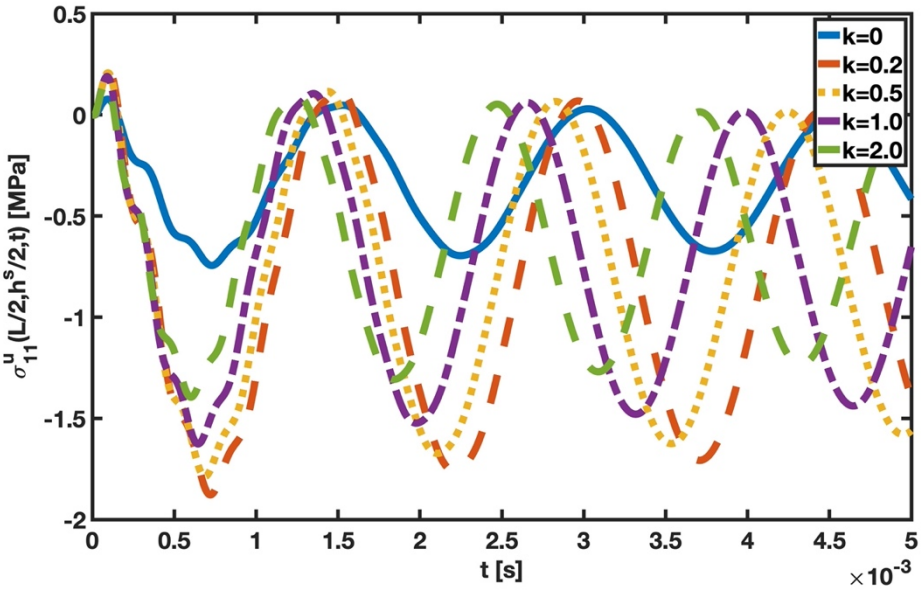
k=0
k=0.2
k=0.5
k=1.0
k=2.0
$\sigma^u_{11}(L/2,h^s/2,t)$ [MPa]
t [s]
$\times 10^{-3}$

(d)

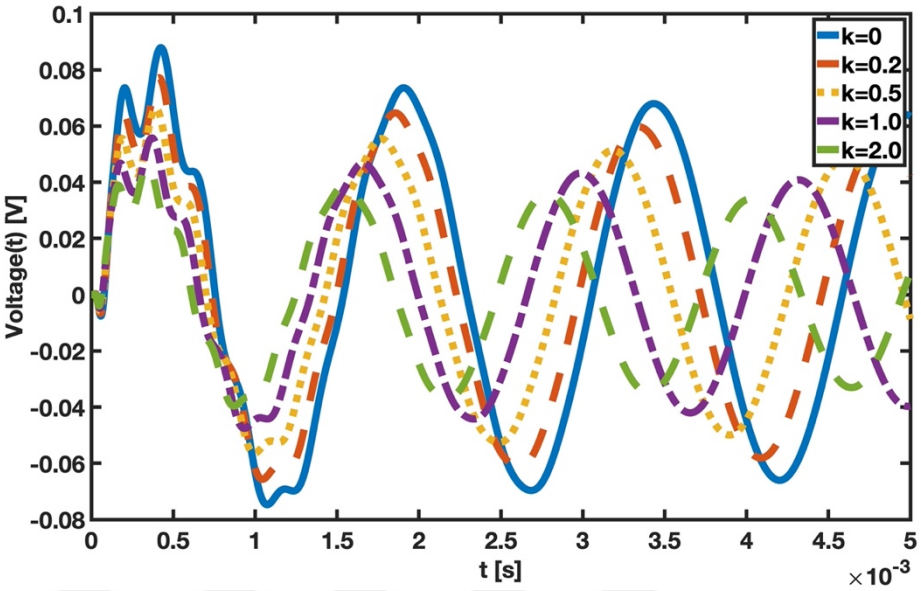
Voltage(t) [V]
t [s]
×10^-3
k=0
k=0.2
k=0.5
k=1.0
k=2.0

(e)

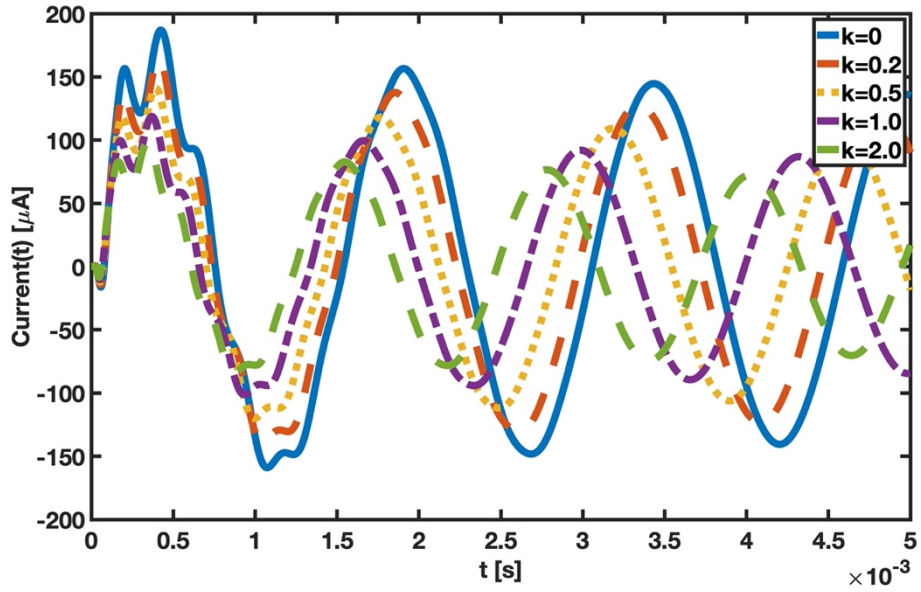
Current(t) [μA]
t [s]
×10^-3
k=0
k=0.2
k=0.5
k=1.0
k=2.0

(f)

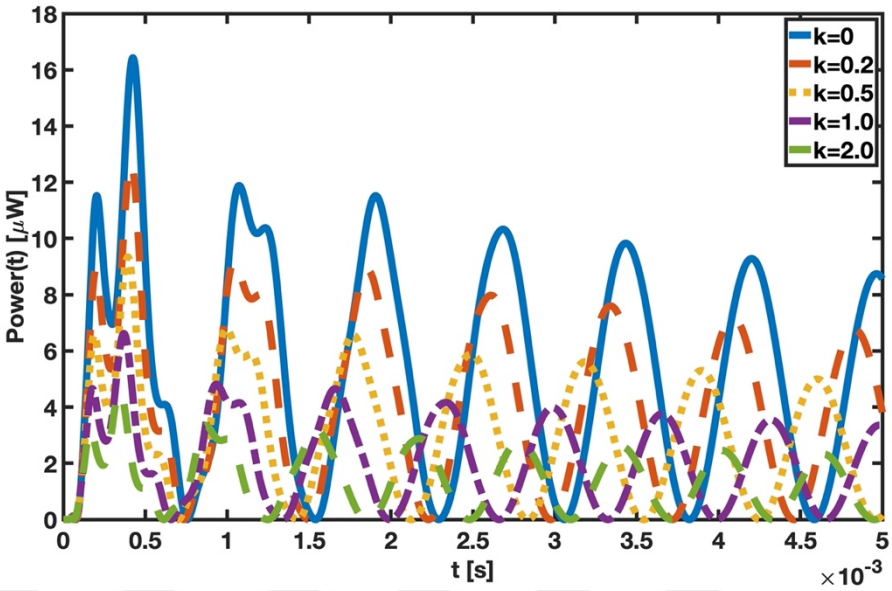

Figure 4.18 Dynamic behavior of a uniformly distributed step-loaded C-F series-connected bimorph FG Timoshenko PEH beam without tip mass configuration for different power-law exponent in terms of (a) midpoint displacement, (b) midpoint and top surface axial stress of the substructure, (c) midpoint and bottom surface axial stress of the upper piezoelectric material, (d) output voltage difference between electrodes, (e) produced current on the system, and (f) generated power.

Assigning the beam's reaction to a single reason is inaccurate because its behavior depends on various factors. The critical elements are the geometric structure and the qualities of the materials. As the power-law exponent rises, it is seen that the displacement and voltage, current, and power output decrease. The increase in the frequency of the outputs is noticeable when k rises. Also, the continuous reduction of the response magnitude at each wavelength aids in understanding the damping effect. The outcomes slowly decline after reaching their peak magnitude in the first two wavelengths. The axial stress of the upper piezoelectric material's bottom surface is lowest when $k = 0$, an unexpected observation of Figure 4.18c. The axial stress value is expected to rise as the k value falls. However, when $k = 0$, the decrease in $\bar{e}_{31}$ and $\bar{c}_{11}^{E}$ exceeds the increase in v_b^s. Finally, different Lame coefficients μ^s and λ^s cause the variation between Figure 4.18b and Figure 4.18c. The outcomes of the concentrated step load are displayed in Figure 4.19.

(a)

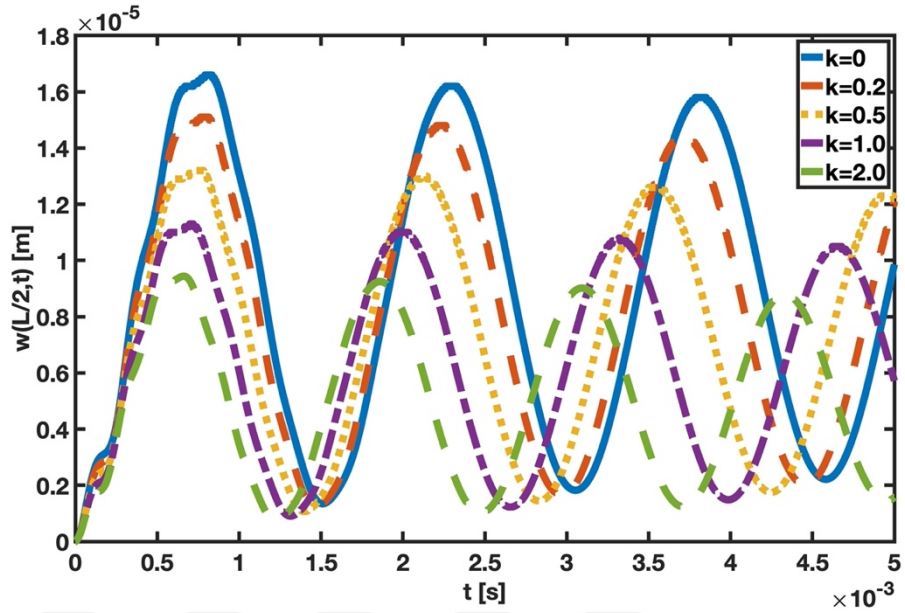
×10^-5
1.8
1.6
1.4
1.2
1
0.8
0.6
0.4
0.2
0
w(L/2,t) [m]
0
0.5
1
1.5
2
2.5
3
3.5
4
4.5
5
t [s]
×10^-3
k=0
k=0.2
k=0.5
k=1.0
k=2.0

(b)

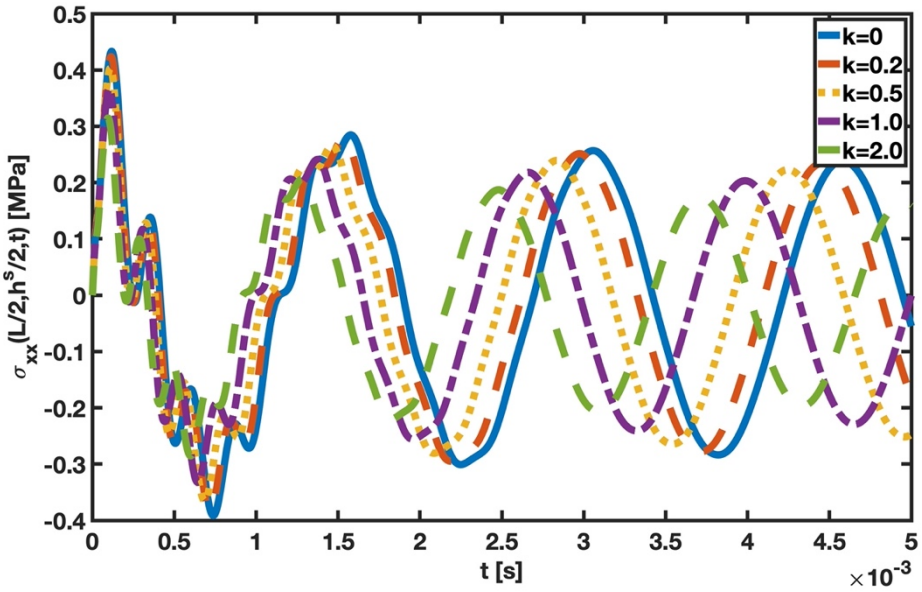
0.5
0.4
0.3
0.2
0.1
0
-0.1
-0.2
-0.3
-0.4
σxx(L/2,hs/2,t) [MPa]
0
0.5
1
1.5
2
2.5
3
3.5
4
4.5
5
t [s]
×10^-3
k=0
k=0.2
k=0.5
k=1.0
k=2.0

(c)

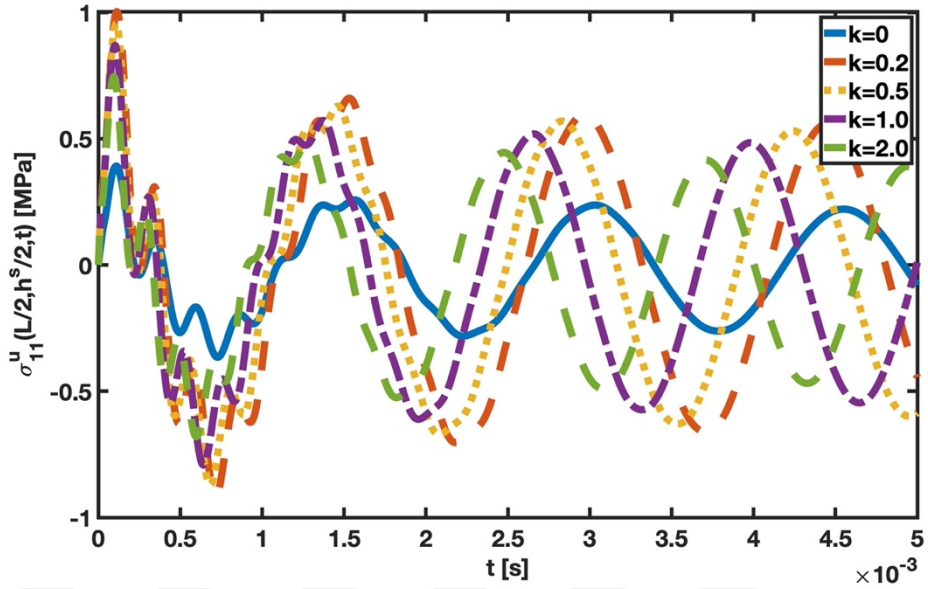
k=0
k=0.2
k=0.5
k=1.0
k=2.0
$\sigma_{11}^{u}(L/2,h^{s}/2,t)$ [MPa]
t [s]
×10^-3

(d)

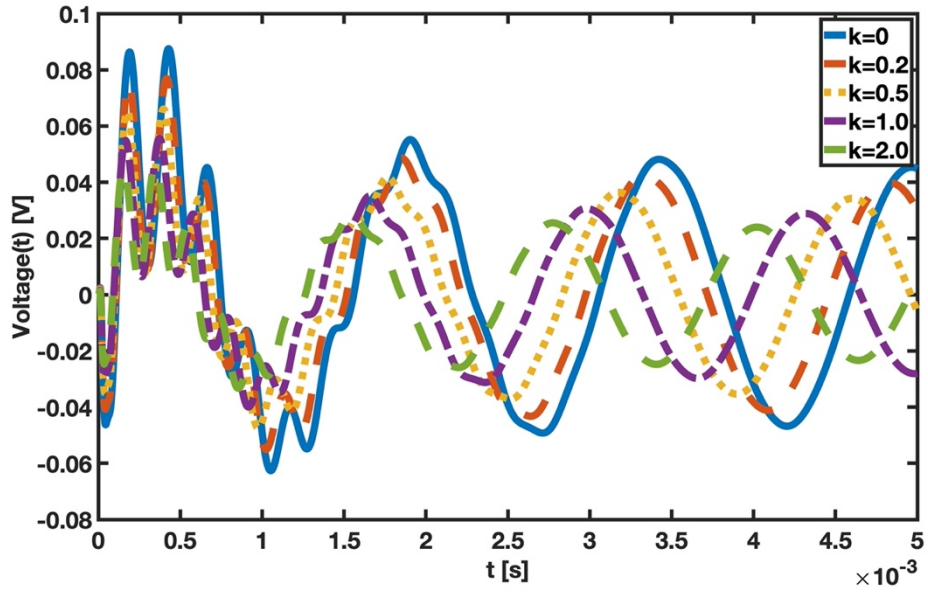
k=0
k=0.2
k=0.5
k=1.0
k=2.0
Voltage(t) [V]
t [s]
×10^-3

(e)

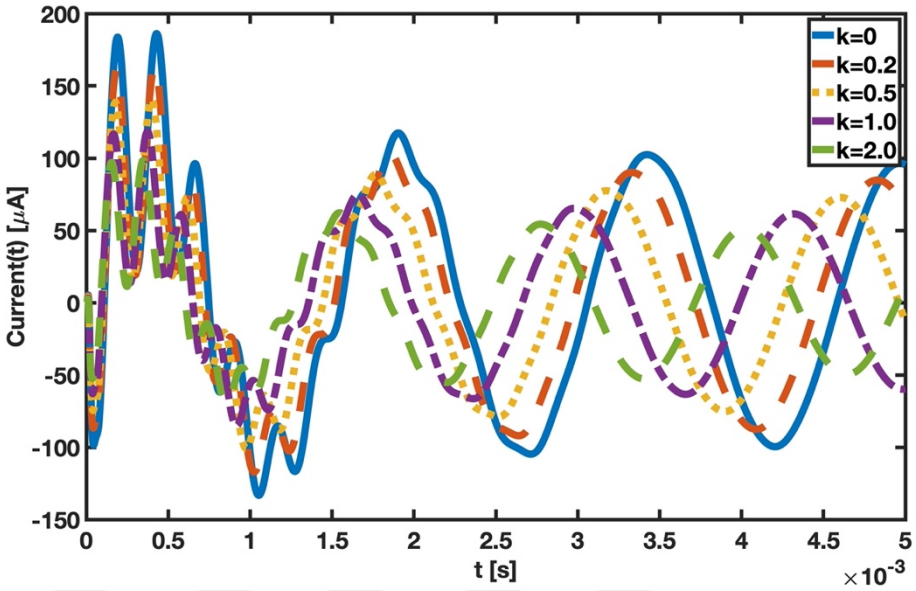

(f)

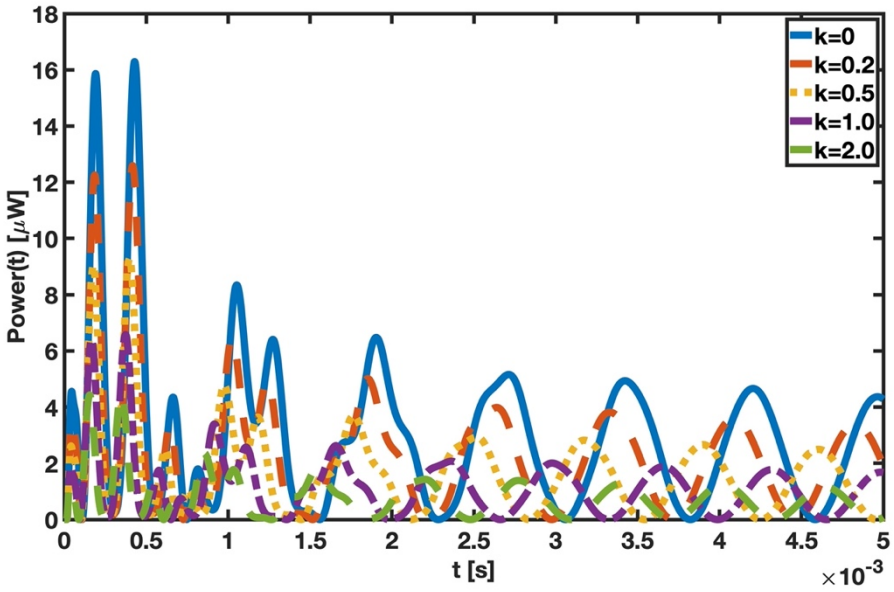

Figure 4.19 Dynamic behavior of a concentrated step-loaded C-F series-connected bimorph FG Timoshenko PEH beam without tip mass configuration for different power-law exponent in terms of (a) midpoint displacement, (b) midpoint and top surface axial stress of the substructure, (c) midpoint and bottom surface axial stress of the upper piezoelectric material, (d) output voltage difference between electrodes, (e) produced current on the system, and (f) generated power.

Applying a concentrated instantaneous load to the middle of the beam rather than distributing it makes a slight difference, so the results of Figure 4.18 also hold for step load. The voltage, current, and power outputs are found to rise as the transverse

displacement increases, indicating a direct relationship between them. Figure 4.20 shows the results of the concentrated harmonic load.

(a)

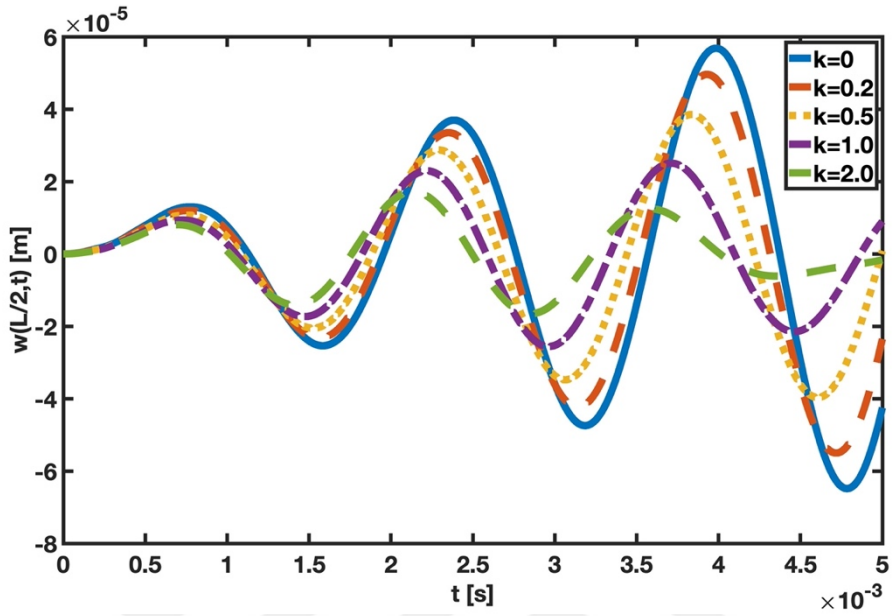

(b)

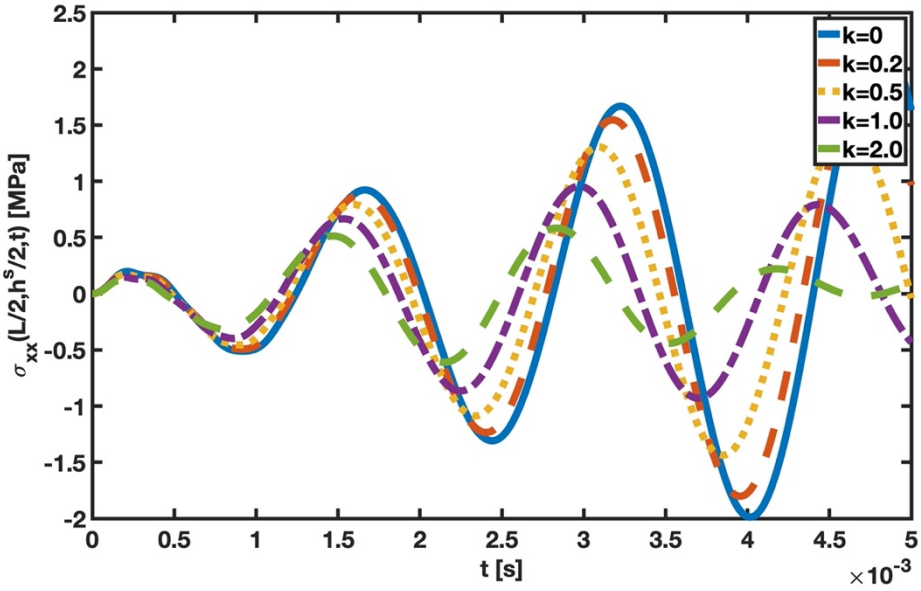

(c)

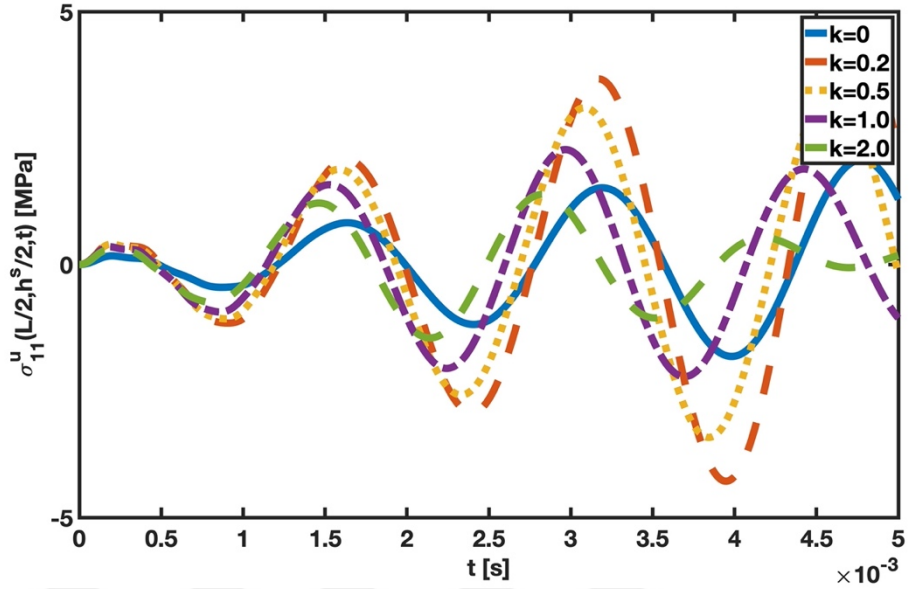
k=0
k=0.2
k=0.5
k=1.0
k=2.0
$\sigma_{11}^{u}(L/2,h^{s}/2,t)$ [MPa]
t [s]
×10^-3

(d)

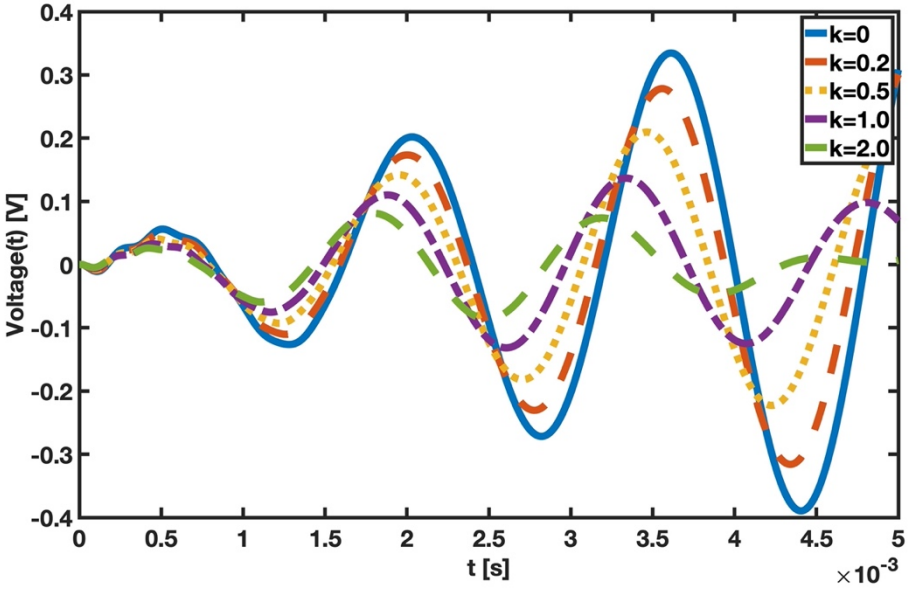
k=0
k=0.2
k=0.5
k=1.0
k=2.0
Voltage(t) [V]
t [s]
×10^-3

(e)

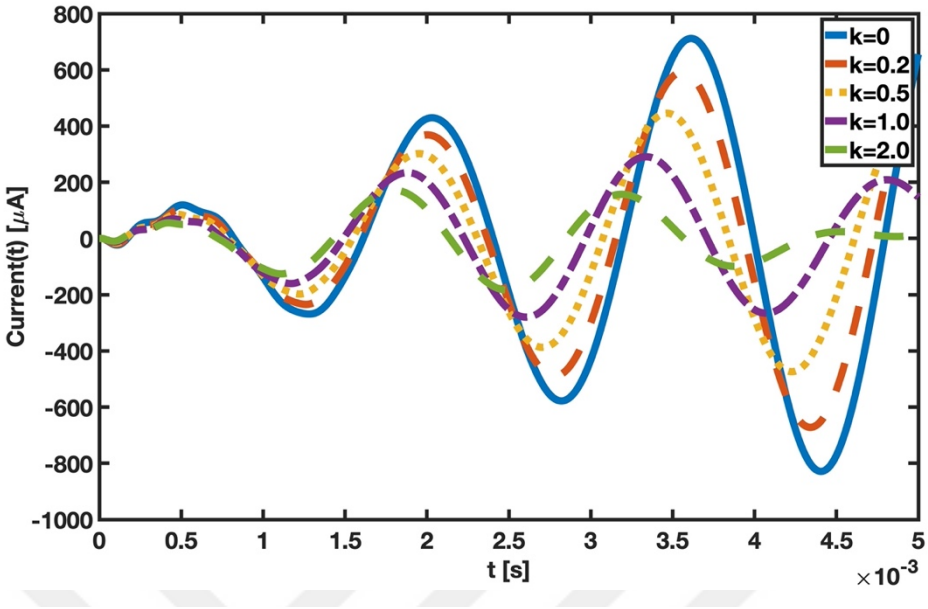

(f)

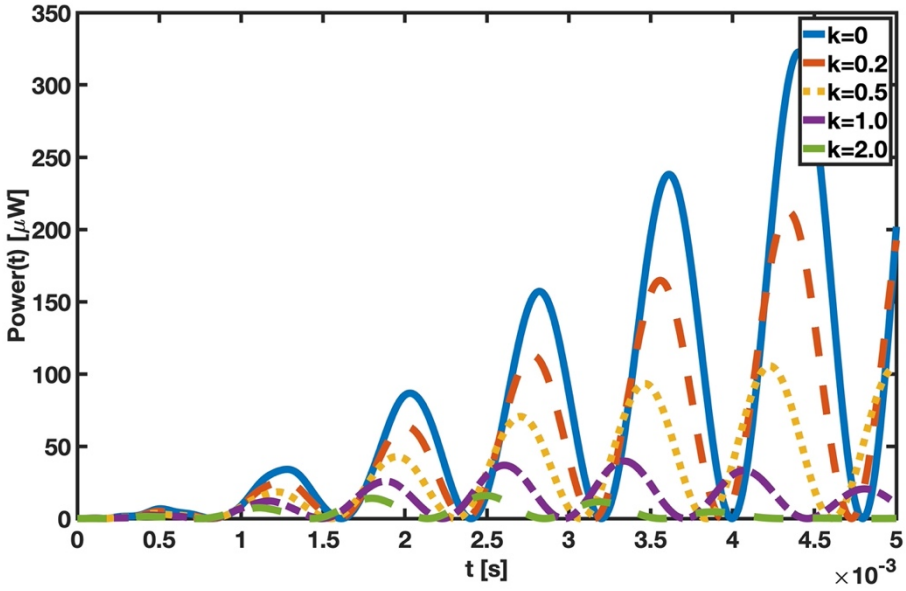

Figure 4.20 Dynamic behavior of a concentrated harmonic-loaded C-F series-connected bimorph FG Timoshenko PEH beam without tip mass configuration for different power-law exponent in terms of (a) midpoint displacement, (b) midpoint and top surface axial stress of the substructure, (c) midpoint and bottom surface axial stress of the upper piezoelectric material, (d) output voltage difference between electrodes, (e) produced current on the system, and (f) generated power.

In this type of load, the damping effect is observed as the k value increases. However, it is not adequate for $k = 0, 0.2$, and 0.5. In other words, the outputs rapidly diminish

at k = 1 and 2. The output values are not going to zero because the system is affected every time step with 600 Hz frequency. A reduction in transverse displacement, stress, voltage difference, current and power generation is also seen as the k value increases for the concentrated harmonic load. The effects of the concentrated impulsive load are depicted in Figure 4.21.

(a)

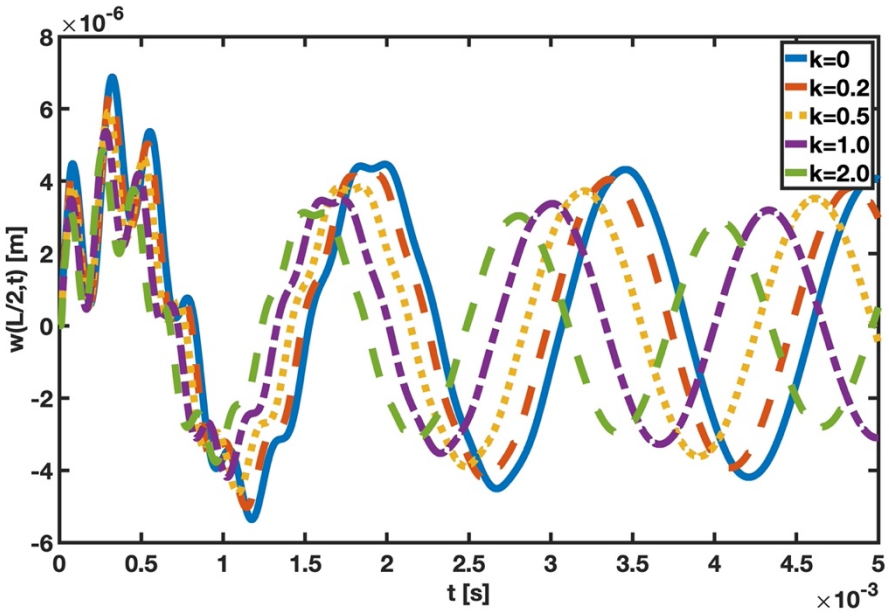

(b)

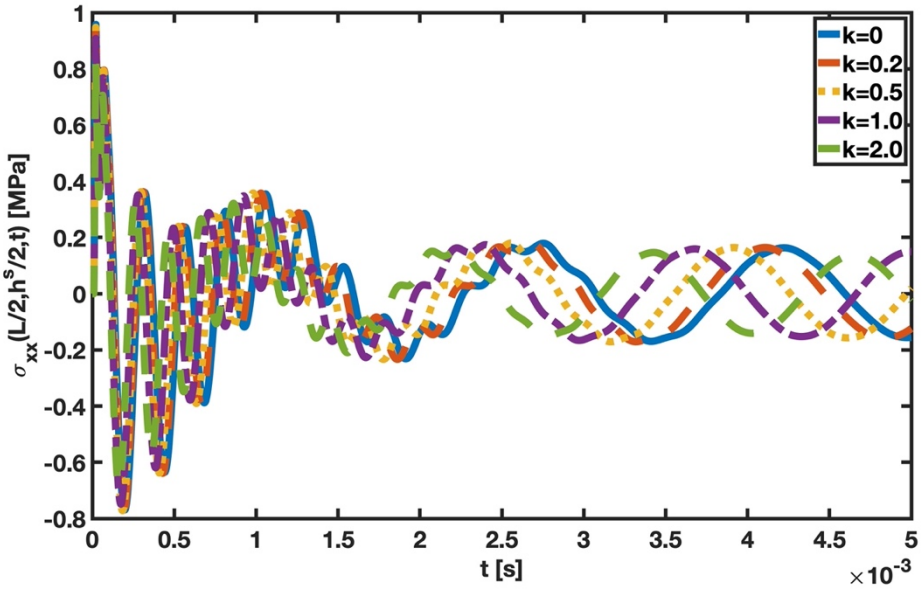

(c)

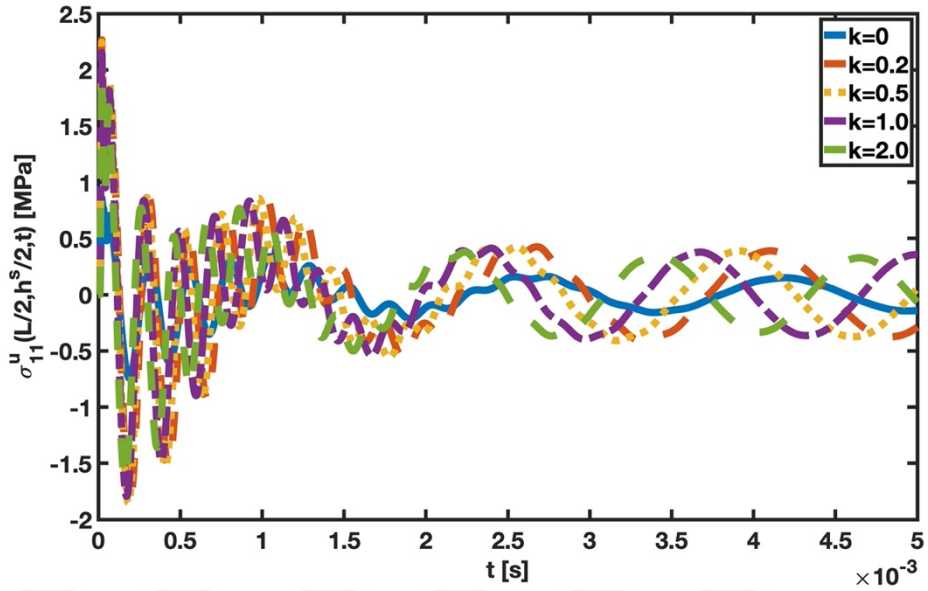
k=0
k=0.2
k=0.5
k=1.0
k=2.0
$\sigma_{11}^{u}(L/2,h^{s}/2,t)$ [MPa]
t [s]
×10^-3

(d)

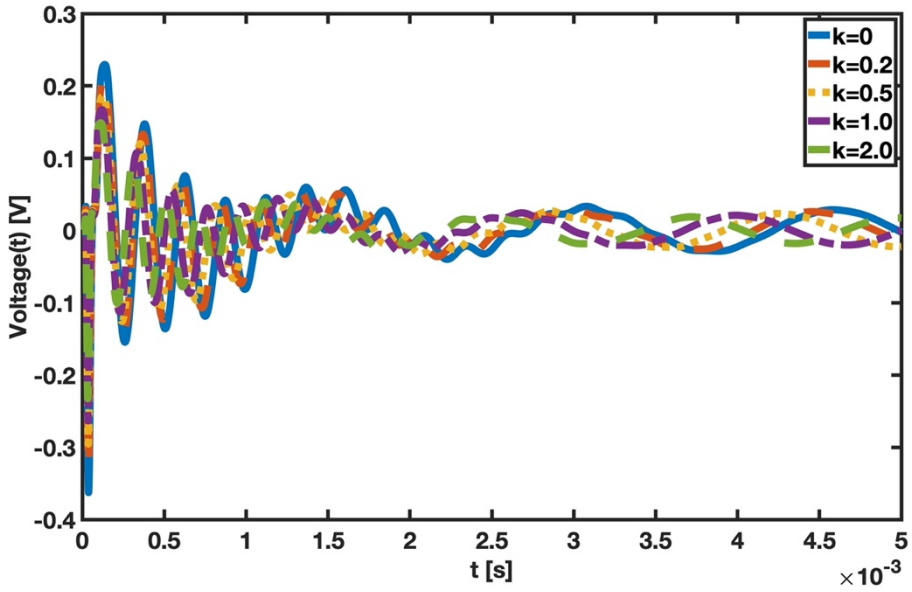
k=0
k=0.2
k=0.5
k=1.0
k=2.0
Voltage(t) [V]
t [s]
×10^-3

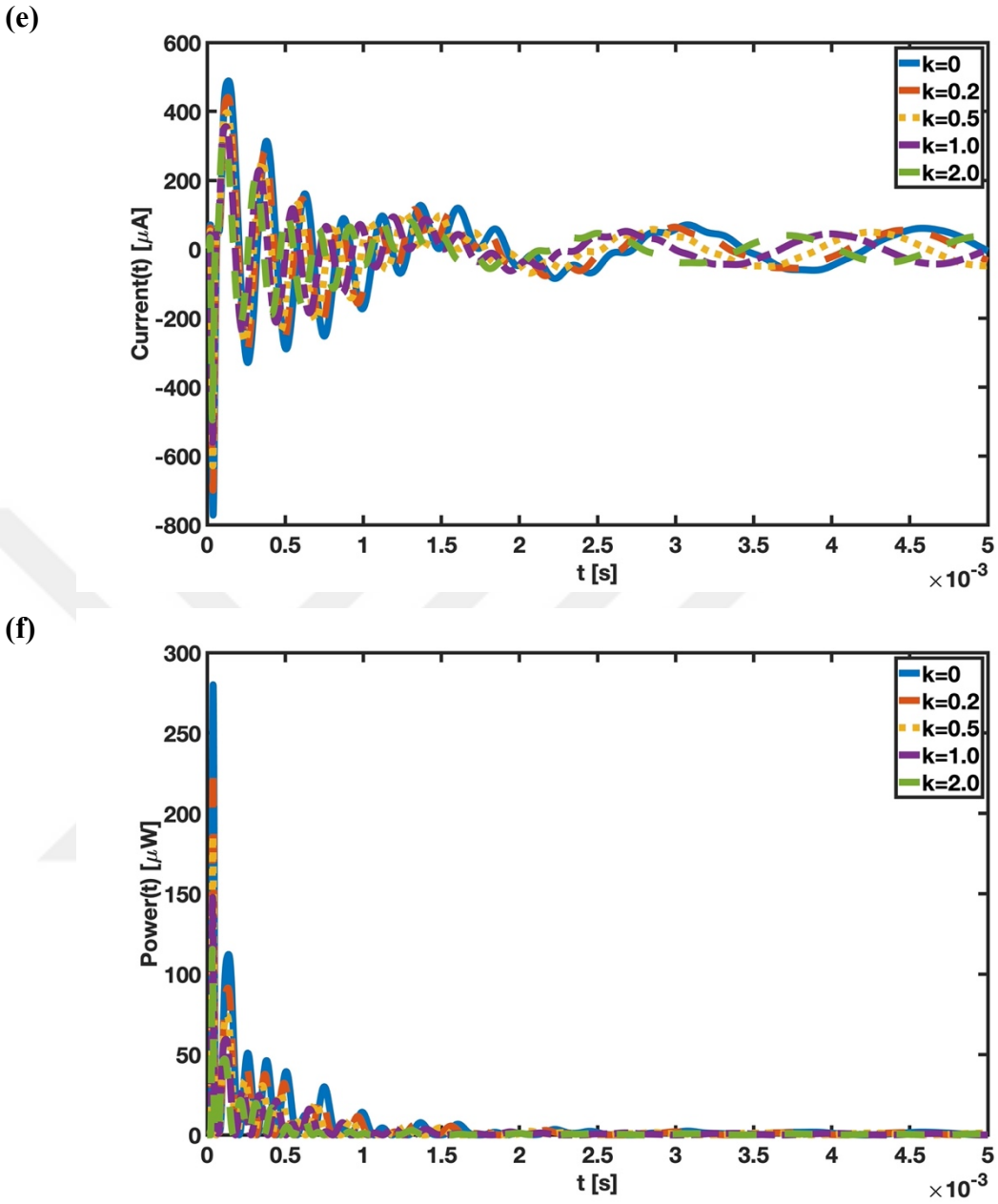

Figure 4.21 Dynamic behavior of a concentrated impulsive-loaded C-F series-connected bimorph FG Timoshenko PEH beam without tip mass configuration for different power-law exponent in terms of (a) midpoint displacement, (b) midpoint and top surface axial stress of the substructure, (c) midpoint and bottom surface axial stress of the upper piezoelectric material, (d) output voltage difference between electrodes, (e) produced current on the system, and (f) generated power.

The load is applied at the beginning of the application in a very brief period. The outputs exhibit variations close to $t = 0$, indicating the impact of the load type. After

2.5 ms, the damping effect is minimal due to the outputs' quick fade. In contrast to other loads, this form of loading produces a very high-power output in a short period, even if the displacement is far smaller than that of other forces. However, this circumstance occurs in a minimal time, near t=0, dropping quickly. Also, the impact of changing the k value is similar to that of other loading types.

4.2.2.2.2 PEH Configuration Change

The impact of tip mass addition, unimorph and bimorph type difference, and connection type are investigated for the Figure 1.3 configurations in forced vibration analysis. The power-law exponent k is 0.5. Figure 4.22 depicts the displacement, stress, voltage, current, and power output data for a uniformly distributed step load.

(a)

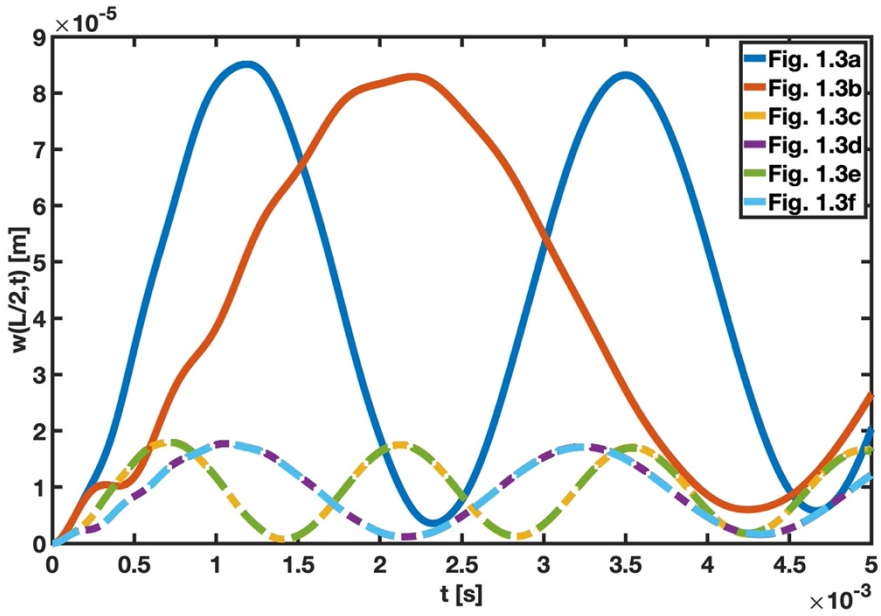

(b)

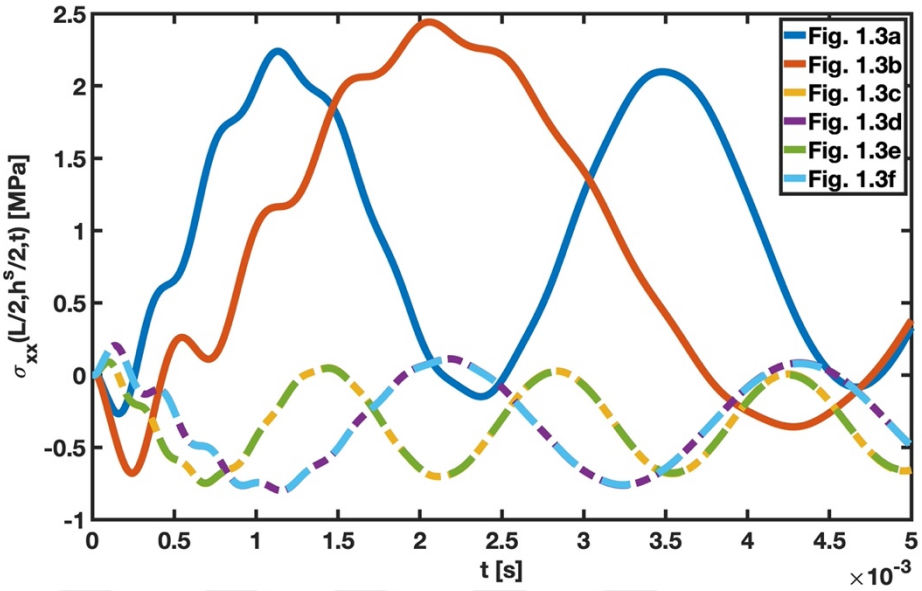
Fig. 1.3a
Fig. 1.3b
Fig. 1.3c
Fig. 1.3d
Fig. 1.3e
Fig. 1.3f
$\sigma_{xx}(L/2,h^s/2,t)$ [MPa]
t [s]
$\times 10^{-3}$

(c)

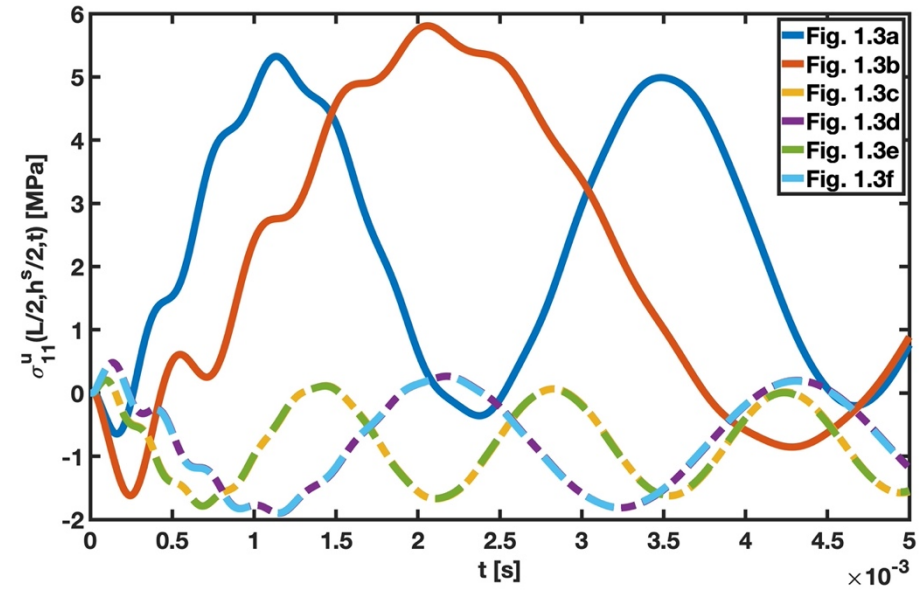
Fig. 1.3a
Fig. 1.3b
Fig. 1.3c
Fig. 1.3d
Fig. 1.3e
Fig. 1.3f
$\sigma^u_{11}(L/2,h^s/2,t)$ [MPa]
t [s]
$\times 10^{-3}$

(d)

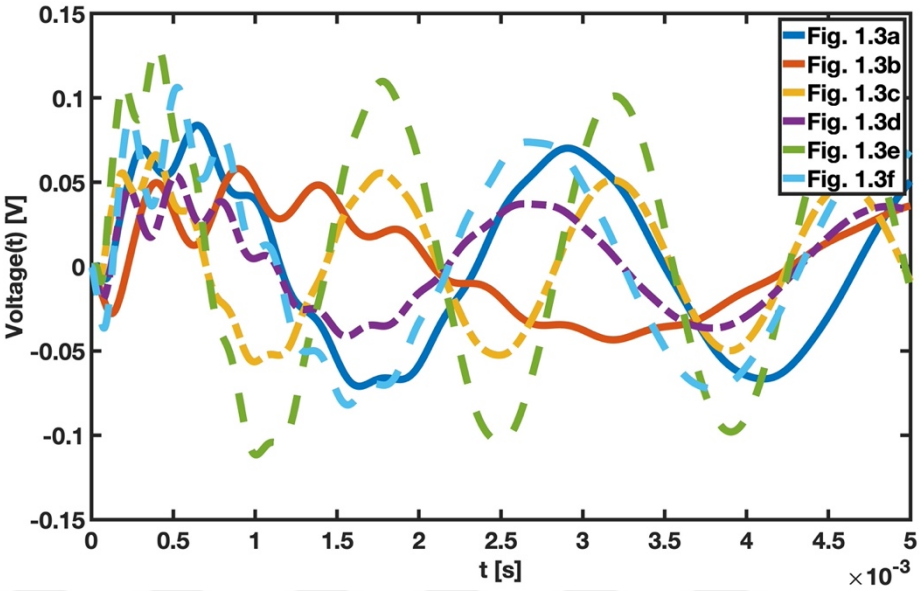
Fig. 1.3a
Fig. 1.3b
Fig. 1.3c
Fig. 1.3d
Fig. 1.3e
Fig. 1.3f
Voltage(t) [V]
t [s]
×10^-3

(e)

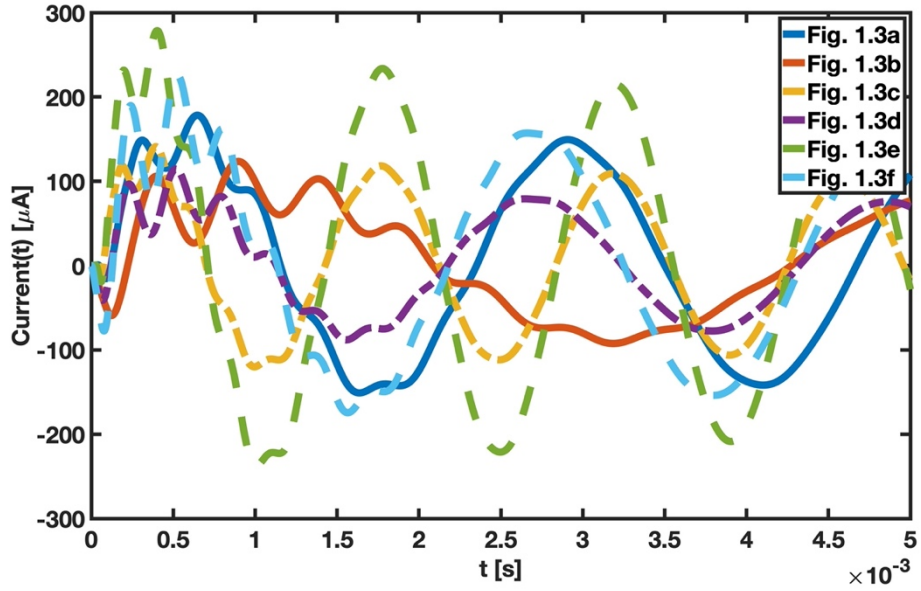
Fig. 1.3a
Fig. 1.3b
Fig. 1.3c
Fig. 1.3d
Fig. 1.3e
Fig. 1.3f
Current(t) [μA]
t [s]
×10^-3

(f)

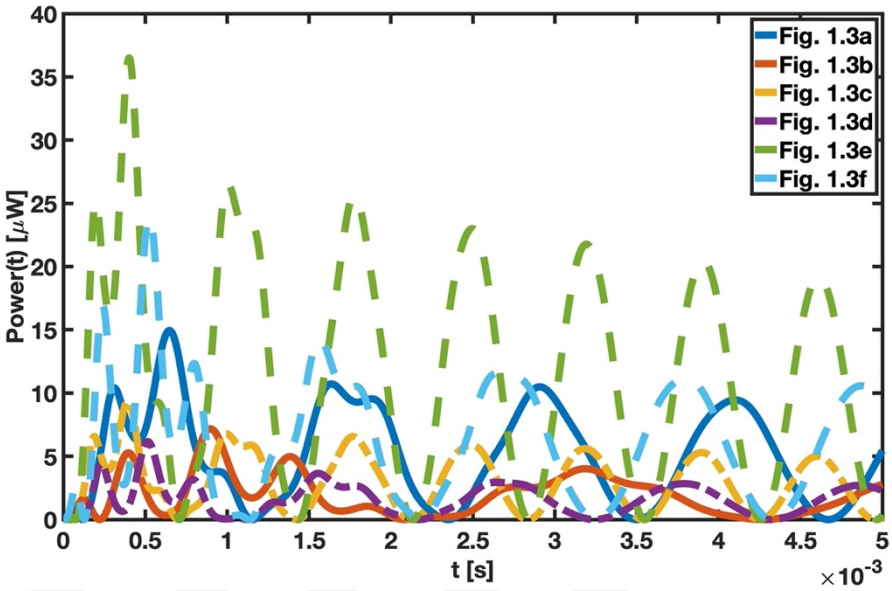

Figure 4.22 Dynamic behavior of a uniformly distributed step-loaded C-F FG Timoshenko PEH beam different configurations in terms of (a) midpoint displacement, (b) midpoint and top surface axial stress of the substructure, (c) midpoint and bottom surface axial stress of the upper piezoelectric material, (d) output voltage difference between electrodes, (e) produced current on the system, and (f) generated power.

The natural frequency decrease of the structure is evident in the free vibration analysis with the addition of the tip mass. Similarly, adding tip mass reduces response frequencies in forced vibration analysis but does not considerably affect displacement and stress output amplitudes. In contrast, voltage, current, and power outputs decrease with the addition of tip mass. Additionally, in unimorph structures, more significant displacement and stresses are attained. Due to the difference in modulus of elasticity and Poisson's ratio, the axial stress components of the top piezoelectric material are greater than the substructure stresses.

Furthermore, the resultant displacement and stresses are unaffected whether the PEH is connected in series or parallel. The highest voltage, current, and power output are seen in PEH parallel-connected bimorph without tip mass configuration. The power output is maximum in the bimorph structures, whereas the displacement is highest in the unimorph forms. Due to this, the direct proportion between displacement and power output in power-law exponent comparisons is not always valid. Under typical

circumstances, series-connected setups are anticipated to produce more voltage and generate less current than parallel-connected ones. However, this is not demonstrated in this study since the materials are FGM, and the base displacement is not applied. Finally, the dampening effect is not predominantly apparent until 5 ms. Results for concentrated step load are presented in Figure 4.23.

(a)

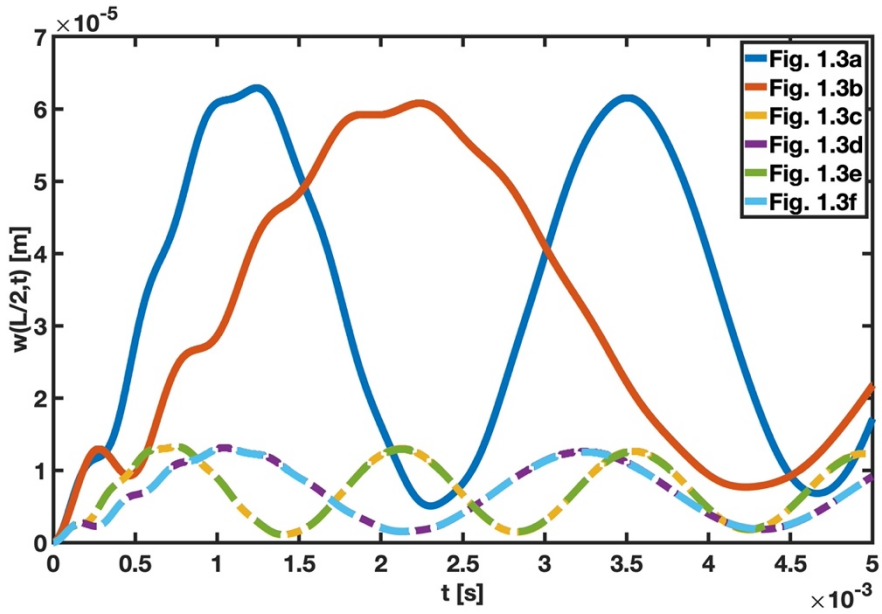

(b)

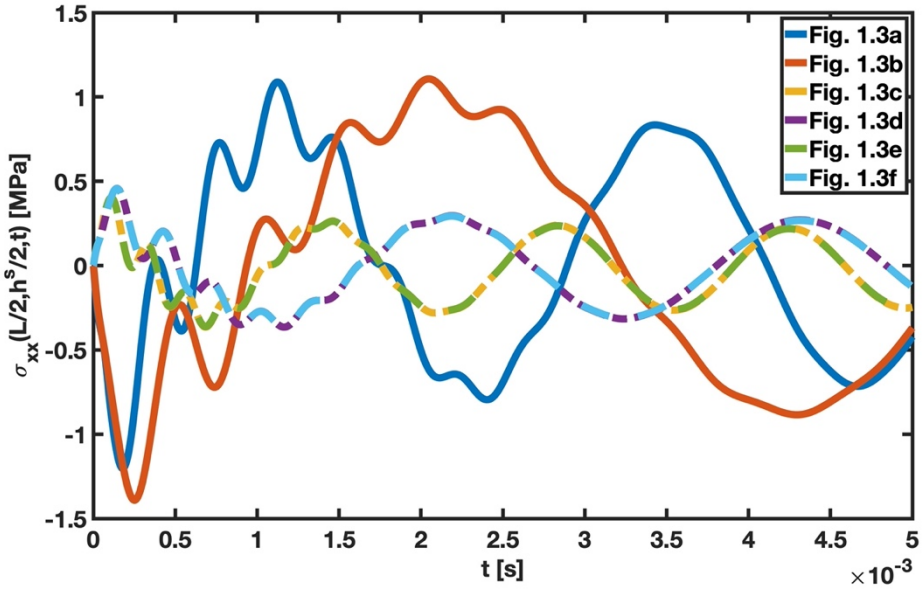

(c)

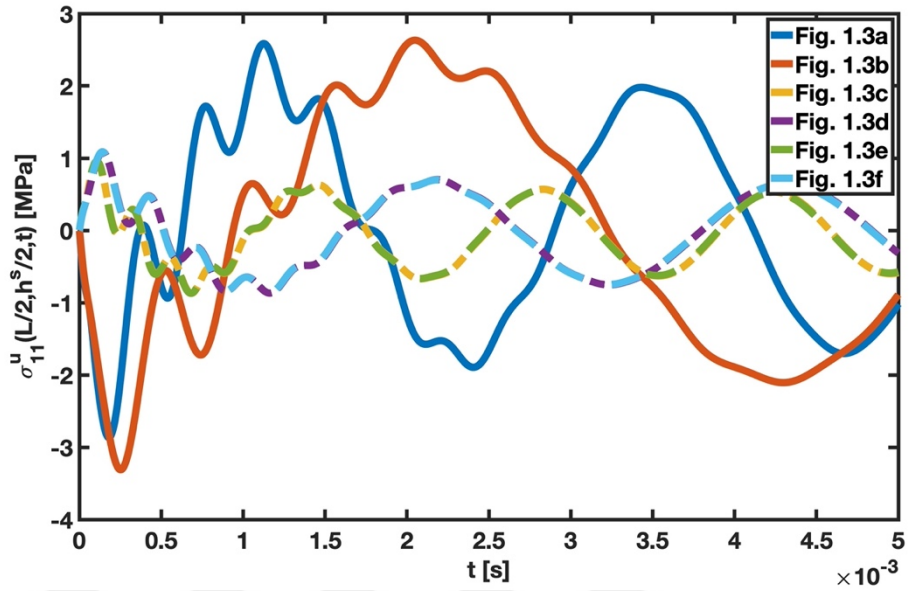
Fig. 1.3a
Fig. 1.3b
Fig. 1.3c
Fig. 1.3d
Fig. 1.3e
Fig. 1.3f
$\sigma_{11}^{u}(L/2,h^{s}/2,t)$ [MPa]
t [s]
×10^-3

(d)

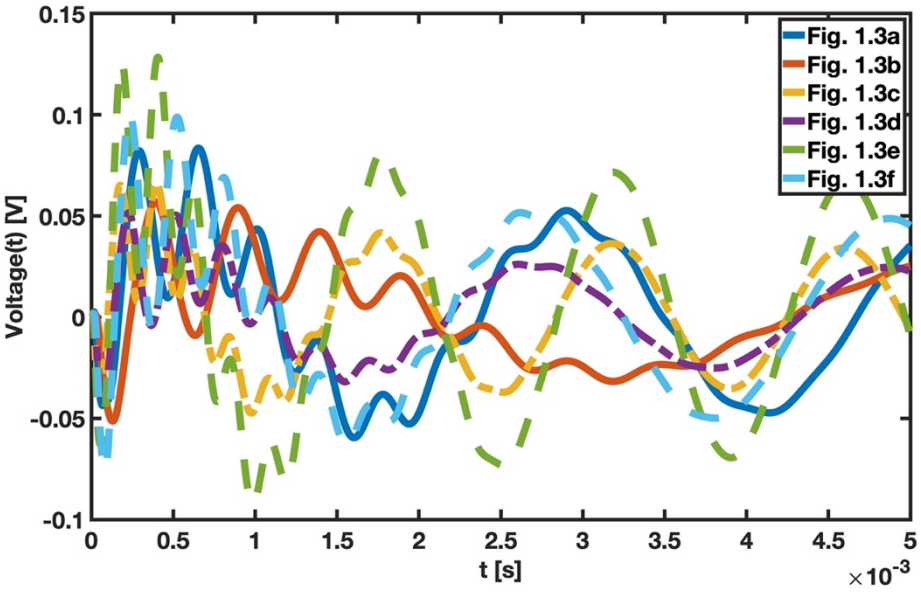
Fig. 1.3a
Fig. 1.3b
Fig. 1.3c
Fig. 1.3d
Fig. 1.3e
Fig. 1.3f
Voltage(t) [V]
t [s]
×10^-3

(e)

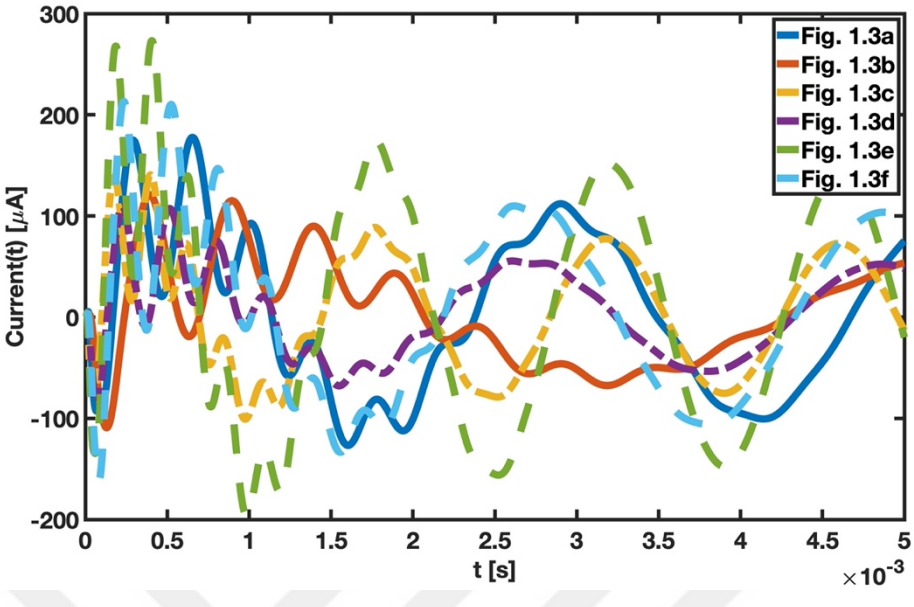

(f)

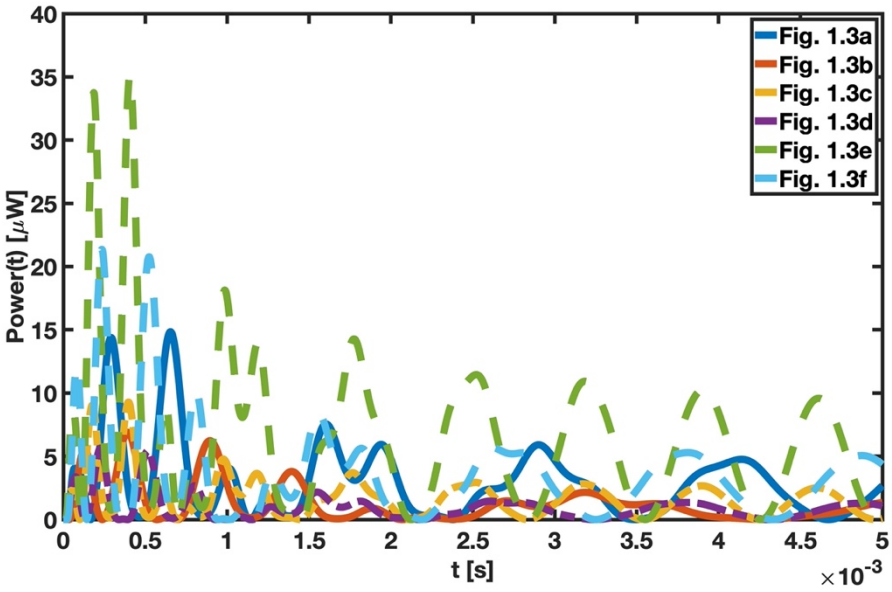

Figure 4.23 Dynamic behavior of a concentrated step-loaded C-F FG Timoshenko PEH beam different configurations in terms of (a) midpoint displacement, (b) midpoint and top surface axial stress of the substructure, (c) midpoint and bottom surface axial stress of the upper piezoelectric material, (d) output voltage difference between electrodes, (e) produced current on the system, and (f) generated power.

All the results given for a uniformly distributed step load are also valid for a concentrated step load. Differently, when tip mass addition is considered, the stress amplitude is not altered, and the power output for the designs shown in Figure 1.3b,

c, and d exhibit a rapid damping effect. Figure 4.24 shows six versions of a PEH's dynamic behavior under concentrated harmonic load.

(a)

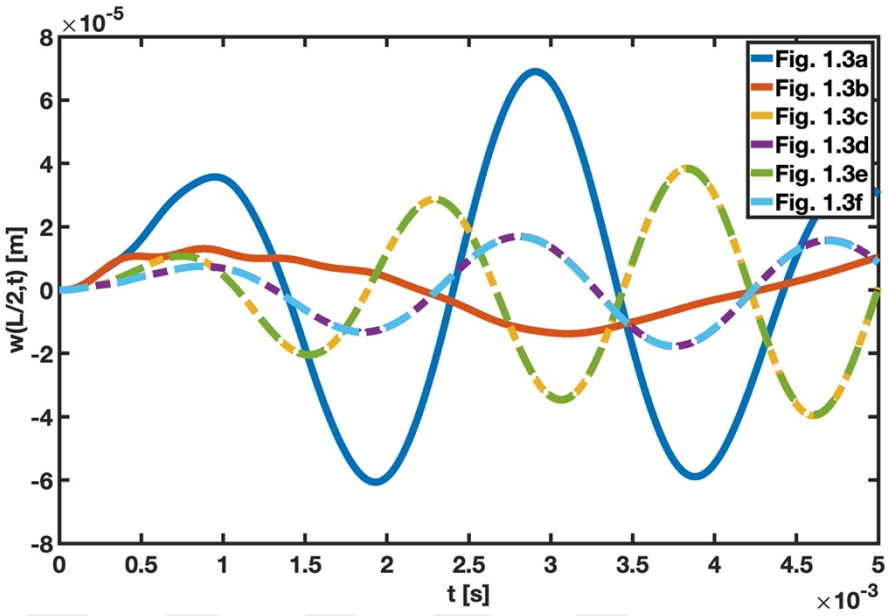

(b)

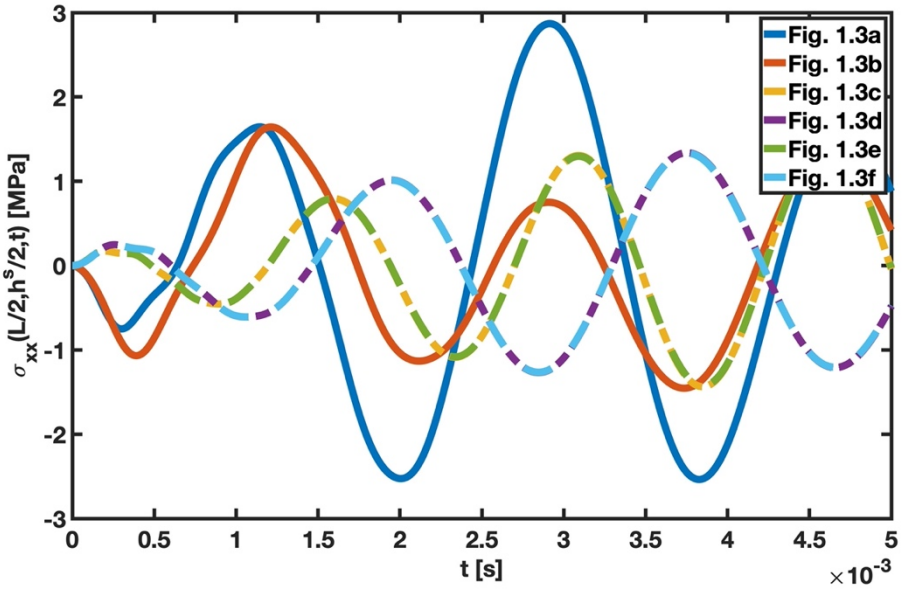

(c)

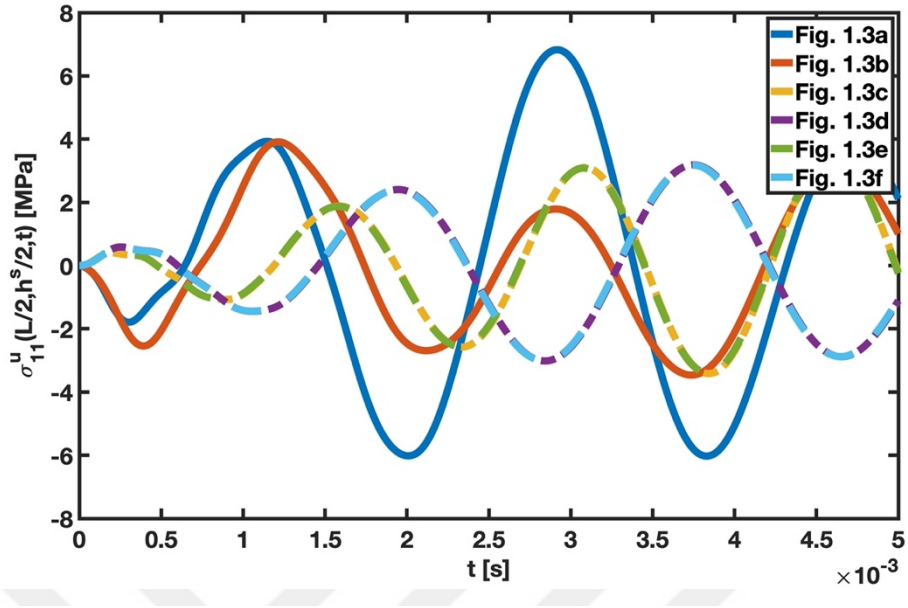
Fig. 1.3a
Fig. 1.3b
Fig. 1.3c
Fig. 1.3d
Fig. 1.3e
Fig. 1.3f
$\sigma_{11}^{u}(L/2,h^{s}/2,t)$ [MPa]
t [s]
×10^-3

(d)

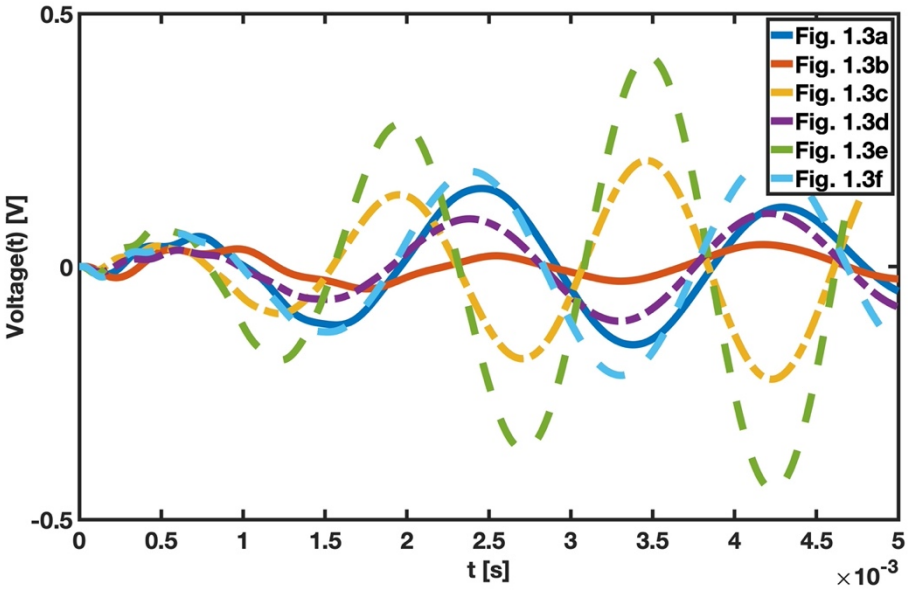
Fig. 1.3a
Fig. 1.3b
Fig. 1.3c
Fig. 1.3d
Fig. 1.3e
Fig. 1.3f
Voltage(t) [V]
t [s]
×10^-3

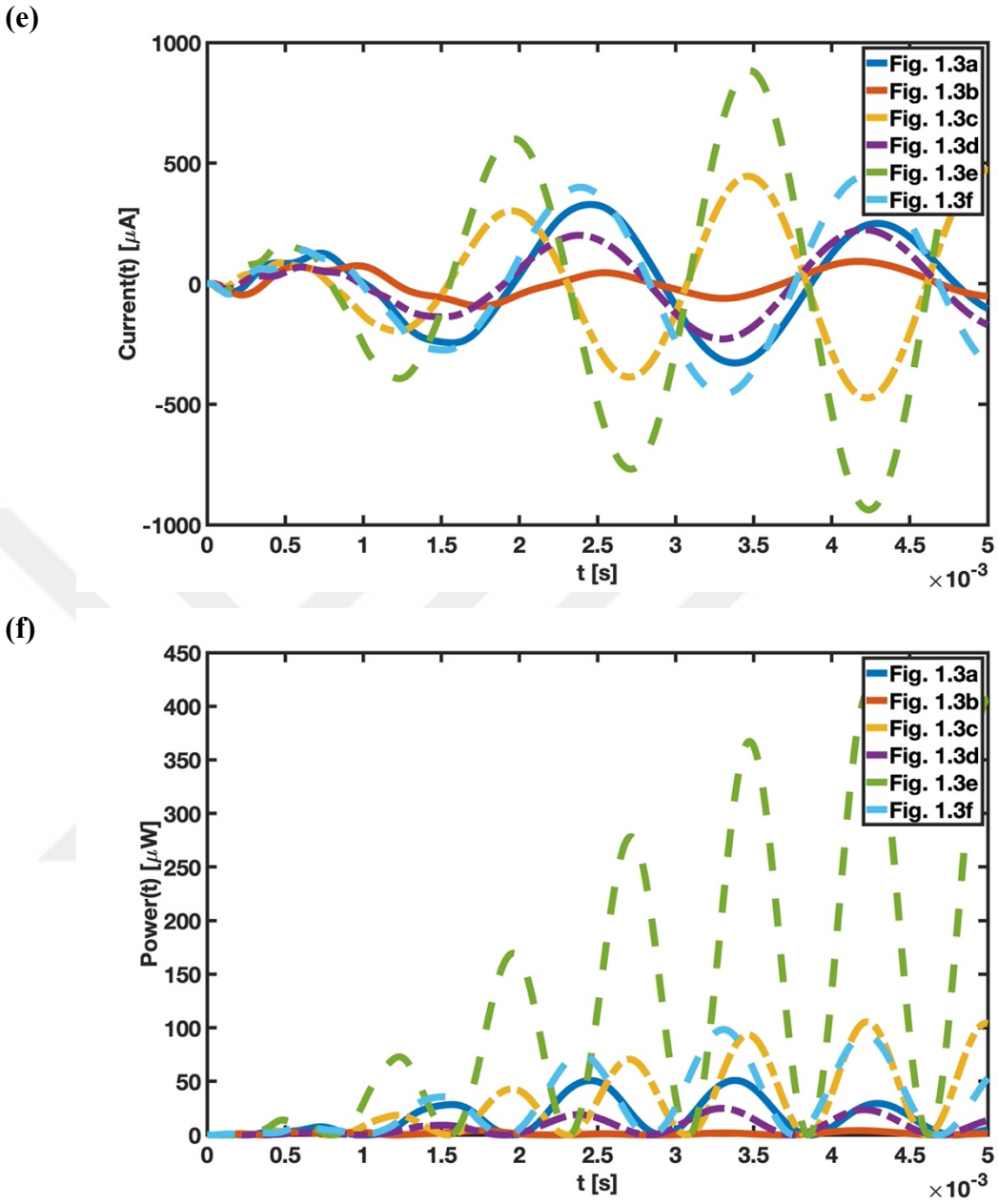

Figure 4.24 Dynamic behavior of a concentrated harmonic-loaded C-F FG Timoshenko PEH beam different configurations in terms of (a) midpoint displacement, (b) midpoint and top surface axial stress of the substructure, (c) midpoint and bottom surface axial stress of the upper piezoelectric material, (d) output voltage difference between electrodes, (e) produced current on the system, and (f) generated power.

The unimorph structure with tip mass has the lowest displacement for concentrated harmonic load despite having the maximum displacement for uniformly distributed and concentrated step loading. Adding tip mass reduces this loading type's electrical

outputs and displacement value for unimorph configuration. The stress value is lower than that of bimorph structures as a result of the tip mass added unimorph structure's primary contribution to the reduction in displacement. Also, both displacements and stresses are unaffected by connecting a parallel or series circuit. The parallel-connected bimorph structure with tip mass produces more significant electrical outputs in the initial phase of the investigation, followed by higher values in the series-connected bimorph configuration without tip mass. It becomes evident that the design of a PEH should be based on the subjected type of load, considering the varied electrical outputs in concentrated harmonic loading compared to the other two forms of loading. Finally, Figure 4.25 displays the outcomes for the concentrated impulsive load used as the last loading type to observe the PEH configuration effect.

(a)

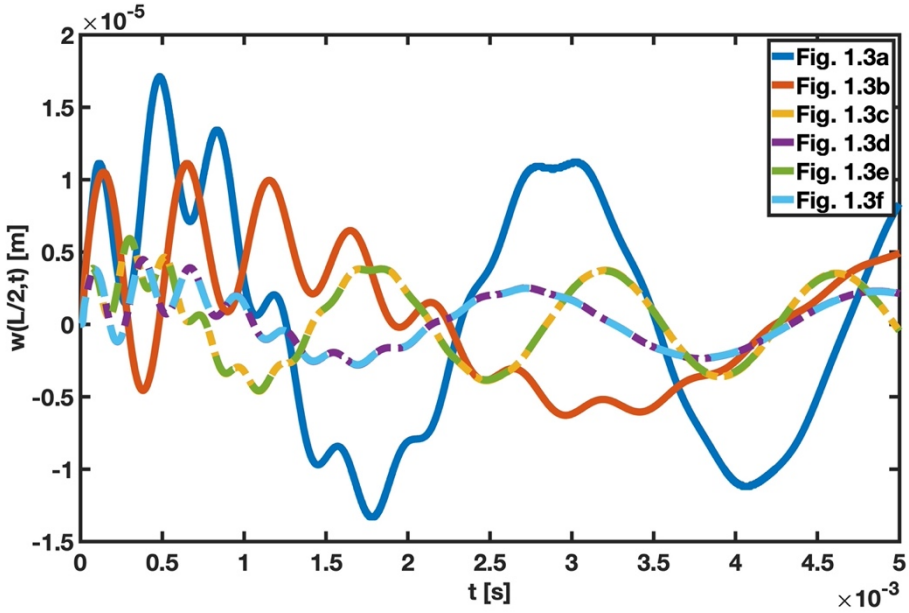

(b)

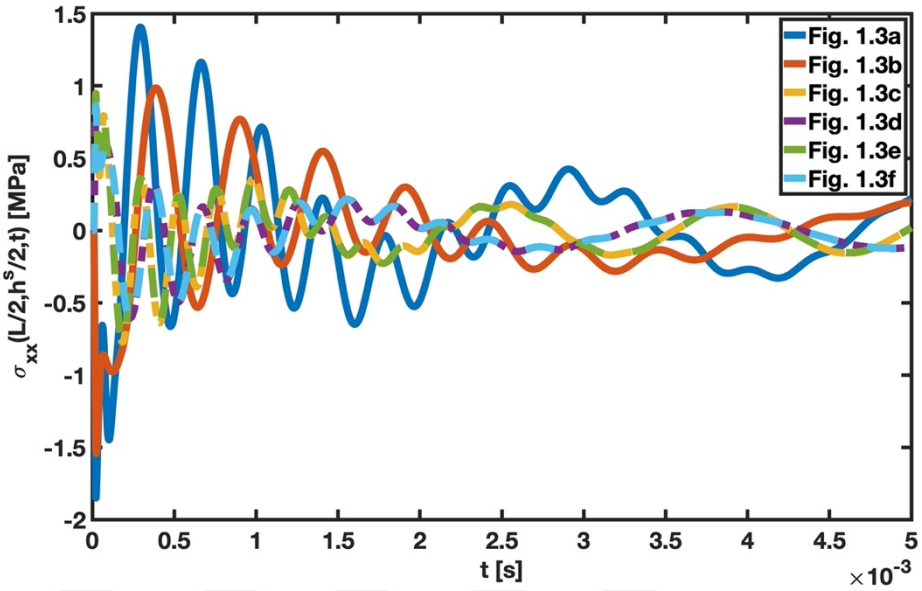
Fig. 1.3a
Fig. 1.3b
Fig. 1.3c
Fig. 1.3d
Fig. 1.3e
Fig. 1.3f
$\sigma_{xx}(L/2,h^s/2,t)$ [MPa]
t [s]
$\times 10^{-3}$

(c)

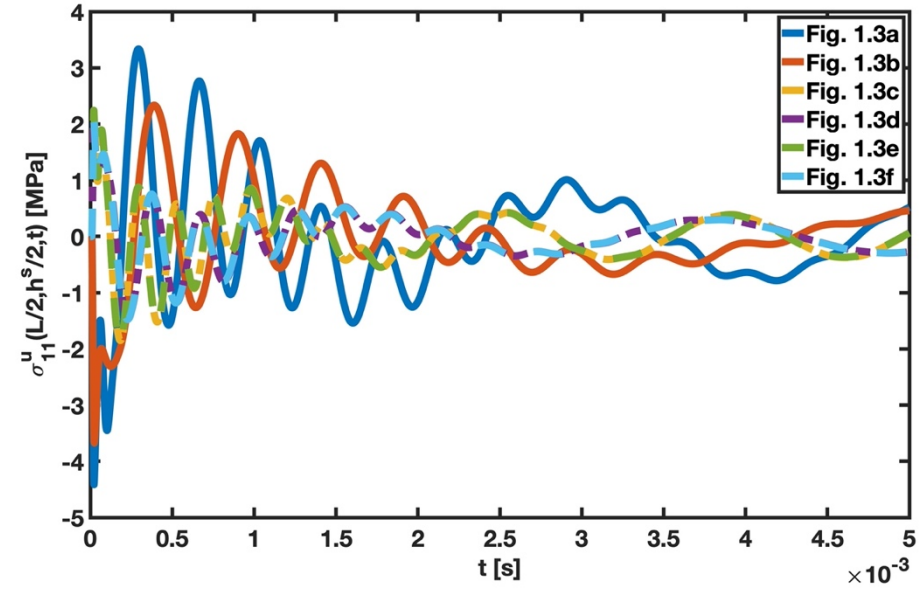
Fig. 1.3a
Fig. 1.3b
Fig. 1.3c
Fig. 1.3d
Fig. 1.3e
Fig. 1.3f
$\sigma^u_{11}(L/2,h^s/2,t)$ [MPa]
t [s]
$\times 10^{-3}$

(d)

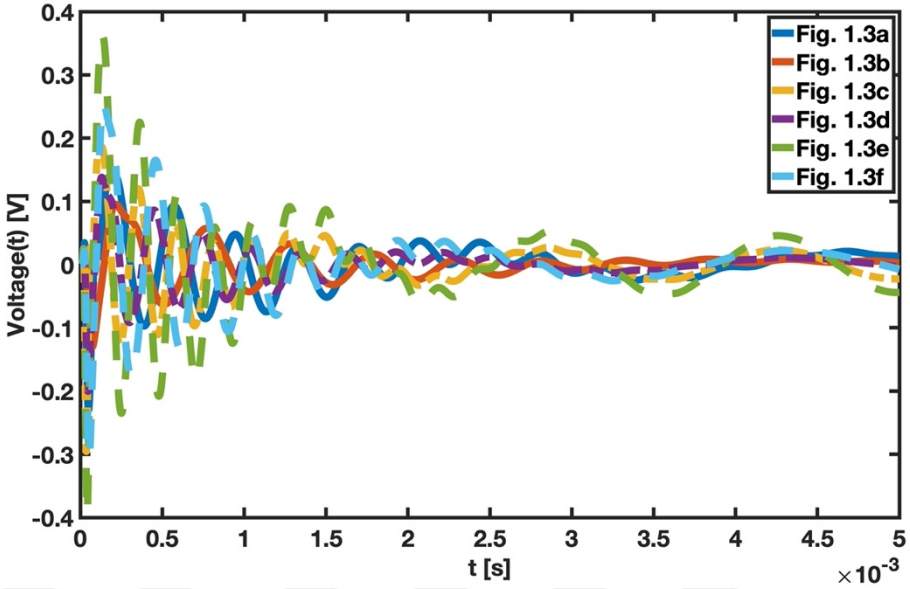
Fig. 1.3a
Fig. 1.3b
Fig. 1.3c
Fig. 1.3d
Fig. 1.3e
Fig. 1.3f
Voltage(t) [V]
t [s]
×10^-3

(e)

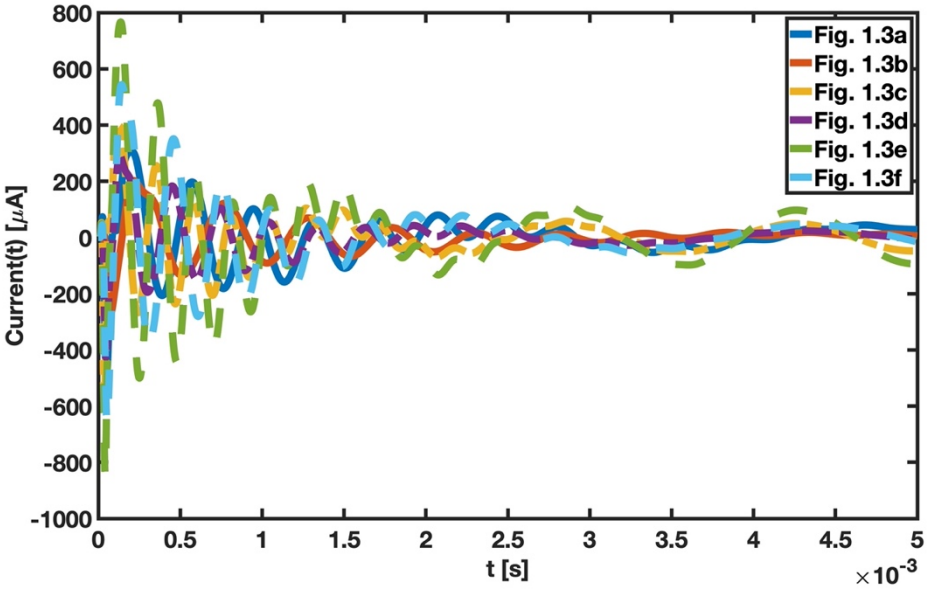
Fig. 1.3a
Fig. 1.3b
Fig. 1.3c
Fig. 1.3d
Fig. 1.3e
Fig. 1.3f
Current(t) [μA]
t [s]
×10^-3

(f)

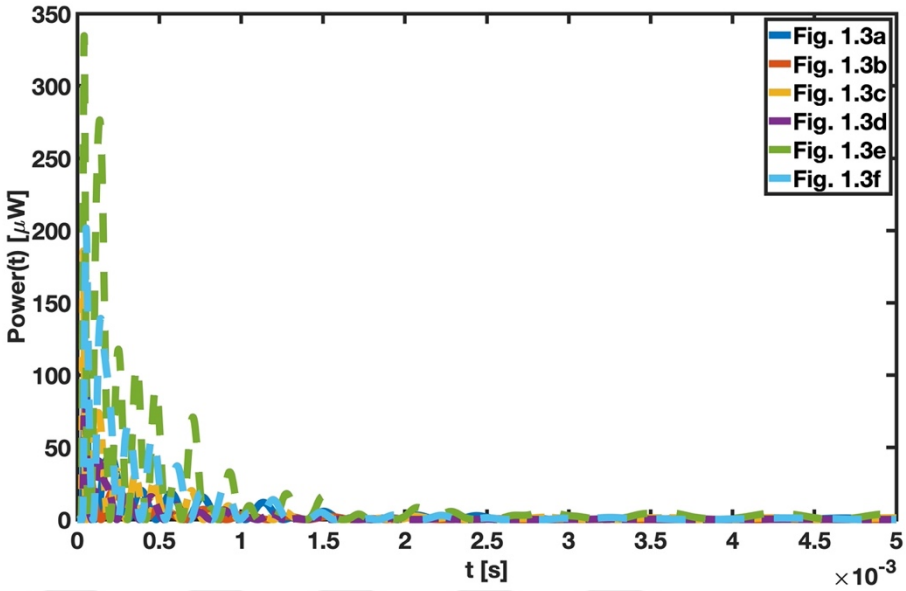

Figure 4.25 Dynamic behavior of a concentrated impulsive-loaded C-F FG Timoshenko PEH beam different configurations in terms of (a) midpoint displacement, (b) midpoint and top surface axial stress of the substructure, (c) midpoint and bottom surface axial stress of the upper piezoelectric material, (d) output voltage difference between electrodes, (e) produced current on the system, and (f) generated power.

Unlike other loadings, the damping is apparent until 5 ms when the wavelengths are compared. It is determined that the damping has a quick effect, mainly when the power formation graph Figure 4.25f is observed. The result of tip mass addition in the uniformly distributed step loadings on displacement, stress, voltage difference, current, and power generation is valid for the concentrated impulsive load. The unimorph structure only varies in that adding tip mass also lessens displacement and stresses. Configuration of Figure 1.3e, f, c, d, a, and b represents the order of voltage difference, producing current, and power.

4.2.2.2.3 Boundary Condition Change

The boundary condition change is investigated for the series-connected bimorph PEH without tip mass configuration. This research similarly uses a k value of 0.5. First, Figure 4.26 displays the outcomes for uniformly distributed step load.

(a)

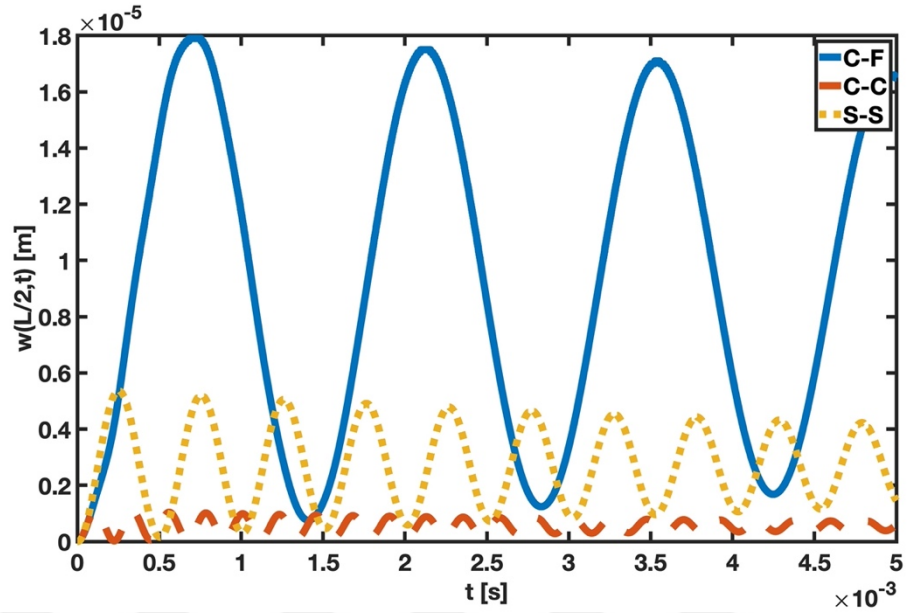
×10^-5
1.8
1.6
1.4
1.2
1
0.8
0.6
0.4
0.2
0
w(L/2,t) [m]
C-F
C-C
S-S
0
0.5
1
1.5
2
2.5
3
3.5
4
4.5
5
t [s]
×10^-3

(b)

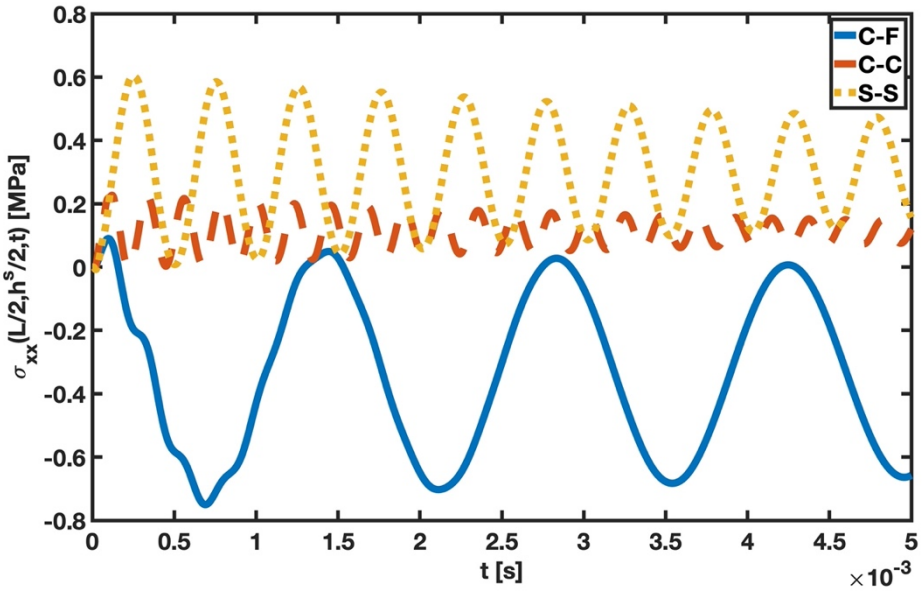
0.8
0.6
0.4
0.2
0
-0.2
-0.4
-0.6
-0.8
σxx(L/2,h^S/2,t) [MPa]
C-F
C-C
S-S
0
0.5
1
1.5
2
2.5
3
3.5
4
4.5
5
t [s]
×10^-3

(c)

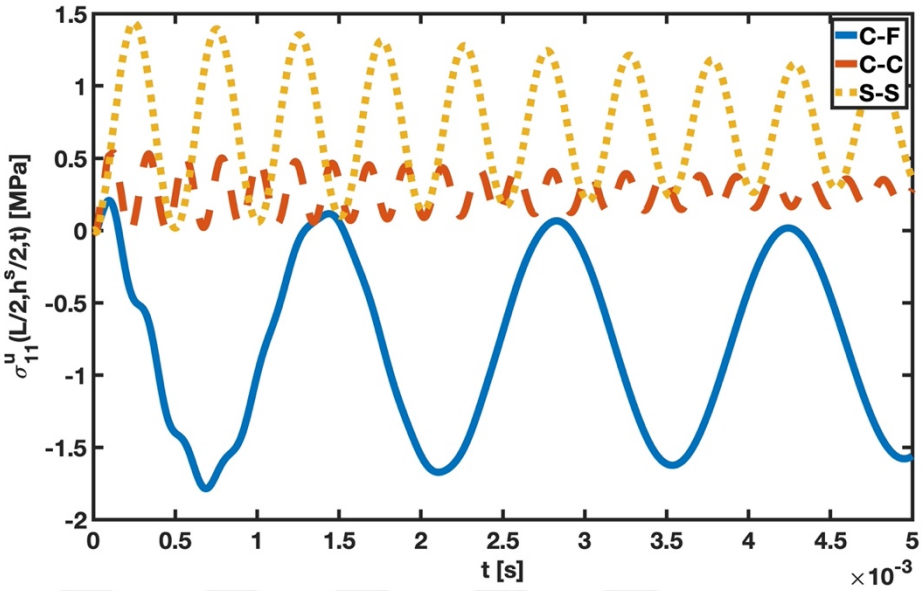

(d)

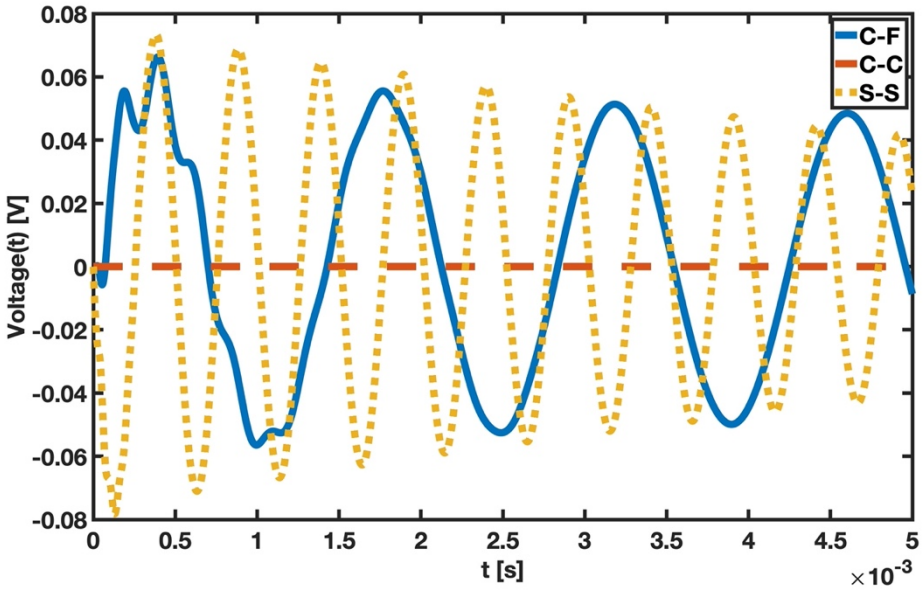

(e)

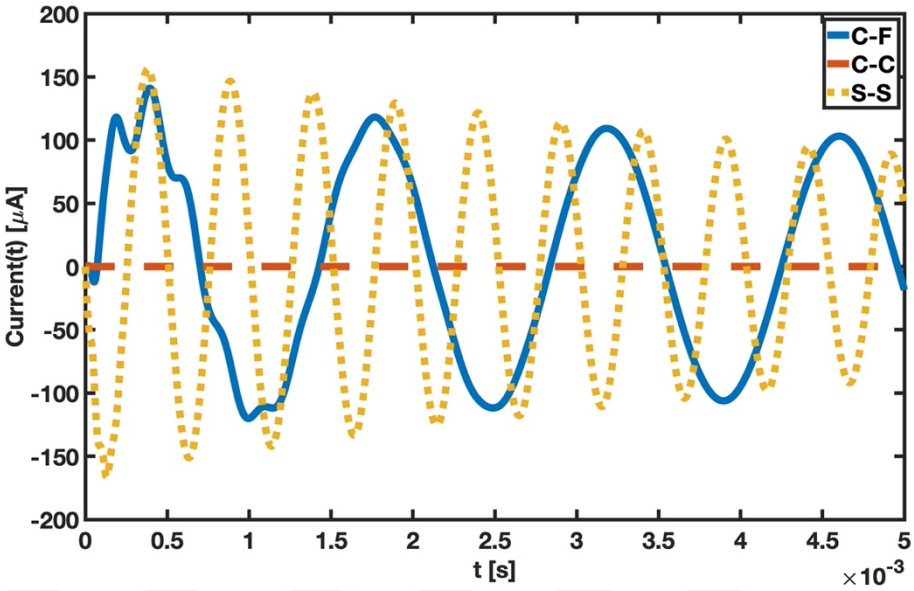

(f)

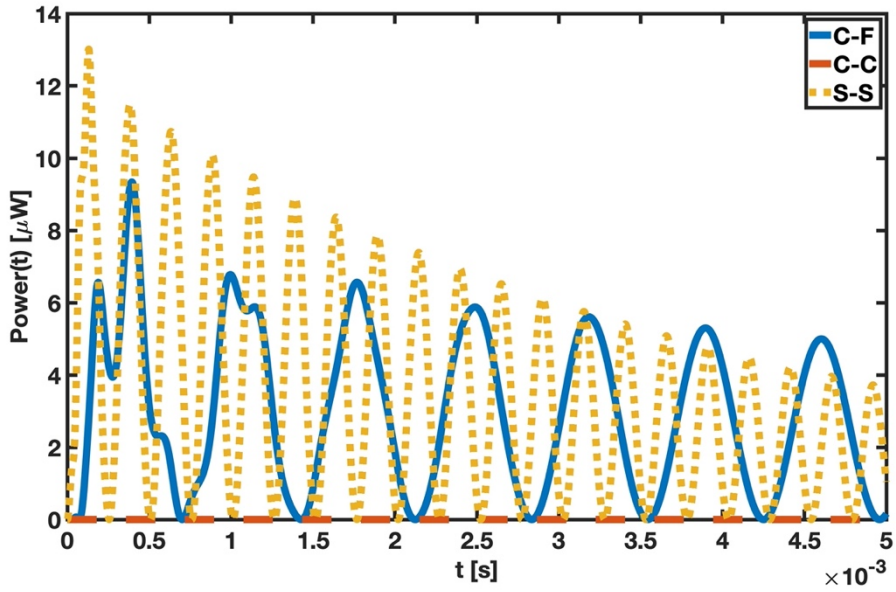

Figure 4.26 Dynamic behavior of a uniformly distributed step-loaded C-F, C-C, S-S series-connected bimorph FG Timoshenko PEH beam without tip mass configuration in terms of (a) midpoint displacement, (b) midpoint and top surface axial stress of the substructure, (c) midpoint and bottom surface axial stress of the upper piezoelectric material, (d) output voltage difference between electrodes, (e) produced current on the system, and (f) generated power.

Voltage, current, and power output are higher in the S-S boundary condition, while displacement and stress values are higher in the C-F boundary condition. Due to the PEH's inability to produce voltage difference and energy, the boundary condition C-

C is illogical. The literature often mentions the beneficial effects of using the C-F BC [45]. However, this study shows that the S-S boundary condition delivers better outcomes depending on the form of load. Finally, the frequency of the outputs is higher in the S-S boundary condition, and it is highest in the C-C boundary condition. The free vibration analysis results show that the natural frequency increases as the boundary condition limitation grows. It is also valid for forced vibration studies. The results for the concentrated step load of the boundary condition effect are given in Figure 4.27.

(a)

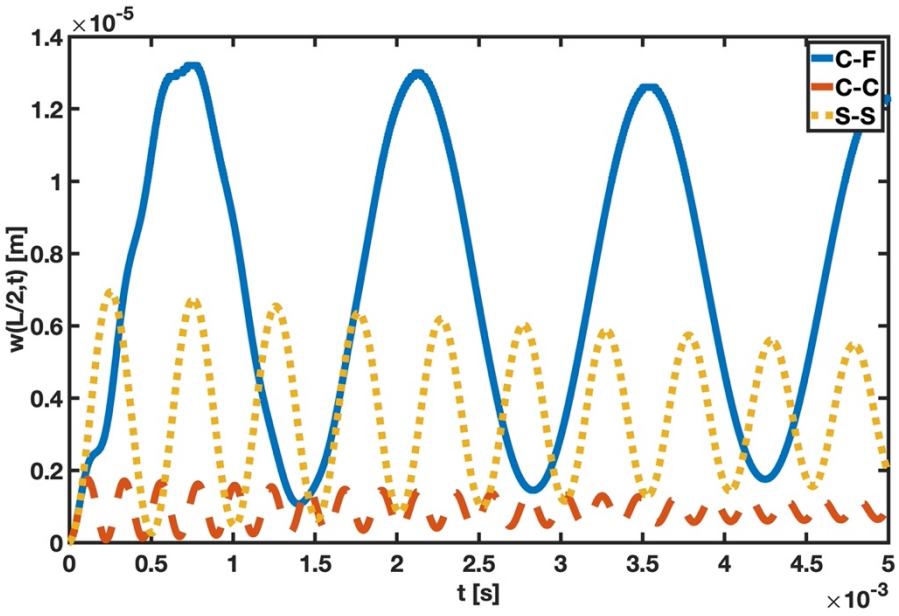

(b)

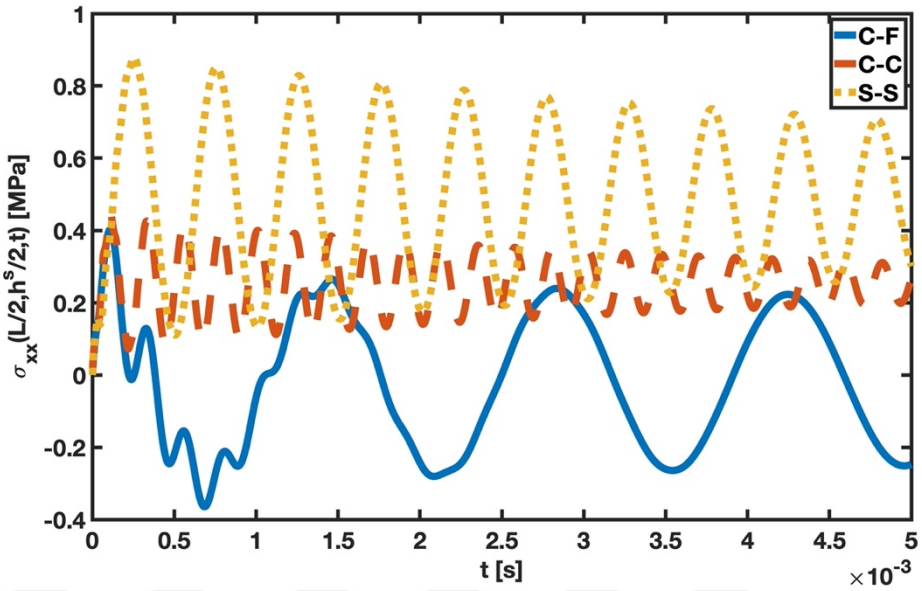
C-F
C-C
S-S
$\sigma_{xx}(L/2,h^s/2,t)$ [MPa]
t [s]
$\times 10^{-3}$

(c)

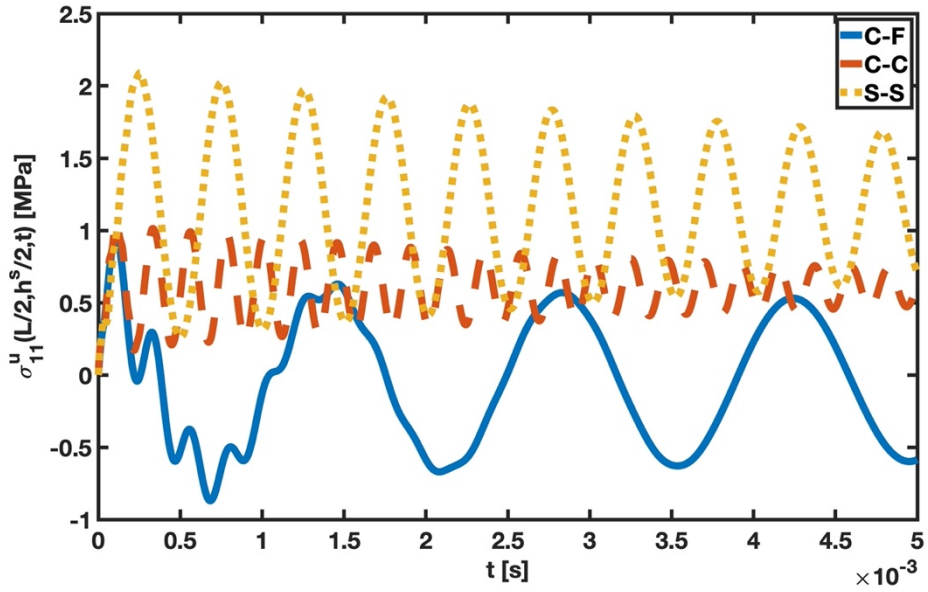
C-F
C-C
S-S
$\sigma^u_{11}(L/2,h^s/2,t)$ [MPa]
t [s]
$\times 10^{-3}$

(d)

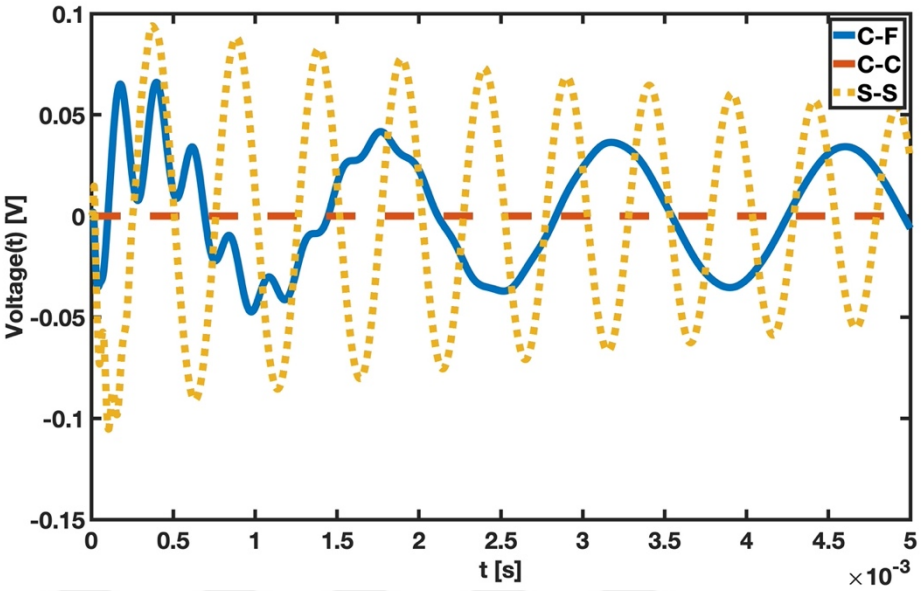

(e)

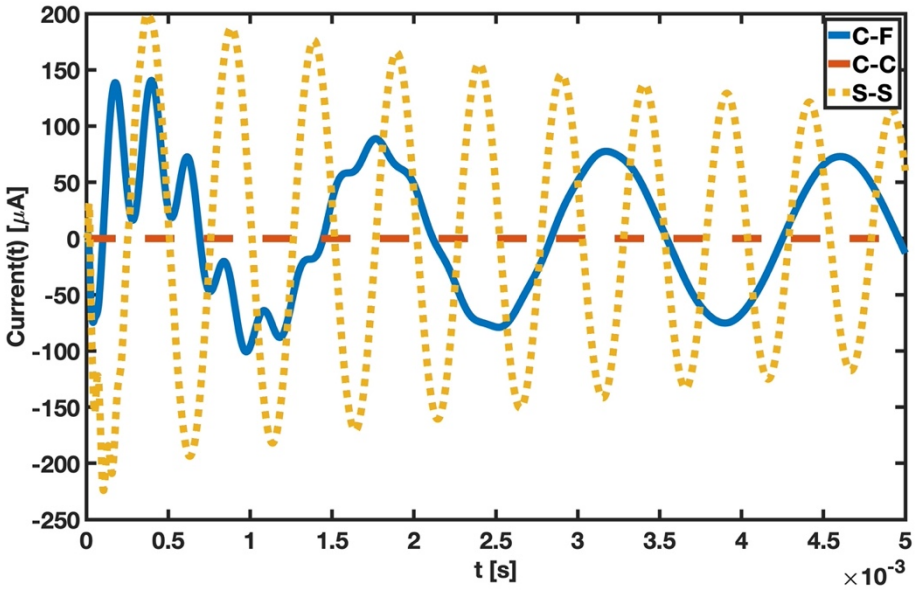

(f)

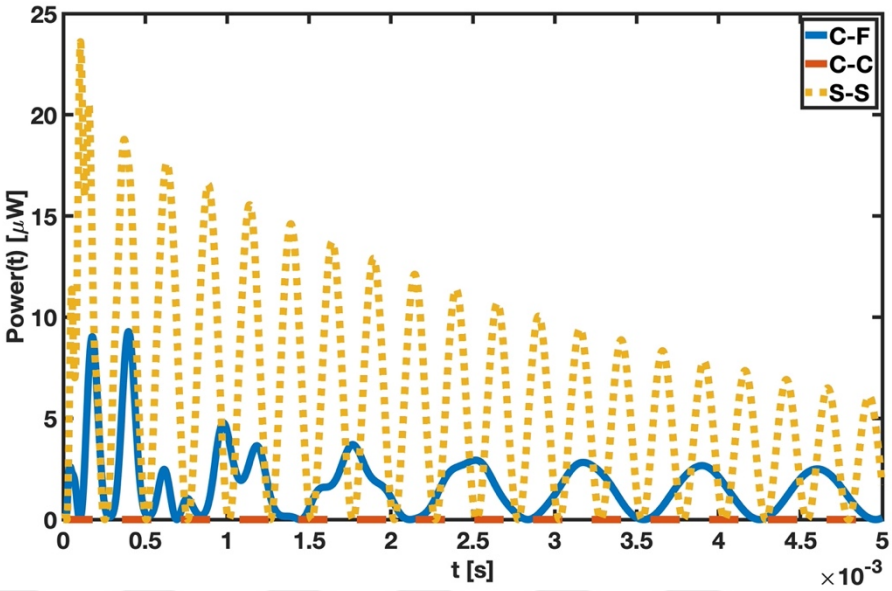

Figure 4.27 Dynamic behavior of a concentrated step-loaded C-F, C-C, S-S series-connected bimorph FG Timoshenko PEH beam without tip mass configuration in terms of (a) midpoint displacement, (b) midpoint and top surface axial stress of the substructure, (c) midpoint and bottom surface axial stress of the upper piezoelectric material, (d) output voltage difference between electrodes, (e) produced current on the system, and (f) generated power.

For a concentrated step load, the same conclusions that apply to a uniformly distributed step load are valid. Differently, the S-S boundary condition's stress levels are higher than the C-F. Figure 4.28 displays the findings for the concentrated harmonic load.

(a)

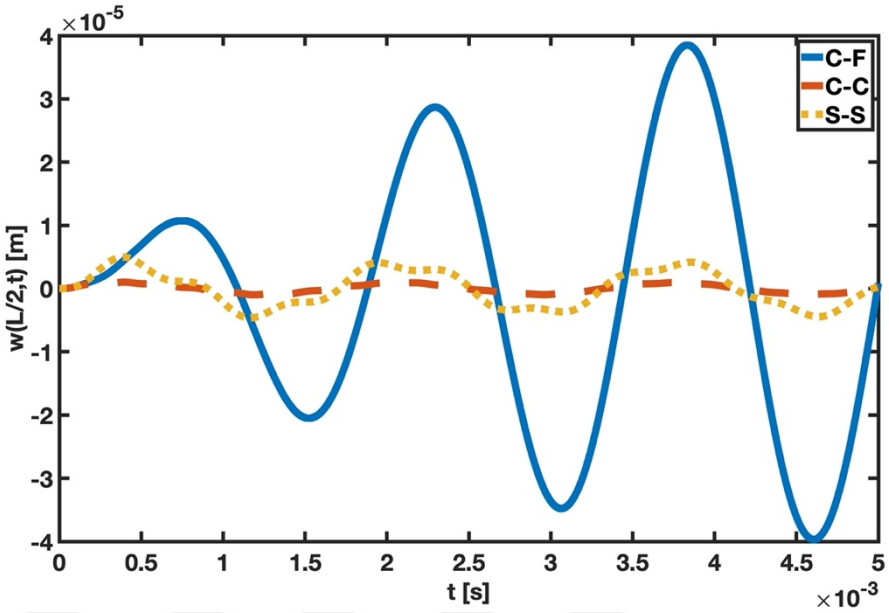
×10^-5
4
3
2
1
0
-1
-2
-3
-4
w(L/2,t) [m]
0
0.5
1
1.5
2
2.5
3
3.5
4
4.5
5
t [s]
×10^-3
C-F
C-C
S-S

(b)

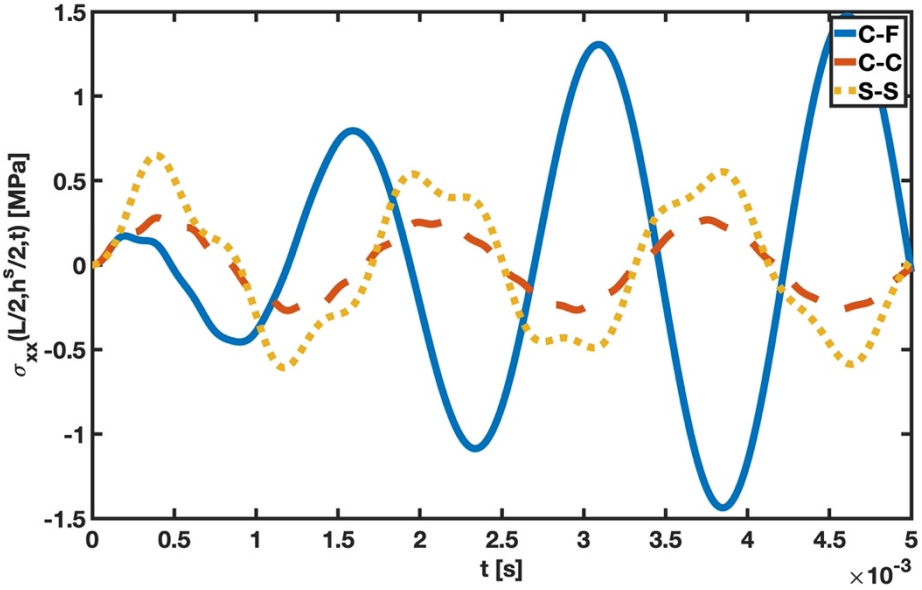
1.5
1
0.5
0
-0.5
-1
-1.5
σxx(L/2,h^s/2,t) [MPa]
0
0.5
1
1.5
2
2.5
3
3.5
4
4.5
5
t [s]
×10^-3
C-F
C-C
S-S

(c)

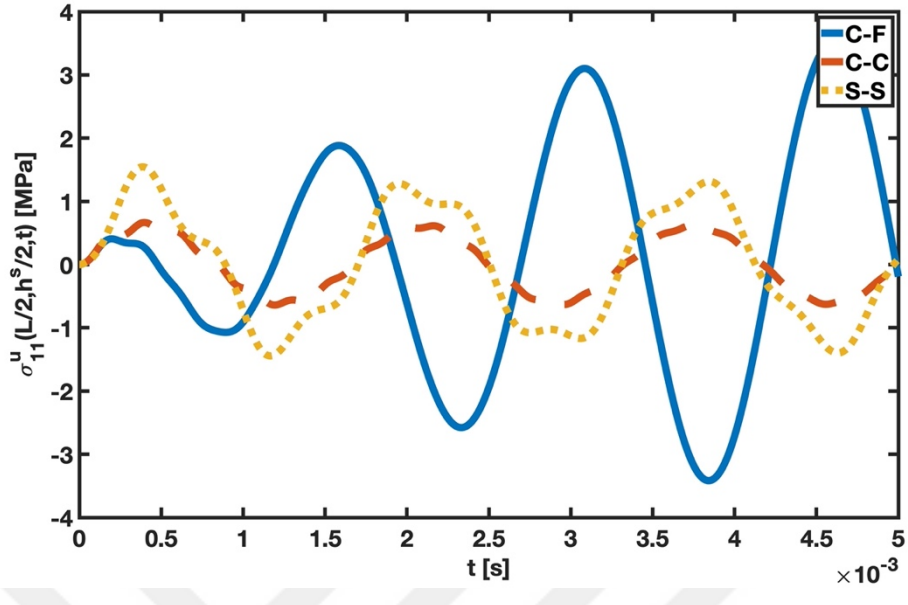

(d)

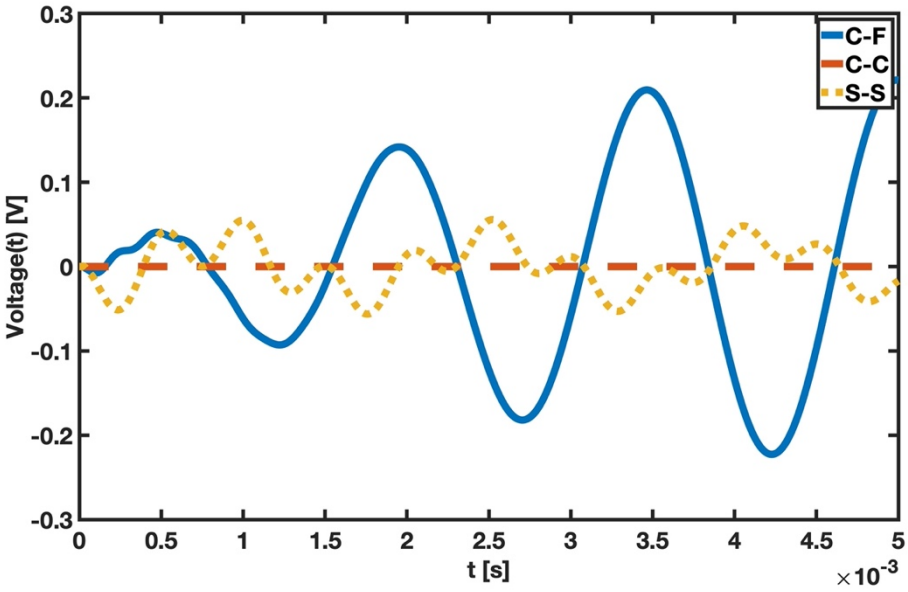

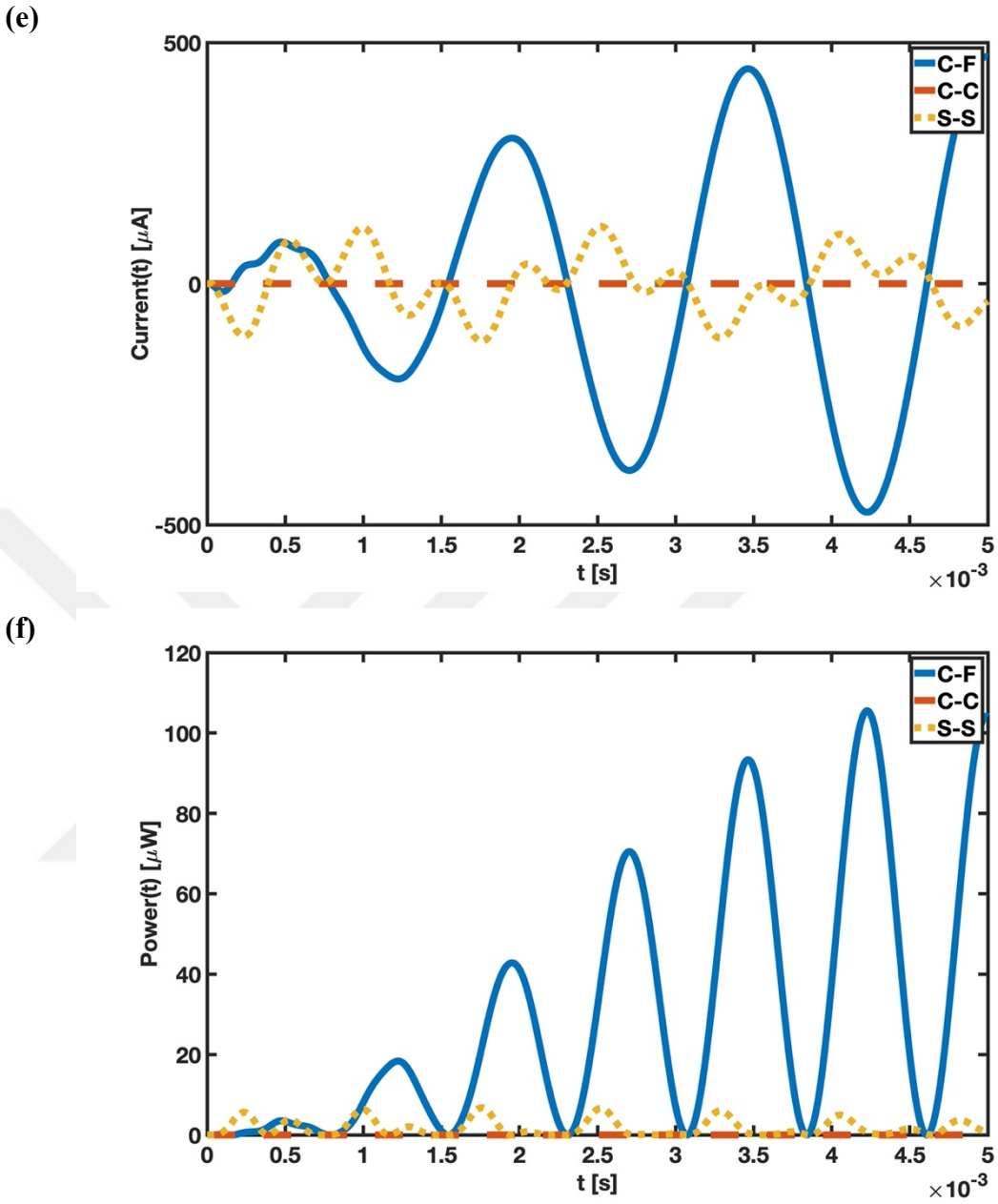

Figure 4.28 Dynamic behavior of a concentrated harmonic-loaded C-F, C-C, S-S series-connected bimorph FG Timoshenko PEH beam without tip mass configuration in terms of (a) midpoint displacement, (b) midpoint and top surface axial stress of the substructure, (c) midpoint and bottom surface axial stress of the upper piezoelectric material, (d) output voltage difference between electrodes, (e) produced current on the system, and (f) generated power.

The highest values are achieved for all outputs in the C-F boundary condition under concentrated harmonic loading. The result is that the applied frequency of 600 Hz is close to the natural frequency of the C-F system of 706.6 Hz. The effect of keeping

the piezoelectric energy harvesters close to the system's natural frequency is observed. The dampening effect cannot be observed until 5 ms since the output values increase for C-F BC. The system will respond in a steady condition after a particular time. Finally, the boundary condition impact is evaluated in Figure 4.29 for concentrated impulsive loading.

(a)

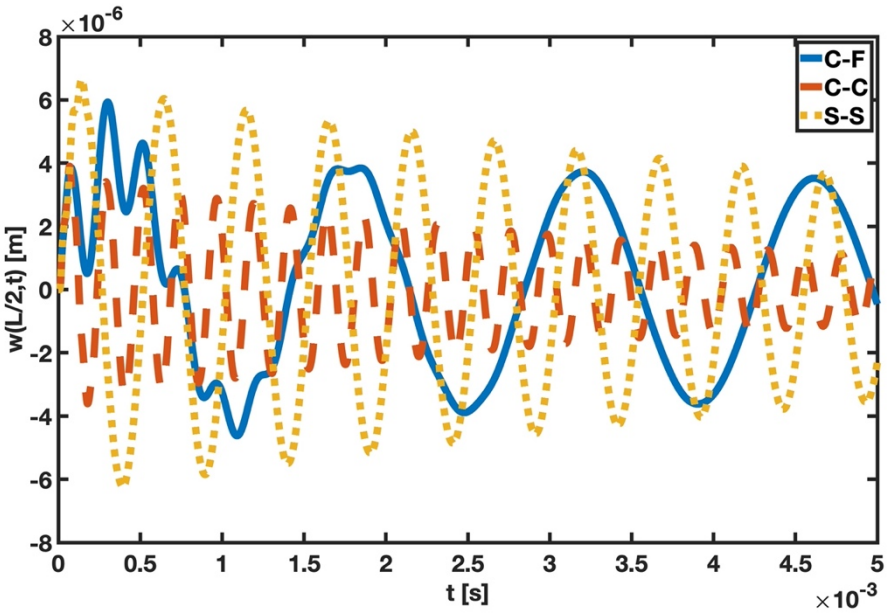

(b)

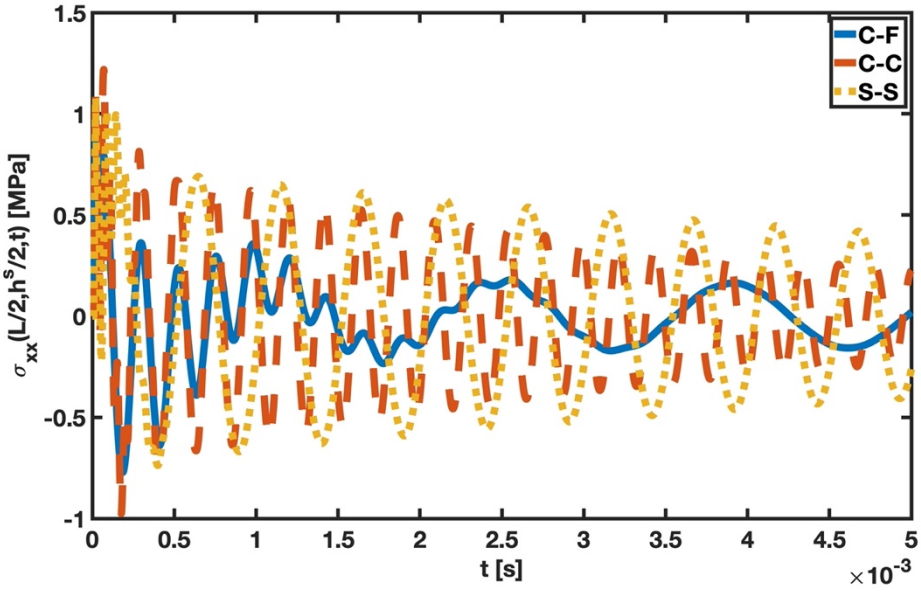

(c)

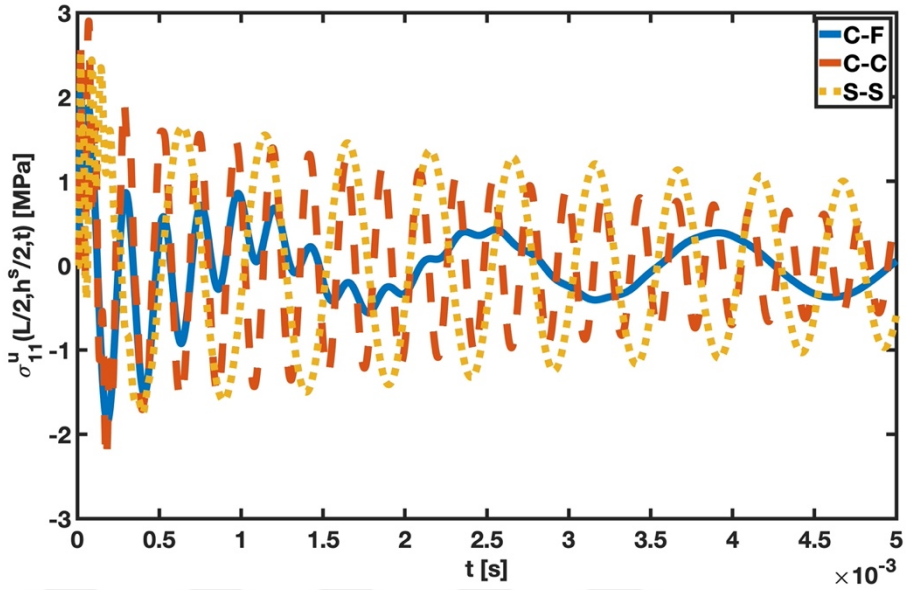

(d)

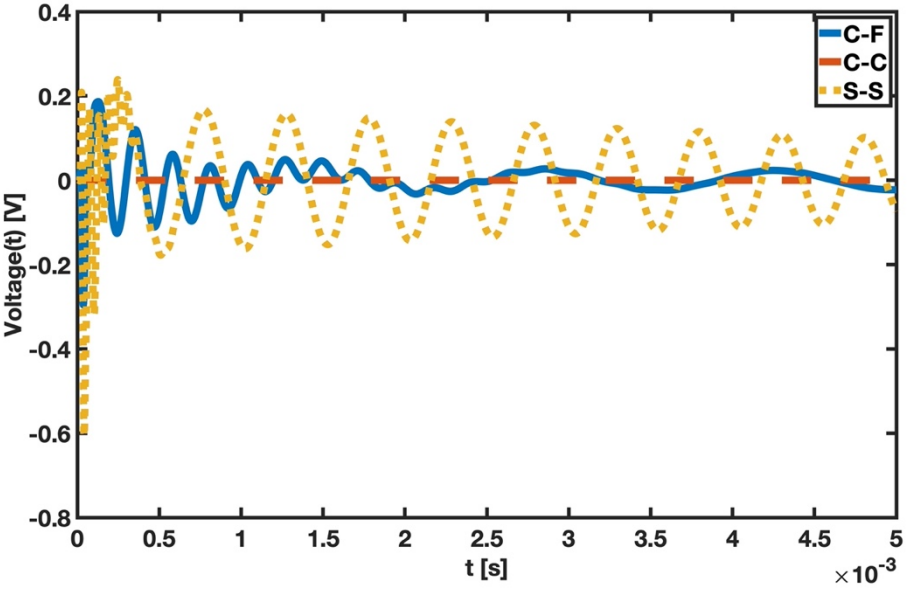

(e)

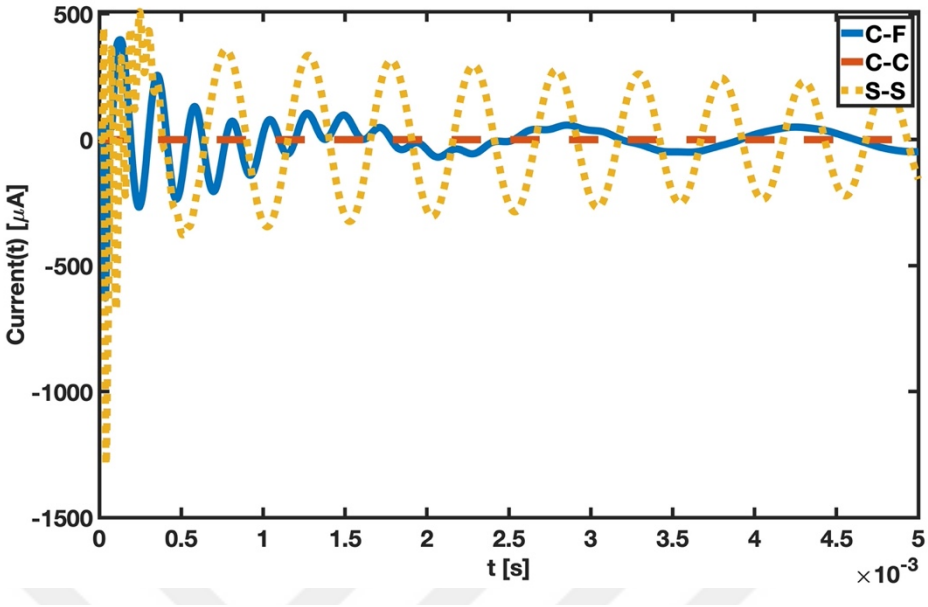

(f)

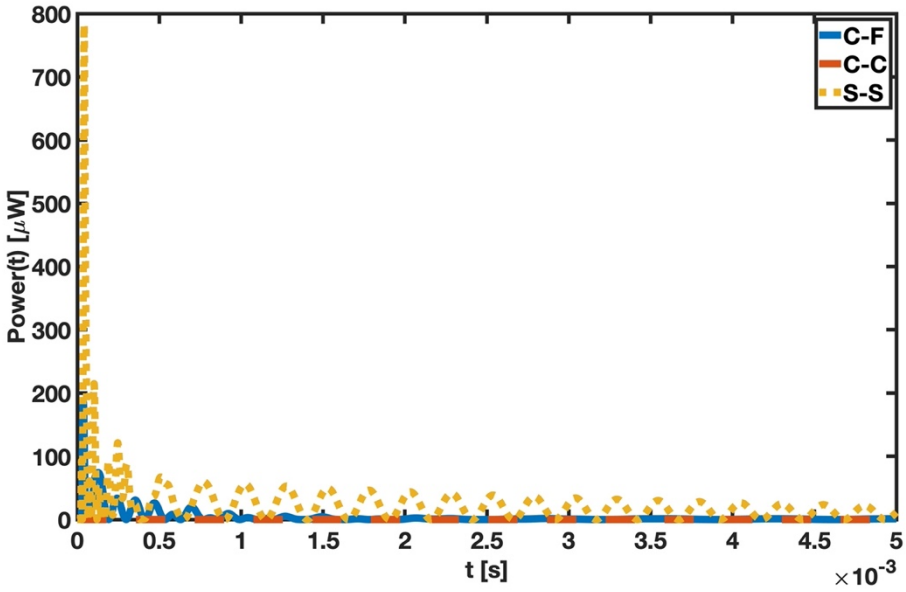

Figure 4.29 Dynamic behavior of a concentrated impulsive-loaded C-F, C-C, S-S series-connected bimorph FG Timoshenko PEH beam without tip mass configuration in terms of (a) midpoint displacement, (b) midpoint and top surface axial stress of the substructure, (c) midpoint and bottom surface axial stress of the upper piezoelectric material, (d) output voltage difference between electrodes, (e) produced current on the system, and (f) generated power.

The S-S boundary condition is shown to have the highest values in this loading for both mechanical and electrical outputs. A diminishing of the results near t=0 for the concentrated impulsive load due to the damping effect is also noticed in this study.

4.2.2.2.4 Material Structure Change

Finally, the FG PEH shown in Figure 4.2b is contrasted with the homogeneous structure PEH displayed in Figure 4.1 under four distinct load types to evaluate material structure change by delivering dynamic results. Series-connected bimorph Timoshenko PEH beam without tip mass configuration is analyzed. The power-law exponent is considered to be 0.5 in FGMs. The response values under a uniformly distributed step load are shown in Figure 4.30.

(a)

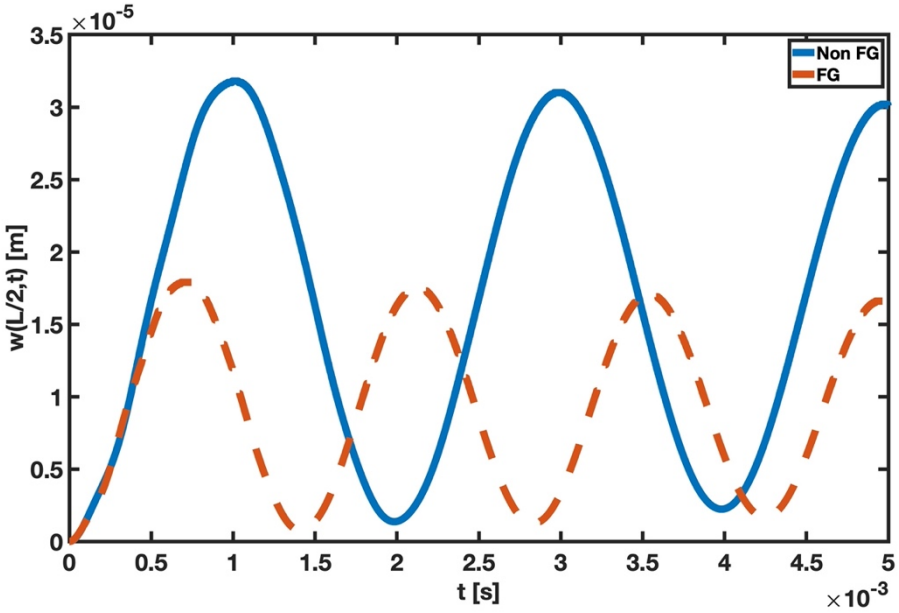

(b)

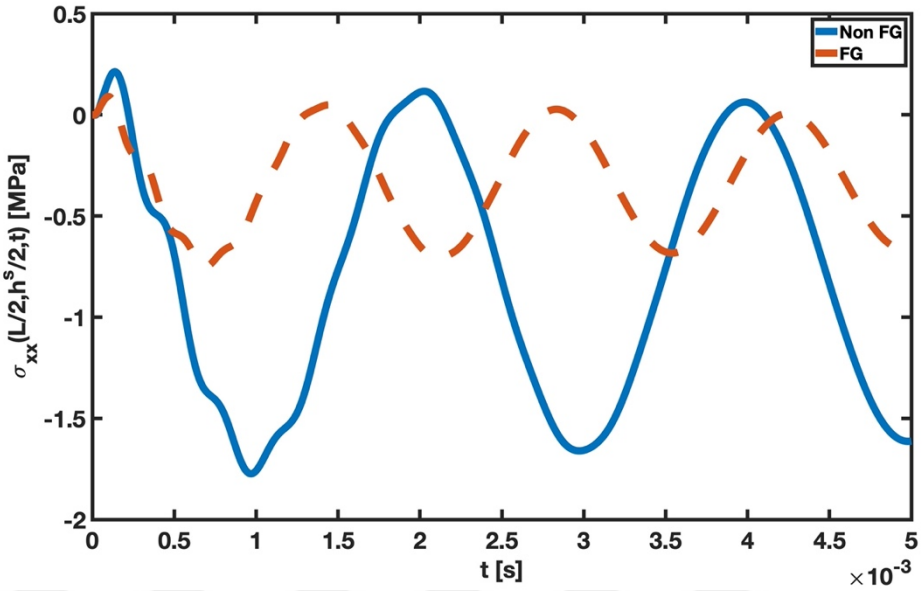
Non FG
FG
$\sigma_{xx}(L/2,h^s/2,t)$ [MPa]
t [s]
$\times 10^{-3}$

(c)

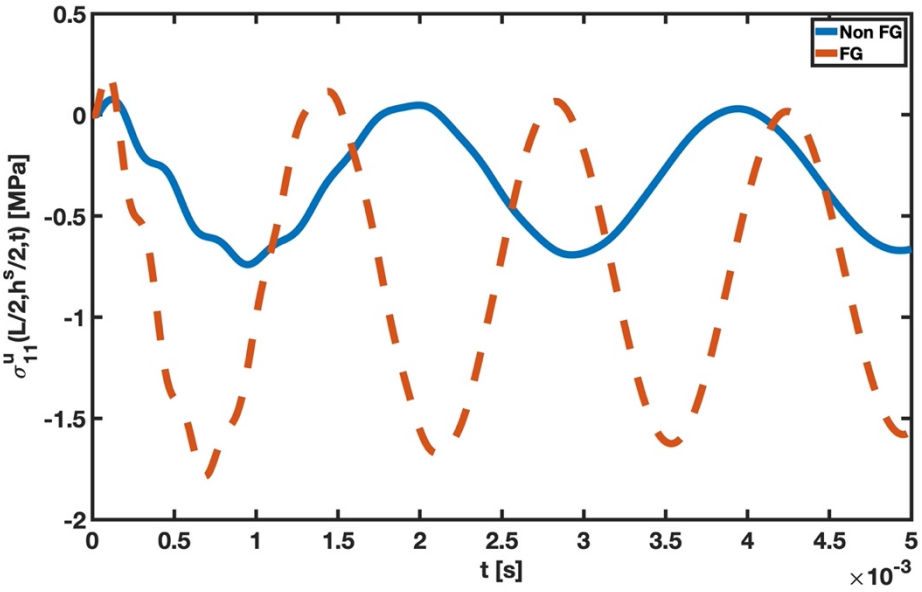
Non FG
FG
$\sigma^u_{11}(L/2,h^s/2,t)$ [MPa]
t [s]
$\times 10^{-3}$

(d)

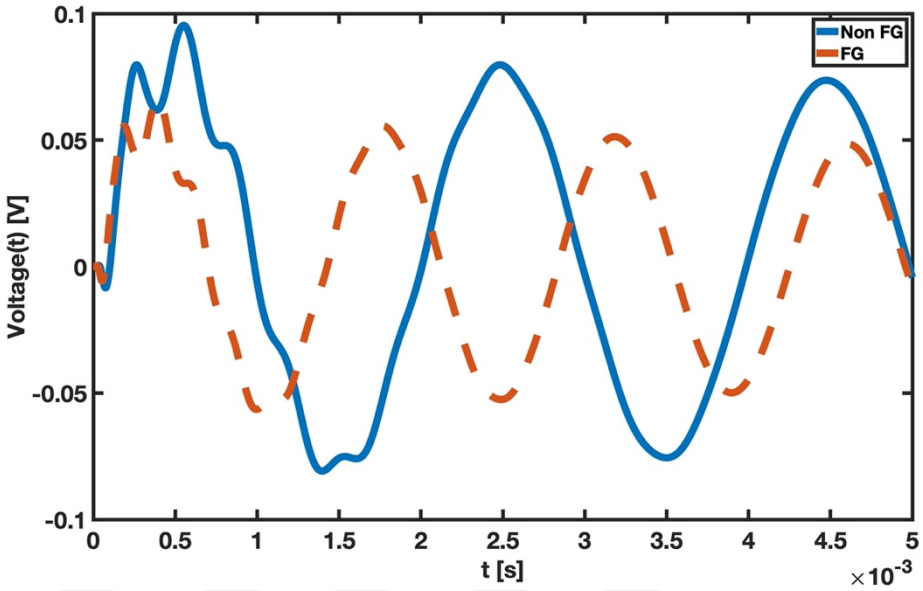
Non FG
FG
Voltage(t) [V]
0.1
0.05
0
-0.05
-0.1
0
0.5
1
1.5
2
2.5
3
3.5
4
4.5
5
t [s]
×10^-3

(e)

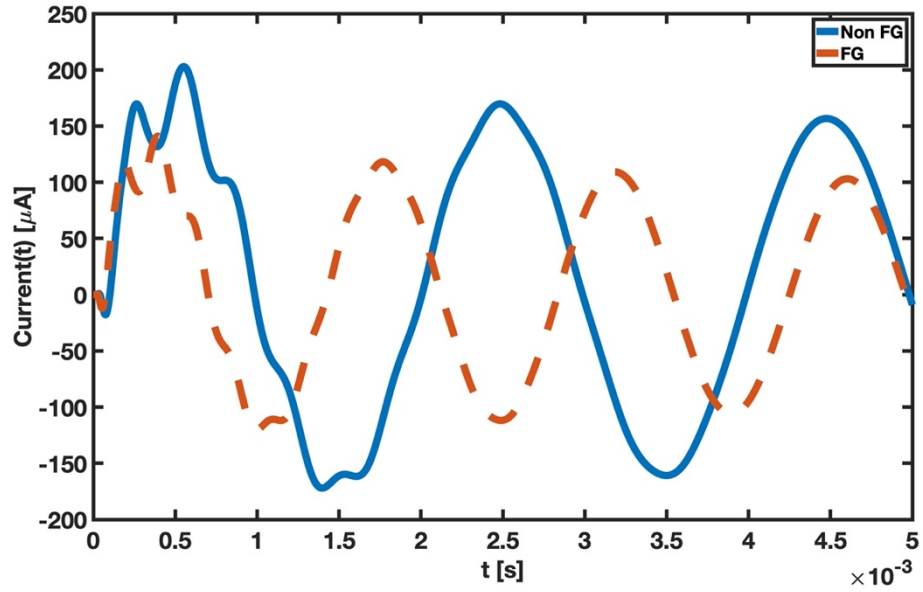
Non FG
FG
Current(t) [μA]
250
200
150
100
50
0
-50
-100
-150
-200
0
0.5
1
1.5
2
2.5
3
3.5
4
4.5
5
t [s]
×10^-3

(f)

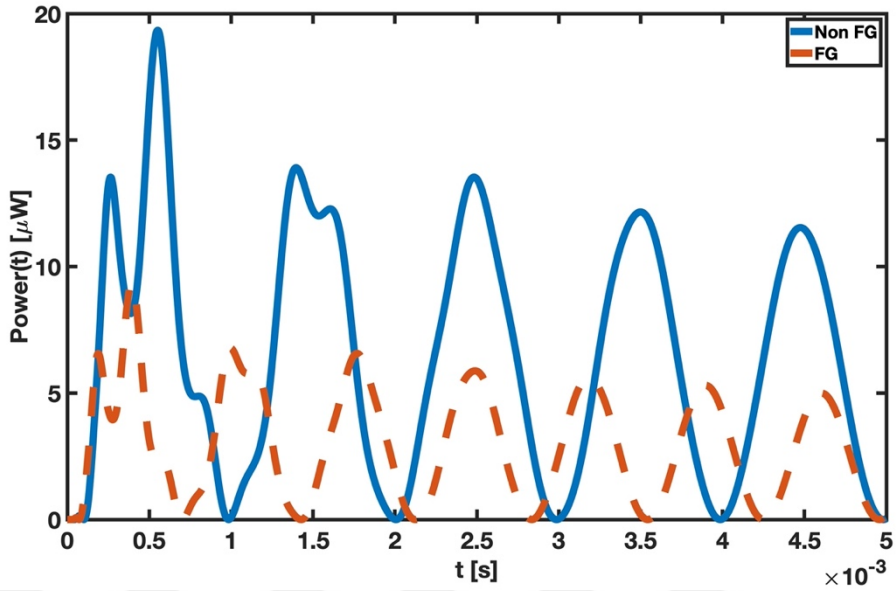

Figure 4.30 Dynamic behavior of a uniformly distributed step-loaded C-F series-connected bimorph Timoshenko PEH beam without tip mass configuration for FG and homogeneous material types in terms of (a) midpoint displacement, (b) midpoint and top surface axial stress of the substructure, (c) midpoint and bottom surface axial stress of the upper piezoelectric material, (d) output voltage difference between electrodes, (e) produced current on the system, and (f) generated power.

The material structure in Figure 4.1 increases the displacement, voltage, and electrical outputs in the PEH compared to Figure 4.2b when applying time-dependent force, consistent with the steady-state results. This situation is due to the use of PZT-5A, which has lower electrical properties. The FGM structure yields a greater axial stress value in the top piezoelectric material. Figure 4.31 shows the results of the concentrated step load.

(a)

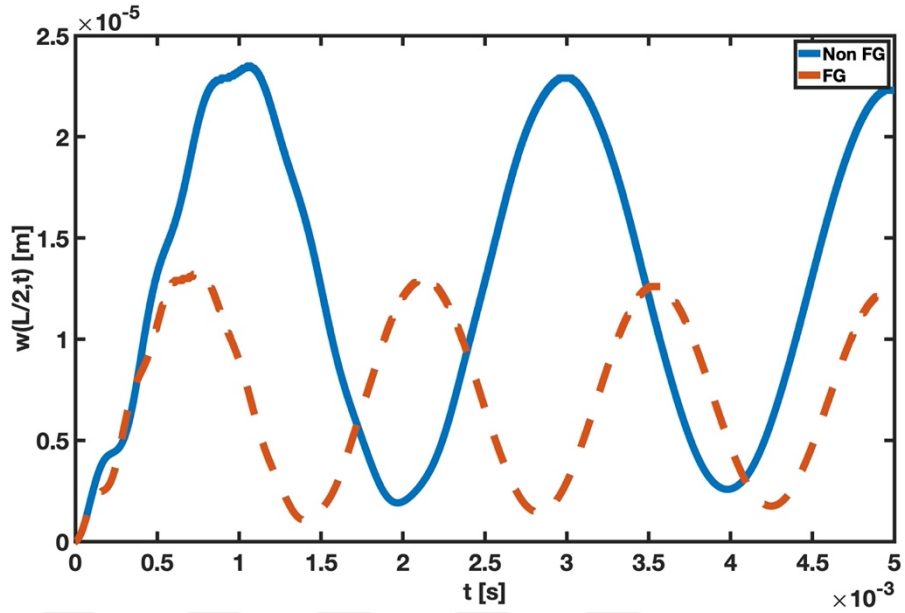
×10^-5
2.5
2
1.5
1
0.5
0
w(L/2,t) [m]
Non FG
FG
0
0.5
1
1.5
2
2.5
3
3.5
4
4.5
5
t [s]
×10^-3

(b)

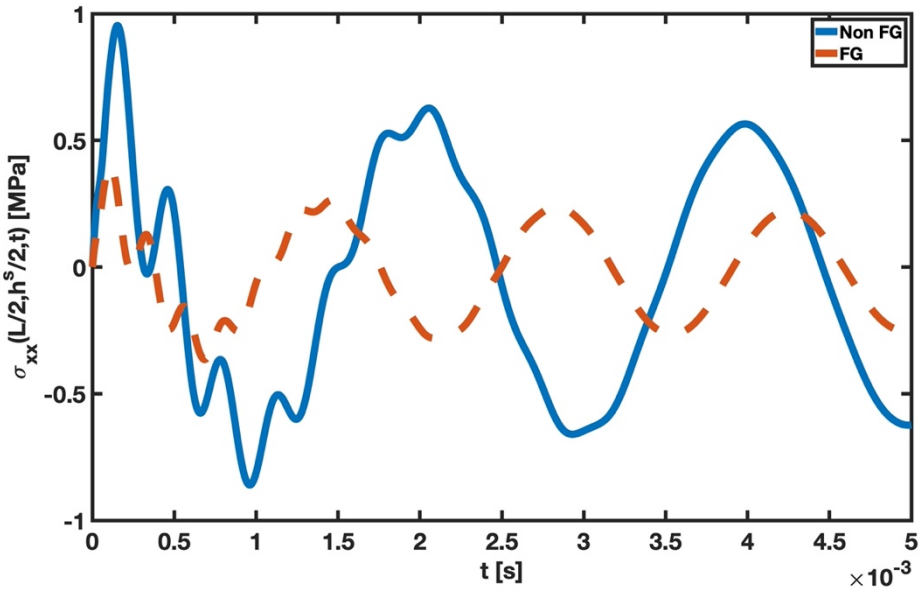
1
0.5
0
-0.5
-1
σxx(L/2,h^s/2,t) [MPa]
Non FG
FG
0
0.5
1
1.5
2
2.5
3
3.5
4
4.5
5
t [s]
×10^-3

(c)

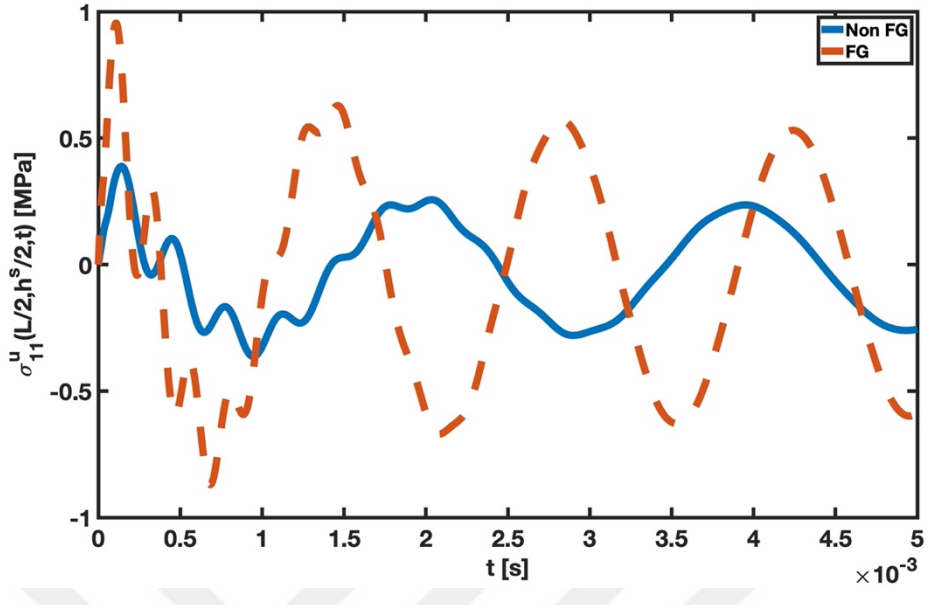
Non FG
FG
$\sigma_{11}^{u}(L/2,h^{s}/2,t)$ [MPa]
t [s]
×10^-3

(d)

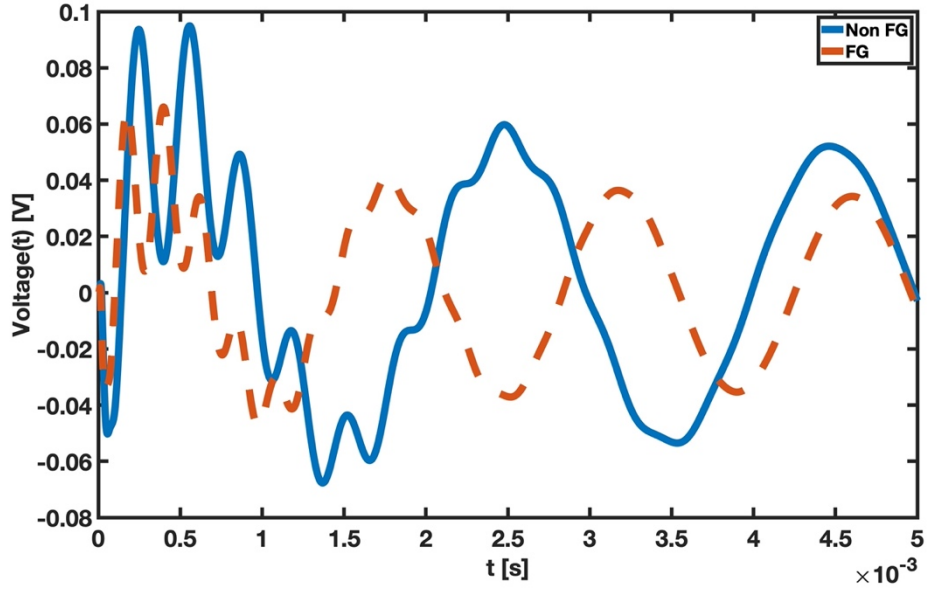
Non FG
FG
Voltage(t) [V]
t [s]
×10^-3

(e)

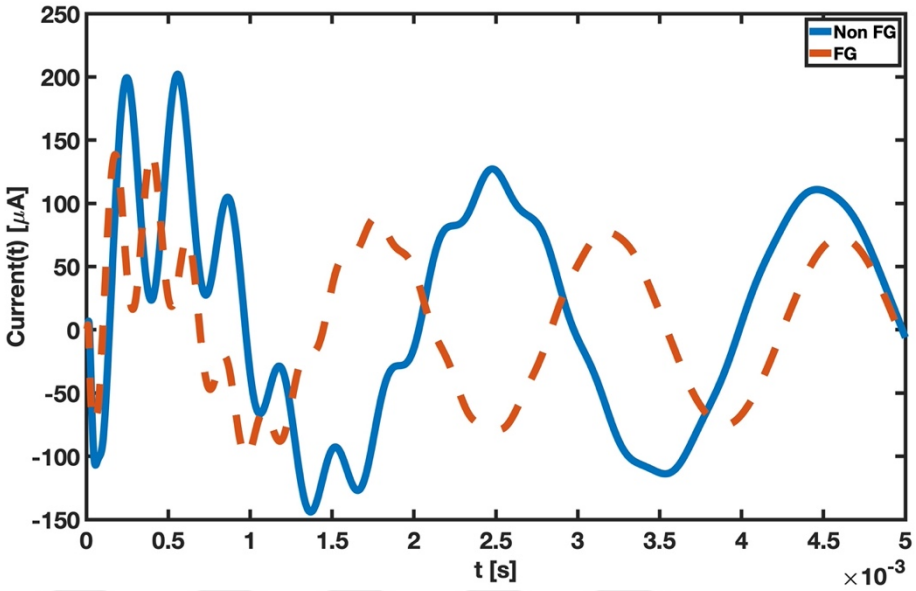

(f)

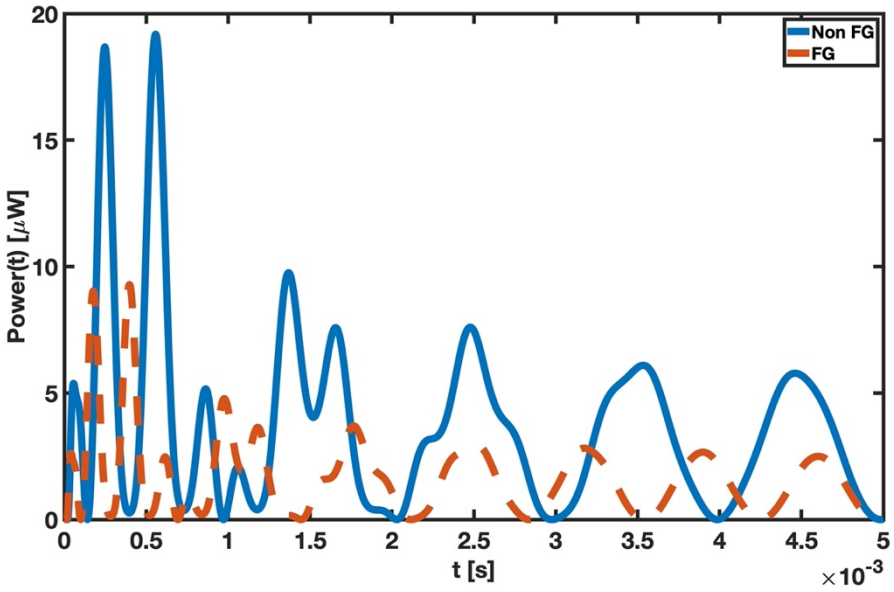

Figure 4.31 Dynamic behavior of a concentrated step-loaded C-F series-connected bimorph Timoshenko PEH beam without tip mass configuration for FG and homogeneous material types in terms of (a) midpoint displacement, (b) midpoint and top surface axial stress of the substructure, (c) midpoint and bottom surface axial stress of the upper piezoelectric material, (d) output voltage difference between electrodes, (e) produced current on the system, and (f) generated power.

The response of the uniformly distributed step load type is valid for the concentrated step load. The FGM structure type has a higher response frequency. Figure 4.32 shows the results of the concentrated harmonic load.

(a)

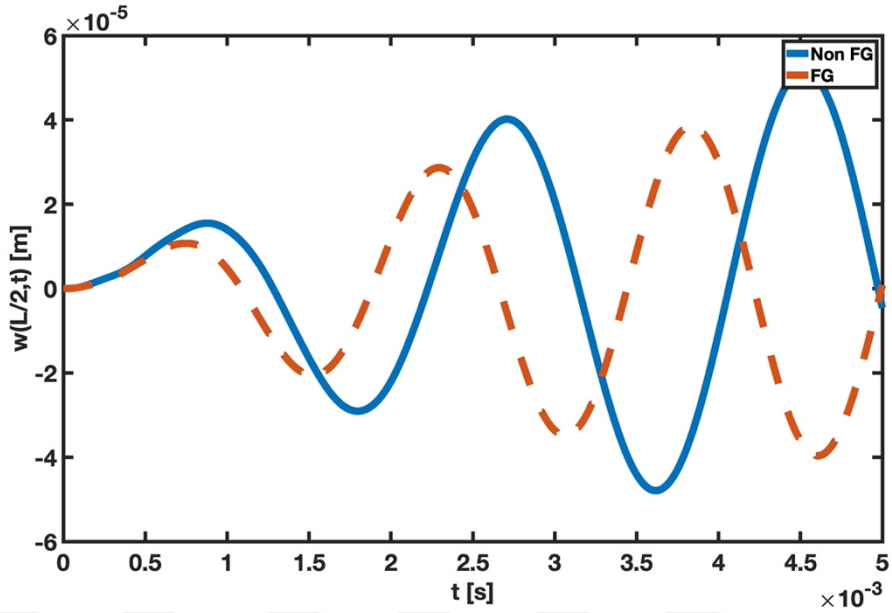
×10^-5
6
4
2
0
-2
-4
-6
w(L/2,t) [m]
0
0.5
1
1.5
2
2.5
3
3.5
4
4.5
5
t [s]
×10^-3
Non FG
FG

(b)

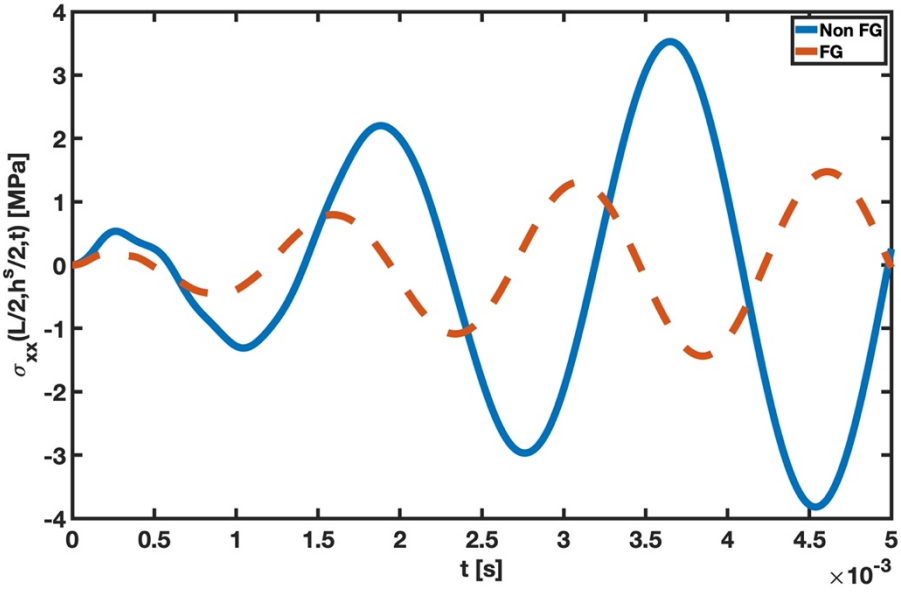
4
3
2
1
0
-1
-2
-3
-4
σxx(L/2,h^s/2,t) [MPa]
0
0.5
1
1.5
2
2.5
3
3.5
4
4.5
5
t [s]
×10^-3
Non FG
FG

(c)

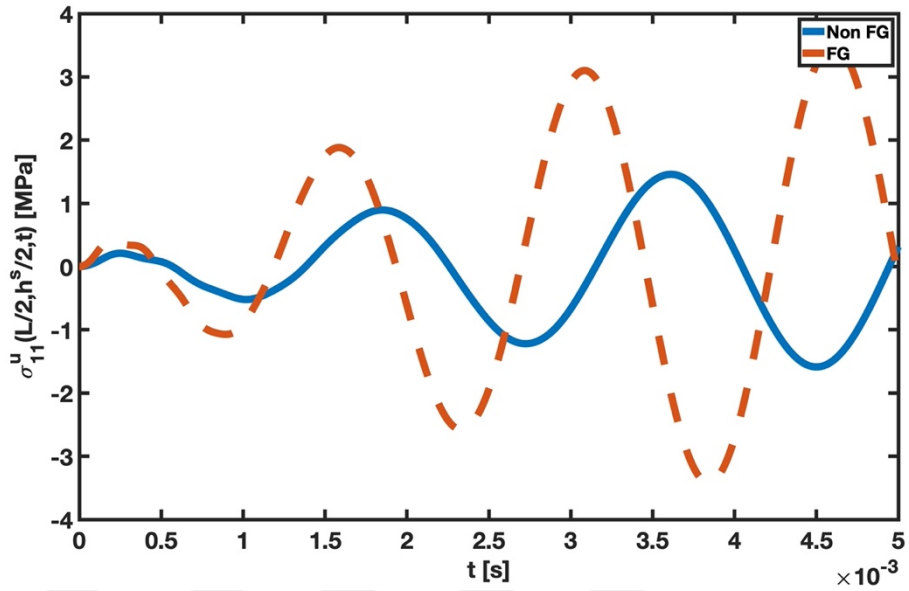
Non FG
FG
$\sigma_{11}^{u}(L/2,h^{s}/2,t)$ [MPa]
t [s]
×10^-3

(d)

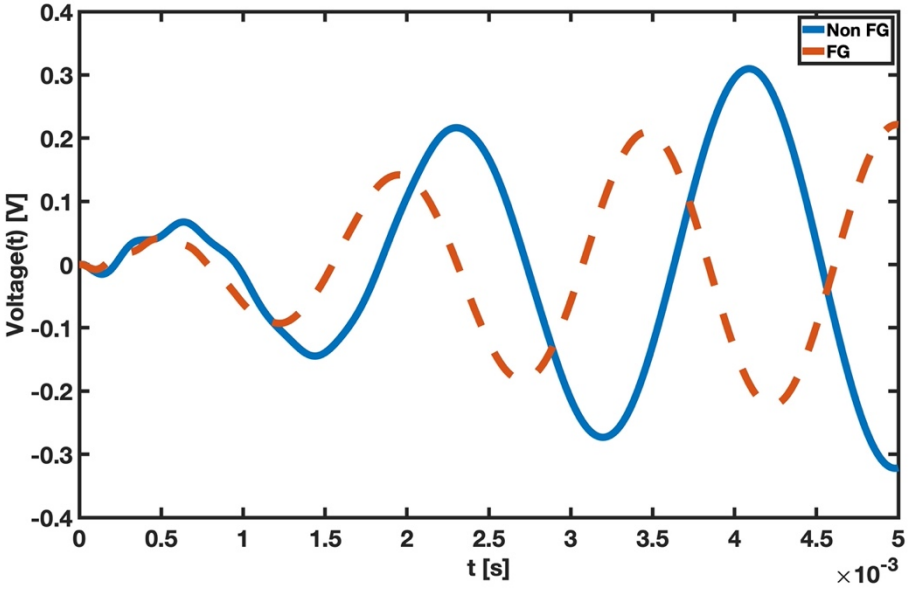
Non FG
FG
Voltage(t) [V]
t [s]
×10^-3

(e)

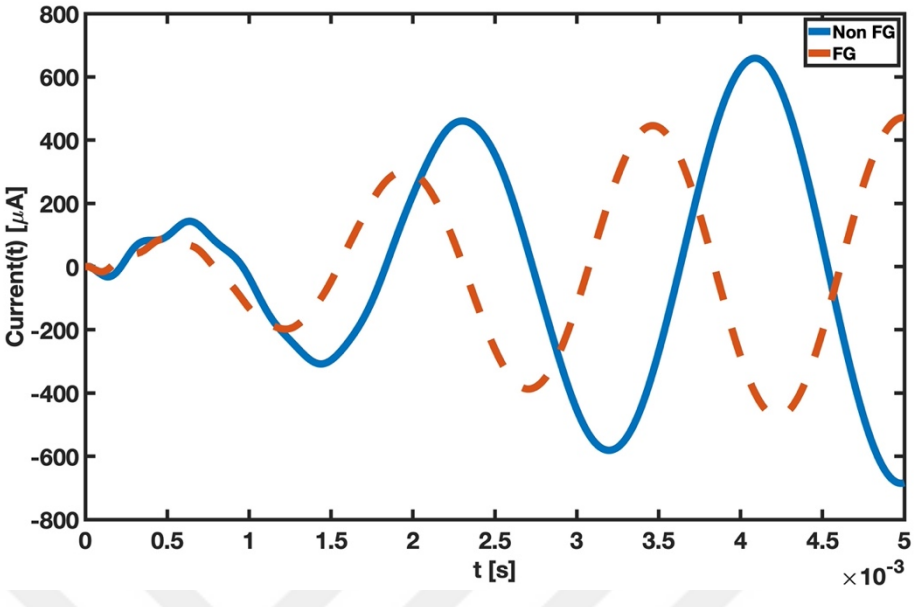

(f)

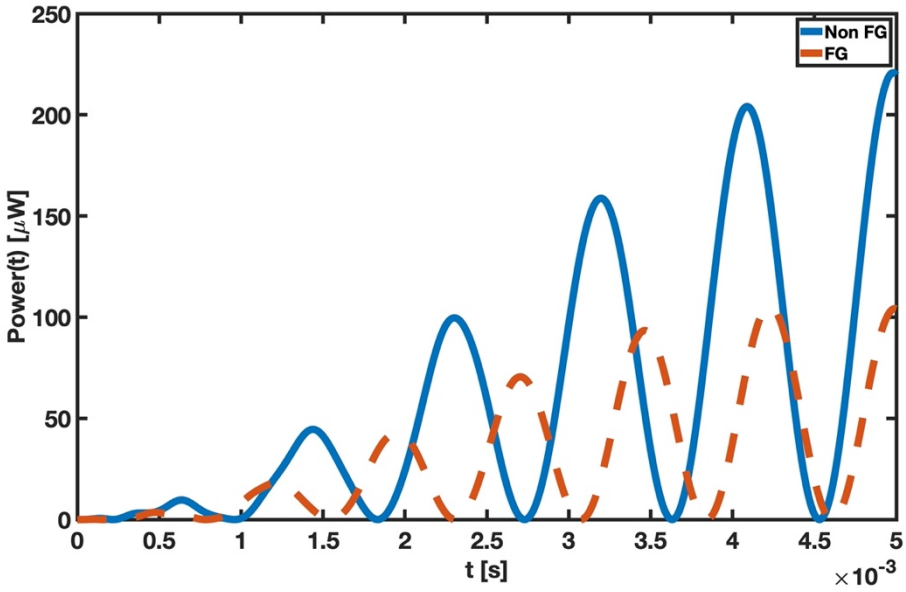

Figure 4.32 Dynamic behavior of a concentrated harmonic-loaded C-F series-connected bimorph Timoshenko PEH beam without tip mass configuration for FG and homogeneous material types in terms of (a) midpoint displacement, (b) midpoint and top surface axial stress of the substructure, (c) midpoint and bottom surface axial stress of the upper piezoelectric material, (d) output voltage difference between electrodes, (e) produced current on the system, and (f) generated power.

There is insufficient time to see the damping effect because the output continues to grow until 5 ms. The utilization of PZT-5A and aluminum materials minimizes outputs. The last load type is investigated in Figure 4.33.

(a)

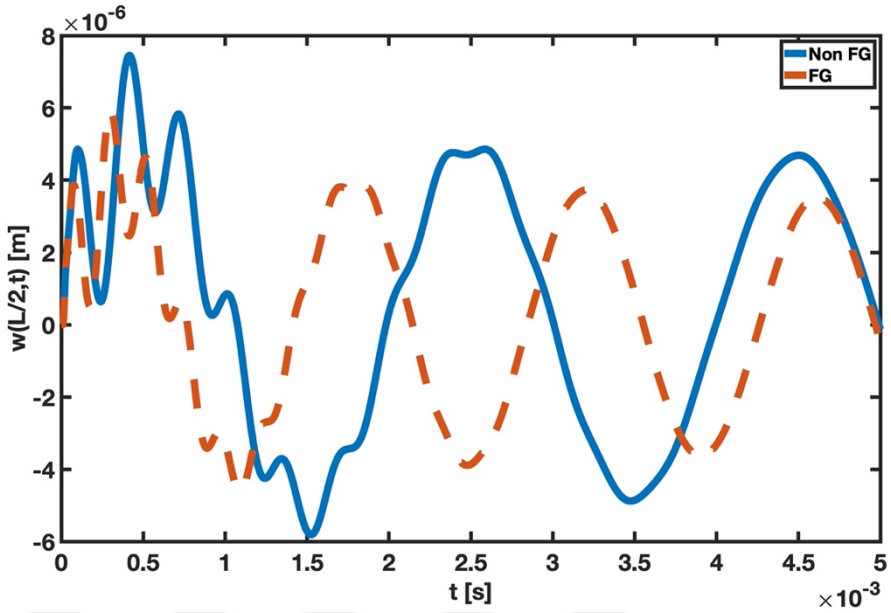
×10^-6
8
6
4
2
0
-2
-4
-6
w(L/2,t) [m]
0
0.5
1
1.5
2
2.5
3
3.5
4
4.5
5
t [s]
×10^-3
Non FG
FG

(b)

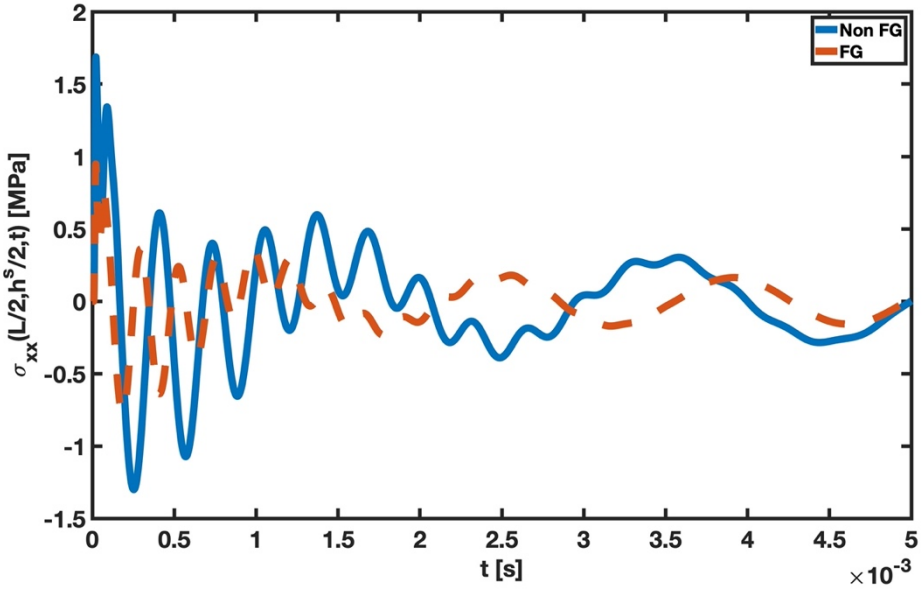
2
1.5
1
0.5
0
-0.5
-1
-1.5
σxx(L/2,h^s/2,t) [MPa]
0
0.5
1
1.5
2
2.5
3
3.5
4
4.5
5
t [s]
×10^-3
Non FG
FG

(c)

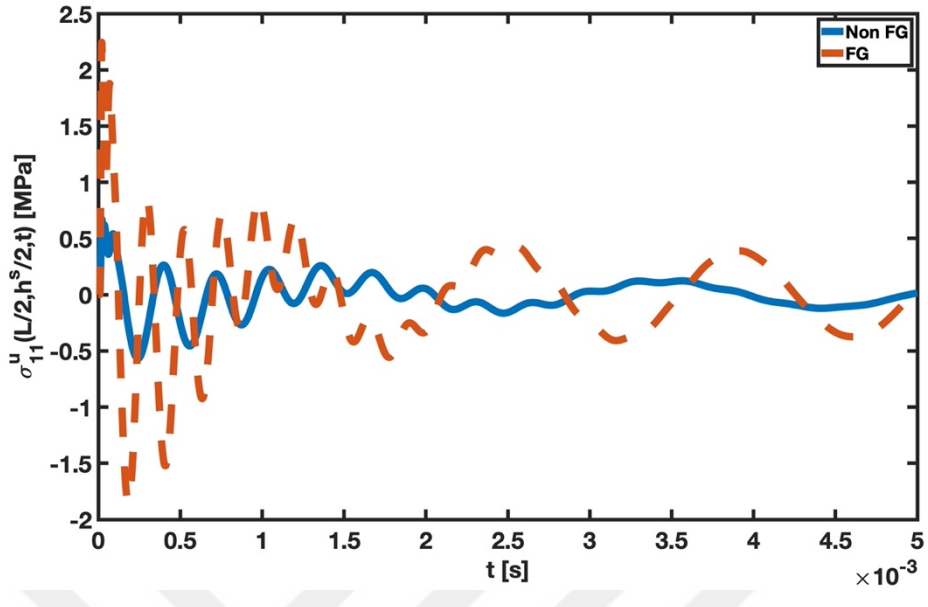
Non FG
FG
$\sigma_{11}^{u}(L/2,h^{s}/2,t)$ [MPa]
t [s]
×10^-3

(d)

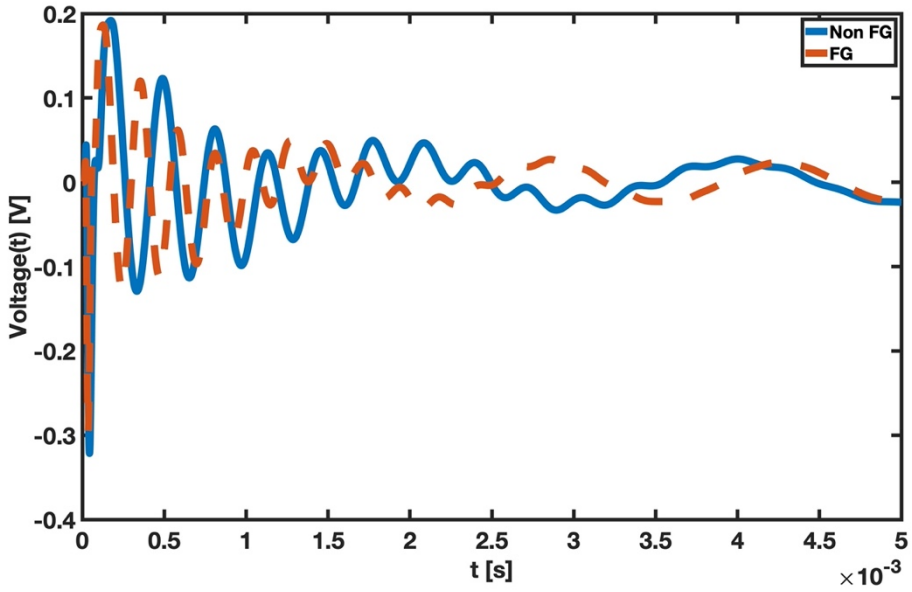
Non FG
FG
Voltage(t) [V]
t [s]
×10^-3

(e)

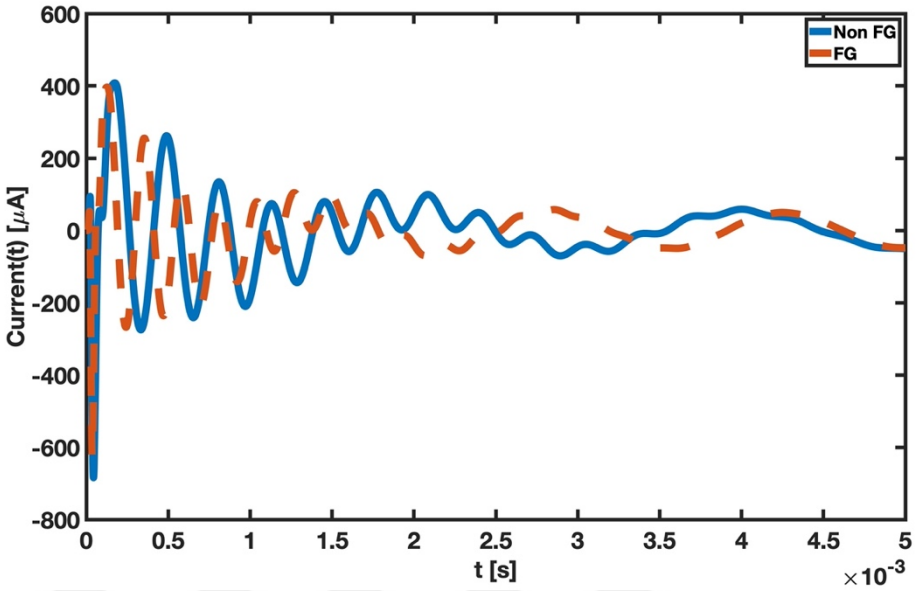

(f)

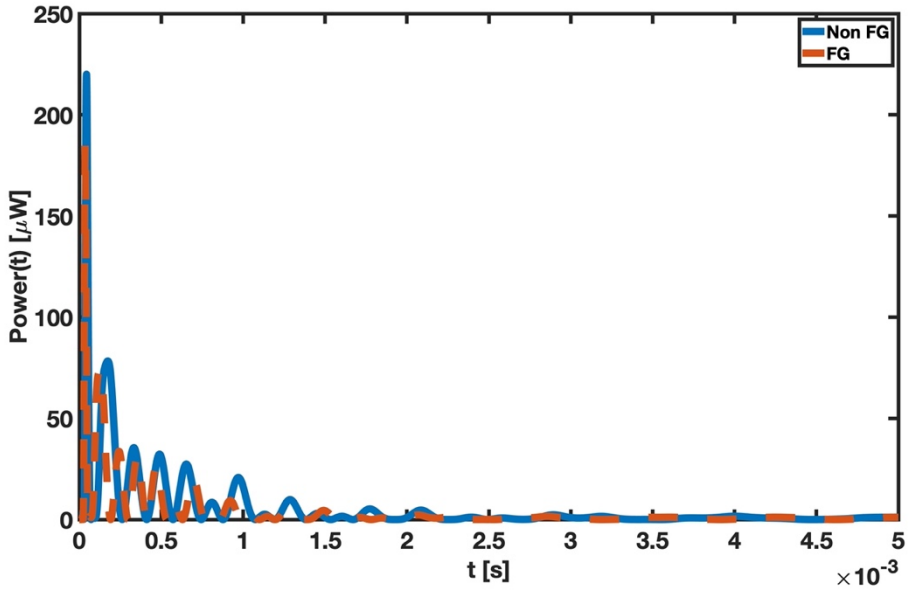

Figure 4.33 Dynamic behavior of a concentrated impulsive-loaded C-F series-connected bimorph Timoshenko PEH beam without tip mass configuration for FG and homogeneous material types in terms of (a) midpoint displacement, (b) midpoint and top surface axial stress of the substructure, (c) midpoint and bottom surface axial stress of the upper piezoelectric material, (d) output voltage difference between electrodes, (e) produced current on the system, and (f) generated power.

There is no apparent distinction between the homogenous type material and the FGM in this load type because the damping effect is observed quickly.

CHAPTER 5

CONCLUSION

This study uses the WQEM to demonstrate the free and forced vibration behavior of the six configurations of the FG Timoshenko PEH beam. The six configurations include the unimorph, the series- and parallel-connected bimorph structure, and the tip mass added to these configurations. In PEHs, materials for the substructure and piezoelectric components are FG. Substructure materials are expressed using the Mori-Tanaka micromechanical model, whereas piezoelectric materials are described using Voigt's rule of mixture. The displacement field equations, derived using the TBT, are transformed from the Cartesian coordinate system to the natural coordinate system for usage in WQEM by applying DQ techniques, making implementing the numerical technique easier. The nodes are combined using the GLL quadrature formulation, with the Lagrange interpolation function as the shape function. Using extended Hamilton's principle, the constitutive equations are utilized to determine the mass, stiffness, damping, and electrical voltage matrices for representing the equations of motion. The Rayleigh damping factor is used in the equations of motion to account for the damping. While the displacement functions are assumed to have a harmonic response when developing the formulation for the steady-state response of PEH, the four type forces are incorporated into the forced vibration formulation using the work equivalent approach. In addition, the Houbolt and Newmark techniques are used to solve the forced vibration analysis for which the boundary conditions are specified. These two techniques provide dynamic outcomes.

The free vibration results are verified using Ertürk's [33] experimental analysis by calculating FRF curves. Analytical solutions for P-P Timoshenko beams subjected to complicated dynamic forces validate the WQEM forced vibration results. The acquired FRF and displacement outcomes are consistent with the experimental and analytical results. The convergence of the method is investigated for both free and

forced vibration analysis. $N = 5$ is adequate to establish convergence. Accurately achieving outcomes in small node numbers under complicated loading implies that desired results can be obtained quickly since the size of the mass, stiffness, damping, electrical voltage, and force matrices decreases. Free and forced vibration results are produced in around two seconds of CPU time. The time step used in the forced vibration analysis is $1 \cdot (10)^{-6}$ s.

Piezoelectric material made of PZT-5A and PZT-5H and substructure material made of aluminum and brass have been employed in parametric analysis. These analyses revealed load resistance, power-law exponent, PEH configuration, boundary condition, material structure effects for the beam under base displacement, and four distinct load types. It is demonstrated that increasing the k value increases the beam's natural frequency for selected materials. Simultaneously, a decrease in displacement and electrical outputs under loading is noted. The PEH tip displacement velocity reduces as the load resistance increases, then increases again as it approaches the open-circuit condition. While the load resistance increases, the voltage difference rises, and the current output decreases. The largest estimated power generation is anticipated at middle levels of load resistance. Moreover, the beam vibrates at the highest frequency at the C-C boundary condition while demonstrating the slightest deformation. However, the C-C boundary condition is inappropriate for PEHs since it does not produce energy. For the examined PEH, connecting the circuit in series reduces electrical output, whereas doing so in parallel enhances it. Compared to bimorph structures, unimorph ones also produce less power. Finally, the system's voltage, current, power output, and natural and response frequencies are reduced by tip mass addition for applying time-dependent forces. However, this circumstance is not observed for the steady-state response of the PEH. The concentrated impulsive load's unique character causes the fluctuation of displacement, and the quickest damping in the outcomes is seen with this loading.

The following may explain the most efficient PEH setups for steady-state response and forced vibration analysis when all studies are examined. For a PEH that operates in steady-state response:

- Load resistance should be 44.9 kΩ.
- The power-law exponent should be zero, so PZT-5H material features should predominate if FGM is to be employed.
- The PEH with a homogenous structure that does not include PZT-5A should be used since it generates more energy than the FGM structure.
- A bimorph parallel-connected PEH with a tip mass should be utilized.

For a PEH operating in a time-dependent force application:

- A PEH with a zero power-law exponent or a homogeneous structure should be employed to produce a dominant configuration with PZT-5H characteristics.
- A parallel-connected bimorph PEH with no tip mass should be used.
- The C-F boundary condition should be used for concentrated harmonic loading, whereas the S-S boundary condition is appropriate for the other three loading forms.

A PEH can be designed in a way that deviates from accepted conventions, thanks to the FGM. The PEH is subjected to various types of force, and altering material structure is a key design factor. Numerical techniques play a growing role in performing these assessments precisely and quickly. The results indicate that WQEM is an alternative technique that can produce reliable results. This approach eliminates specific problems in other techniques and has no reason not to be applied more frequently. The presentation of the curved PEH formulation under thermal and magnetic loads in further work will be interesting.

REFERENCES

[1] H. S. Shen and Z. X. Wang, “Assessment of Voigt and Mori–Tanaka models for vibration analysis of functionally graded plates,” *Compos Struct*, vol. 94, no. 7, pp. 2197–2208, Jun. 2012, doi: 10.1016/J.COMPSTRUCT.2012.02.018.

[2] X. Wang, “Differential Quadrature and Differential Quadrature Based Element Methods,” *Differential Quadrature and Differential Quadrature Based Element Methods*, 2015, doi: 10.1016/C2014-0-03612-X.

[3] M. Koizumi, “FGM activities in Japan,” *Compos B Eng*, vol. 28, no. 1–2, pp. 1–4, Jan. 1997, doi: 10.1016/S1359-8368(96)00016-9.

[4] J. M. Dietl, A. M. Wickenheiser, and E. Garcia, “A Timoshenko beam model for cantilevered piezoelectric energy harvesters,” *Smart Mater Struct*, vol. 19, no. 5, p. 055018, Mar. 2010, doi: 10.1088/0964-1726/19/5/055018.

[5] D. Wu, A. Liu, Y. Huang, Y. Huang, Y. Pi, and W. Gao, “Dynamic analysis of functionally graded porous structures through finite element analysis,” *Eng Struct*, vol. 165, pp. 287–301, Jun. 2018, doi: 10.1016/J.ENGSTRUCT.2018.03.023.

[6] W. Songsuwan, M. Pimsarn, and N. Wattanasakulpong, “Dynamic Responses of Functionally Graded Sandwich Beams Resting on Elastic Foundation Under Harmonic Moving Loads,” *https://doi.org/10.1142/S0219455418501122*, vol. 18, no. 9, Sep. 2018, doi: 10.1142/S0219455418501122.

[7] R. Ansari, M. Faghih Shojaei, V. Mohammadi, R. Gholami, and F. Sadeghi, “Nonlinear forced vibration analysis of functionally graded carbon nanotube-reinforced composite Timoshenko beams,” *Compos Struct*, vol. 113, no. 1, pp. 316–327, Jul. 2014, doi: 10.1016/J.COMPSTRUCT.2014.03.015.

[8] F. F. Calim, “Free and forced vibration analysis of axially functionally graded Timoshenko beams on two-parameter viscoelastic foundation,” *Compos B Eng*, vol. 103, pp. 98–112, Oct. 2016, doi: 10.1016/J.COMPOSITESB.2016.08.008.

[9] N. Wattanasakulpong and Q. Mao, “Dynamic response of Timoshenko functionally graded beams with classical and non-classical boundary conditions using Chebyshev collocation method,” *Compos Struct*, vol. 119, pp. 346–354, Jan. 2015, doi: 10.1016/J.COMPSTRUCT.2014.09.004.

[10] I. Eshraghi and S. Dag, “Domain-boundary element method for elastodynamics of functionally graded Timoshenko beams,” *Comput Struct*, vol. 195, pp. 113–125, Jan. 2018, doi: 10.1016/J.COMPSTRUC.2017.10.007.

[11] H. Zhong and T. Yu, “A weak form quadrature element method for plane elasticity problems,” *Appl Math Model*, vol. 33, no. 10, pp. 3801–3814, Oct. 2009, doi: 10.1016/J.APM.2008.12.007.

[12] Z. H. Zhi and Y. Z. Guang, “Analysis of thin plates by the weak form quadrature element method,” *Sci China Phys Mech Astron*, vol. 55, no. 5, pp. 861–871, May 2012, doi: 10.1007/S11433-012-4684-Y/METRICS.

[13] S. Yuan and J. Du, “Effective stress-based upper bound limit analysis of unsaturated soils using the weak form quadrature element method,” *Comput Geotech*, vol. 98, pp. 172–180, Jun. 2018, doi: 10.1016/J.COMPGEO.2018.02.008.

[14] S. Yuan and H. Zhong, “Three dimensional analysis of unconfined seepage in earth dams by the weak form quadrature element method,” *J Hydrol (Amst)*, vol. 533, pp. 403–411, Feb. 2016, doi: 10.1016/J.JHYDROL.2015.12.034.

[15] C. Jin, X. Wang, and L. Ge, “Novel weak form quadrature element method with expanded Chebyshev nodes,” *Appl Math Lett*, vol. 34, no. 1, pp. 51–59, Aug. 2014, doi: 10.1016/J.AML.2014.03.015.

[16] Y. Wang and X. Wang, “Free vibration analysis of soft-core sandwich beams by the novel weak form quadrature element method,” *Journal of Sandwich Structures and Materials*, vol. 18, no. 3, pp. 294–320, May 2016, doi: 10.1177/1099636215601373/ASSET/IMAGES/LARGE/10.1177_1099636215601373-FIG2.JPEG.

[17] N. Xiao and H. Zhong, “Non-linear quadrature element analysis of planar frames based on geometrically exact beam theory,” *Int J Non Linear Mech*, vol. 47, no. 5, pp. 481–488, Jun. 2012, doi: 10.1016/J.IJNONLINMEC.2011.09.021.

[18] R. Zhang and H. Zhong, “A quadrature element formulation of an energy–momentum conserving algorithm for dynamic analysis of geometrically exact beams,” *Comput Struct*, vol. 165, pp. 96–106, Mar. 2016, doi: 10.1016/J.COMPSTRUC.2015.12.007.

[19] R. He and H. Zhong, “Large deflection elasto-plastic analysis of frames using the weak-form quadrature element method,” *Finite Elements in Analysis and Design*, vol. 50, pp. 125–133, Mar. 2012, doi: 10.1016/J.FINEL.2011.09.003.

[20] X. Zhou, K. Huang, and Z. Li, “Geometrically nonlinear beam analysis of composite wind turbine blades based on quadrature element method,” *Int J Non Linear Mech*, vol. 104, pp. 87–99, Sep. 2018, doi: 10.1016/J.IJNONLINMEC.2018.05.007.

[21] H. Hou and G. He, “Static and dynamic analysis of two-layer Timoshenko composite beams by weak-form quadrature element method,” *Appl Math Model*, vol. 55, pp. 466–483, Mar. 2018, doi: 10.1016/J.APM.2017.11.007.

[22] K. Kim, K. Ri, C. Yun, C. Kim, and Y. Kim, “Analysis of the nonlinear forced vibration and stability of composite beams using the reduced-order model,” *AIP Adv*, vol. 11, no. 3, Mar. 2021, doi: 10.1063/5.0039212/991666.

[23] M. Trabelssi, S. El-Borgi, and M. I. Friswell, “A high-order FEM formulation for free and forced vibration analysis of a nonlocal nonlinear graded

Timoshenko nanobeam based on the weak form quadrature element method," *Archive of Applied Mechanics*, vol. 90, no. 10, pp. 2133–2156, Oct. 2020, doi: 10.1007/S00419-020-01713-3/FIGURES/3.

[24] C. Jin and X. Wang, "Accurate free vibration analysis of Euler functionally graded beams by the weak form quadrature element method," *Compos Struct*, vol. 125, pp. 41–50, Jul. 2015, doi: 10.1016/J.COMPSTRUCT.2015.01.039.

[25] K. Ri, W. Han, C. Pak, K. Kim, and C. Yun, "Nonlinear forced vibration analysis of the composite shaft-disk system combined the reduced-order model with the IHB method," *Nonlinear Dyn*, vol. 104, no. 4, pp. 3347–3364, Jun. 2021, doi: 10.1007/S11071-021-06510-3/FIGURES/13.

[26] X. Wang, Z. Yuan, and C. Jin, "3D free vibration analysis of multi-directional FGM parallelepipeds using the quadrature element method," *Appl Math Model*, vol. 68, pp. 383–404, Apr. 2019, doi: 10.1016/J.APM.2018.11.030.

[27] X. Wang, X. Liang, and C. Jin, "Accurate dynamic analysis of functionally graded beams under a moving point load," *http://dx.doi.org/10.1080/15397734.2016.1145060*, vol. 45, no. 1, pp. 76–91, Jan. 2016, doi: 10.1080/15397734.2016.1145060.

[28] Z. Shen, J. Xia, and P. Cheng, "Geometrically nonlinear dynamic analysis of FG-CNTRC plates subjected to blast loads using the weak form quadrature element method," *Compos Struct*, vol. 209, pp. 775–788, Feb. 2019, doi: 10.1016/J.COMPSTRUCT.2018.11.009.

[29] C. Jin and X. Wang, "Quadrature element method for vibration analysis of functionally graded beams," *Eng Comput (Swansea)*, vol. 34, no. 4, pp. 1293–1313, Jun. 2017, doi: 10.1108/EC-07-2016-0271.

[30] H. A. Sodano, G. Park, and D. J. Inman, "Estimation of Electric Charge Output for Piezoelectric Energy Harvesting," *Strain*, vol. 40, no. 2, pp. 49–58, May 2004, doi: 10.1111/J.1475-1305.2004.00120.X.

[31] C. De Marqui Junior, A. Erturk, and D. J. Inman, “An electromechanical finite element model for piezoelectric energy harvester plates,” *J Sound Vib*, vol. 327, no. 1–2, pp. 9–25, Oct. 2009, doi: 10.1016/J.JSV.2009.05.015.

[32] W. Zhou, B. Wang, C. W. Lim, and Z. Yang, “A distributed-parameter electromechanical coupling model for a segmented arc-shaped piezoelectric energy harvester,” *Mech Syst Signal Process*, vol. 146, p. 107005, Jan. 2021, doi: 10.1016/J.YMSSP.2020.107005.

[33] A. Erturk, “Assumed-modes modeling of piezoelectric energy harvesters: Euler–Bernoulli, Rayleigh, and Timoshenko models with axial deformations,” *Comput Struct*, vol. 106–107, pp. 214–227, Sep. 2012, doi: 10.1016/J.COMPSTRUC.2012.05.010.

[34] G. Wang, “Analysis of bimorph piezoelectric beam energy harvesters using Timoshenko and Euler-Bernoulli beam theory,” *J Intell Mater Syst Struct*, vol. 24, no. 2, pp. 226–239, Jan. 2013, doi: 10.1177/1045389X12461080/ASSET/IMAGES/LARGE/10.1177_1045389X12461080-FIG10.JPEG.

[35] Y. Amini, H. Emdad, and M. Farid, “An accurate model for numerical prediction of piezoelectric energy harvesting from fluid structure interaction problems,” *Smart Mater Struct*, vol. 23, no. 9, p. 095034, Aug. 2014, doi: 10.1088/0964-1726/23/9/095034.

[36] J. Yang and H. J. Xiang, “Thermo-electro-mechanical characteristics of functionally graded piezoelectric actuators,” *Smart Mater Struct*, vol. 16, no. 3, p. 784, Apr. 2007, doi: 10.1088/0964-1726/16/3/028.

[37] A. Doroushi, M. R. Eslami, and A. Komeili, “Vibration Analysis and Transient Response of an FGPM Beam under Thermo-Electro-Mechanical Loads using Higher-Order Shear Deformation Theory,” *http://dx.doi.org/10.1177/1045389X11398162*, vol. 22, no. 3, pp. 231–243, Feb. 2011, doi: 10.1177/1045389X11398162.

[38] Y. Amini, H. Emdad, and M. Farid, “Finite element modeling of functionally graded piezoelectric harvesters,” *Compos Struct*, vol. 129, pp. 165–176, Oct. 2015, doi: 10.1016/J.COMPSTRUCT.2015.04.011.

[39] S. K. Parashar and P. Sharma, “Modal analysis of shear-induced flexural vibration of FGPM beam using Generalized Differential Quadrature method,” *Compos Struct*, vol. 139, pp. 222–232, Apr. 2016, doi: 10.1016/J.COMPSTRUCT.2015.12.012.

[40] M. Derayatifar, M. Tahani, and H. Moeenfard, “Nonlinear analysis of functionally graded piezoelectric energy harvesters,” *Compos Struct*, vol. 182, pp. 199–208, Dec. 2017, doi: 10.1016/J.COMPSTRUCT.2017.09.030.

[41] T. Mori and K. Tanaka, “Average stress in matrix and average elastic energy of materials with misfitting inclusions,” *Acta Metallurgica*, vol. 21, no. 5, pp. 571–574, May 1973, doi: 10.1016/0001-6160(73)90064-3.

[42] Prof. S. P. Timoshenko, “X. On the transverse vibrations of bars of uniform cross-section,” *https://doi.org/10.1080/14786442208633855*, vol. 43, no. 253, pp. 125–131, Jan. 2009, doi: 10.1080/14786442208633855.

[43] G. R. Cowper, “The Shear Coefficient in Timoshenko’s Beam Theory,” *J Appl Mech*, vol. 33, no. 2, pp. 335–340, Jun. 1966, doi: 10.1115/1.3625046.

[44] J. A. M. Carrer, S. A. Fleischfresser, L. F. T. Garcia, and W. J. Mansur, “Dynamic analysis of Timoshenko beams by the boundary element method,” *Eng Anal Bound Elem*, vol. 37, no. 12, pp. 1602–1616, Dec. 2013, doi: 10.1016/j.enganabound.2013.08.007.

[45] P. Hajheidari, I. Stiharu, and R. Bhat, “Performance of tapered cantilever piezoelectric energy harvester based on Euler–Bernoulli and Timoshenko Beam theories,” *J Intell Mater Syst Struct*, vol. 31, no. 4, pp. 487–502, Mar. 2020,doi:10.1177/1045389X19891526/ASSET/IMAGES/LARGE/10.1177_1045389X19891526-FIG17.JPEG.

APPENDICES

A. Stiffness Matrix and the Strain Energy Coefficients

$$K_{ij}^{uu} = \int_0^L \left(\mathbf{A}^{(A\,1)}\right) \cdot \frac{dl_i(x)}{dx} \cdot \frac{dl_j(x)}{dx} \cdot dx = \left(\mathbf{A}^{(A\,1)}\right) \cdot \frac{2}{L} \cdot \sum_{k=1}^{\tilde{N}} H_k \cdot A_{ki} \cdot A_{kj} \qquad (A\,1)$$

$$K_{ij}^{u\varphi} = -\int_0^L \left(\mathbf{A}^{(A\,2)}\right) \cdot \frac{dl_i(x)}{dx} \cdot \frac{dl_j(x)}{dx} \cdot dx = -\left(\mathbf{A}^{(A\,2)}\right) \cdot \frac{2}{L} \cdot \sum_{k=1}^{\tilde{N}} H_k \cdot A_{ki} \cdot A_{kj} \qquad (A\,2)$$

$$K_{ij}^{uw} = 0 \qquad (A\,3)$$

$$K_{ij}^{\varphi u} = -\int_0^L \left(\mathbf{A}^{(A\,4)}\right) \cdot \frac{dl_j(x)}{dx} \cdot \frac{dl_i(x)}{dx} \cdot dx = -\left(\mathbf{A}^{(A\,4)}\right) \cdot \frac{2}{L} \cdot \sum_{k=1}^{\tilde{N}} H_k \cdot A_{kj} \cdot A_{ki} \qquad (A\,4)$$

$$K_{ij}^{\varphi\varphi} = \int_0^L \left(\mathbf{A}^{(A\,5)}\right) \cdot \frac{dl_i(x)}{dx} \cdot \frac{dl_j(x)}{dx} \cdot dx + \int_0^L \left(\mathbf{B}^{(A\,5)}\right) \cdot l_i(x) \cdot l_j(x) \cdot dx$$

$$= \left(\mathbf{A}^{(A\,5)}\right) \cdot \frac{2}{L} \cdot \sum_{k=1}^{\tilde{N}} H_k \cdot A_{ki} \cdot A_{kj} + \left(\mathbf{B}^{(A\,5)}\right) \cdot \frac{L}{2} \cdot \sum_{k=1}^{\tilde{N}} H_k \cdot l_i(\xi_k) \cdot l_j(\xi_k) \qquad (A\,5)$$

$$K_{ij}^{\varphi w} = -\int_0^L \left(\mathbf{A}^{(A\,6)}\right) \cdot l_i(x) \cdot \frac{dl_j(x)}{dx} \cdot dx = -\left(\mathbf{A}^{(A\,6)}\right) \cdot \sum_{k=1}^{\tilde{N}} H_k \cdot l_i(\xi_k) \cdot A_{kj} \tag{A 6}$$

$$K_{ij}^{wu} = 0 \tag{A 7}$$

$$K_{ij}^{w\varphi} = -\int_0^L \left(\mathbf{A}^{(A\,8)}\right) \cdot \frac{dl_i(x)}{dx} \cdot l_j(x) \cdot dx = -\left(\mathbf{A}^{(A\,8)}\right) \cdot \sum_{k=1}^{\tilde{N}} H_k \cdot A_{ki} \cdot l_j(\xi_k) \tag{A 8}$$

$$K_{ij}^{ww} = \int_0^L \left(\mathbf{A}^{(A\,9)}\right) \cdot \frac{dl_i(x)}{dx} \cdot \frac{dl_j(x)}{dx} \cdot dx = \left(\mathbf{A}^{(A\,9)}\right) \cdot \frac{2}{L} \cdot \sum_{k=1}^{\tilde{N}} H_k \cdot A_{ki} \cdot A_{kj} \tag{A 9}$$

$$\theta_i^u = \int_0^L \left(\mathbf{A}^{(A\,10)}\right) \cdot \frac{dl_i(x)}{dx} \cdot dx = \left(\mathbf{A}^{(A\,10)}\right) \cdot \sum_{k=1}^{\tilde{N}} H_k \cdot A_{ki} \tag{A 10}$$

$$\theta_i^{\varphi} = \int_0^L \left(\mathbf{A}^{(A\,11)}\right) \cdot \frac{dl_i(x)}{dx} \cdot dx = \left(\mathbf{A}^{(A\,11)}\right) \cdot \sum_{k=1}^{\tilde{N}} H_k \cdot A_{ki} \tag{A 11}$$

$$\theta_i^w = 0 \tag{A 12}$$

Table A-1 The stiffness matrix and additional coefficients for six different PEH configurations depicted in Figure 1.3.

Stiffness Matrix Coefficients	**PEH Configurations**					
	The unimorph PEH without tip mass. (Figure 1.3a)	The unimorph PEH with tip mass at $x = L$. (Figure 1.3b)	The series-connected bimorph PEH without tip mass. (Figure 1.3c)	The series-connected bimorph PEH with tip mass at $x = L$. (Figure 1.3d)	The parallel-connected bimorph PEH without tip mass. (Figure 1.3e)	The parallel-connected bimorph PEH with tip mass at $x = L$. (Figure 1.3f)
$\mathbf{A}^{(A\,1)}$	$A_{11}^{s} + A_{11}^{pu}$	$A_{11}^{s} + A_{11}^{pu}$	$A_{11}^{s} + A_{11}^{pu} + A_{11}^{pl}$	$A_{11}^{s} + A_{11}^{pu} + A_{11}^{pl}$	$A_{11}^{s} + A_{11}^{pu} + A_{11}^{pl}$	$A_{11}^{s} + A_{11}^{pu} + A_{11}^{pl}$
$\mathbf{A}^{(A\,2)}$	$B_{11}^{s} + B_{11}^{pu}$	$B_{11}^{s} + B_{11}^{pu}$	$B_{11}^{s} + B_{11}^{pu} + B_{11}^{pl}$	$B_{11}^{s} + B_{11}^{pu} + B_{11}^{pl}$	$B_{11}^{s} + B_{11}^{pu} + B_{11}^{pl}$	$B_{11}^{s} + B_{11}^{pu} + B_{11}^{pl}$
$\mathbf{A}^{(A\,4)}$	$B_{11}^{s} + B_{11}^{pu}$	$B_{11}^{s} + B_{11}^{pu}$	$B_{11}^{s} + B_{11}^{pu} + B_{11}^{pl}$	$B_{11}^{s} + B_{11}^{pu} + B_{11}^{pl}$	$B_{11}^{s} + B_{11}^{pu} + B_{11}^{pl}$	$B_{11}^{s} + B_{11}^{pu} + B_{11}^{pl}$
$\mathbf{A}^{(A\,5)}$	$D_{11}^{s} + D_{11}^{pu}$	$D_{11}^{s} + D_{11}^{pu}$	$D_{11}^{s} + D_{11}^{pu} + D_{11}^{pl}$	$D_{11}^{s} + D_{11}^{pu} + D_{11}^{pl}$	$D_{11}^{s} + D_{11}^{pu} + D_{11}^{pl}$	$D_{11}^{s} + D_{11}^{pu} + D_{11}^{pl}$

Table A-1 (continued)

$\mathbf{B}^{(A\ 5)}$	$F_{55}^{s} + F_{55}^{pu}$	$F_{55}^{s} + F_{55}^{pu}$	$F_{55}^{s} + F_{55}^{pu} + F_{55}^{pl}$	$F_{55}^{s} + F_{55}^{pu} + F_{55}^{pl}$	$F_{55}^{s} + F_{55}^{pu} + F_{55}^{pl}$	$F_{55}^{s} + F_{55}^{pu} + F_{55}^{pl}$
$\mathbf{A}^{(A\ 6)}$	$F_{55}^{s} + F_{55}^{pu}$	$F_{55}^{s} + F_{55}^{pu}$	$F_{55}^{s} + F_{55}^{pu} + F_{55}^{pl}$	$F_{55}^{s} + F_{55}^{pu} + F_{55}^{pl}$	$F_{55}^{s} + F_{55}^{pu} + F_{55}^{pl}$	$F_{55}^{s} + F_{55}^{pu} + F_{55}^{pl}$
$\mathbf{A}^{(A\ 8)}$	$F_{55}^{s} + F_{55}^{pu}$	$F_{55}^{s} + F_{55}^{pu}$	$F_{55}^{s} + F_{55}^{pu} + F_{55}^{pl}$	$F_{55}^{s} + F_{55}^{pu} + F_{55}^{pl}$	$F_{55}^{s} + F_{55}^{pu} + F_{55}^{pl}$	$F_{55}^{s} + F_{55}^{pu} + F_{55}^{pl}$
$\mathbf{A}^{(A\ 9)}$	$F_{55}^{s} + F_{55}^{pu}$	$F_{55}^{s} + F_{55}^{pu}$	$F_{55}^{s} + F_{55}^{pu} + F_{55}^{pl}$	$F_{55}^{s} + F_{55}^{pu} + F_{55}^{pl}$	$F_{55}^{s} + F_{55}^{pu} + F_{55}^{pl}$	$F_{55}^{s} + F_{55}^{pu} + F_{55}^{pl}$
$\mathbf{A}^{(A\ 10)}$	B_{u}^{pu}	B_{u}^{pu}	$B_{bs}^{pu} + B_{bs}^{pl}$	$B_{bs}^{pu} + B_{bs}^{pl}$	$B_{bp}^{pu} + B_{bp}^{pl}$	$B_{bp}^{pu} + B_{bp}^{pl}$
$\mathbf{A}^{(A\ 11)}$	J_{u}^{pu}	J_{u}^{pu}	$J_{bs}^{pu} + J_{bs}^{pl}$	$J_{bs}^{pu} + J_{bs}^{pl}$	$J_{bp}^{pu} + J_{bp}^{pl}$	$J_{bp}^{pu} + J_{bp}^{pl}$

B. Mass Matrix and the Kinetic Energy Coefficients

$$M_{ij}^{uu} = \int_0^L \left(\mathbf{A}^{(B\,1)}\right) \cdot l_i(x) \cdot l_j(x) \cdot dx = \left(\mathbf{A}^{(B\,1)}\right) \cdot \frac{L}{2} \cdot \sum_{k=1}^{\tilde{N}} H_k \cdot l_i(\xi_k) \cdot l_j(\xi_k) \tag{B 1}$$

$$M_{ij}^{u\varphi} = \int_0^L -\left(\mathbf{A}^{(B\,2)}\right) \cdot l_i(x) \cdot l_j(x) \cdot dx = -\left(\mathbf{A}^{(B\,2)}\right) \cdot \frac{L}{2} \cdot \sum_{k=1}^{\tilde{N}} H_k \cdot l_i(\xi_k) \cdot l_j(\xi_k) \tag{B 2}$$

$$M_{ij}^{uw} = 0 \tag{B 3}$$

$$M_{ij}^{\varphi u} = \int_0^L -\left(\mathbf{A}^{(B\,4)}\right) \cdot l_j(x) \cdot l_i(x) \cdot dx = -\left(\mathbf{A}^{(B\,4)}\right) \cdot \frac{L}{2} \cdot \sum_{k=1}^{\tilde{N}} H_k \cdot l_j(\xi_k) \cdot l_i(\xi_k) \tag{B 4}$$

$$M_{ij}^{\varphi\varphi} = \int_0^L \left(\mathbf{A}^{(B\,5)}\right) \cdot l_i(x) \cdot l_j(x) \cdot dx + \left(\mathbf{B}^{(B\,5)}\right) \cdot l_i(x)\big|_{x=L} \cdot l_j(x)\big|_{x=L} = \left(\mathbf{A}^{(B\,5)}\right) \cdot \frac{L}{2} \cdot \sum_{k=1}^{\tilde{N}} H_k \cdot l_i(\xi_k) \cdot l_j(\xi_k) + \left(\mathbf{B}^{(B\,5)}\right) \cdot l_i(\xi_N) \cdot l_j(\xi_N) \tag{B 5}$$

$$M_{ij}^{\varphi w} = 0 \tag{B 6}$$

$$M_{ij}^{wu} = 0 \tag{B 7}$$

$$M_{ij}^{w\varphi} = 0 \tag{B 8}$$

$$\begin{aligned} M_{ij}^{ww} = \int_0^L \left(\left(\mathbf{A}^{(B\,9)} \right) \cdot l_i(x) \cdot l_j(x) \cdot dx \right) + \left(\mathbf{B}^{(B\,9)} \right) \cdot l_i(x)|_{x=L} \cdot l_j(x)\big|_{x=L} \\ = \left(\mathbf{A}^{(B\,9)} \right) \cdot \frac{L}{2} \cdot \sum_{k=1}^{\tilde{N}} H_k \cdot l_i(\xi_k) \cdot l_j(\xi_k) \\ + \left(\mathbf{B}^{(B\,9)} \right) \cdot l_i(\xi_N) \cdot l_j(\xi_N) \end{aligned} \tag{B 9}$$

$$\begin{aligned} p_i = \int_0^L \left(\mathbf{A}^{(B\,10)} \right) \cdot l_i(x) \cdot \frac{\partial}{\partial t} \left(g(t) + x \cdot h(t) \right) \cdot dx + \left(\mathbf{B}^{(B\,10)} \right) \cdot l_i(x)|_{x=L} \\ \cdot \frac{\partial}{\partial t} \left(g(t) + x|_{x=L} \cdot h(t) \right) \\ = \frac{dg(t)}{dt} \cdot \left(\mathbf{A}^{(B\,10)} \right) \cdot \frac{L}{2} \cdot \sum_{k=1}^{\tilde{N}} H_k \cdot l_i(\xi_k) \\ + \frac{dh(t)}{dt} \cdot \left(\mathbf{A}^{(B\,10)} \right) \cdot \frac{L}{2} \cdot \sum_{k=1}^{\tilde{N}} H_k \cdot l_i(\xi_k) \cdot \frac{L \cdot (1 + \xi_k)}{2} \\ + \frac{dg(t)}{dt} \cdot \left(\mathbf{B}^{(B\,10)} \right) \cdot l_i(\xi_N) \\ + \frac{dh(t)}{dt} \cdot \left(\mathbf{B}^{(B\,10)} \right) \cdot l_i(\xi_N) \cdot \frac{L \cdot (1 + \xi_N)}{2} \end{aligned} \tag{B 10}$$

Table B-1 The mass matrix and additional coefficients for six different PEH configurations depicted in Figure 1.3.

Mass Matrix Coefficients	**PEH Configurations**					
	The unimorph PEH without tip mass. (Figure 1.3a)	The unimorph PEH with tip mass at x = L. (Figure 1.3b)	The series-connected bimorph PEH without tip mass. (Figure 1.3c)	The series-connected bimorph PEH with tip mass at x = L. (Figure 1.3d)	The parallel-connected bimorph PEH without tip mass. (Figure 1.3e)	The parallel-connected bimorph PEH with tip mass at x = L. (Figure 1.3f)
$\mathbf{A}^{(\mathrm{B}\,1)}$	$\mathrm{I}_1^{\mathrm{s}} + \mathrm{I}_1^{\mathrm{pu}}$	$\mathrm{I}_1^{\mathrm{s}} + \mathrm{I}_1^{\mathrm{pu}}$	$\mathrm{I}_1^{\mathrm{s}} + \mathrm{I}_1^{\mathrm{pu}} + \mathrm{I}_1^{\mathrm{pl}}$	$\mathrm{I}_1^{\mathrm{s}} + \mathrm{I}_1^{\mathrm{pu}} + \mathrm{I}_1^{\mathrm{pl}}$	$\mathrm{I}_1^{\mathrm{s}} + \mathrm{I}_1^{\mathrm{pu}} + \mathrm{I}_1^{\mathrm{pl}}$	$\mathrm{I}_1^{\mathrm{s}} + \mathrm{I}_1^{\mathrm{pu}} + \mathrm{I}_1^{\mathrm{pl}}$
$\mathbf{A}^{(\mathrm{B}\,2)}$	$\mathrm{I}_2^{\mathrm{s}} + \mathrm{I}_2^{\mathrm{pu}}$	$\mathrm{I}_2^{\mathrm{s}} + \mathrm{I}_2^{\mathrm{pu}}$	$\mathrm{I}_2^{\mathrm{s}} + \mathrm{I}_2^{\mathrm{pu}} + \mathrm{I}_2^{\mathrm{pl}}$	$\mathrm{I}_2^{\mathrm{s}} + \mathrm{I}_2^{\mathrm{pu}} + \mathrm{I}_2^{\mathrm{pl}}$	$\mathrm{I}_2^{\mathrm{s}} + \mathrm{I}_2^{\mathrm{pu}} + \mathrm{I}_2^{\mathrm{pl}}$	$\mathrm{I}_2^{\mathrm{s}} + \mathrm{I}_2^{\mathrm{pu}} + \mathrm{I}_2^{\mathrm{pl}}$
$\mathbf{A}^{(\mathrm{B}\,4)}$	$\mathrm{I}_2^{\mathrm{s}} + \mathrm{I}_2^{\mathrm{pu}}$	$\mathrm{I}_2^{\mathrm{s}} + \mathrm{I}_2^{\mathrm{pu}}$	$\mathrm{I}_2^{\mathrm{s}} + \mathrm{I}_2^{\mathrm{pu}} + \mathrm{I}_2^{\mathrm{pl}}$	$\mathrm{I}_2^{\mathrm{s}} + \mathrm{I}_2^{\mathrm{pu}} + \mathrm{I}_2^{\mathrm{pl}}$	$\mathrm{I}_2^{\mathrm{s}} + \mathrm{I}_2^{\mathrm{pu}} + \mathrm{I}_2^{\mathrm{pl}}$	$\mathrm{I}_2^{\mathrm{s}} + \mathrm{I}_2^{\mathrm{pu}} + \mathrm{I}_2^{\mathrm{pl}}$
$\mathbf{A}^{(\mathrm{B}\,5)}$	$\mathrm{I}_3^{\mathrm{s}} + \mathrm{I}_3^{\mathrm{pu}}$	$\mathrm{I}_3^{\mathrm{s}} + \mathrm{I}_3^{\mathrm{pu}}$	$\mathrm{I}_3^{\mathrm{s}} + \mathrm{I}_3^{\mathrm{pu}} + \mathrm{I}_3^{\mathrm{pl}}$	$\mathrm{I}_3^{\mathrm{s}} + \mathrm{I}_3^{\mathrm{pu}} + \mathrm{I}_3^{\mathrm{pl}}$	$\mathrm{I}_3^{\mathrm{s}} + \mathrm{I}_3^{\mathrm{pu}} + \mathrm{I}_3^{\mathrm{pl}}$	$\mathrm{I}_3^{\mathrm{s}} + \mathrm{I}_3^{\mathrm{pu}} + \mathrm{I}_3^{\mathrm{pl}}$
$\mathbf{B}^{(\mathrm{B}\,5)}$	0	I_{t}	0	I_{t}	0	I_{t}
$\mathbf{A}^{(\mathrm{B}\,9)}$	$\mathrm{I}_1^{\mathrm{s}} + \mathrm{I}_1^{\mathrm{pu}}$	$\mathrm{I}_1^{\mathrm{s}} + \mathrm{I}_1^{\mathrm{pu}}$	$\mathrm{I}_1^{\mathrm{s}} + \mathrm{I}_1^{\mathrm{pu}} + \mathrm{I}_1^{\mathrm{pl}}$	$\mathrm{I}_1^{\mathrm{s}} + \mathrm{I}_1^{\mathrm{pu}} + \mathrm{I}_1^{\mathrm{pl}}$	$\mathrm{I}_1^{\mathrm{s}} + \mathrm{I}_1^{\mathrm{pu}} + \mathrm{I}_1^{\mathrm{pl}}$	$\mathrm{I}_1^{\mathrm{s}} + \mathrm{I}_1^{\mathrm{pu}} + \mathrm{I}_1^{\mathrm{pl}}$

Table B-1 (continued)

$\mathbf{B}^{(B\,9)}$	0	M_t	0	M_t	0	M_t
$\mathbf{A}^{(B\,10)}$	$I_1^s + I_1^{pu}$	$I_1^s + I_1^{pu}$	$I_1^s + I_1^{pu} + I_1^{pl}$	$I_1^s + I_1^{pu} + I_1^{pl}$	$I_1^s + I_1^{pu} + I_1^{pl}$	$I_1^s + I_1^{pu} + I_1^{pl}$
$\mathbf{B}^{(B\,10)}$	0	M_t	0	M_t	0	M_t
$\mathbf{A}^{(B\,1)}$	$I_1^s + I_1^{pu}$	$I_1^s + I_1^{pu}$	$I_1^s + I_1^{pu} + I_1^{pl}$	$I_1^s + I_1^{pu} + I_1^{pl}$	$I_1^s + I_1^{pu} + I_1^{pl}$	$I_1^s + I_1^{pu} + I_1^{pl}$

C. GLL Abscissa and Weights MATLAB Code

```
function [weight , abscissa] = gll(N)

syms x

exp1 = diff(legendreP(N - 1, x), x);
exp2 = sort(double(subs(x,solve(exp1 == 0, x))), 'Ascend');
exp3 = zeros(1,N-2);

for i = 1:N-2

    exp3(i) = 2 / ((N * (N - 1)) * legendreP(N - 1, exp2(i))^2);

end

abscissa = [-1; exp2; 1];
weight = [(2 / (N * (N - 1))), exp3, (2 / (N * (N - 1)))]';

end
```